

Universidade de Santiago de Compostela  
Departamento de Física de Partículas



**PERIPHERAL COLLISIONS INDUCED  
BY  $^{124}\text{Xe}$  AND  $^{136}\text{Xe}$  PROJECTILES AT  
RELATIVISTIC ENERGIES**

**Manuel Fernández Ordóñez**  
under the supervision of  
José Benlliure Anaya

January 2007



UNIVERSIDAD DE SANTIAGO DE COMPOSTELA



**FACULTAD DE FISICA**

Departamento de Física de Partículas

**Peripheral collisions induced by  $^{124}\text{Xe}$  and  $^{136}\text{Xe}$   
projectiles at relativistic energies**

Memoria presentada por:

**Manuel Fernández Ordóñez**

como disertación para optar al

**Grado de Doctor en Ciencias Físicas**

18 de Enero de 2007



# Contents

<b>Introduction</b>	<b>1</b>
<b>1 Physics with heavy ions: peripheral reactions</b>	<b>5</b>
1.1 Present understanding of heavy-ion collisions . . . . .	6
1.1.1 First stage: Abrasion and INC models . . . . .	7
1.1.2 Second stage: Evaporation . . . . .	8
1.1.3 Residual nuclei produced in fragmentation reactions . . . . .	8
1.2 Codes describing relativistic peripheral heavy-ion collisions . . . . .	9
1.2.1 Semi-classical approach: the Glauber model . . . . .	10
1.2.2 Semi-empirical models . . . . .	11
1.2.2.1 Silberberg-Tsao . . . . .	11
1.2.2.2 EPAX . . . . .	11
1.2.3 Abrasion codes: ABRA . . . . .	12
1.2.4 Intra-nuclear cascade codes . . . . .	13
1.2.4.1 ISABEL . . . . .	14
1.2.4.2 INCL4 . . . . .	14
1.2.5 Evaporation codes: ABLA . . . . .	16
1.2.6 Modelization of the longitudinal momentum of the projectile residues . . . . .	18
<b>2 Experimental Technique</b>	<b>21</b>
2.1 The experimental facilities . . . . .	22
2.1.1 The GSI accelerator system . . . . .	22
2.1.2 Beam monitoring . . . . .	23
2.1.3 The targets . . . . .	24
2.1.4 The fragment separator: FRS . . . . .	25
2.2 Separation and Identification of the Projectile Residues . . . . .	27
2.2.0.1 Multi-wire proportional chambers . . . . .	29
2.2.0.2 Plastic scintillators . . . . .	29
2.2.1 Measurement of the reduced momentum . . . . .	30
2.2.2 Energy-loss measurement . . . . .	31
2.2.3 Isotopic identification . . . . .	32
2.2.3.1 Atomic number . . . . .	32

2.2.3.2	Mass number identification	34
<b>3</b>	<b>Measured cross sections and momentum distributions</b>	<b>39</b>
3.1	Beam current normalization . . . . .	40
3.2	Target normalization . . . . .	41
3.3	Production yields and associated corrections . . . . .	42
3.3.1	Momentum distributions . . . . .	43
3.3.2	Corrections to the production yields . . . . .	45
3.3.2.1	Dead time	45
3.3.2.2	Multiple reactions in the target	46
3.3.2.3	Transmission	47
3.3.2.4	Secondary reactions	48
3.3.2.5	Ionic charge states	49
3.4	Uncertainties . . . . .	52
3.5	Measured cross-sections and momentum distributions . . . . .	53
<b>4</b>	<b>Systematic investigation of heavy-ion peripheral collisions at relativistic energies.</b>	<b>57</b>
4.1	Role of the target size . . . . .	58
4.2	Role of the neutron excess of the projectile . . . . .	64
4.3	Role of the projectile energy . . . . .	67
4.4	Longitudinal momentum distributions . . . . .	75
4.4.1	Role of the target size . . . . .	75
4.4.2	Neutron excess of the projectile . . . . .	80
4.4.3	Role of the projectile energy . . . . .	81
4.4.4	Width of the longitudinal momentum distributions . . . . .	81
<b>5</b>	<b>Charge-exchange reactions</b>	<b>87</b>
5.1	Single charge-pickup reactions . . . . .	88
5.1.1	Measured data: isotopic distributions . . . . .	88
5.1.2	Systematic comparison to other data . . . . .	91
5.1.3	Benchmark of model calculations . . . . .	98
5.2	Double charge-exchange reactions . . . . .	101
5.2.1	Measured data: isotopic distributions . . . . .	102
5.2.2	Total cross-sections: systematics . . . . .	103
5.2.3	Benchmark of model calculations . . . . .	104
5.3	Isobaric charge-exchange reactions. . . . .	106
5.3.1	Mechanism of the resonant charge-exchange: isobar model . .	107
5.3.2	Mechanism for quasielastic charge-exchanges: Gamow-Teller strengths . . . . .	108
5.4	Determination of matter and charge radii using $\Delta$ -resonance excitation in isobaric charge-exchange reactions . . . . .	109
5.4.1	Existing methods for matter and charge radii determination .	109

5.4.2	$\Delta$ -resonance excitation in isobar charge-exchange reactions . .	112
5.4.2.1	Determination of the experimental resonant cross section in isobar charge-exchange reactions	112
5.4.3	Experimental Results. . . . .	118
5.4.4	Neutron and proton r.m.s. radii determination using Glauber model calculations . . . . .	123
5.4.5	Discussion of the results . . . . .	129
5.4.6	Comparison with the antiproton annihilation method . . . . .	131
<b>Conclusions</b>		<b>135</b>
<b>Resumen en Castellano</b>		<b>145</b>
<b>A Layers of matter in the beam line</b>		<b>161</b>
<b>B Measured cross-sections</b>		<b>165</b>
<b>C Isobar Model description</b>		<b>177</b>
C.1	Proton-pickup reactions . . . . .	179
C.1.1	In proton-Nucleus reactions . . . . .	180
C.1.2	In neutron-Nucleus reactions . . . . .	181
C.1.3	Extension to the Nucleus-Nucleus reactions . . . . .	182
C.2	Neutron-pickup reactions . . . . .	182
C.2.1	In proton-Nucleus reactions . . . . .	182
C.2.2	In neutron-Nucleus reactions . . . . .	183
C.2.3	Extension to the Nucleus-Nucleus reactions . . . . .	183
<b>D Glauber model notes</b>		<b>187</b>
D.1	Special simplifications for the charge-pickup reactions . . . . .	189



# Introduction

Nuclear Physics is, as every scientific area, an evolving discipline where new frontiers are open up continuously. A vast number of scientists and efforts have been made in the last century but, in retrospect, we can only wonder at the quality and predictive value of nuclear models which have been developed over the last 50 years. Three of the four interactions existing in the Universe are present inside the nucleus, being one of the best laboratories to study the strong and weak forces. However nowadays, a global description of nuclei cannot be formally derived from fundamental interactions. Many things are known about nuclear matter, but much more are still unclear. This is one of the most exciting topics concerning nuclear physics and many efforts are focused in this area of science.

For these reasons, a large and extensive campaign of measurements focused on the heavy-ion collisions at relativistic energies has been developed at the GSI laboratory (Darmstadt, Germany) during the last years, being this work included in the frame of those experiments. The purposes of the project were to study a set of nuclear reactions to obtain a systematic overview in the fission-fragmentation processes involved, and to define a benchmark data collection in order to compare the results of the simulation codes related to the subject. The involved institutes together with the GSI were the *Institute de Physique Nucleaire* IPN (Orsay, France), *Commissariat a l'Energie Atomique* DAPNIA/SPhN (Saclay, France) and the *Universidad de Santiago de Compostela* (Spain).

The subject of this dissertation is the study of the nuclear phenomena appearing in the most peripheral fragmentation reactions of heavy-ion collisions and, in particular, we will address the mechanism of the intranuclear cascade occurring as a sequence of nucleon-nucleon collisions. Using our measurements we will investigate the nature of these nucleon-nucleon collisions, the energy deposited in the nucleus and their sensitivity to the radial distribution of protons and neutrons in the nucleus. These studies could put some light into the reaction mechanisms occurring at lower excitation energies where the impact parameter of the collision is large. Several reactions were studied in this work:  $^{136}\text{Xe} + \text{H}$ , Be, Ti, Pb at 1000 MeV/u,  $^{136}\text{Xe} + \text{H}$ , D, Ti at 500 MeV/u,  $^{136}\text{Xe} + \text{H}$ , Ti at 200 MeV/u measured in 2002

and  $^{124}\text{Xe} + \text{Be}, \text{Pb}$  at 1000 MeV/u measured in 2003. The variety of the data measured in this work will provide valuable information concerning the fragmentation process. The influence of certain parameters as the nature of target and projectile, or its energy, as well as benchmark the predictive power of several codes extensively used to describe the fragmentation reactions will be explored.

The experiments were performed by accelerating  $^{124,136}\text{Xe}$  projectiles in the conditions described above and studying the residues outcoming from the reaction. The produced residual nuclides were fully identified in mass and atomic numbers in a time shorter than 300 ns, while flying forward, using the FRS magnetic spectrometer and a dedicated detection setup. This is a very exigent technique called *inverse kinematics*, and the develop of this kind of experiments is already a challenge itself. As the main goal of the work is the measurement of the production cross sections of the projectile residues created in the reaction, three independent parameters have to be measured: the production rate of each residue, the beam intensity and the target thickness. Different detectors were used to fully identify, unambiguously, the reaction residues, as well as determine their longitudinal momentum distributions.

This dissertation opens with a discussion concerning the present understanding of the peripheral heavy-ion reactions at relativistic energies. The picture of participants and spectators will be presented here and, the image of heavy-ion reactions taking place in two different stages will be introduced. Several useful concepts which will be used later in this work as evaporation corridor, limiting fragmentation, memory effect or factorization will be presented here. Exploring the predictive power of the models describing the fragmentation reactions is a key topic in this work. The first chapter of this work is also devoted to the description of several models and codes commonly used in relativistic heavy-ion collisions. The Glauber or Silberberg-Tsao models, as well as the EPAX, ISABEL, INCL4, ABRA or ABLA codes will be introduced here. The final part of the chapter will concern the models describing the velocity distribution of fragmentation residues.

The following chapter concerns the experimental method used in this work. The separation of heavy-ions is a very exigent task, specially at low energies, and it is worth to explain some points that characterize this technique. A detailed discussion concerning the FRagment Separator, the specific experimental setup used in this work and the identification procedure will be given in this chapter.

The corrections applied to the measured yields are the main topic of the third chapter in this work. Several factors affecting the measurements must be corrected in order to determine the projectile residues cross sections with high accuracy. The charge-states contaminating the residues yields are one of the most important difficulties in this analysis, specially at low energies. The target normalization and the beam intensity determination are key parameters of the cross sections measurements

and, consequently, will be carefully discussed. At the end of the chapter, the complete set of data measured in this work (production cross sections and longitudinal velocities) will be schematically presented.

The discussion of the measured data will be performed in chapter 4, the outline of the main features observed in the cross sections and momentum distributions will be presented. Due to the variety and precision of the measured data, we will be able to explore the dependence of the production cross sections and momenta with parameters as the projectile or target nature, projectile neutron excess, projectile energy or the role played by the excitation energy in the reactions. The predictive power of several codes describing the fragmentation reactions will be also benchmarked.

Chapter 5 is devoted, specifically, to a special kind of very peripheral reactions, the charge-exchange process, where residues with atomic numbers beyond the projectile appear in the reaction. The isotopic cross sections and momenta of the single and double charge-exchange reactions will be presented in this chapter. The discussion of the data obtained, comparisons with previous existing data and the available codes will be systematically performed, exploring the influence of different parameters as the projectile energy and target or projectile nature. These kind of reactions can take place by two different mechanisms -both driven by the exchange of virtual pions- quasielastic and resonant, and the study of the latter can provide valuable information on the matter distributions inside the nucleus. Measuring both charge-exchange channels (n,p) and (p,n), relevant information on the neutron thickness of the projectile could be derived from the velocity distributions of residues created in what we have called *isobar charge-exchange reactions*. In the final part of this chapter we will propose a method based on the charge-exchange reactions and relying on the Glauber model to extract information concerning the r.m.s. radii of a nucleus.

In order to simplify the dissertation, several theoretical and technical discussions have been consigned to external appendixes attached at the end of this work. A summary of the measured production cross sections, as well as a list of the layers of matter placed in the beam line within the FRS have been also relegated to the final place of this manuscript.



# Chapter 1

## Physics with heavy ions: peripheral reactions

Nuclei are quantum many-body systems of strongly interacting particles called nucleons. Through many years, nucleons were thought to be the most fundamental blocks of matter, and nuclei were described as a densely packed assembly of neutrons and protons, bound together by a strong force carried by pions and other mesons. Since the discovery of the quarks in the 1960s, our knowledge in nuclear and particle physics has dramatically increased and nowadays, we understand that the nucleus constituents are made up of more fundamental pointlike constituents bound together through interactions mediated by gluons.

The interactions between the constituents of the nucleus are well known when they are free in nature. However, their interactions are modified when they are inside a nucleus, and the nature of these in-medium modifications are still unrevealed. The main objective of this work is devoted to the microscopic processes that drive the reaction mechanism between heavy-ions at relativistic energies and, in particular, the influence of the in-medium properties in the nucleon-nucleon interactions and the distributions of matter (neutrons and protons) inside the nucleus. For this goal we have performed a systematic study of the isotopic production cross sections and longitudinal momentum of projectile residues created in peripheral reactions of heavy-ions at relativistic energies. The large variety of projectile-target-energy combinations studied in this work will be very useful to test the influence of several parameters in the reaction mechanism.

This chapter opens with a discussion concerning the present understanding of the peripheral heavy-ion reactions at relativistic energies, concepts as participant, spectator, abrasion and evaporation will be introduced here. Also, the hypothesis of

a fragmentation reaction taking place in two subsequent stages will be pointed out. The chapter continues with the introduction of some relevant concepts that will be used in this work later on, as the memory effect, the limiting fragmentation or the evaporation corridor.

Deriving expressions -from fundamental interactions- which put some light in what really happens inside a nucleus is an unrealistic task, and we can only rely on models. Models are valuable tools in the study of nuclear reactions which are continuously updated and each new measurement is a chance to benchmark their predictive power. Several of these models will be extensively used in this work, being the second part of this chapter devoted to describe, briefly, their main characteristics.

## 1.1 Present understanding of heavy-ion collisions

The reactions between nuclei at relativistic energies can be described in the frame of the participant-spectator image. Actually this is a geometrical separation relying on the following observation: residues with large longitudinal momentum come from reactions with small scattering angles, meaning that during a relativistic-energy collision the nucleons move almost on a straight line. This leads to the following conclusion: for a given impact parameter, the nucleons lying in the geometrical overlap between projectile and target nuclei interact and are called *participants*, while nucleons outside this interaction zone will be the *spectators*. In the zone of the participants, a considerable part of the beam energy is converted into heat and high temperatures are reached (fireball), while the spectator matter remains relatively cold. After this stage, usually called *abrasion*, the target spectator is nearly at rest and the projectile spectator moves with almost beam velocity. The spectator pieces, called *prefragments*, are excited due to the additional surface energy, few participants which have penetrated the spectator matter and the energy of the holes left by the nucleons removed in the collision. This excitation energy could decompose the prefragment into one or several heavy fragments plus a number of nucleons by several mechanisms as evaporation, fission or multifragmentation. As the impact parameter decreases, the size of the spectator nuclei also decreases in favor of the fireball size, which is maximum in the case of central collisions.

The reactions between two nuclei at relativistic energies proceed in two subsequent steps with very different characteristic times, as already proposed by Serber [1] in 1947. In the first abrasion stage, the participant nucleons from target and projectile interact very fast -about  $10^{-23}$  s- and introduces a certain amount of excitation energy in the system. During the second slow stage -  $\sim 10^{-20}$  s- the projectile residue thermalizes and decays to the stable nuclei by particle evaporation. As Ser-

ber wrote: *"In some sense the two-step model is the idea of a compound nucleus reaction extended to high energies"*. In what follows we will describe, roughly, these two stages of the fragmentation reactions.

### 1.1.1 First stage: Abrasion and INC models

There are several models describing the first stage of the fragmentation reactions, we can divide them according to their microscopic or macroscopic description of the interaction between projectile and target. Concerning the formers we are dealing with the Intra-Nuclear Cascade models (INC), already explored by Goldberger [2] in 1948 using Monte-Carlo methods and a two-dimensional model of the nucleus. The evolution of the INC models continued with the work of Metropolis [3] and Bertini [4]. There are most recent INC codes, being nowadays the most extended, ISABEL by Yariv and Fraenkel [5, 6] and INCL by Cugnon [7, 8, 9]

In these models the nuclear reaction is treated as a series of individual nucleon-nucleon interactions considered in a classical way, taking into account some quantum considerations as the Pauli blocking. The relativistic energy of the projectile allows to use this picture because the wavelength of the incoming particle is of the order than the average inter-nucleon distance within the nucleus. Typically, there are two kinds of INC models, depending of the treatment of the nuclear medium: the Bertini-like models, where the nucleus is considered as a Fermi sea of nucleons and the nuclear density is step-like with up to 16 divisions including diffuse boundaries; and Cugnon-like models, where all the nucleons present in the projectile and target are followed during all the reaction process. Examples of these models are the ISABEL and INCL4 codes, respectively, which will be discussed in detail later in this chapter.

Concerning the macroscopic description, we have to talk about the Abrasion model [10]. This relies in the assumption of a clean cut between the target and projectile. If the velocity of the projectile is much larger than the Fermi velocity of the nucleons in the potential well, nucleon-nucleon collisions are mainly restricted to the overlapping volume between target and projectile. Depending on the impact parameter, a distribution of projectile fragments with different masses and charges are formed during the abrasion stage. The mass loss can be determined geometrically integrating the overlapping volume and, for a given mass loss, the  $N/Z$  distribution is determined by the neutron-to-proton ratio of the precursor nucleus. This geometrical hypothesis has been justified using Glauber-type calculations [11], which will be extensively used in this work and will be also described in detail later in this chapter. All of these features are implemented in the code ABRABLA [12, 13], which will be also discussed below.

### 1.1.2 Second stage: Evaporation

The second part of the reaction, the evaporation (*ablation*) or deexcitation of the prefragment, is based on the statistical model. The pre-fragments may be considered as an ensemble characterized by a few macroscopic variables as the mass number, the neutron excess, the excitation energy or the angular momentum. Assuming that the pre-fragment resulting from the abrasion cascade is thermalized, one deals with a compound nucleus, as proposed initially by Weisskopf [14] already in 1937. The excitation energy is dissipated by either particle emission (evaporation) or fission. In the modern models, the nucleus may evaporate single nucleons as well as  $\alpha$ -particles, and light-nuclei (deuterium,  $^3\text{He}$ , ...). ABLA ([12] and [13]) is one of the most extended codes for the description of the evaporation stage. It will be carefully discussed in section 1.2.5.

### 1.1.3 Residual nuclei produced in fragmentation reactions

The nature of the final projectile residues produced in fragmentation reactions depends on both stages of the reaction. The impact parameter will be related with the number of abraded nucleons in the first stage, while the number of abraded nucleons will provide the excitation energy for the evaporation stage. In this work we will concentrate our study in projectile residues with mass losses up to 30 nucleons. As stated in [15], residues close to the primary projectile arise from peripheral collisions of heavy-ions or relativistic protons with the target nucleus, understanding peripheral as collisions with a large impact parameter. There have been many experimental works concerning the production cross sections of fragmentation residues and several general features have been learned since then. In this section we will perform a brief discussion concerning key topics concluded from the experimental results obtained in fragmentation reactions.

The isotopic distribution of projectile residues becomes approximately independent from the energy above a certain threshold of the projectile total kinetic energy. This is the main idea relying under the concept of *limiting fragmentation*, first proposed by Benecke [16] in the frame of particle physics and subsequently applied to heavy-ion reactions by Heckman[17] and Cumming [18] We will be able to check this hypothesis with our experimental data.

The role of the neutron excess of the projectile in the reaction mechanism will be also treated in this work, thus the concept of *memory effect* must be introduced here. As higher is the mass number of the projectile, so does its N/Z ratio. It is reasonable to think that this neutron excess could be partially lost during the evaporation stage, due to the preference for neutron emission (caused for the Coulomb

barrier in the case of proton emission). Summerer [19] stated that there exists a complete memory loss for residues very far in mass from the projectile, and this fact is related with the excitation energy gained in the abrasion stage, concluding that the loss of memory develops gradually with increasing the length of the evaporation chain. Also, when the prefragment is highly excited, this long evaporation chain leads to final residues close to the  $\Gamma_n/\Gamma_p = 1$  line <sup>1</sup> [20, 21] in what Dufour [22] called the *evaporation corridor*, where the isotopic distributions of the residues are largely independent from the original nucleus.

Another observed feature in the fragmentation reactions with different targets is that the cross sections for a specific near-projectile residue differ only by a constant factor that is close to the ratio of the total reaction cross sections. The concept of *factorization* [18] is hidden behind this behavior. For high energies, this states that the cross section for forming the residue  $c$  will depend on the nature of the target  $b$  only via a total cross section term:

$$F_{ab}^c = \sigma_{ab} \gamma_a^c(q_{||}, q_{\perp}) \quad (1.1)$$

where  $\sigma_{ab}$  is the total cross section for the projectile  $a$  impinging onto a target  $b$  and  $\gamma_a^c$  is a factor describing the production of the residues  $c$  from the projectile  $a$  independently of the nature of the target  $b$ . Thus we expect to observe residue production cross sections independent of the target nature (except for a total cross section).

All of these concepts introduced here will be helpful in the description of the amount of data measured in this work. This discussion will be held in chapters 4 and 5.

## 1.2 Codes describing relativistic peripheral heavy-ion collisions

The complexity of the interactions between nucleons inside a nucleus makes it very difficult to extract any formalism derived from fundamental interactions. This has lead, during the evolution of nuclear physics, to the appearance of models describing the nature of nuclei. Models are very useful tools providing valuable infor-

---

<sup>1</sup>The probability of neutron emission is higher than the proton emission due to the Coulomb barrier. However, for projectile prefragments with large excitation energies, the evaporation chain can reach the region where the  $\Gamma_n = \Gamma_p$ . Beyond this point it is more probable the emission of protons, thus being the limit for neutron evaporation.

mation concerning the reaction mechanism or key parameters involved in nuclear reactions. They are also very useful to plan experiments with exotic nuclei beams, where count rates predictions are needed. In addition, they provide nuclear data bases very useful in other fields as radiation physics, shieldings or material studies. However, generally models have different ranges of validity, and stating the validity of each code is a key point for producing reliable data bases in nuclear reactions. There exist many codes describing heavy-ion reactions reactions, theoretical models as Glauber or the Eikonal approximation, semi-empirical models as EPAX or the Silberberg-Tsao, the abrasion-ablation models or the intra-nuclear cascades further coupled to evaporation codes. In this work we will be able to benchmark the predictive power of several codes by comparing with our experimental data. In what follows we will describe the main characteristic of some of these codes.

### 1.2.1 Semi-classical approach: the Glauber model

The Glauber model [11] is a semiclassical approach extensively applied to heavy ion collision for describing a number of interaction processes over a wide range of energies above the Fermi energy. The model gives the nucleus-nucleus interaction in terms of interaction between the constituent nucleons with a given density distribution, in the impact parameter representation and with the nuclei moving along the collision direction in a straight path.

Glauber model will be extensively discussed in chapter 5, here we will only mention that this model states that the reaction cross sections between two nuclei with mass numbers  $A$  and  $B$  is given by the expression:

$$\sigma^{AB} = \int d\mathbf{b} \{1 - [1 - T(\mathbf{b})\sigma_{NN}]^{AB}\} \quad (1.2)$$

where the  $T(b)$  is the *thickness function*, derived from the matter densities distributions of both nuclei in the impact parameter ( $b$ ) representation. This expression reveals the importance of studying the distributions of matter inside the nuclei. Accurate descriptions of the r.m.s. radii and smoothness of the matter distributions are key topics in order to obtain reliable predictions from the abrasion and INC models, being important parameters in the calculation of the overlapping volume between target and projectile.

## 1.2.2 Semi-empirical models

Semi-empirical models are based on analytical expressions derived from fits to experimental data. Compared to physical models of high-energy fragmentation reactions (as the intra-nuclear cascades), which in general involve time-consuming Monte Carlo calculations, the virtue of an analytical formula lies in the short computing time and the possibility to calculate easily cross sections that are beyond the reach of physical model calculations.

### 1.2.2.1 Silberberg-Tsao

The Silberberg-Tsao model [23] describes a scaling algorithm by which partial elemental cross-sections from nucleus-nucleus collisions can be estimated by scaling the corresponding proton-nucleus cross-sections. This procedure relies on the experimentally verified [24] concept that the projectile fragmentation cross-section obey the so-called weak factorization property. In this concept the partial cross-section for the production of fragment  $f$  can be expressed as:

$$\sigma_c = \Gamma_a^c \Gamma_{a,b} \quad (1.3)$$

where  $\Gamma_a^c$  is a factor which depends upon the species of projectile and fragment, and  $\Gamma_{a,b}$  is a factor which depends only on the species of the projectile and target, as already stated in expression 1.1.

This Silberberg-Tsao model uses the participant-spectator models and Glauber scattering theory to estimate the projectile and target (average) participants. This algorithm has been tested sufficiently robust over the energy range 0.1-2.0 GeV/u with no restrictions on the sizes of target nor projectile nuclei, predicting the cross-section within a 10 % around 1 GeV/u . The S-T algorithm is an efficient tool for modelling of cosmic rays and other nuclear spallation data.

### 1.2.2.2 EPAX

In 1990, K.Summerer [19] proposed a universal empirical parametrization of fragmentation cross-sections which has been updated several times until the last version [25]. This expression has certain constrictions: a) is valid only in the *limiting fragmentation* regime, that is, for projectile energies where the fragmentation yields are no longer energy dependent (well above the Fermi energy  $\sim 40$  MeV/u). b)

The range of validity is limited to projectiles from around Argon to below the Lead and Bismuth isotopes. With these assumptions, the cross-section of a fragment with mass  $A$  and charge  $Z$  produced by projectile fragmentation from a projectile  $(A_p, Z_p)$  impinging on a target  $(A_t, Z_t)$  is given by:

$$\sigma(A, Z) = Y_A \cdot \sigma(Z_{prob} - Z) = Y_A \cdot n \cdot e^{-R \cdot |Z_{prob} - Z|^{U_n(p)}} \quad (1.4)$$

where the first term  $Y_A$  represents the mass yield, that is, the sum of the isobaric cross-sections with fragment mass  $A$ . The second term describes the charge dispersion, the distribution of elemental cross-sections with a given mass around its maximum,  $Z_{prob}$ . The shape of the charge distribution is controlled by the width parameter  $R$  and the exponent  $U_n$  ( $U_p$ ) on the neutron (proton) rich side of the residue corridor<sup>2</sup>. The factor  $n = \sqrt{R/\pi}$  is the normalization the charge dispersion. For clarity we will mention that the dependence on the target and projectile combination is hidden in the  $Y_A$  factor.

### 1.2.3 Abrasion codes: ABRA

Abra [12] is an abrasion code developed for the description of the fragmentation process in the relativistic energy domain. The number of removed nucleons is determined by the volume of the overlapping zone and depends only on the impact parameter. From the number of removed nucleons and their nature (neutrons or protons), the code must determine the initial conditions for the subsequent evaporation stage, that is mass number, neutron excess, excitation energy and angular momentum. The N/Z ratio of the prefragment is calculated according to the hypergeometrical model, where there is no correlation at all between the nucleons during the abrasion, that is, each nucleon has a statistical chance to be neutron or proton.

During the abrasion, a certain number of single particle levels is vacated (holes), thus the excitation energy of the prefragments is calculated by the sum of the energies of these holes with respect to the Fermi surface. Including final-state interactions derived from measured isotopic cross-sections [26], an average excitation energy of 27 MeV per abraded nucleon has been induced.

The angular momentum distribution [27] is given in analogy to Goldhaber's description for the linear momentum (section 1.2.6), and is defined as the the angular momenta of the nucleons removed:

---

<sup>2</sup>For fragments far away from the projectile (mass losses larger than 15%) the isotopic distributions are independent of the original nucleus, this is called the residue corridor. Here, the distributions are governed by statistical evaporation from highly excited prefragments.

$$\langle J^2 \rangle = \langle j^2 \rangle \frac{A'(A_p - A')}{A_p - 1} \quad (1.5)$$

where  $A'$  is the prefragment mass number and  $\langle j^2 \rangle$  is the quadratic mean value of the angular momentum of a nucleon in the nucleus. This value grows with the mass number, according to the shell model.

Actually this code takes into account an additional intermediate stage between the abrasion and the evaporation, the multifragmentation. This stage accounts for the simultaneous emission of nucleons and clusters (simultaneous break-up) that take place due to thermal instabilities when the temperature of the projectile spectator exceeds 5.5 MeV (see [28]). This measured effect has been modeled in ABRA in a rough way, if the temperature of the prefragment after the abrasion is larger than 5.5 MeV, the additional energy is used for the formation of clusters and their simultaneous emission together with single nucleons. The influence of the multifragmentation will not play a key role in the discussion of our data, however it is included here for completeness.

### 1.2.4 Intra-nuclear cascade codes

Microscopic calculations concerning the first stage of the reactions, the abrasion, can be performed with the so called intra-nuclear cascade (INC) models. At relativistic energies the nucleon-nucleon sequential interactions may be considered as intra-nuclear cascade interactions rather than interactions in the mean-field. This assumption is used in the INC codes briefly introduced here, which can be considered as transport codes of hadrons within the nucleus. The INC study as a two-body interaction propagated through the nucleus, was first investigated by Goldberger in 1948 by using a two-dimensional Monte-Carlo model [2]. A more realistic study was the one of Metropolis in 1958 [3], considered as the pioneering of all the later produced codes.

Typically there are two types of INC codes, depending on the treatment of the nuclear medium: the Bertini-like codes, where the nuclear density is considered continuous; and the Cugnon-like codes where the nucleons are treated individually from the beginning. Common to all modern codes is the semi-classical treatment: particle's (and quasiparticle's) positions and momenta are defined according to relativistic classical mechanics. The nucleon-nucleon interactions are defined from free-NN cross sections. The cascade is initiated by the projectile's nucleon hitting somewhere on the target sphere (only the radial density dependence is considered). The first NN impact triggers the cascade and it runs until some cutoff condition is fulfilled. We

will describe in this section two different codes, ISABEL and INCL4. Both are semiclassical approaches in the sense that all the particles involved in the process (neutrons, protons, pions and  $\Delta$ -resonances) have perfectly known trajectories in the phase-space and the unique quantum consideration is the Pauli principle.

#### 1.2.4.1 ISABEL

ISABEL code ([5], [6]) can treat nucleon-nucleus and nucleus-nucleus interactions. The ion-ion collisions are performed by selecting first the overlapping areas of the nuclei, and then the initial interacting nucleons. The overlapping nucleons can interact with the Fermi-sea of the partner nucleus. ISABEL includes diffuseness, what makes it well suited for peripheral reactions studies. But the nuclear matter compressibility is not included, so it cannot deal with central collisions.

The nuclear density is step-like with up to 16 divisions and includes diffuse boundaries. The target and projectile nucleons are considered within a potential well, and their momentum distributions are defined according to that of the degenerated Fermi gas. At a given time interval defined by the velocity, and mean-free-path defined by free-NN cross sections, the situation is examined. In case of no interaction, the particle goes on. In case of interaction, it can be either elastic (definition of the new four-momentum vector) or inelastic ( $NN \rightarrow N\Delta$  and  $\Delta \rightarrow \pi N$ ). In the latter case the pion is propagated till it is absorbed in a recombination  $\pi N \rightarrow \Delta$ . After each step the number of cascade nucleons increases and so the density is depleted. The density rearrangement is treated in several ways. The later versions allow the interaction among cascade-particles, in addition to collisions of cascade particles with nucleons of the Fermi-sea. Pauli blocking, the only quantum restriction, is taken into account excluding the cascade particles with an energy below the Fermi level. The cascade continues till the most energetic cascade particle falls below a certain energy level, or it has left the nucleus before. The final energy is evaluated according to the sum of the hole and particle energies which fall below the cutoff energy. The cutoff is selected as the Coulomb barrier plus two times the binding-energy (all above the Fermi energy).

#### 1.2.4.2 INCL4

The INCL4 code [7] is characterized by the fact that it follows all the nucleons present in the target and projectile during all the intra-nuclear process. In this code, all the particles are moving around, and when two of them fall below a *minimal distance*, defined as the radius of a sphere with area equal to the particle-particle cross section, the collision takes place. The elastic and inelastic treatment is conceptually

the same as ISABEL, through the excitation of  $\Delta$ -resonances and  $\pi$  decays. For NN-collisions the free cross sections are used above 400 MeV. Below that energy in-medium correction are considered. The resulting position-momenta of the interaction are calculated, and the collision is allowed only if the phase-space is not yet occupied by another particle. In that way the Pauli blocking is included. A realistic surface of the nuclear potential has been included in the new version of the code (version 4), thus the nucleons suffer refraction effects when reaching the boundary of the nucleus.

Actually, an INC-code follows till a final de-excited residue is produced, but it is stopped at a certain time before. The reason for including that halt-condition, is that the evaporation pattern depends sensitively on the level density from complicated configurations, different from the single-particle motion to which INC implicitly corresponds, so the description would not be realistic. The energy of the pre-fragment will correspond to the difference between the final kinetic energies sum, referred to the potential well, and that of the ground state; i.e., the kinetic energy of a Fermi gas with the final number of nucleons, again referred to the potential well.

An important improvement in the version 4 of INCL, is the introduction of a diffuse nuclear surface. corresponding to a Saxon-Woods density distribution up to a maximum distance  $R_{max}$ , fixed to  $R_0 + 8a$ :

$$\rho(r) = \begin{cases} \frac{\rho_0}{1 + \exp(\frac{r-R_0}{a})} & \text{for } r < R_{max} \\ 0 & \text{for } r > R_{max} \end{cases} \quad (1.6)$$

The values of  $R_0$  and  $a$  are taken from electron scattering measurements and parametrized, from Al to U, as  $R_0 = (2.745 \times 10^{-4} A + 1.063) A^{1/3}$  fm,  $a = 0.510 + 1.63 \times 10^{-4} A$  fm. In the code, other values, as well as another shape for  $\rho(r)$  can optionally be introduced. The quantity  $\rho_0$  is such that the distribution is normalized to the mass number  $A$ . The reader must regard that the matter distribution is not divided on its neutron and proton parts.

Both intra-nuclear cascade models, ISABEL and INCL4 are coupled to the code ABLA to simulate the evaporation stage of the reaction, with the method described below.

### 1.2.5 Evaporation codes: ABLA

The ABLA code ([12] and [13]) was developed to describe the second part of the reaction, the *ablation* or deexcitation of the prefragment, and is based on the statistical model [14]. Assuming that the pre-fragment resulting from the abrasion cascade is thermalized, the excitation energy is dissipated by either particle emission (evaporation) or fission and the deexcitation chain continues while there is available excitation energy.

The probability  $P(\omega)$  of a certain deexcitation channel  $\omega$  in each deexcitation step  $n$ , is evaluated as the ratio of its width  $\Gamma_\omega^n$  over the sum of the widths of all present channels

$$P(\omega)^n = \frac{\Gamma_\omega^n}{\sum_{\Omega} \Gamma_{\Omega}^n} \quad (1.7)$$

The particle decay widths are obtained in the basis of the statistical model, as proposed initially by Weisskopf. The original description only preserves the energy of the compound nucleus, while the conservation of the angular momentum was added latter by Wolfstein [29] and Hauser-Feshbach [30]. For the curious reader, all those results are reviewed in the works of Ericsson [31] and Darrah-Thomas [32]. Following the description of the latter, we can write the width of a certain channel by integrating the probability of emission from a certain initial compound nucleus with energy  $E_i$  and momentum  $J_i$  to a final compound nucleus given by  $E_f$  and  $J_f$ :

$$\Gamma_{\Omega} = \int_{S_{\Omega}-B_{\Omega}}^{E_i-B_{\Omega}} \left[ \sum_{J_f} \frac{1}{2\pi} \cdot \frac{\rho(E_f, J_f)}{\rho(E_i, J_i)} \cdot \sum_{S=|J_f-s|}^{|J_f+s|} \sum_{l=|J_i-s|}^{|J_i+s|} \tau_l(u) \right] du \quad (1.8)$$

where  $\rho_{i|f}$  are the level densities of the initial and final states, respectively.  $s$  the spin of the emitted particle,  $l$  the angular momentum between the residue and the emitted particle,  $B$  refers to the Coulomb barrier,  $S$  concerns to the separation energies and  $\tau$  is the transmission coefficient given by the penetration through the potential barrier for the particle capture process. The possibility of realistic evaluations of  $\Gamma_{\nu}$  depends on the simplifications applied to expression 1.8. If the level density is described as  $\rho(U) \propto e^{(aU)^{1/2}}$  and the temperature as  $U = aT^2$ , where  $a$  is the level density parameter, the expression 1.8 can be integrated:

$$\Gamma_{\nu} \approx \frac{2m_{\nu}R_f^2g_{\nu}T_f^2}{\hbar^2} \frac{\rho_f(E^* - S_{\nu} - B_{\nu})}{\rho_i(E^*)} \quad (1.9)$$

where  $\nu$  refers to the particle type,  $S$  its separation energy,  $m$  its mass,  $g$  its spin degeneracy,  $B$  the Coulomb barrier,  $E^*$  the excitation energy of the initial compound nucleus,  $R$  its radius,  $T$  the temperature of the initial nucleus, and  $\rho_{i|f}$  is the level density describing the initial and final states, respectively. The Coulomb barrier in the evaporation of protons, deuterium,  $\alpha$  particles, etc are parametrized as:

$$B_\nu = \frac{e^2 Z_\nu \cdot (Z - Z_\nu)}{r_0 (A - A_\nu)^{1/3}} \quad (1.10)$$

where  $A_\nu$  is the particle mass,  $Z_\nu$  the particle charge,  $e$  is the charge unit and  $r_0=2.08$  fm.

The fission width is described by using the Bohr-Wheeler model [33] according to the Moretto formulation [34]

$$\Gamma_f = \frac{1}{2\pi} \frac{1}{\rho(E_i, J_i)} \int_0^{E_i - B_{sad}} \rho(E_i - B_{sad} - u, J_i) du \quad (1.11)$$

where  $sad$  denotes the saddle point and  $B_{sad}$  is the fission barrier. The same description of the level density used above leads to:

$$\Gamma_f = \frac{T_f \rho_f(E^* - B_f)}{2\pi \rho_i(E^*)} \quad (1.12)$$

where  $E^* - B_f$  is the energy above the saddle point,  $B_f$  is the fission barrier as described in [35]. In our study we will neglect the fission channels, having a minor role in the population of the residual production we have measured, but the concept was introduced here for a complete picture of the deexcitation process.

Also  $\gamma$ -ray emission is treated in this code, for a complete description see [36]. The channel is always open if no transitional restrictions appear. Usually only giant resonances are of importance, and the electric dipole resonance E1 (GDR) gives the largest contribution. In our region of study, for nuclei with masses  $A \sim 100-200$ , the  $\gamma$ -emission is known to exceed the neutron emission only for excitation energies below 20 KeV above the neutron-threshold [37]. Only below the nucleon binding energies or in case of strongly momentum-restricted available states (nearly the reaction energy threshold), the  $\gamma$ -ray emission competes appreciably with particle emission. The ABLA code also includes the microscopic effects of shells and pairing in the level density as described in [12].

### 1.2.6 Modelization of the longitudinal momentum of the projectile residues

In this work, one of the important observables is the longitudinal momentum of projectile residues. Basically, two models are the most extended to describe the linear momentum transfer in the fragmentation reactions, Morrisey and Goldhaber models. The former one [38] is an empirical fit to existing data. This model is compatible with a two-step reaction process, where the momentum transferred to the residue is a function of the mass loss (excitation energy) and projectile velocity, but independent of the mass of the target-projectile combination. The excitation energy induced in the collision is dissipated in a further evaporation stage. This stage induces a certain dispersion around the mean momenta, which affects the width of the momentum distributions. Empirically, the available data on the average longitudinal momenta induced by relativistic heavy-ion collisions show a linear dependence with the mass difference between the final fragment and the projectile:

$$q = -8 \cdot (A_p - A_f) = -8 \cdot \Delta A \quad (MeV/c) \quad (1.13)$$

Morrisey also found in the data a systematic behavior on the widths of the momentum distributions depending on the mass difference between final fragment and projectile. This relation is given by:

$$\sigma_{(p_{\parallel})} = \frac{150}{\sqrt{3}} \cdot \sqrt{A_p - A_f} \quad (MeV/c) \quad (1.14)$$

The width of the momentum distributions show a dependence on the square-root of the mass loss. This empirical observation has been also pointed out by Goldhaber in the frame of the statistical model [39]. He showed that this dependence arises simply due to the conservation of momentum and leads to a Gaussian momentum distribution related with the Fermi momentum of the clusters inside the projectile as follows:

$$\sigma_{(p_{\parallel})} = \frac{p_F}{\sqrt{5}} \cdot \sqrt{\frac{A_f \cdot (A_p - A_f)}{A_p - 1}} (MeV/c) \quad (1.15)$$

This Fermi momentum of the nucleons inside the nucleus,  $p_F$ , depends on the nucleus under study and is taken to be 265 MeV/c in our work [40]. Both models predict a parabolic dependence of the momentum width with the mass loss. The

differences between them arises from the evaporation stage. Morrissey systematic is an empirical fit to the measured data, and consequently, the evaporation stage is already included in the behavior of the expression 1.14. However, in the Goldhaber model, the evaporation is not considered, being specially suitable for describing residues very close to the projectile, where the excitation energy is small.



# Chapter 2

## Experimental Technique

To investigate the fragmentation process in reactions induced by the  $^{124}\text{Xe}$  and  $^{136}\text{Xe}$  projectiles with several targets, we decided to measure the isotopic production cross sections and longitudinal velocities of the reaction residues. In this work we have investigated projectile fragmentation residues using a technique called *inverse kinematics*. These are reactions where the projectile fragments produced in the reaction are projected in the forward direction, allowing to analyze them with a magnetic spectrometer. The experiments took place at GSI, Darmstadt. Nowadays, this is the only facility worldwide that makes it possible to perform this kind of measurements: accelerating heavy-ions at relativistic energies (up to 1 GeV/u for  $^{238}\text{U}$  or 1.4 GeV/u for  $^{136}\text{Xe}$  projectiles) with high intensities (up to  $10^8$  ions/s for  $^{136}\text{Xe}$  projectiles) and the further identification of the reaction residues with a magnetic spectrometer. The short time needed for the isotopic identification of projectile residues, below 300 ns, makes it possible to measure their primary production before any radioactive decay.

In this chapter we open make a brief description of the experimental facilities used in these experiments: the acceleration systems, the beam monitoring device, the targets and the fragment separator. Finally we also describe in detail the identification procedure.

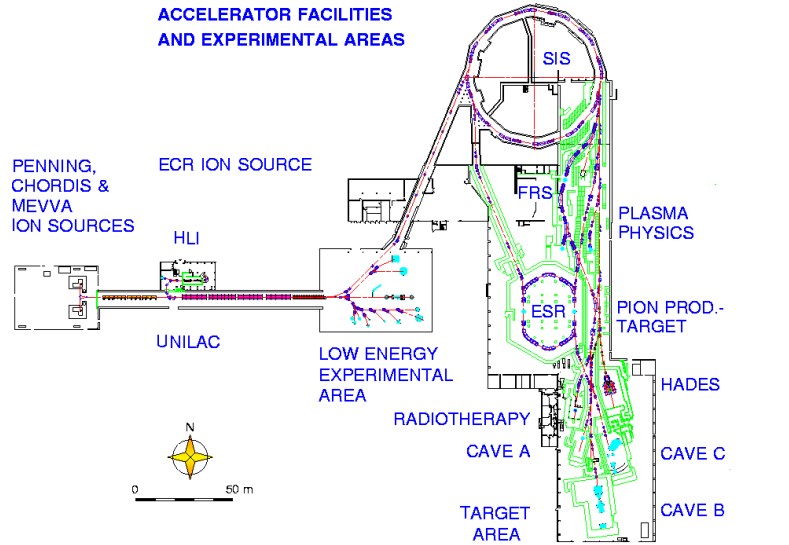


Figure 2.1: Schematic representatio of the GSI (Darmstadt) experimental facilities. In this drawing we can observe the two acceleration stages, the UNILAC and SIS, and the experimental areas, in particular the Fragment Separator, FRS.

## 2.1 The experimental facilities

### 2.1.1 The GSI accelerator system

The GSI accelerator system is composed by several ion sources and two consecutive stages of acceleration (see fig 2.1). In our experiments, the Xenon gas was ionized and extracted from the ion source, being injected then into the first acceleration stage, consisting in a 30 m linear accelerator (UNILAC). This accelerator is subdivided in two sections, being the first one the so-called prestripper linac, consisting of a combination of RFQ (Radio Frequency Quadrupole) and IH (Interdigital H-Mode) structures, operated at 36 MHz. This linac accelerates beam currents up to  $I_{max} = A/q \cdot 0.25$  mA ( $A$  mass,  $q$  charge state of ion). The 36 MHz high current prestripper linac was commissioned in 1999 and replaced the 25 years old 27 MHz Wideroe type linac. The ions are then stripped at 1400 keV/u in a transverse nitrogen gas jet and are charge-analyzed before injection into the main linac, with its Alvarez-type structure, operated at 108 MHz. In the Alvarez section three different ions can be accelerated to individual energies in a pulse-switched mode, either for injection into the SIS, or for low energy experiments downstream the UNILAC. In our case, the Xenon isotopes were accelerated untill 11.4 MeV/u and injected into the synchrotron.

The second acceleration stage consist on the SIS [41] synchrotron, with a perimeter of 216 m and a maximum bending power of 18 Tm. It consist on 24 dipoles, 36 quadrupoles and few additional magnetic sextupoles to correct chromatic aberrations. The 18 Tm bending power corresponds to a maximum energy of 1.4 GeV/u for a  $^{136}\text{Xe}$  beam. The slow extraction mode, used for this experiment, leads to a low emittance of the beam and to a spill length of few seconds (see fig 2.2), maintaining the momentum spread  $\delta p = \frac{\Delta p}{p}$  below  $10^{-3}$  during the whole experiment.

Another key point for the production rate of the fragments is the intensity of the primary beam. The GSI accelerators can deliver beams of  $^{136}\text{Xe}$  with an intensity up to  $10^9$  particles/spill. The beam profile can be suitable selected during the experiment as desired, but standard values used in this measurements were a cycle length of 10 s with a spill length of 6 s (see figure 2.2).

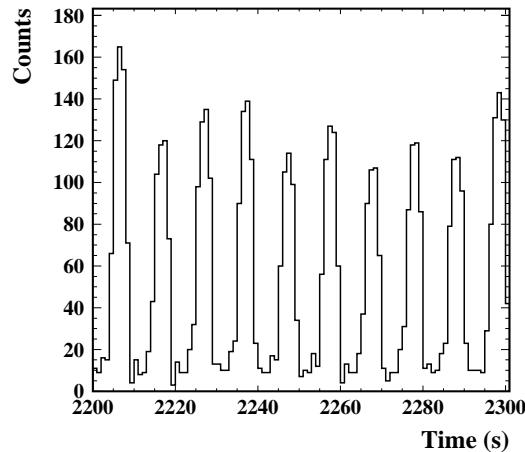


Figure 2.2: *Beam profile as a function of time for this experiment measured with the beam monitor SEETRAM. The typical beam cycle of this experiment is shown in the figure, with a cycle length of 10 s and a spill length of 6 s.*

## 2.1.2 Beam monitoring

The intensity of the primary beam impinging on the target was continuously monitored during the experiment in order to normalize the measured yields of projectile residues. This beam monitor must fulfill several requirements: it should keep a linear response with the beam intensity, even for the highest beam rates ( $10^8$  particles/second), it should preserve the quality of the beam emittance and, finally, the reaction rate of the beam particles within the atoms of the detector should be kept as low as possible. For this purpose we used a **SE**condary **E**lectron **TR**ansmission **M**onitor (SEETRAM) [42]. This detector consists on three titanium foils of  $10\ \mu\text{m}$  thickness each, placed in the beam line in front of the target. The outer titanium

foils are connected to a potential of +80 V, while the inner one is grounded. The secondary electron emission induced by a relativistic heavy ion passing through the inner foil is driven to the outer layers due to the potential. The resulting positive current in the inner foil is measured with a current digitizer, producing a digital output signal (SEETRAM units) which is recorded with a scaler.

Even if no beam is passing through the SEETRAM, there is a black current which produces a nearly constant background that must be subtracted from the measured current in order to determine the beam flux (see figure 2.2):

$$N_0 = N_{SEETRAM} - N_{background} \quad (2.1)$$

The absolute calibration of the monitor has to be determined using a reference detector providing the number of projectiles per time unit [43] (in this case a plastic scintillator). The range of the SEETRAM must be adjusted during the experiment depending on the intensity and the energy of the beam, in order to avoid saturation problems. This range scales from  $10^{-4}$  to  $10^{-10}$ . The relation between the number of SEETRAM units and the real number of beam projectiles ( $N_{beam}$ ) is given by:

$$N_{beam} = N_0 \cdot f \cdot 10^{10} \cdot sensitivity \quad (2.2)$$

where  $f$  is the calibration factor, which depends on the nature of the projectile and its energy. The method applied to obtain this factor will be explained in chapter 2 (see section 3.1).

### 2.1.3 The targets

Several targets were used in these measurements. We have used solid targets of berillium, titanium and lead, and liquid targets of hydrogen and deuterium. Their thicknesses are presented in table 2.1

The hydrogen and deuterium targets were inside a container [44] and the contribution of this layers of matter to the production yields must be removed. In order to do that, measurements with the empty target container were performed. This target consist on four titanium foils and thin mylar foils coated with a very thin aluminium layer for thermal isolation of the cryogenic target. In addition the SEETRAM monitor and the accelerator window contribute to the production yields in the case of the dummy target. The summary of the thickness of all layers of matter

Target	Thickness ( $mg/cm^2$ )
hydrogen	$87.2 \pm 3.0$
deuterium	$201.0 \pm 6.7$
titanium	$54.3 \pm 2.8$
beryllium	$1023.0 \pm 35.5 \dagger$
beryllium	$2526.0 \pm 113.6 \dagger$
lead	$635.0 \pm 10.6$

Table 2.1: *Thicknesses of the different targets used in the experiments presented in this work. The targets marked as  $\dagger$  also have a  $221 \pm 2$   $mg/cm^2$  thickness niobium stripper. In the case of the titanium target, the thickness corresponds to the sum of all layers of matter listed in table 2.2.*

present in the target area during the empty target measurements are shown in table 2.2

Layer	Material	Thickness ( $mg/cm^2$ )	Atoms $\times 10^{20}/cm^2$
Ti window	Ti	4.5	0.57
SEETRAM	Ti	13.5	1.69
Ti target	Ti	36.32	4.57
Mylar	$C_5H_4O_2$	8.3	0.52
Aluminium	Al	0.1	0.02

Table 2.2: *Thicknesses of all different layers of matter placed in the target area for the empty target measurements.*

The target thicknesses were chosen as a compromise between the production rates and the secondary-reaction rates [45]. The accuracy of the final cross-sections depends on a precise knowledge of the target thickness ( $l_T$ ). The thickness of the liquid targets can change along the direction perpendicular to the beam due to the pressure inside the container. A specific experiment was performed to quantify this contribution [46] and the final variation of the target thickness inside the beam spot was estimated to be less than 3% for the cross-sections measurements.

### 2.1.4 The fragment separator: FRS

The FRS is an achromatic zero-degree magnetic spectrometer [47] consisting in four independent identical stages (see Fig 2.3). Each stage is composed by one H-type  $30^\circ$  dipole, five quadrupoles and a set of sextupoles. Two of the quadrupoles

are placed before the dipole to enlarge the horizontal component of the emittance, while minimizing the vertical one. The three other quadrupoles are placed behind the dipole and are used to achieve the first-order optical conditions within the four image planes of the FRS. The sextupoles, in-front and behind the dipoles, are used for higher-order optical corrections.

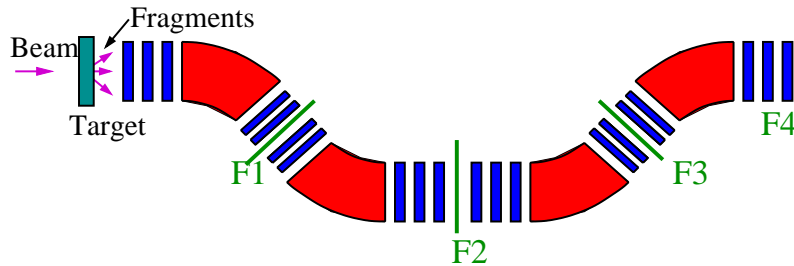


Figure 2.3: *Schematic view of the FFragment Separator. This magnetic spectrometer consists on four identical stages, the separator is composed by four dipoles, twenty quadrupoles and a set of sextupoles (not included in the figure). This magnetic device has four focal planes, denoted as F1, F2, F3 and F4 in the figure.*

The FRS can be driven in three different operation modes: achromatic, monoenergetic and high-acceptance mode [47]. In the present experiment we used the achromatic mode, where point-to-point images are obtained between the entrance and the final image plane all along the  $\sim 70$  m of flight path. This is achieved because the dispersion<sup>1</sup> of the dipoles in the second half ( $D_{24}=8.41$  cm/%) of the FRS compensate that of the first half ( $D_{02}=7.25$  cm/%), resulting the whole system achromatic with a magnification of  $V=D_{24}/D_{02}=1.160$ . This values were calibrated during the experiment by registering the trajectory of the primary beam through the spectrometer with different values of the magnetic fields in the dipoles.

The FRS has a maximum angular acceptance of  $\pm 15$  mrad for its central trajectory, and a momentum acceptance of  $\pm 1.5\%$ , given by the physical transversal apertures and its ion-optical properties. Further constraints are given by the radii of the four dipoles ( $\sim 11$  m), and their maximum magnetic field (1.6 T), which result in a maximum magnetic rigidity of 18 T·m. Another characteristic is its high resolving power of 1500, determined for an emittance of  $20\pi$  mm·mrad and a beam spot of 2.7 mm (FWHM).

<sup>1</sup>The dispersion of an optical system relates the change in position due to a difference in momentum. This magnitude is usually given in cm/%, that is, a variation in momentum  $\Delta p/p$  of a given percentage, results in a variation in position of some cm.

## 2.2 Separation and Identification of the Projectile Residues

The challenge of these kind of experiments is the unambiguous identification of all projectile residues outcoming the reaction with the target. This identification relies in the behavior of charged particles moving in the presence of a magnetic field. According to the electromagnetic laws, these particles follow curved trajectories, and the most relevant features of this movement can be summarized in the following expression:

$$B\rho = 3.107 \cdot \frac{A}{Q} \cdot \beta\gamma \quad (2.3)$$

where the magnetic rigidity,  $B\rho$ , is simply the magnetic field where the particle moves multiplied by the curvature radius of the particle trajectory.  $A$  and  $Q$  are the mass number and atomic charge<sup>2</sup> of the ion,  $\beta\gamma$  is its reduced momentum and 3.107 is a proportionality constant which takes into account the dimensions.

In figure 2.4 we represent the experimental setup used in our experiment. Measuring the magnetic rigidity ( $B\rho$ ) and the velocity ( $\beta\gamma$ ) we can determine the value of the ratio  $A/Q$ . The magnetic rigidity is determined by measuring the transversal positions and the time-of-flight with the scintillators SC2 and SC4 in the figure. If we additionally measure the atomic charge ( $Q$ ), we are able to identify, without any doubt, all the nuclei arriving at the final focal plane (F4) of the FRS. This measurement is done with the multi-sampling ionization chambers MUSIC's. In the following we will describe in detail the experimental method and the detectors.

The four magnetic dipoles of the FRS make it possible to bend the trajectory of a nucleus according to expression 2.3. Depending on this bending, the nucleus will reach the focal planes of the FRS at different transversal positions. The ion-optical theory [48] states that the transversal position of a nucleus at a given focal plane  $s$ , with respect to the phase-space configuration at the initial position  $i$  can be written as:

$$x_s = (x|x_i)_s x_i + (x|x'_i)_s x'_i + (x|y_i)_s y_i + (x|y'_i)_s y'_i + (x|(\delta B\rho)_i)_s (\delta B\rho)_i \quad (2.4)$$

By definition, at the focal planes, there is no correlation between the transversal

---

<sup>2</sup> $Q$  can actually differs from the atomic number of the ion  $Z$  if the nucleus is not fully stripped.

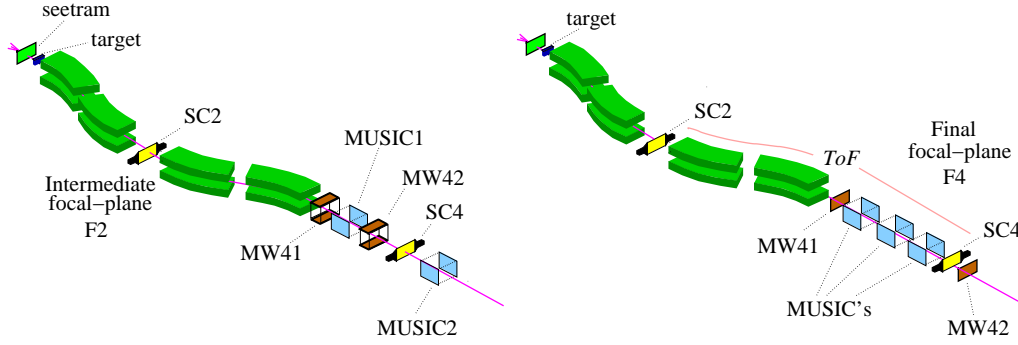


Figure 2.4: *Experimental setups used for the experiments described in this work at 1000 MeV/u and 500 MeV/u (left panel). At 200 MeV/u (right panel) three ionization chambers were used to improve the resolution in the energy-loss measurements.*

positions  $x$  and the transversal angles  $x'$  and  $y'$ , and expression 2.4 will transform in:

$$x_s = (x|x_i)_s x_i + (x|y_i)_s y_i + (x|(\delta B\rho)_i)_s (\delta B\rho)_i \quad (2.5)$$

where  $(x|y_i)_s y_i$  is the variation of the transversal position with the vertical position, the parameters  $(x|x_i)$  and  $(x|(\delta B\rho)_i)$  represent the magnification and the dispersion of the spectrometer, respectively. We have to clarify that the magnetic rigidity is usually denoted as the relative deviation from the corresponding value of a particle following the central trajectory,  $(B\rho)_0$ , along the separator:

$$(\delta B\rho)_s = \frac{(B\rho)_s - (B\rho)_0}{(B\rho)_0} \quad (2.6)$$

If we concentrate now in the second half of the FRS, we can combine expressions 2.5 and 2.6 to get the following equation:

$$(B\rho)_{24} = (B\rho)_0 \cdot \left( 1 - \frac{1}{D_{24}} \cdot (x_4 - V_{24} \cdot x_2) \right) \quad (2.7)$$

where  $x_2$  and  $x_4$  are the positions of the ion at the intermediate and final focal planes, respectively,  $D_{24}$  is the dispersion in the second half of the FRS and  $V_{24}$  its magnification.

As we can derive from expression 2.7, knowing the ion-optics parameters in the second half of the FRS ( $D_{24}$  and  $V_{24}$ ) and the magnetic rigidity of the central

trajectory, we can determine the magnetic rigidity of any nucleus traversing the FRS from its transversal positions at the two focal planes, F2 and F4. The magnitude  $(B\rho)_0$  is determined by passing the primary beam centered through the FRS and determining the effective values of the radii. For the measurements of the transversal positions two plastic scintillators and several multi-wire chambers were used. In the following we will describe the main characteristics of these detectors.

### 2.2.0.1 Multi-wire proportional chambers

These position sensitive detectors were specially designed to stand high beam intensities and to provide precise measurements in both transversal directions to the beam trajectory. We have used 6 multi-wire (MW) detectors [49, 50], two at the intermediate focal plane, two at the final focal plane, one at the first and one at the third focal planes. All of them, except those placed at the final focal plane F4 are isolated from the vacuum by 100  $\mu\text{m}$  titanium windows. The F4 MW is isolated from the air by 25  $\mu\text{m}$  kapton windows. Any material placed through the FRS beam line affects the achromatism of the system, for this reason, these detectors are used only for calibration purposes. Therefore, during the physical measurements all MW except those placed at F4 (which are already out of the FRS) were removed from the beam line.

The MW detectors used at the FRS consist on three parallel wire planes (actually five, but only three of them were used in these experiments [49]) connected to different high voltages. The central plane is grounded and is made of 20  $\mu\text{m}$  tungsten wires separated by 2 mm. The others are made of 50  $\mu\text{m}$  wires separated by 1 mm. The gap between the planes is filled with a mixture of Ar,  $\text{CO}_2$  and alcohol at atmospheric pressure.

### 2.2.0.2 Plastic scintillators

A detector system composed by two plastic scintillators [51] was used to measure the transversal positions of the fragments at the two focal planes F2 and F4 (see fig. 2.4). These detectors have to stand high intensities ( $\leq 10^5$  Hz) with a high efficiency, and, at the same time introduce the less possible non-uniformities in order to preserve the achromaticity of the system and its high resolution. The thicknesses of the plastics are  $\sim 5$  mm and their sensitive areas ( $219 \times 80$  mm<sup>2</sup> for the plastic placed at the intermediate focal plane SC2, and  $200 \times 80$  mm<sup>2</sup> for the plastic placed at the final focal plane, SC4) assures the complete covering of the focal planes.

The scintillators are made of BC420 plastic material, providing a high light

output which is driven by total internal reflection to both UV-transmissive light guides placed at the borders of each plastic and connected to two fast response photomultipliers HAMAMATSU R2083. The position of the ions is determined by the time difference between the signals arriving to each side of the plastic. The signals from the photomultipliers are filtered by a constant-fraction-discriminator with a given threshold which allows to eliminate the noise and cut the lighter nuclei that have less interest for this work.

As explained above, the multi-wire detectors were used only for calibrations purposes, in particular to calibrate in position both plastic scintillators, SC2 and SC4. In figure 2.5, the position spectrum measured with one of the multi-wire proportional chambers is plotted versus the response given by the plastic SC2. In this plot we can observe how the response given by this plastic was not linear, actually, we have used a 5<sup>th</sup> degree polynomial fit for its position calibration.

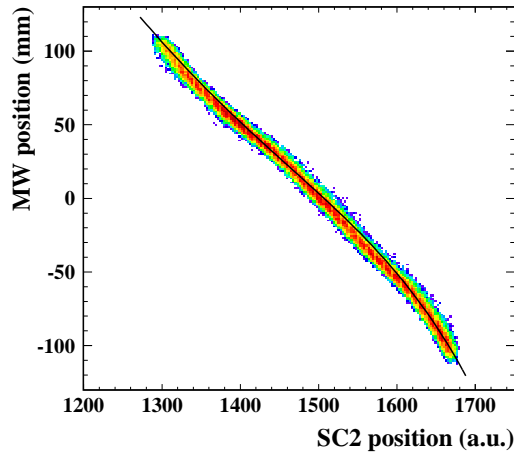


Figure 2.5: Cluster plot of the response given by the plastic scintillator at F2 compared with the position given by the multi-wire proportional chamber placed close to the plastic. The calibration fit corresponds to the solid line in the spectrum.

### 2.2.1 Measurement of the reduced momentum

The determination of the reduced momenta  $\beta\gamma$  of the projectile fragments is achieved by measuring the time of flight (ToF) through the spectrometer (see the figure 2.4). The ToF is measured in the second-half of the FRS using the time-difference signals between the scintillators placed at F2 and F4. As explained above, each scintillator provides two signals, one from each side. These signals filtered with a constant fraction discriminator (CFD) are sent to a time-to-amplitude converter (TAC). We measured the time of flight combining both signals, left (L) and right (R) in the following way to obtain an average ToF\*:

$$ToF^* = \alpha_L \cdot ToF_L^* + \alpha_R \cdot ToF_R^* = (T_2 - T_0) - T_4 \quad (2.8)$$

where  $\alpha_L$  and  $\alpha_R$  are the TAC calibration factors obtained with a pulse generator of adjustable frequency. We have to clarify that the start signal ( $T_4$ ) for the ToF measurement is given by the scintillator at F4, while the stop signal ( $T_2$ ) is given by the scintillator at F2 delayed by a quantity  $T_0$  in order to assured the arrival of stop the signal after the start. The real ToF is then obtained as:

$$ToF = T_4 - T_2 = T_0 - ToF^* \quad (2.9)$$

The parameter  $T_0$  was obtained by comparing the  $ToF^*$  signals of the primary beam with the inverse of its velocity,  $1/v$  after traversing different layers of matter. The velocity was calculated with the code AMADEUS [52], and the results were fitted to a first degree polynomial function:

$$\frac{1}{v} = \frac{T_0}{l_0} - \frac{ToF^*}{l_0} \quad (2.10)$$

where the two parameters of the fit are  $l_0$  (the path length of the primary beam from the scintillator at F2 till the scintillator at F4 (see figure 2.4)) and  $T_0$  the signal delay. Typical times of light involved in this experiment are  $\sim 200$  ns, with a time resolution around 150 ps (FWHM).

## 2.2.2 Energy-loss measurement

Once we have determined the reduced momentum  $\beta\gamma$  and the magnetic rigidity  $B\rho$  of the projectile residues, from equation 2.3 we can derive the quantity  $A/Q$ . To identify now the isotope we need an additional measurement of the atomic number  $Z^3$ , and the identification of its charge-state. For these measurements we have used two or three multi-sampling ionization chambers, depending on the energy range of the residues to be measured<sup>4</sup>.

---

<sup>3</sup>The charges under study ( $\leq 55$ ) have a lower contamination due to ionic charge-states, that is the nuclear charge  $Z$  is equal to the ionic charge  $Q$  in most of the cases, we will treat this point in detail in the next chapter.

<sup>4</sup>The charge-states contamination increases as going down in energy. For low energies, as 200 MeV/u, the contamination due to the charge-states would spoil out the energy-loss resolution if we do not use three ionization chambers (see reference [53]).

The Multi-Sampling Ionization Chambers (MUSIC's) [54] are placed at the exit of the FRS, close to the final focal plane F4. The four independent anodes per chamber provide a four-fold measurement of the energy loss of the projectile fragments with a 100% efficiency for the typical counting rates of our experiment ( $\leq 10^3$  particles/s). The MUSIC volume which contains the sensitive part is 600 mm long, the window area is about  $276 \times 150$  mm<sup>2</sup> and is filled with P10 gas (10% Methane and 90% Argon) at atmospheric pressure and room temperature as active medium. The windows are made up of 25  $\mu$ m Al-coated kapton.

A charged particle traversing a medium, loses energy proportionally to the square of its charge and the inverse of its velocity, according to the Bethe-Bloch expression. The gas of a MUSIC is ionized when the projectile residues traverses its active area, and the cloud of secondary electrons drifts to the anodes due the electric field of 4000 V applied inside. The electron drift velocities in this gas is  $\sim 5$  cm/ $\mu$ s, which corresponds to a drift time of approximately 5  $\mu$ s.

The independent anode signals may be used also for time measurements: the plastic scintillator at F4 provides a start signal for a TAC, while the stop signal is provided by the anode. In this way, the four independent drift times can be used to measure both, the position along the horizontal direction transversal to the beam axis and the angle of the fragment trajectory.

## 2.2.3 Isotopic identification

### 2.2.3.1 Atomic number

The energy lost by the projectile fragments in the MUSIC chambers ( $\Delta E_f$ ), is a function of its atomic number( $Z$ ), velocity( $v$ ) and transversal position( $x$ ). The latter dependence is due to the drift time of the charge carriers and recombination effects in the gas. All these dependencies must be corrected if we want to determine the atomic number of the projectile fragments according to the following expression:

$$\Delta E_f \propto \frac{Z^2}{f(v) \cdot g(x)} \quad (2.11)$$

where the dependence in the fragment velocity,  $f(v)$ , was determined by analyzing the functional velocity dependence of the energy loss with the code AMADEUS [52]. The dependence with the fragment transversal position,  $g(x)$ , was determined by fitting the dependence of the mean energy-loss value for the four anodes with the transversal positions given by the scintillator at F4. In figure 2.6 it is shown

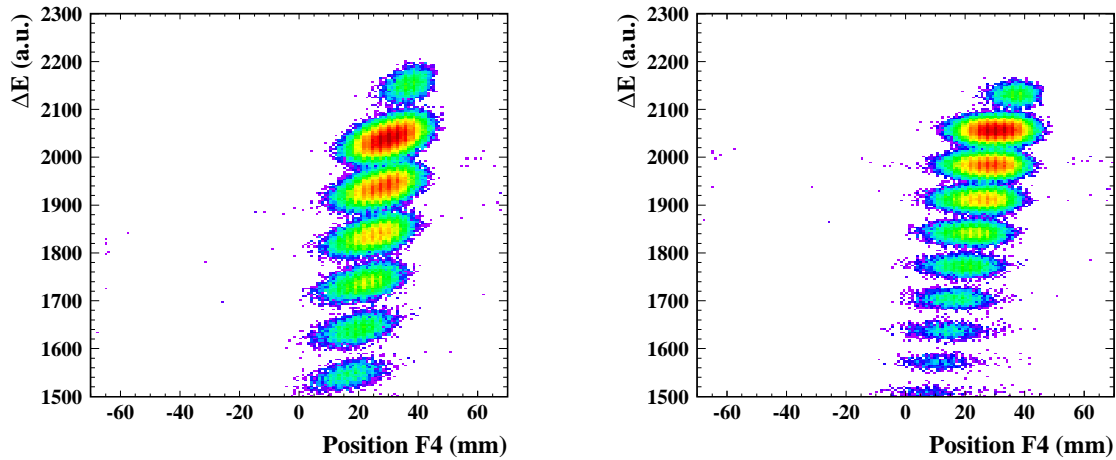


Figure 2.6: *Dependence of the energy lost by the fragments with the transversal position (left panel). This dependence was corrected by the function  $g(x)$  (see expression 2.11) and the result is shown in the right panel. This plot corresponds to the reaction  $^{136}\text{Xe} + \text{H}$  at 1000 MeV/u.*

how this dependence looks like, on the left panel the raw energy-loss signals coming from the MUSIC's are plotted as a function of the transversal position of the fragments. In the right panel we show the energy-loss signals after correcting the linear dependence with the transversal position. The improvement achieved in the charge resolution is considerable, as can be observed in the figure 2.7, in this plot the energy-loss signals are corrected from the the transversal position and the velocity dependence. Moreover, the signals coming from both MUSIC's were combined in order to improve the charge resolution and discard secondary reactions, and also changes in the atomic charge-states between both chambers. In the measurements performed at 200 MeV/u, three ionization chambers were used in order to improve the energy-loss resolution.

The charge resolution is energy-dependent. The resolutions decreases with the projectile energy, as can be seen in the figure 2.7 and 2.8 for the three energies analyzed in this work. As decreasing the energy of the residues, the probability of charge exchanges during the crossing of the fragments through the gas dramatically increases. Therefore, the energy-loss distribution becomes wider as a result of the fluctuations in the atomic charge of the residues, leading to a decrease of the resolution of the ionization chambers. The results of the energy-loss resolutions obtained in this work are summarized in table 2.3 as a function of the energy of the primary projectile.

The identification of the atomic number for each fragment is achieved by comparing its energy-loss signal with those corresponding to the projectile (see figure 2.9). The later can be unambiguously known because we have performed measurements

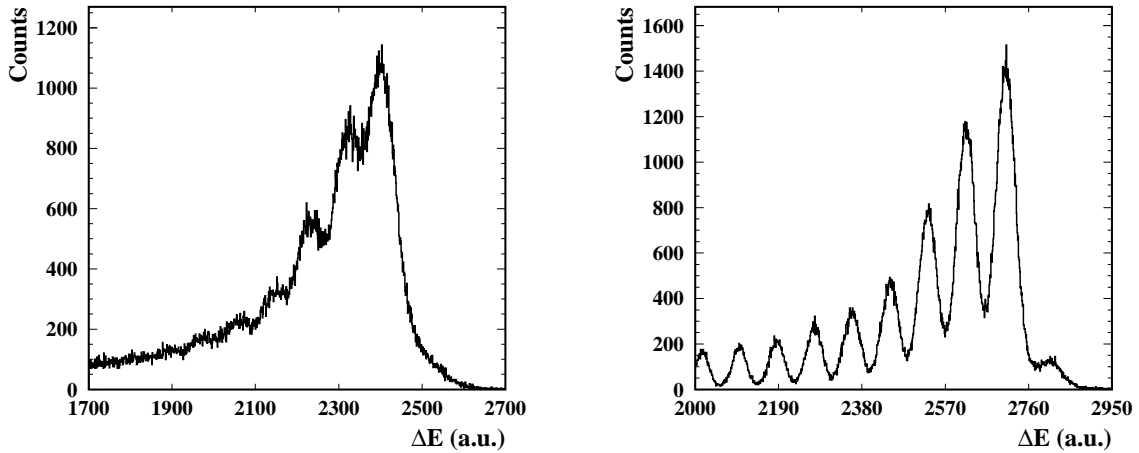


Figure 2.7: Charge resolution obtained with one ionization chamber (left panel) and the improved resolution after combining three MUSIC's and apply the corrections discussed in the text. These spectra were obtained in the reaction of  $^{136}\text{Xe} + ^1\text{H}$  at 200 MeV/u.

Energy	$\Delta Z/Z$ (FWHM)
1000 MeV/u	$4.7 \times 10^{-3}$
500 MeV/u	$6.11 \times 10^{-3}$
200 MeV/u	$9.4 \times 10^{-3}$

Table 2.3: Charge resolution (FWHM) achieved in this work as a function of the projectile energy. These values corresponds to element  $Z=53$  measured in the reactions  $^{136}\text{Xe} + ^1\text{H}$  at several energies.

where only the primary beam is transmitted through the FRS.

### 2.2.3.2 Mass number identification

In the preceding sections we have explained how do we determine the  $(A/Q)$  ratio and energy-loss ( $\Delta E$ ) of the projectile fragments. In figure 2.10 are represented both, in a typical  $\Delta E - (A/Q)$  identification matrix. In this kind of plots each spot corresponds to nucleus.

The mass identification is achieved with the help of the LIESCHEN code [45]. This code predicts the ion-optical separation of secondary beams with the Fragment Separator of GSI and provides a list of all the isotopes transmitted through the FRS in a given magnetic setting and also their positions at both focal planes. Selecting fully stripped isotopes and comparing the measured positions at the intermediate

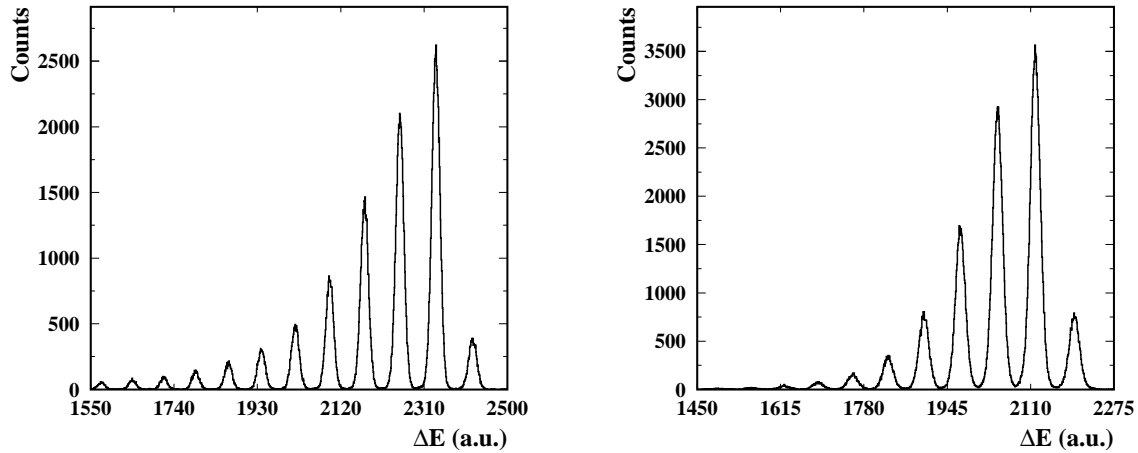


Figure 2.8: Charge resolution obtained in this work at 1000 MeV/u (left panel) and at 500 MeV/u (right panel). Both settings are centered in the  $^{116}\text{Cd}$  for the reaction  $^{136}\text{Xe} + ^9\text{Be}$  (left) and  $^{136}\text{Xe} + ^1\text{H}$  (right).

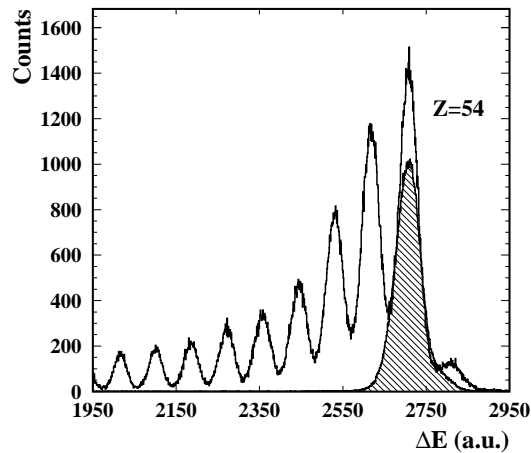


Figure 2.9: Atomic number identification using the primary beam as reference. In the figure, the energy-loss signal left by the primary beam in the MUSIC (dashed histogram) is superimposed on a plot of the energy-loss left by several fragments. With this method we can unambiguously identify the atomic number  $Z=54$  and, from here, the rest of the elements. These spectra were obtained in the reaction of  $^{136}\text{Xe} + ^1\text{H}$  at 200 MeV/u.

focal plane, F2, with those predicted by Lieschen we were able to identify all the nuclei. This code requires the correct thicknesses of all the layers of matter placed in the beam line in order to simulate the propagation of the nuclides inside the FRS. The thicknesses of these layers were calibrated with the  $B\rho$  difference of the primary beam before and after traversing each layer of matter. In table 2.4 we present an example of the positions of different iodine isotopes transmitted in a

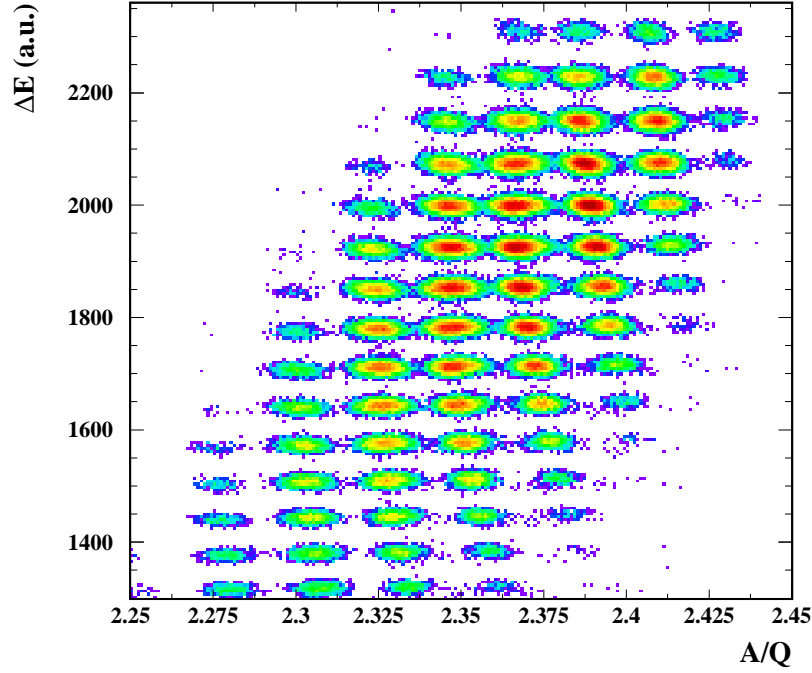


Figure 2.10: Identification plot ( $\Delta E$  vs.  $A/Q$ ) of the fragments produced in the reaction  $^{136}\text{Xe} + ^1\text{H}$  at 1000 MeV/u and transmitted in a magnetic setting centered in  $^{107}\text{Ag}$ .

magnetic setting centered in the  $^{118}\text{Cd}$ , as calculated by Lieschen.

Mass	Position at F2 (cm)
128	-13.6   -9.5
129	-7.6   -4.1
130	-1.7   1.4
131	4.2   7.0
132	10.0   12.6

Table 2.4: Lieschen position predictions (FWHM) at the intermediate focal plane of the FRS for all the isotope of charge  $Z=53$  transmitted in a given setting.

The measured transversal positions for all these isotopes of the table 2.4 which are transmitted in one setting are shown in figure 2.11 (left panel). As can be observed, the identification is easily obtained with this method because the isotopes are well separated at the intermediate focal plane, leading to an unambiguous identification. An example of the ( $A/Q$ ) resolution achieved in our experiments is shown in the right panel of the figure 2.11 for the Iodine isotopes outcoming in the reactions  $^{136}\text{Xe} + ^9\text{Be}$  at 1000 MeV/u. In the table 2.5 we can observe the mass resolution achieved

as a function of the projectile energy.

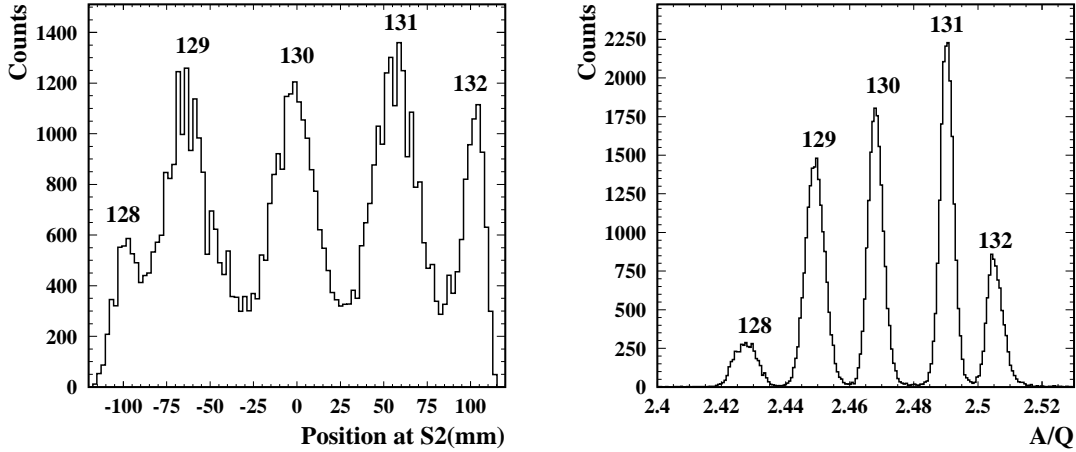


Figure 2.11: (Left panel) Measured transversal positions at the intermediate focal plane,  $F2$ , of the FRS. These positions correspond to the isotopic chain of element  $Z=53$  measured in the reaction  $^{136}\text{Xe} + ^9\text{Be}$  at 1000 MeV/u and transmitted in a magnetic setting centered in the isotope  $^{118}\text{Cd}$ . The comparison of this spectrum with the ion optic calculations given by the Lieshen code is used to identify the mass number of the nuclides transmitted in each magnetic setting of the FRS. (Right panel)  $A/Q$  spectrum obtained from the measured positions in the left panel and the time-of-flight. The  $A/Q$  resolution obtained is  $\frac{\Delta A}{A} \sim 1.5 \times 10^{-3}$ .

Energy	$\Delta A/A$ ( $\sigma$ )
1000 MeV/u	$2 \times 10^{-3}$
500 MeV/u	$1 \times 10^{-3}$
200 MeV/u	$7.5 \times 10^{-4}$

Table 2.5: Mass resolution ( $\sigma$ ) achieved in this work as a function of the projectile energy. These values corresponds to the isotope  $^{124}\text{I}$  outcoming from the reaction of  $^{136}\text{Xe}$  projectiles impinging on  $^{48}\text{Ti}$  at several energies.

This method relies in the comparison of the transversal position of fully stripped projectile residues. Nuclei with one electron either in the first or second stage of the FRS arrives at the final focal plane (F4) at different transversal positions than the fully stripped isotope, therefore these contaminants are easily disgarded by comparing the signals in the ionization chambers and the plastic scintillator at F4. Nuclei that traverses both stages with one electron cannot be disentangled from the fully stripped ions and will be wrongly identified. However, the probability of those events has been calculated with AMADEUS [52] to be less than 1 per mil at 1000 MeV/u, less than 1% at 500 MeV/u and less than 6% at 200 MeV/u in the

worst case. The calculations of the charge-exchange contaminations will be carefully discussed further in this work (see section 3.3.2.5).

# Chapter 3

## Measured cross sections and momentum distributions

In this chapter we describe the procedure followed to determine the physical observables (isotopic cross sections and longitudinal velocities), of the projectile residues produced in the investigated reactions. The production cross sections for a given fragment of mass number  $A$  and atomic number  $Z$  is given by:

$$\sigma(A, Z) = \frac{y(Z, A)}{N_t \cdot N_b} \quad (3.1)$$

where  $N_b$  is the number of impinging projectiles,  $N_t$  is the number of target atoms per unit area and  $y(Z, A)$  is the production yield for the projectile residues after several corrections that will be explained in this chapter. In order to determine the cross sections with good accuracy, the three quantities in expression 3.1 have to be evaluated carefully.

The mean-value and width of the momentum distributions of the residues are obtained by measuring their magnetic rigidities at the intermediate focal plane of the FRS, as will be explained in what follows. The main goal of this chapter consist on a detailed explanation of the method followed to evaluate the three parameters in expression 3.1, together with corrections needed to achieve the real values for cross-sections and velocity distributions.

### 3.1 Beam current normalization

In order to determine the number of incoming projectiles, we have monitored the beam with the SEETRAM detector, as explained in the previous chapter. For its calibration we have used a plastic scintillator, Sc0, which is placed in the target area close to the SEETRAM monitor. This plastic scintillator is much thicker than the SEETRAM itself, and then is only used for calibration purposes, otherwise the reactions in this detector would contaminate our measurements. Moreover, this detector saturates for high beam intensities.

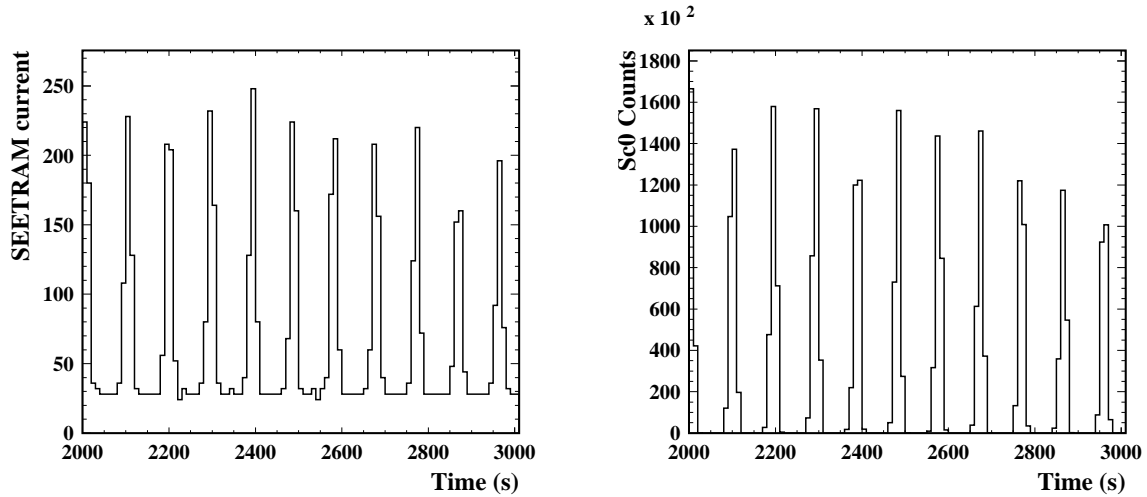


Figure 3.1: *Beam current measured with the SEETRAM detector (left panel) and the number of incident projectiles measured with the scintillator (right panel), in the same time interval.*

In figure 3.1 we can see the response of both detectors, the SEETRAM and the plastic scintillator in the same time period. In figure 3.2 the number of incoming projectiles measured by the scintillator is plotted versus the integrated current (the offset has to be subtracted from the spectrum measured by the SEETRAM monitor). At high intensities we can observe the scintillator saturation effects. Restricting our analysis to the non-saturation region of the plot we can determine the proportionality between the number of impinging projectiles and the current measured by the SEETRAM. By fitting this region to a parabolic function and taking the linear factor, we got the SEETRAM calibration factors for the intensities of the beams used in this work. In the table 3.1 we show these calibration factors. The errors in the calibration factors are obtained from the accuracy of the fit.

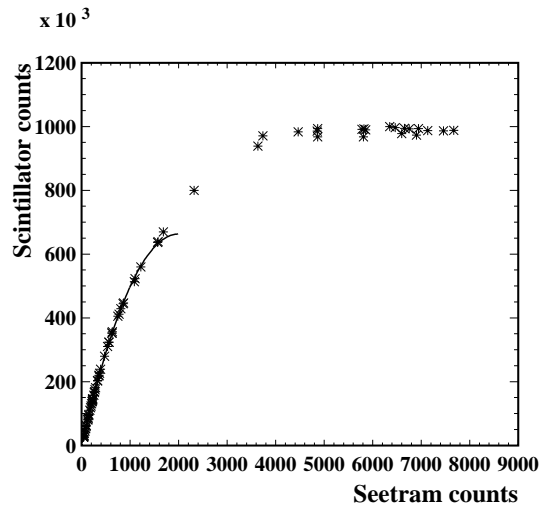


Figure 3.2: *Integrated current per spill measured with the SEETRAM detector versus the counting rate given by the plastic scintillator. The solid line represents the result of the parabolic fit restricted to the non-saturation region of the plastic scintillator. These data correspond to the  $^{136}\text{Xe}$  at 1000 MeV/u beam.*

Experiment	Calibration Factor
$^{136}\text{Xe}$ at 1000 MeV/u	$840 \pm 49$
$^{136}\text{Xe}$ at 500 MeV/u	$720 \pm 37$
$^{136}\text{Xe}$ at 200 MeV/u	$379 \pm 24$
$^{124}\text{Xe}$ at 1000 MeV/u	$800 \pm 42$

Table 3.1: *Calibration factors obtained with the plastic scintillator Sc0 for the different beams used in this work.*

## 3.2 Target normalization

In this work we have used the nominal values for the target thicknesses, as shown in table 2.1. The case of the titanium target is special and must be discussed carefully. The accelerator window and the SEETRAM monitor are also made of titanium. The contribution of these layers of matter to the yields of the fragmentation residues is negligible for the thick targets, but not for the titanium target. In this case, the thickness of the accelerator window and the SEETRAM have to be taken into account together with the titanium target thickness. In addition, there exists another problem, the fragments created in those layers have different transmissions, and this has to be taken into account in order to normalize the production yields to the target thickness. The transmissions of the residues in this case were estimated according to the method described in [55] and the equivalent target thickness as a function of the mass number of the projectile residue is shown in figure 3.3.

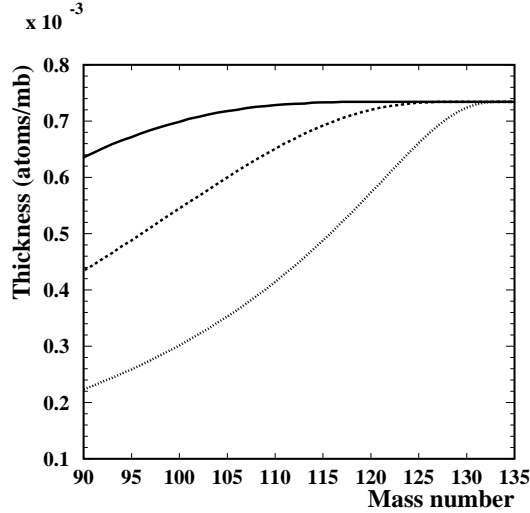


Figure 3.3: Equivalent thickness of the dummy target as a function of the projectile residue mass number. The curves are calculated at 1000 MeV/u (solid line), 500 MeV/u (dashed line) and 200 MeV/u (dotted line). The transmissions have been calculated using the method described in [55].

### 3.3 Production yields and associated corrections

It is important to keep in mind that the measured quantity in this kind of experiments is the differential yield relative to the longitudinal momentum of the fragments produced in the reaction,  $dy_{meas}(Z, A)/dp_{\parallel}$ . The integration of these distributions provides the measured yield for each nucleus, and from it, the cross-section. For this reason, the measurements of the longitudinal momenta is a key point in this work. Moreover, the measured production of a given nucleus ( $y_{meas}$ ) differs from the real production yield ( $y(Z, A)$ ) due to several effects inherent to the experimental technique used in this work, and they are related by the expression:

$$y(Z, A) = y_{meas}(Z, A) \cdot f_{dead} \cdot f_{trans} \cdot f_{ch.st} \cdot f_{mult} \cdot f_{sec} \quad (3.2)$$

Where  $f_{dead}$ ,  $f_{trans}$ ,  $f_{ch.st}$ ,  $f_{mult}$  and  $f_{sec}$  are the correction factors to take into account the dead time of the data acquisition, the transmission trough the FRS, the ionic charge states, the multiple reactions within the target and the secondary reactions in all layers of matter along the FRS, respectively. These factors will be discussed later in detail.

In the case of the liquid targets (hydrogen and deuterium), the production of the fragments is affected by the titanium windows of the vessel that contains the liquid and the Mylar used as thermal isolator. A dummy target, with a thickness equivalent to these titanium windows and the Mylar foils is used to quantify the

contribution of the Windows to the cross-sections. The production yields measured with the dummy only, must be subtracted from the total measured yields:

$$y(Z, A) = y_{meas}(Z, A) - y_{dummy}(Z, A) \quad (3.3)$$

In figure 3.4, we show the measured yields for the reactions  $^{136}\text{Xe} + \text{H}$  and dummy at 500 MeV/u. The contribution of the dummy has been quantified to be, approximately, 1% of the measured yields up to element  $Z=50$ .

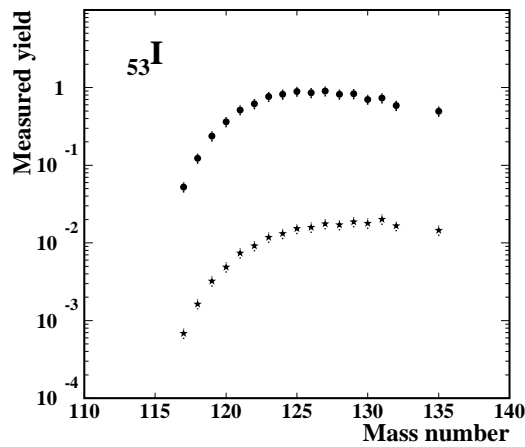


Figure 3.4: Measured yields normalized to the number of primary projectiles in the reactions  $^{136}\text{Xe} + \text{H}$  (solid circles) and  $^{136}\text{Xe} + \text{dummy}$  (solid stars) at 500 MeV/u.

### 3.3.1 Momentum distributions

The longitudinal momentum of a nucleus is related to its magnetic rigidity  $B\rho$  (see equation 2.3), and then, to its position at the intermediate focal plane of the spectrometer, F2. This distribution is characterized by a mean value  $\langle p_{\parallel} \rangle$  and a width  $\langle \sigma_{p_{\parallel}} \rangle$ . As explained by Morrissey [38] and Goldhaber [39], the width of the momentum distribution is expected to grow with the square-root of the mass difference between the fragment and the projectile. Due to the limited momentum acceptance of the FRS ( $\pm 1.5\%$ ) the momentum distribution for masses far from the projectile will not be fully transmitted in one magnetic setting of the FRS. In order to overcome this limitation, we have overlapped several magnetic settings in order to obtain the complete momentum distribution. In figure 3.5 we can observe the overlapping of the partial distributions measured in three different settings to obtain the whole momentum distribution of the fragment  $^{124}\text{Te}$ , produced in the reaction  $^{136}\text{Xe} + \text{Pb}$  at 1000 MeV/u.

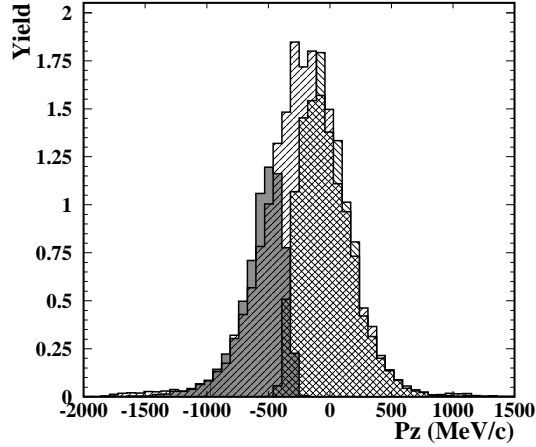


Figure 3.5: Momentum distribution of the fragment  $^{124}\text{Te}$  produced in the reaction  $^{136}\text{Xe} + \text{Pb}$  at  $1000 \text{ MeV/u}$ . The fragment is partially transmitted in three different magnetic settings and it is necessary to overlap these three measurements in order to reconstruct the complete momentum distribution.

In order to avoid the transmission of the primary beam or its charge-states through the FRS, some slits placed in the first focal plane of the Fragment Separator were used in some specific settings. Consequently, projectile fragments with a value of  $A/Q$  similar to the one of the projectile or its charge-states could not be measured. In this particular cases, the transmission was estimated using the Lieschen code.

The momentum distributions are given in a reference frame where the beam is at rest in the center of the target. With the measurement of the transversal position of a given fragment at the intermediate focal plane of the FRS, we can determine its magnetic rigidity:

$$B\rho_{|F2} = B\rho_0 \cdot \left(1 + \frac{x_2}{D_{12}}\right) \quad (3.4)$$

where  $B\rho_0$  is the magnetic rigidity of the central fragment and  $D_{12}$  is the dispersion of the first stage of the FRS. From here we determine the kinetic energy of the fragment:

$$T_{F2} = u \cdot \left[ \sqrt{1 + \left(\frac{B\rho_{|F2} \cdot Z \cdot c}{A \cdot u}\right)^2} - 1 \right] \quad (3.5)$$

and from the kinetic energy, we get easily the velocity distribution as:

$$v = c \cdot \sqrt{1 - \left( \frac{1}{\frac{T_{F2}}{u} + 1} \right)^2} \quad (3.6)$$

To determine the velocity of the fragments we assume that they are produced in the middle of the target. Therefore, the values obtained from equation 3.6 have to be corrected by the slowing down of the fragment through all the layers of matter from the center of the target until the plastic scintillator at F2. Finally, in order to give the results in the beam-frame of reference, we have to apply the correct Lorentz boost. In this frame, a negative velocity means a velocity lower than the one of the primary beam. Concerning the width of the velocity distributions, we are interested in the width induced by the reaction mechanism. To isolate this value, we have to disentangle the contribution coming from the beam emittance, the resolving power of the FRS and the location straggling within the target. This was achieved by unfolding the measured velocity distributions with a response function constructed with the contribution of these three effects. The beam emittance and resolving power of the FRS have been determined by performing measurements with the primary beam while the location straggling within the target has been calculated with the code AMADEUS [52].

### 3.3.2 Corrections to the production yields

In this section we describe in detail all corrections that must be applied to the measured yields in order to determine the real production of the nuclides in the investigated reactions.

#### 3.3.2.1 Dead time

Due to the limited data acquisition rates, not all of the events triggering the electronics are processed. This dead-time has to be taken into account in order to correct the measured yields appropriately. The acquisition determines the number of events that produce a trigger ( $N_{free}$ ) and the number of events actually processed ( $N_{lam}$ ). The dead-time factor applied in expression 3.2 is then given by the ratio of both quantities:

$$f_{dead} = \frac{N_{free}}{N_{lam}} \quad (3.7)$$

To obtain reliable results, the dead-time must be kept below 30 %. The uncertainty in this factor is always below 1 %.

### 3.3.2.2 Multiple reactions in the target

The projectile residues produced in the reactions investigated in this work may undergo a secondary reaction before leaving the target. These secondary reactions do not spread uniformly over all residues produced but concentrate in some specific regions close to the evaporation corridor. In order to correct the measured yields from this contribution, we have used the method proposed in [56]. The measured production rates (referred to as apparent cross-sections  $\sigma^*$ ) can be formulated through a system of equations that includes the losses of the primary beam in the target, the losses of residues due to their interaction in the target and the gain due to the contamination from intermediate multiple reactions:

$$X^* = G \cdot X - L \cdot X \quad (3.8)$$

where  $G$  and  $L$  are the matrices describing the gain and loss terms and  $X^*$  and  $X$  are the vectors containing the measured apparent cross-sections  $\sigma^*$  and the unknown primary cross-sections  $\sigma$ , respectively. The real values of the cross-sections are extracted by solving the equation 3.8. This method is extensively discussed in [56] and we will make here only a brief introduction.

The real production cross-section of a given residue  $(Z, A)$  in the fragmentation of the primary projectile  $(Z_0, A_0)$  can be expressed as:

$$\sigma_{(Z_0, A_0) \rightarrow (Z, A)} = \sigma_{(Z_0, A_0) \rightarrow (Z, A)}^* \cdot e^{\frac{\xi}{2}(\sigma_{(Z_0, A_0)}^{tot} + \sigma_{(Z, A)}^{tot})} - \frac{\xi}{2} \sum_{A_i \geq A_i, Z_i \geq Z} \left[ \sigma_{(Z_0, A_0) \rightarrow (Z_i, A_i)} \cdot \sigma_{(Z_i, A_i) \rightarrow (Z, A)} e^{\frac{\xi}{6}(\sigma_{(Z_0, A_0)}^{tot} + 2\sigma_{(Z_i, A_i)}^{tot} + \sigma_{(Z, A)}^{tot})} \right] \quad (3.9)$$

where  $\xi$  is the thickness of the target,  $\sigma_{(Z, A)}^{tot}$  is the total reaction cross-section of the nucleus  $(Z, A)$  with the target as computed with the Karol code [57].  $\sigma_{(Z_0, A_0) \rightarrow (Z, A)}$  is the cross-sections of the residue  $(Z, A)$  from the projectile  $(Z_0, A_0)$ . The expression 3.9 is solved numerically following this order, the unknown primary reaction cross-section  $\sigma_{(Z_0, A_0) \rightarrow (Z_i, A_i)}$  had already been calculated in a previous step. The intermediate cross-sections  $\sigma_{(Z_i, A_i) \rightarrow (Z, A)}$  were calculated numerically by using computational codes based on the two-step model of fragmentation reactions. In the

case of the beryllium, titanium and lead targets we have used the ABRABLA code [12], while in the case of the hydrogen and deuterium targets we have used the INCL4 [8] cascade coupled to the ABLA code for the evaporation.

The solution of the equation 3.9 provides the correction factor  $f_{mult}$  in expression 3.2:

$$f_{mult} = \frac{\sigma_{(Z_0, A_0) \rightarrow (Z, A)}}{\sigma_{(Z_0, A_0) \rightarrow (Z, A)}^*} \quad (3.10)$$

An estimation of this effect can be seen in figure 3.6.

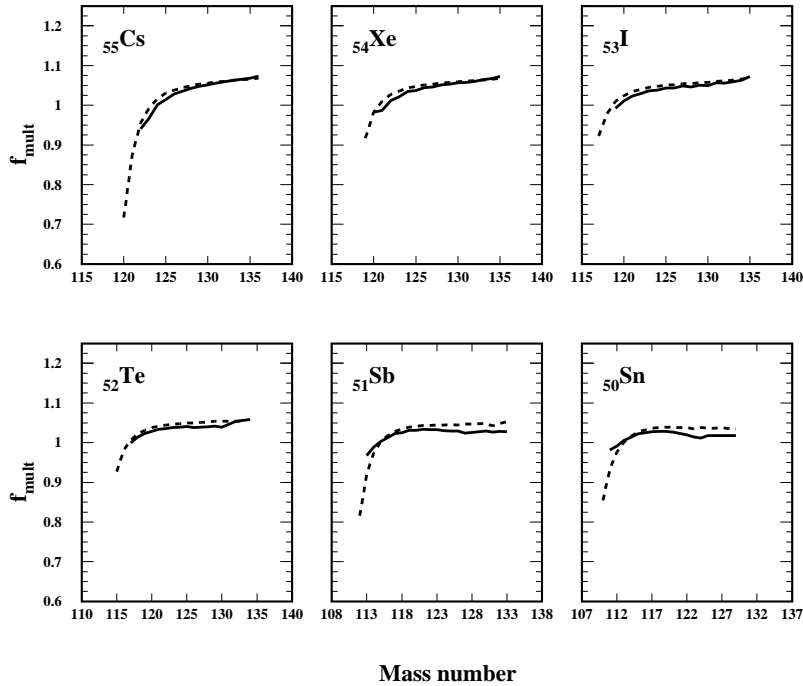


Figure 3.6: Correction factor due to multiple reactions in the target for the isotopes measured in the reactions  $^{136}\text{Xe} + ^{48}\text{Ti}$  at 1000 MeV/u (solid line) and 500 MeV/u (dashed line).

### 3.3.2.3 Transmission

We have seen in Chapter 2 that the FRS has a limited acceptance in both, angle ( $\pm 15$  mrad) and momentum ( $\pm 1.5\%$ ). The later can be avoided, as explained,

by overlapping consecutive magnetic settings and almost all the measured residues has 100 % momentum transmission. Only few exceptional cases, as residues with a magnetic rigidity close to the projectile or its charge-states, will be cut due to the slits. In these cases the transmission must be estimated with the help of the Lieschen code.

With respect to the angular acceptance, the typical angular distribution of fragmentation residues is a gaussian distribution with a sigma below 5mrad for the mass range of the residues studied in this work, being the transmission then close to 100%. However, a more complicated situation is present with the dummy target. The projectile residues created within the vacuum window and the SEETRAM have different transmissions which have been estimated using the method described in [55]. However, this effect has been already taken into account while treating the thickness of the titanium target in section 3.2.

### 3.3.2.4 Secondary reactions

The residual fragments produced in the target have a certain probability to undergo a nuclear reaction in the different layers of matter placed along the FRS. This will translate in a reduction in the measured yields that has to be corrected. The total nuclear interaction cross-sections for all the fragment-layer combinations have been calculated with the Karol [57] code and we have used these values to compute the survival probability for each isotope with the expression 3.11.

$$P_s = e^{-\frac{N_A}{A_l} \cdot t \cdot \sigma_{tot}} \quad (3.11)$$

where  $N_A$  is the Avogadro number,  $A_l$  the mass number and  $t$  the thickness (in mg/cm<sup>2</sup>) of the corresponding layer of matter<sup>1</sup> and  $\sigma_{tot}$  the total reaction cross-section for a given layer-projectile combination. This total cross-section can be calculated with the code Karol with an accuracy around a 10% [57]. The survival probabilities have to be determined for each layer of matter, and the factor  $f_{sec}$  in the expression 3.2 will be given by:

$$f_{sec} = \prod_{i=1}^n P_i \quad (3.12)$$

where the factor  $P_i$  is the survival probability in the  $i^{th}$  layer of matter.

---

<sup>1</sup>In Appendix B we show the list of all the layers of matter placed in the beam line

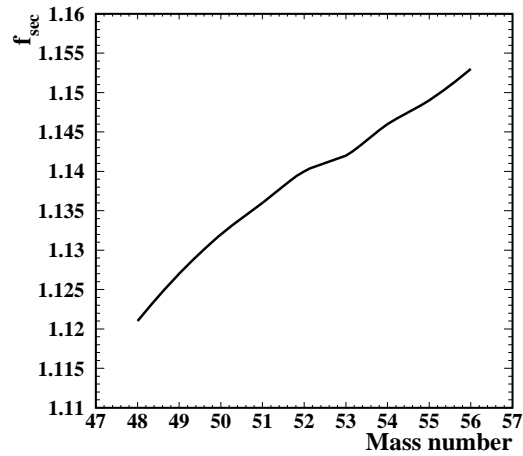


Figure 3.7: *Correction factor due to secondary reactions within the layers of matter of the experimental setup of the FRS.*

These corrections amount for, approximately, a 14% of the production yields in the range of elements around  $Z=50$ . This feature can be observed in figure 3.7, where the reaction probability has been calculated for several residual nuclei in the range investigated in this work.

At 200 MeV/u we observed an interesting effect that must be taken into account in order to obtain the production yields with high accuracy. At these energies, the projectile residues can lose a small fraction of their kinetic energy in the tungsten wire of the multi-wire detectors placed at the final focal plane of the FRS. This behaviour would lead to a “satellite” spot in the identification cluster plot. As those residues have a slightly lower longitudinal momentum, appears in the plot with an apparent higher charge and  $A/Q$ . This effect has been estimated to be about 7 % of the primary yield and it seems to be constant for all the projectile residues analyzed in this work. The deviations of the  $A/Q$  and  $\Delta E$  of these residues are not large enough to contaminate the neighbor nuclei and, consequently, they will not affect our measurements.

### 3.3.2.5 Ionic charge states

The equilibrium charge-state distribution behind the target area is altered from the first stage of the FRS to the second due to the layers of matter placed at the intermediate focal plane. This feature leads to a change in the  $A/Q$  ratio of the fragment that could induce a wrong identification. The strong correlation between the position of the projectile residues at the final focal plane and their charge-states makes it possible to discriminate the charge-state changing from the first to the

second stage of the FRS. But apart from these changing residues, it also exists the contamination from residues that have 1 electron in both stages of the FRS. In our work, only fully stripped isotopes are analyzed and, in order to determine the production yield with high precision, two correction factors have to be taken into account:

1. The fraction of residues that are not fully stripped. This fraction has to be added to the measured yields.
2. The fraction of residues  $(A - 3)/Z$  that traverses the FRS with one electron and loose this electron in the MUSIC chambers. These isotopes have similar magnetic rigidities than the  $A/Z$  isotope, leading to larger yields than expected.

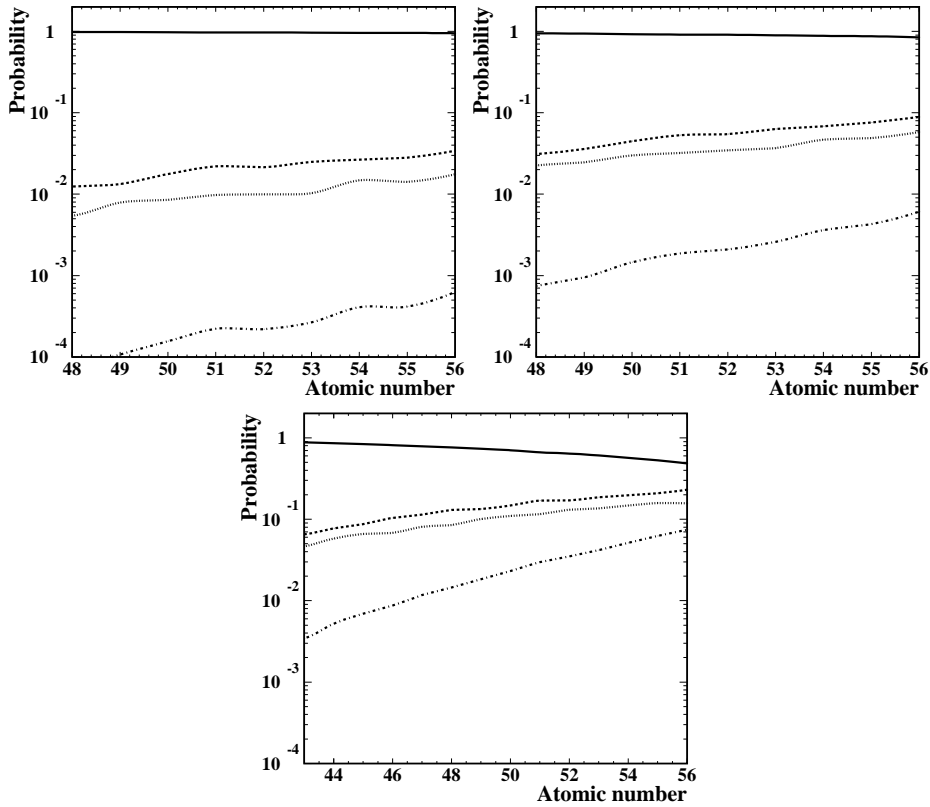


Figure 3.8: Probability of different charge-states combinations for the fragments created in the reactions  $^{136}\text{Xe} + \text{H}$  at 1000 MeV/u (left panel),  $^{136}\text{Xe} + \text{H}$  at 500 MeV/u (right panel) and  $^{136}\text{Xe} + \text{H}$  at 200 MeV/u. In the figures are shown the probabilities of have charge-states 0 in both parts of the FRS (solid line), 1-0 (dashed line), 0-1 (dot line) and 1-1 (dashed-dot line). See text for details.

In figure 3.8 we show the probability of any possible combination of the charge-states inside the FRS for all the projectile residues created in the reaction  $^{136}\text{Xe} + \text{H}$  at 1000 MeV/u, 500 MeV/u and 200 MeV/u. The solid lines show the probability of bare-ions in both sections of the FRS (0-0), the dashed lines represent the probability of hydrogen-like residues in the first section and a bare-ion in the second one (1-0). The dot line shows the probability of bare-ions in the first section and a hydrogen-like in the second one (0-1). Finally, the lowest probability corresponds to those fragments which are hydrogen-like in both sections of the FRS (1-1, dashed-dot line). Higher combinations of charge-states have been neglected due to their extremely low probability.

In section 2.2.3.2 we show that the mass resolution achieved in this work improves as decreasing the energy of the primary beam. At 500 MeV/u, the mass resolution is sufficient to separate both residues, the  $A/Z$  from the  $(A-3)/Z$ . In figure 3.9 we show this effect for the reaction  $^{136}\text{Xe} + \text{H}$  at 500 MeV/u. At 200 MeV/u the behavior is analogous, resulting in an unambiguous and non-contaminated identification of the fully stripped isotopes.

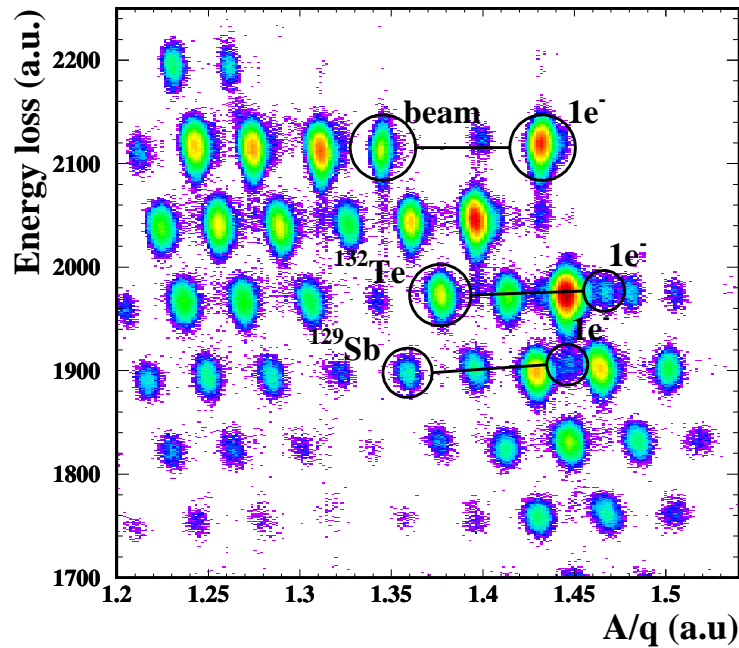


Figure 3.9: *Identification matrix of several projectile residues produced in the reaction  $^{136}\text{Xe} + \text{H}$  at 500 MeV/u. The positions of the 1-1 charge-states are shown in the figure.*

Anyhow, the contribution of the  $(A-3)/Z$  contaminants has a small influence on the measured yields of the projectile residues, their quantitative effect remains always below 1% at 500 MeV/u and below 7% at 200 MeV/u in the most defavourable cases, as can be seen in figure 3.8. In addition, the contamination of these isotopes

would be important only in the very neutron-rich region of the yield distributions, as can be also observed in figure 3.8.

As summary, the factor  $f_{ch.st}$  in the expression 3.2 is given only by the fraction of projectile residues that are not fully stripped, because the contamination of the  $(A - 3)/Z$  residues can be disregarded in our work as explained above. This factor is calculated as the inverse of the solid lines in figure 3.8.

### 3.4 Uncertainties

The uncertainties associated to the cross sections measured in this work will correspond to the quadratically sum of the statistical uncertainty and the systematic ones. The first, being the Poissonian error of the accumulated statistics ( $\sqrt{n}$ ), will be always kept below 2-3%<sup>2</sup>. The systematic uncertainty of the measurements is given by the accuracy in the determination of the beam intensity, the target thickness and the correction factors discussed along this chapter. An estimation of the uncertainties associated to these factors is presented in table 3.2.

Effect	Uncertainty
Beam intensity	$\sim 5-7\%$
Target thickness	$\sim 2-3\%$
Dead time	$\sim 1\%$
Secondary reactions	$\sim 1-2\%$
Multiple reactions	$\sim 1-2\%$
Detector efficiency	$< 1\%$
Ionic charge states	$< 2\%$

Table 3.2: *Uncertainties associated to the different correction factors discussed in this chapter.*

The uncertainty range given in the table 3.2 for each correction factor accounts for the different reactions investigated in this work. As can be deduced from table 3.2, the highest contribution to the systematic error in the cross-section measurements is the uncertainty on the SEETRAM calibration factor. Taking into account all the contribution added quadratically, the cross-sections will be given with a total error ranging from 8% to 11%, except for some specific cases with low statistic mentioned above.

---

<sup>2</sup>Except some specific cases with low yields, as the double charge-pickup processes and the 5 or 6-proton removal channels, the accumulated statistics of the fragments will be large enough to assure that the statistical uncertainty remains below 5%.

## 3.5 Measured cross-sections and momentum distributions

In the final section of this chapter we present the complete set of data measured in this work, cross-sections and longitudinal momenta. These data are shown in figures 3.10, 3.11 and 3.12. The cross-sections are scaled by a factor as a function of the charge, for clarity in the figure. The error bars are included in the plots, but are not visible due to the scale of the figures (15 orders of magnitude). Some holes are present in the isotopic cross-section distributions, corresponding to projectile residues not measured because of transmission causes.

The smooth evolution of the isotopic cross-sections is one of the characteristics of the data measured in the experimental program developed at the FRS in the last years. That is the result of the precision of the experimental method, which allows the unambiguous identification of the projectile residues and to fully reconstruct the momentum distributions, as well as the careful description of the included corrections. The isotopic cross-sections of elements  $^{55}\text{Cs}$  and  $^{56}\text{Ba}$ , corresponding to the single and double charge-pickup reactions, are one of the main challenges in this work. Also the first observation of the 6 proton-removal channel ( $^{128}\text{Cd}$ ) in relativistic heavy-ion collisions, measured in the reaction  $^{136}\text{Xe} + \text{Be}$  at 1000 MeV/u is also a key stone of this work. The measurement of the production cross-sections of projectile residues at 1000, 500 and 200 MeV/u in the case of the proton and titanium targets are also of great importance. In the following chapters we will perform detailed discussions in the basis of these set of data.

The measured mean-values of the longitudinal momentum distributions are compared with the systematic predictions given by Morrissey in figures 3.10, 3.11 and 3.12, this is denoted by the solid line on the plots. In the Morrissey model, the longitudinal momentum of the residue is directly proportional to the mass loss in the reaction mechanism. The slope of the solid line on each plot is the proportionality constant, 8 MeV/c, but in the next chapter we will demonstrate that this slope is dependent on the atomic number of the residue.

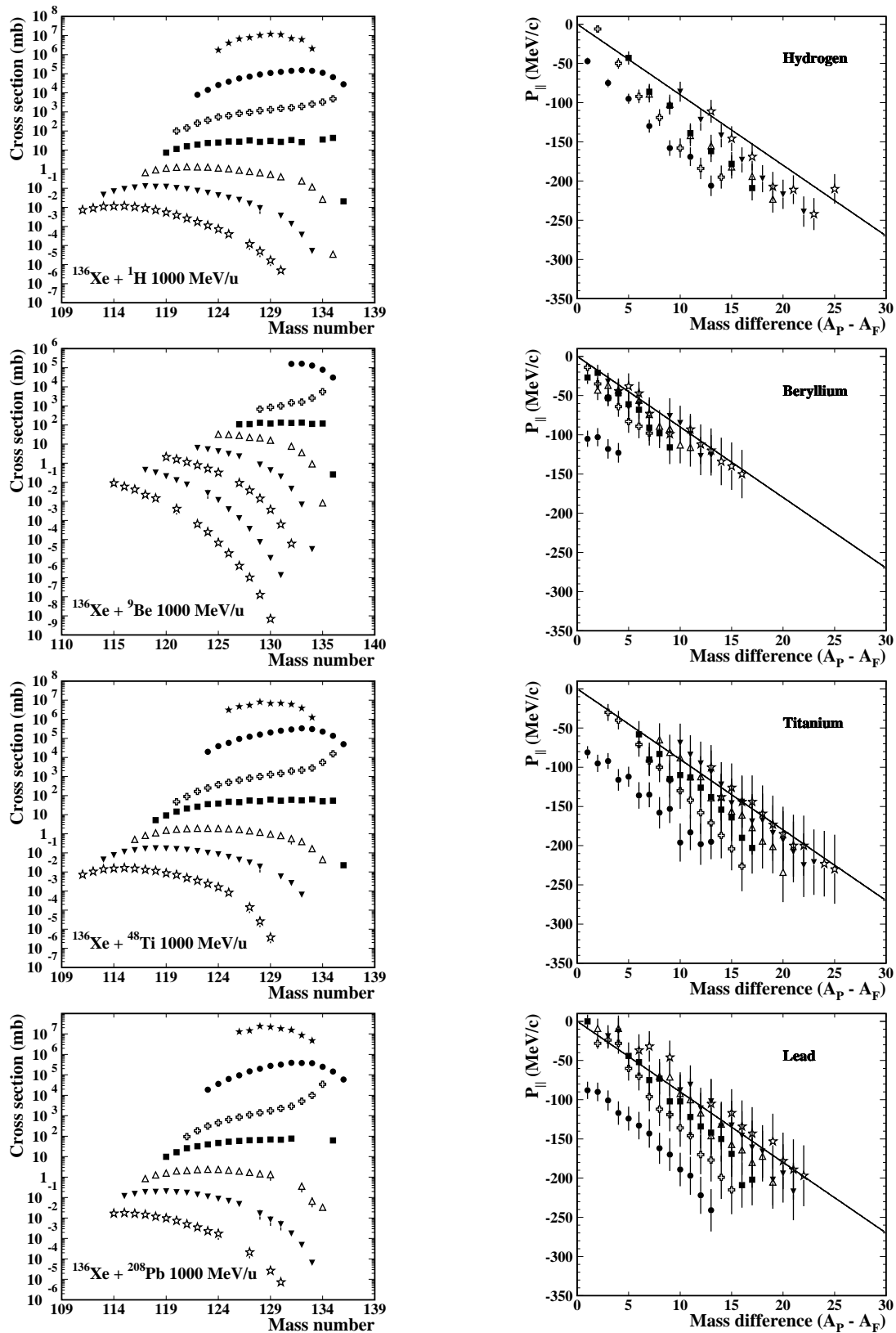


Figure 3.10: Complete set of data measured in this work in the reaction of  $^{136}\text{Xe}$  projectiles at 1000 MeV/u with different targets.

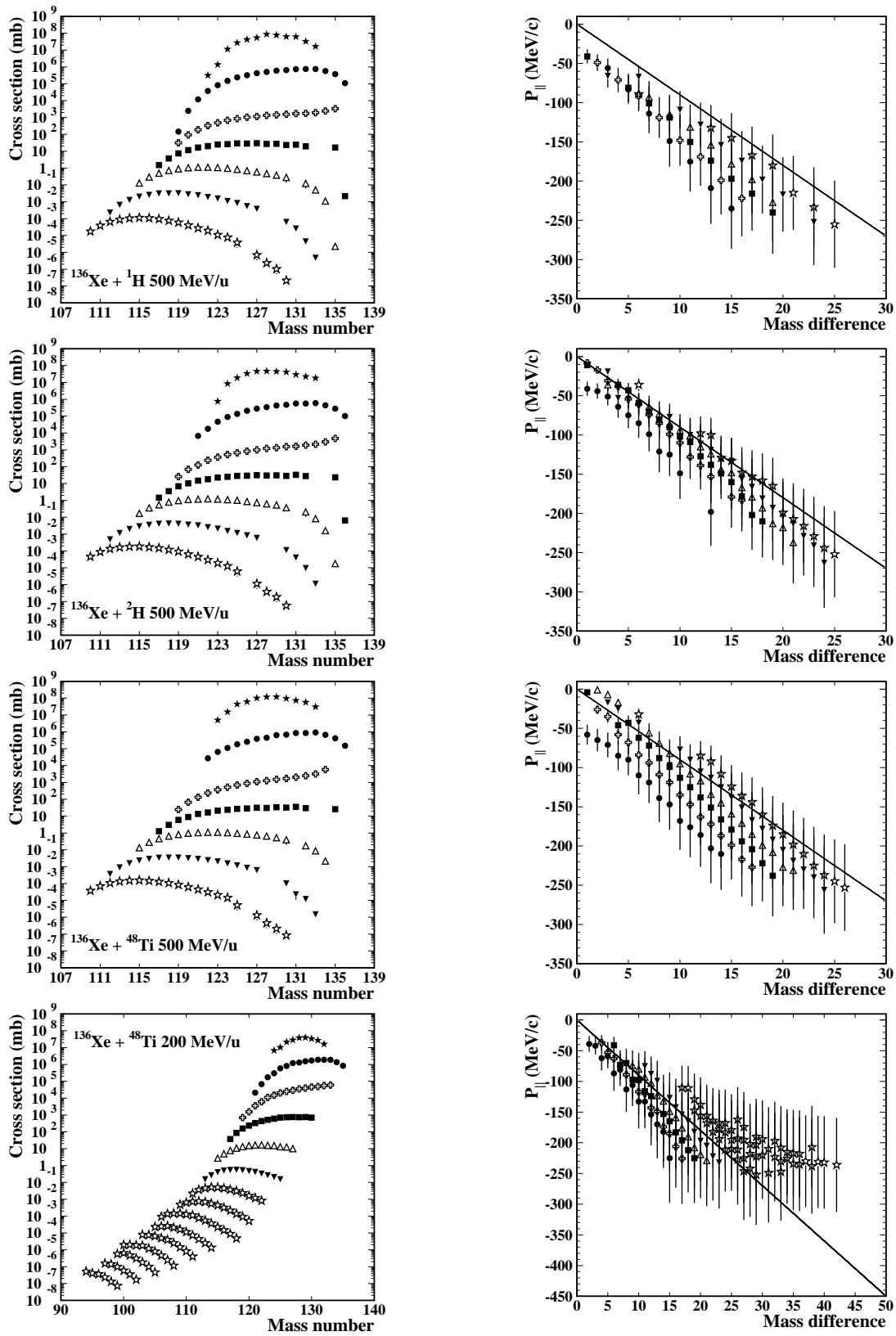


Figure 3.11: Complete set of data measured in this work in the reaction of <sup>136</sup>Xe projectiles at 500 MeV/u with different targets.

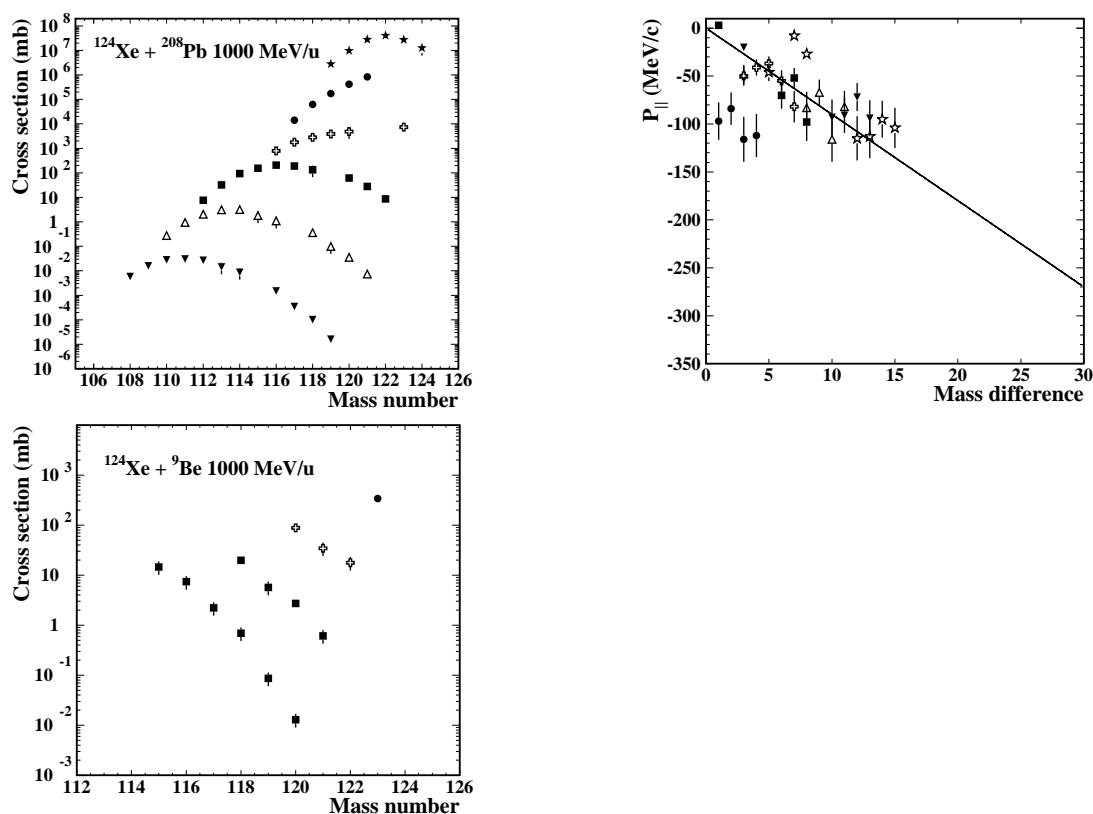


Figure 3.12: Set of all the data measured in this work. In the left column, the data corresponding to the cross-sections are shown. For clarity in the plot, these data are scaled by a constant factor depending on the isotopic chain. In the right column are shown the data corresponding to the mean value of the longitudinal momentum distributions. The data are compared with the Morrisey systematic ( $P_{||} = -8.0 \times \Delta A$ ).

# Chapter 4

## Systematic investigation of heavy-ion peripheral collisions at relativistic energies.

The systematic study of the production cross sections and longitudinal momentum distributions of residual nuclei close to the projectile in fragmentation reactions provide valuable information on the reaction mechanism, in particular about the first stage of the collision. The abrasion stage has been described by Glauber [11] and extensively applied to heavy ion collisions over a wide range of energies above the Fermi energy. This model describes the nucleus-nucleus interaction in terms of the fundamental nucleon-nucleon cross sections and the impact parameter, hence only geometrical considerations are taken into account in this model. In addition, several reaction models described in the first chapter (ABRABLA, INCL4+ABLA, ISABEL+ABLA, EPAX, etc) are generally used to describe the fragmentation reactions and to provide the production cross sections of projectile residues. Due to the variety of our measured data, in this chapter we will be able to systematically investigate the validity of these model calculations.

The discussion concerning the influence of the target size in the projectile residues isotopic cross sections will open this chapter. In this work we have measured the cross sections of residues produced in the reactions of  $^{136}\text{Xe}$  projectiles at 1000 MeV/u with  $^1\text{H}$ ,  $^9\text{Be}$ ,  $^{48}\text{Ti}$  and  $^{208}\text{Pb}$  targets. The differences observed in the production cross sections for these projectile-target combinations will be explored by means of the Glauber model, the number of abraded nucleons in the abrasion stage and the excitation energies induced in these collisions.

The role of the neutron excess of the projectile in the reaction mechanism will

be also discussed using the measured production cross sections of residual nuclei produced in reactions induced by  $^{124}\text{Xe}$  and  $^{136}\text{Xe}$  projectiles. This discussion will be very much related to the concept of *evaporation corridor* [25], also introduced in chapter 1.

The influence of the projectile energy will be also explored in this chapter, as we have measured the residue production cross sections of the reaction  $^{136}\text{Xe}+^{48}\text{Ti}$  at 1000, 500 and 200 MeV/u. This investigation will allow us to validate the concept of *limiting fragmentation* [16, 17, 18]. These results have relevant implications in next generation RNB facilities planning to use fragmentation of projectiles at few hundreds of MeV per nucleon as is the case for EURISOL [58] where a two-step reaction scheme [59] is proposed to produce intense beams of refractory elements.

In addition to the production cross sections, valuable information concerning the reaction mechanism can be obtained from the velocity distributions of the projectile residues. The last sections of this chapter will be devoted to the description of the measured data concerning the mean values and widths of the velocity distributions of residual nuclei, exploring the role of the projectile energy and neutron excess and the target size, as well as benchmarking the predictive power of the models such as the ones proposed by Morrissey [38] and Goldhaber [39].

## 4.1 Role of the target size

In order to investigate the influence of the target nature in fragmentation reactions we will use the production cross sections of projectile residues produced in collisions of  $^{136}\text{Xe}$  projectiles at 1000 MeV/u on hydrogen, beryllium, titanium and lead targets. In figure 4.1 we show the measured isotopic distributions of production cross sections of projectile residues obtained with these four targets.

In this figure we can observe a clear dependence of the measured cross sections with the mass number of the target nucleus. This effect is specially evident for projectile residues with atomic number close to the one of the projectile, as it is the case for the xenon isotopic chain. For lighter projectile residues, this difference is less clear, as can be observed in the isotopic chain of tin. In principle, this effect is expected to be related to the geometrical nature of the abrasion process. According to the Glauber model, the total reaction cross section is proportional to the size of the target nucleus. Consequently, we expect larger cross sections for the heavier target nuclei, as shown in figure 4.1.

In order to clarify this question, in figure 4.2 we represent the isotopic distri-

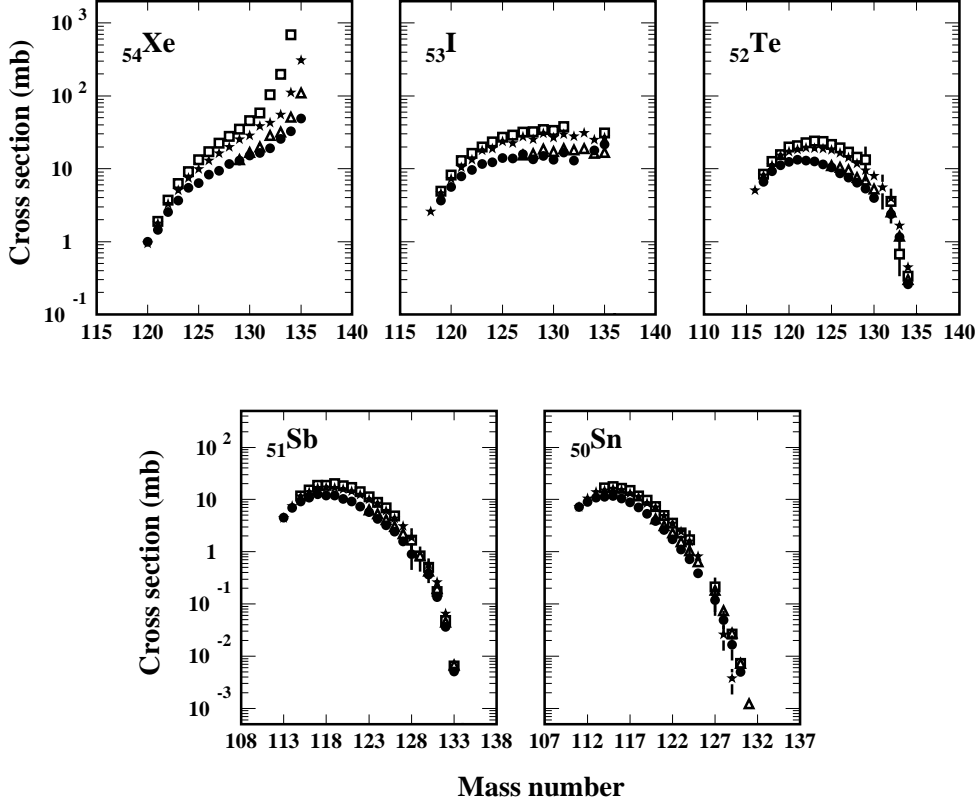


Figure 4.1: Measured isotopic cross sections of projectile residues produced in reactions induced by  $^{136}\text{Xe}$  at 1 GeV/u with  $^{208}\text{Pb}$  (open squares),  $^{48}\text{Ti}$  (solid stars),  $^9\text{Be}$  (open triangles), and hydrogen (solid circles).

System	$\sigma_{TOT}$ (mb)
$^{136}\text{Xe} + ^1\text{H}$	1353
$^{136}\text{Xe} + ^9\text{Be}$	2620
$^{136}\text{Xe} + ^{48}\text{Ti}$	3954
$^{136}\text{Xe} + ^{208}\text{Pb}$	6233

Table 4.1: Total reaction cross sections calculated with the Karol code [57] for residues induced by  $^{136}\text{Xe}$  at 1000 MeV/u on different targets.

Contributions of production cross sections of projectile residues normalized to the total reaction cross section obtained with the code Karol [57] and shown in table 4.1). In this figure we observe that the normalized cross sections are similar, within the

error bars, for all targets except for hydrogen. Therefore, we can conclude that the difference in the production cross section seems to be due to the geometrical effect induced by the size of the target nucleus, except for the hydrogen case.

However, it should be noticed that residues that have lost only few neutrons present different cross sections in the lead target compared to the others. This effect is due to the Coulomb excitation mechanism, which in principle is very weak for light target nuclei, but important in the case of the lead target. The excitation energy induced into the projectile residue is relatively small in the case of Coulomb excitations, being the most probable de-excitation channels the evaporation of few neutrons, resulting in a high population of the residues close to the primary projectile, as can be observed in the xenon isotopic chain for the lead target in figure 4.2.

The data in figure 4.2 are compared with the predictions of the ABRABLA code [26, 12] (dashed line) for the system  $^{136}\text{Xe} + ^{48}\text{Ti}$  at 1 GeV/u, also normalized to the total reaction cross section calculated with KAROL [57]. The data are also compared with the predictions obtained with INCL4 [7] for the reaction  $^{136}\text{Xe} + ^1\text{H}$  at 1 GeV/u coupled to the ABLA evaporation code [12].

The calculations with INCL4 have been performed with strict (dotted line) and statistical Pauli blocking (solid line), some details must be mentioned concerning these blockings. In the case of the strict Pauli blocking, only collisions leading to final states with nucleon momenta above the Fermi momentum are allowed. This method is too restrictive after a certain number of nucleon-nucleon collisions producing a noticeable amount of holes in the Fermi sea. In the statistical Pauli blocking, for each nucleon-nucleon collision or  $\Delta$ -decay, the code determines how many neighbor nucleons exist in a sphere of volume  $h^3$  around the nucleon ( $r$  and  $p$  spaces) with the condition that only 2 protons or 2 neutrons (for the 2 spin states) can stay within the volume  $h^3$ . In the first collision, the target is on its ground state and no holes should be found below the Fermi level, but due to statistical arrangement of the nucleons in the target, the code can find a dummy hole. In the first collision this excitation energy is calculated as the sum of all energies of the nucleons within the target. The predictions of INCL4 with strict Pauli blocking provide the best agreement with the data, as can be seen in the tin isotopic chain of figure 4.2, appearing the discrepancies between both calculations for the most neutron-rich residues produced in the most peripheral collisions.

In figure 4.3 we compare the same data with the predictions obtained with the ISABEL code [5] coupled to the ABLA evaporation code. In the case of the hydrogen target, ISABEL (solid line) clearly overpredicts the yields of the most neutron-deficient residues. This effect can be related with an overestimation of the excitation energy induced in the collision. Nevertheless, the code reproduces the data quite

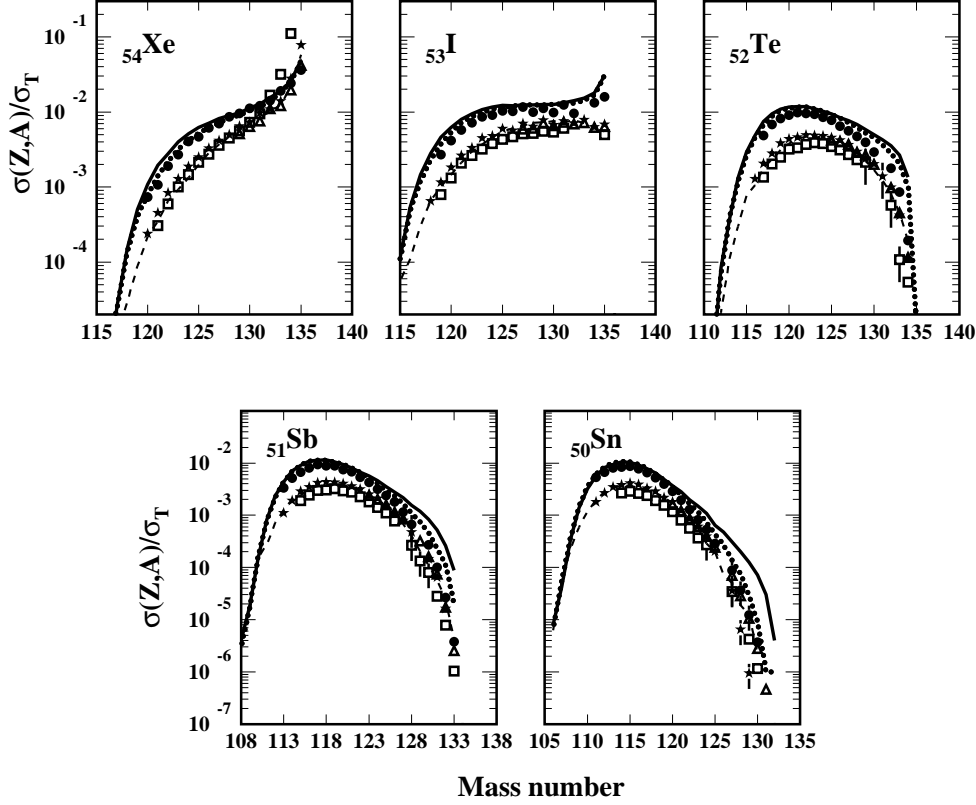


Figure 4.2: Measured isotopic cross sections of projectile residues produced in reactions induced by  $^{136}\text{Xe}$  at 1 GeV/u with several targets,  $^{208}\text{Pb}$  (open squares),  $^{48}\text{Ti}$  (solid stars),  $^9\text{Be}$  (open triangles), and hydrogen (solid circles). The data are compared with the predictions of the ABRABLA code for the  $^{136}\text{Xe} + ^{48}\text{Ti}$  at 1 GeV/u reaction (dashed line) and the prediction from INCL4+ABLA for the reaction  $^{136}\text{Xe} + ^1\text{H}$  at 1 GeV/u with statistical Pauli blocking (solid line) and strict Pauli blocking (dotted line). Both, data and model calculations, are normalized to the total reaction cross sections obtained with the KAROL code [57].

well in the case of heavy targets, as shown by the dashed line in figure 4.3, except for the most neutron-rich nuclei where the calculations overpredict the measured cross sections. A reason for this effect could be an overestimation of the excitation energy induced in reactions where a small number of nucleons are abraded.

As mentioned above, the case of the hydrogen target is completely different from the others. The total reaction cross section does not explain the differences respect to the other systems. However, the behavior of the cross sections with the

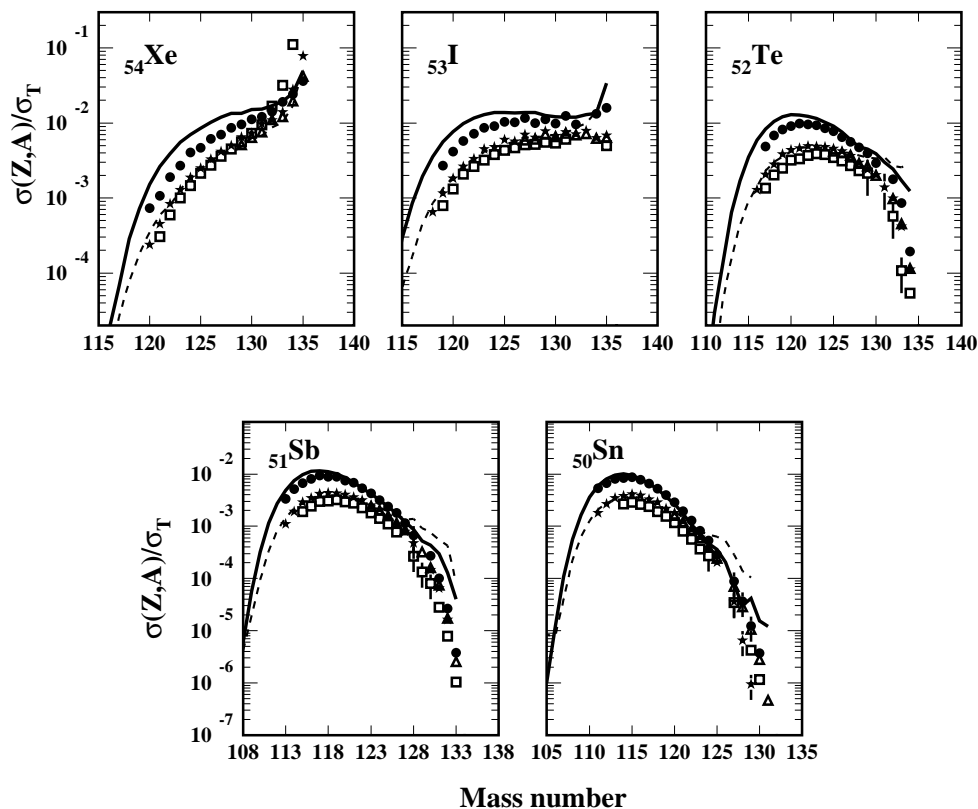


Figure 4.3: Same data as 4.2 but compared with predictions of the ISABEL code [5] for the  $^{136}\text{Xe} + ^{48}\text{Ti}$  at 1 GeV/u (dashed line) and  $^{136}\text{Xe} + ^1\text{H}$  at 1 GeV/u (solid line).

hydrogen target is described correctly by both codes (ISABEL and INCL4), therefore we will make use of these codes to understand why reactions induced by protons are different. In the left panel of figure 4.4 we show the isobaric cross sections calculated with ISABEL+ABLA for the reactions  $^{136}\text{Xe} + \text{Ti, Pb}$  at 1 GeV/u and with INCL4+ABLA for the reaction  $^{136}\text{Xe} + ^1\text{H}$ . As can be deduced from the figure, for mass losses between 4 and 35 nucleons, the cross sections are larger in the case of the hydrogen target, as we observe in the measured data of figures 4.2 and 4.3. This effect can be understood by investigating the number of abraded nucleons and the excitation energy distribution of the prefragments after the abrasion.

In the right-panel of figure 4.4 we represent the number of abraded nucleons in the first stage of the fragmentation reaction as calculated with ISABEL (solid line) for the titanium target and with INCL4 (dashed line) for the hydrogen target. In

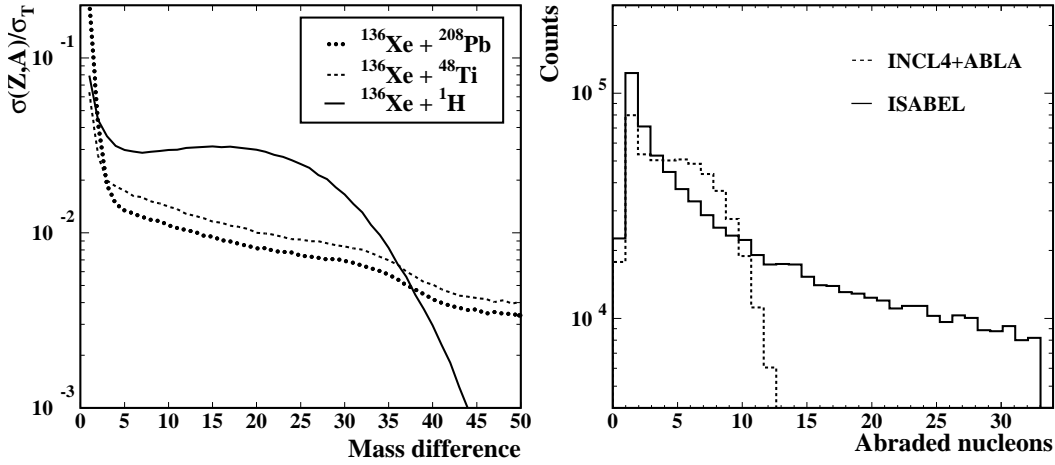


Figure 4.4: (Left Panel) Isobaric cross sections calculated with the INCL4+ABLA code for the reaction  $^{136}\text{Xe} + ^1\text{H}$  at 1000 MeV/u (solid line), and with the code ISABEL for the reactions  $^{136}\text{Xe} + ^{48}\text{Ti}$  (dashed line) and  $^{136}\text{Xe} + ^{208}\text{Pb}$  at 1000 MeV/u (dot line). The predictions of both codes are normalized to the total reaction cross section calculated with the Karol model. (Right Panel) Number of abraded nucleons calculated with the INCL4 code for the reaction  $^{136}\text{Xe} + ^1\text{H}$  at 1000 MeV/u (dashed line), and with the code ISABEL for the reaction  $^{136}\text{Xe} + ^{48}\text{Ti}$  at 1000 MeV/u (solid line).

figure 4.5 we show the excitation energy distributions after the abrasion of 1, 2, 3 and 4 nucleons as calculated with ISABEL (solid line), ABRABLA (dotted line) and INCL4 (dashed line). The mean values of the excitation energy induced in the system are also shown in the figure. From these figures we can conclude that, in general, the number of abraded nucleons is smaller in the case of the hydrogen target, leading thus to a concentration of the residue production in the region close to the projectile. In addition, as the mean value of the excitation energy per abraded nucleon are similar for the hydrogen and the heavier targets, the final residues cross sections are larger for the hydrogen target in the region close to the projectile.

Some remarks must be made concerning to the predictions of ISABEL+ABLA and ABRABLA in the case of heavy targets. From figures 4.2 and 4.3 we have concluded that both codes reproduce accurately the measured data for the  $^9\text{Be}$ ,  $^{48}\text{Ti}$  and  $^{208}\text{Pb}$  targets. In figure 4.6 we show the distribution of abraded nucleons in the first stage of the reaction calculated with ABRABLA and ISABEL in the case of the  $^{136}\text{Xe} + ^{48}\text{Ti}$  at 1000 MeV/u reaction. From this figure and the excitation energy distributions shown in figure 4.5 it is surprising that both codes provide similar results for the production cross sections when the excitation energy and the number of abraded nucleons are so different in both codes. The number of abraded nucleons predicted by ISABEL is much larger than in the case of ABRABLA, however this effect seems to be compensated in the evaporation stage by the lower excitation

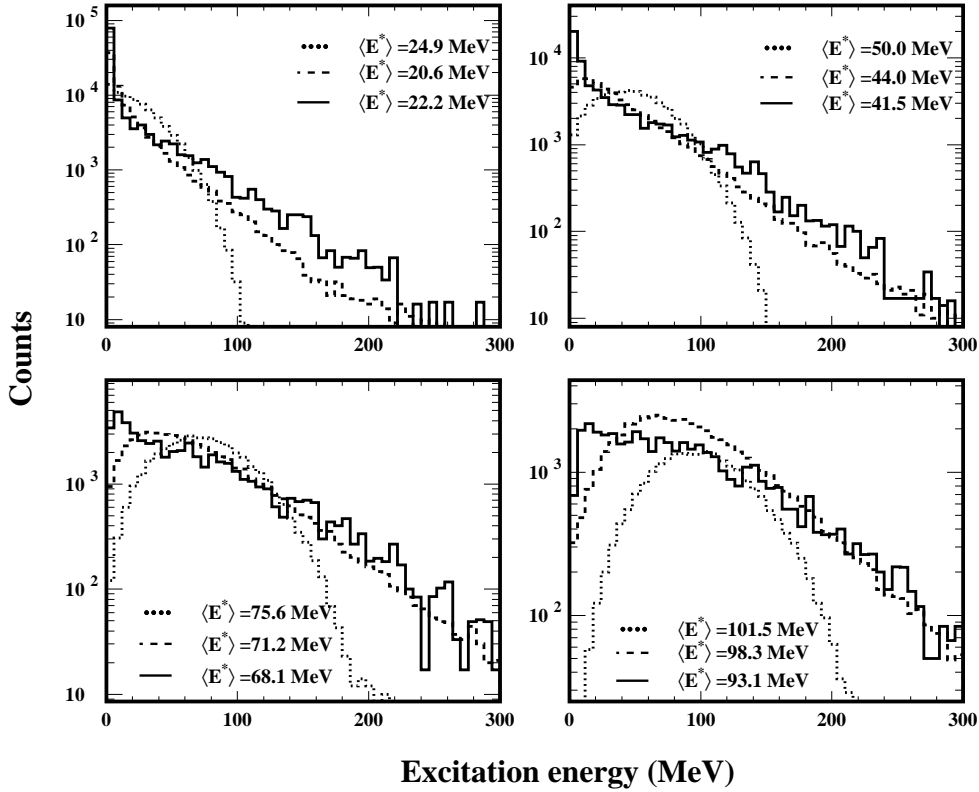


Figure 4.5: Prefragment excitation energy distribution after the abrasion of 1,2,3 and 4 nucleons as calculated with the codes ISABEL+ABLA (solid histogram) and ABRABLA (dotted histogram) for the reaction  $^{136}\text{Xe} + ^{48}\text{Ti}$  at 1000 MeV/u and with the code INCL4+ABLA (dashed histogram) for the reaction  $^{136}\text{Xe} + ^1\text{H}$  at 1000 MeV/u. The mean values of the excitation energy induced in the system are also shown.

energy predicted by this code. Therefore, there is a compensation between the number of abraded nucleons and the excitation energy induced per abraded nucleon, providing thus similar results for the projectile residues cross sections.

## 4.2 Role of the neutron excess of the projectile

In this work we have also performed measurements with two different projectiles,  $^{124}\text{Xe}$  and  $^{136}\text{Xe}$ , in order to investigate the role of the projectile neutron excess in the fragmentation cross sections. This primary projectiles are, respectively, the most neutron-deficient and neutron-rich stable isotopes of xenon. The fragmentation

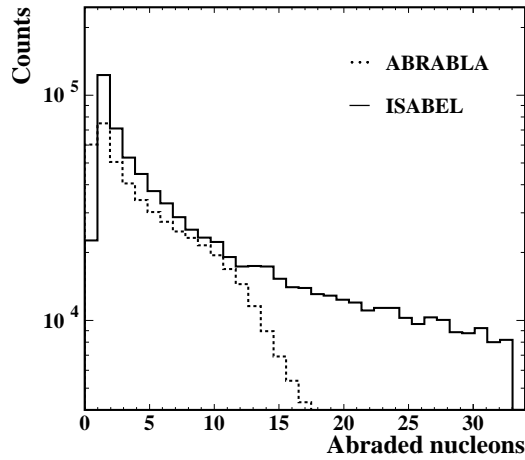


Figure 4.6: *Distributions of abraded nucleons as predicted by the codes ISABEL (solid line) and ABRABLA (dashed line) for the reaction  $^{136}\text{Xe} + ^{48}\text{Ti}$  at 1000 MeV/u.*

residues measured in this work, together with those measured in the fragmentation of  $^{129}\text{Xe} + ^{27}\text{Al}$  [60] are shown in the figure 4.7, normalized to the total cross sections calculated with the Karol code.

The most remarkable behavior of these data is the difference in the width of the isotopic distributions of the projectile residues for the three systems, corresponding the broadest distribution to those residues produced by the projectile with larger neutron excess. This can be explained in terms of the *memory effect* [25]. For prefragments close to the projectile, the excitation energy gained in the abrasion stage is not sufficient to reach the universal evaporation corridor by neutron evaporation. Therefore these projectile residues keep some memory on the N/Z ratio of the primary projectile, the memory effect.

Another remark should be done concerning the maximum of the isotopic distribution of projectile residues. This maximum increases as decreasing the neutron excess, as can be seen in the figure 4.7 or 4.8. This behavior is also related to the N/Z difference between the projectile and the evaporation corridor. In the table 4.2 we present the integral of the isotopic distribution for each element, as well as the number of isotopes corresponding to each chain. The ratio between both values corresponds to the  $\chi$  factor shown in the table. The values of the  $\chi$  factors are always larger in the case of  $^{124}\text{Xe}$  projectiles because the number of isotopes on each chain is shorter while the  $\sigma_Z$  are similar for both projectiles. This explains the differences observed in the figure 4.7 concerning to the maximum of the mass distributions.

In figures 4.7 and 4.8 we compare the measured data with two model calculations, ABRABLA and EPAX, respectively. In general, ABRABLA reproduces the

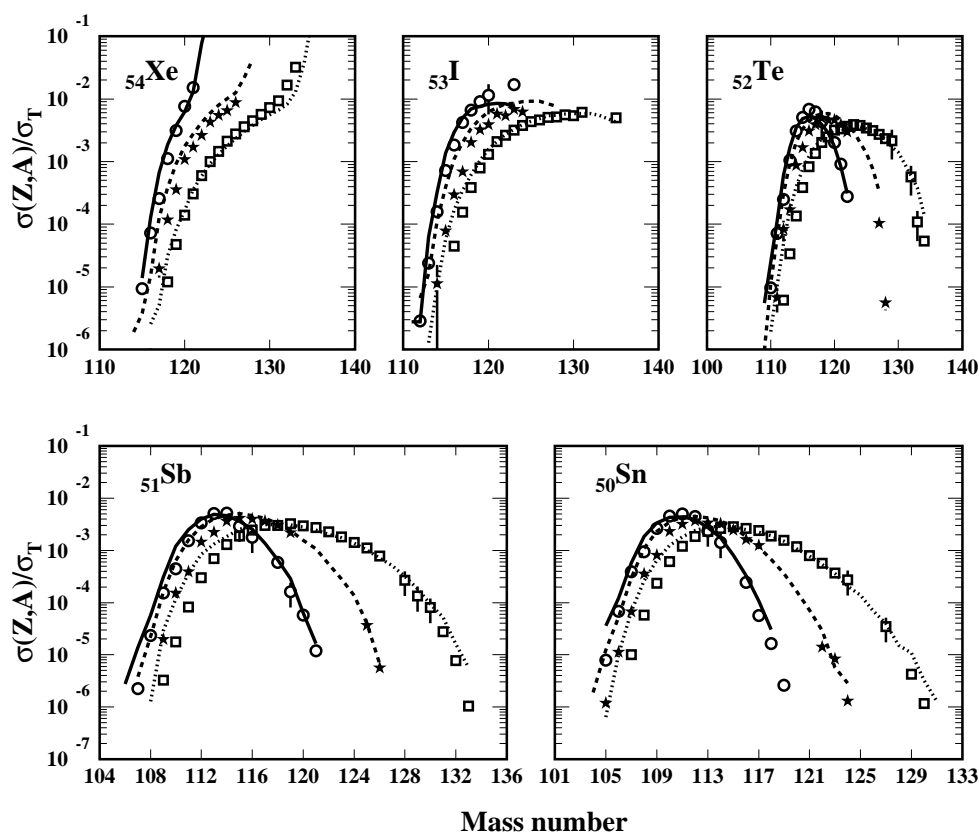


Figure 4.7: Measured isotopic cross sections in the reactions of  $^{124}\text{Xe}$  projectiles at 1 GeV/u with  $^{208}\text{Pb}$  (open circles),  $^{129}\text{Xe}$  projectiles at 790 MeV/u with  $^{27}\text{Al}$  [60] (solid stars) and  $^{136}\text{Xe}$  projectiles at 1 GeV/u with  $^{208}\text{Pb}$  (open squares). The data are normalized to the total cross section as predicted by the Karol code and compared the predictions of the ABRABLA code (lines)

experimental data better than EPAX does, specially in the neutron-rich region, but it overpredicts the yields of the most neutron-deficient residues. This could mean that, in this case, the high-energy tail of the excitation-energy distribution is overestimated for these fragments in the code. Both codes propose a totally different shape of the yield distributions for charges  $Z=54$  and  $Z=53$ . ABRABLA reproduces with great precision the mass distribution of fragments with the charge of the projectile, as well as the residues with charges  $Z=53$  and  $Z=52$ . However, below the  $Z=52$  the code overestimates the production cross sections in the neutron deficient region. In the case of the  $^{124}\text{Xe}$  reproduces better the neutron-deficient side of the mass distribution, but ABRABLA clearly underestimates the region very close to the projectile in the iodine isotopic chain. This effect could be related to the Coulomb excitation

Atomic Number	Projectile	$\sigma_Z$ (mb)	Number of fragments	$\chi$
Z=53	$^{136}\text{Xe}$	453	22	20.6
Z=53	$^{124}\text{Xe}$	348	13	26.8
Z=52	$^{136}\text{Xe}$	262	23	11.4
Z=52	$^{124}\text{Xe}$	187	13	14.4
Z=51	$^{136}\text{Xe}$	193	24	8.0
Z=51	$^{124}\text{Xe}$	161	15	10.7
Z=50	$^{136}\text{Xe}$	171	21	8.1
Z=50	$^{124}\text{Xe}$	148	14	10.6

Table 4.2: *Integral of the isotopic distributions for both projectiles studied in this work. The number of fragments of each isotopic chain and the ratio between this number and the integral are also shown. The cross sections were calculated with the ABRABLA code.*

channel.

The EPAX code (figure 4.8), however, does not reproduce so accurately the shape of the yield distribution. It predicts quite well the data from the  $^{129}\text{Xe}$  projectile, but it even failures in the neutron-rich side of these mass distributions. Indeed, EPAX is a semiempirical code that, among others, was fitted to the measured isotopic cross sections for the reaction  $^{129}\text{Xe} + ^{27}\text{Al}$ . The code does not reproduce at all the projectile residues with charge  $Z=54$ , neither the shape of the mass distribution or the position of its maximum. In general, EPAX has problems with the shape of the yield distributions, it is too broad in the case of the  $^{124}\text{Xe}$  projectile and too narrow in the case of the  $^{136}\text{Xe}$  projectile. This effect translates into an overestimation in the cross sections of the most neutron-rich side of the residues and an underestimation of the neutron-deficient side, as can be extracted from the figure 4.8. This effect is amplified when the primary projectile has a large neutron excess (as  $^{136}\text{Xe}$ ).

### 4.3 Role of the projectile energy

In this section we are going to discuss the role of the energy of the projectile in the final production cross sections of the reaction residues. For these investigations we will make use of the fragmentation cross sections of  $^{136}\text{Xe}$  with a titanium target at different energies, 1000, 500 and 200 MeV/u. In figure 4.9 we present the isotopic distributions of the measured cross sections.

From the Glauber model [11] we do not expect any dependence of the cross

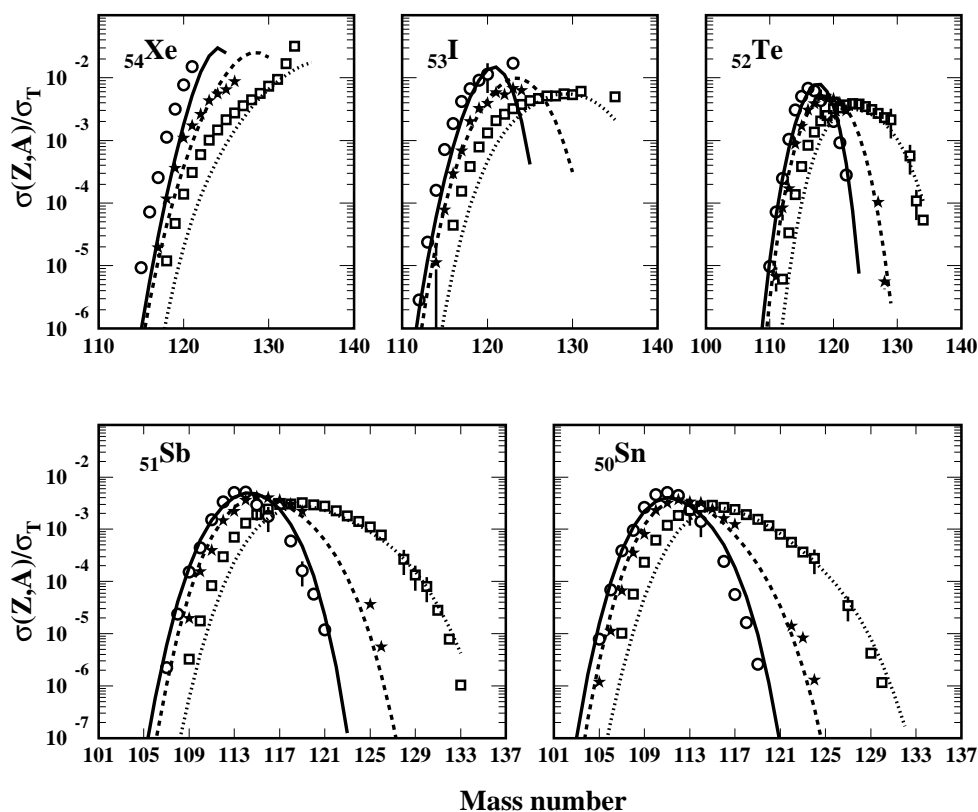


Figure 4.8: Measured isotopic cross sections in the reactions of  $^{124}\text{Xe}$  projectiles at 1 GeV/u with  $^{208}\text{Pb}$  (open circles),  $^{129}\text{Xe}$  projectiles at 790 MeV/u with  $^{27}\text{Al}$  (solid stars) and  $^{136}\text{Xe}$  projectiles at 1 GeV/u with  $^{208}\text{Pb}$  (open squares). The data are normalized to the total cross section as predicted by the Karol code and compared the predictions of the EPAX code (lines)

sections with the energy of the projectile. This model states that the reaction cross sections are purely geometrical, playing the energy no role on the reactions. However, the isotopic chains of xenon and iodine residues shown in Figure 4.9 present cross sections that clearly depends on the initial energy of the projectile, but this effect vanishes very fast and, actually, for  $Z=52$  the cross sections are equivalent for the three systems, independently of the energy. This can be explained by means of the *limiting fragmentation* concept ([17], [18]), stating that, beyond a certain value of the kinetic energy of the projectile, the production cross sections of reaction residues are independent of the energy. From our data we can conclude that, down to 200 MeV/u, the limiting fragmentation hypothesis is fulfilled for charges below  $Z=53$ , as demonstrated in the data from figure 4.9.

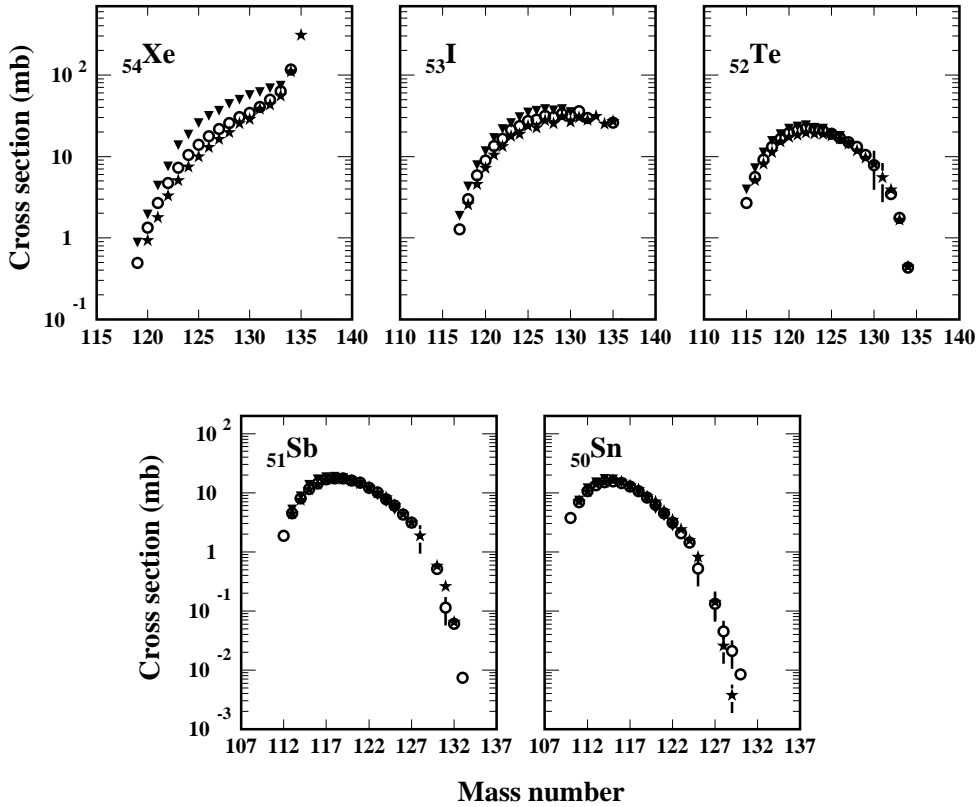


Figure 4.9: Measured isotopic distributions of cross sections of projectile residues in reactions of  $^{136}\text{Xe}$  projectiles with a  $^{48}\text{Ti}$  target at 1000 MeV/u (solid stars), 500 MeV/u (open circles) and 200 MeV/u (solid triangles).

However, very close to the projectile the measured data do not follow the limiting fragmentation hypothesis. This effect cannot be explained by means of the total reaction cross section, as can be seen in the table 4.3, where these cross sections have been calculated with the Karol code. Karol is based on the Glauber model, and hence on the nucleon-nucleon cross sections, which are almost independent of the energy down to 200 MeV/u, providing total cross sections similar at the three energies. There must then exist a different mechanism which produces this behavior in the region close to the projectile.

In order to understand these results, we have used different model calculations in order to reproduce the behavior of the measured cross sections for residual nuclei with atomic number close to the one of the projectile. The solid line in figure 4.10 represents the predictions obtained with the ABRABLA code for the reaction  $^{136}\text{Xe}$

Energy (MeV/u)	$\sigma_{TOT}$ (mb)
200	3855
500	3827
1000	3954

Table 4.3: *Total reaction cross sections as calculated with the Karol code for the reaction  $^{136}\text{Xe} + ^{48}\text{Ti}$  at several energies investigated in this work.*

+  $^{48}\text{Ti}$  at 500 MeV/u. As can be observed, the code fails in describing the data for the isotopic chains of xenon and iodine. A possible explanation for this discrepancy could be the excitation energy gained by the prefragment during the abrasion stage of the reaction. To check this possibility we have performed calculations with ABRABLA modifying the mean value of the excitation energy per abraded nucleon introduced into the system. This energy is fixed in the code to be 27 MeV [26], and we have made calculations with 13.5 and 40.5 MeV/u corresponding to the dashed and dotted lines in the figure 4.10, respectively. As can be observed in the figure, the variation of the excitation energy does not improve the description of the measured data, being the discrepancies remarkably important in the neutron-rich side of the isotopic chain. Similar results were obtained at 200 and 1000 MeV/u, confirming that 27 MeV/u is the most reliable value for the mean excitation energy per abraded nucleon, thus we can conclude that this is not the reason of the discrepancies between ABRABLA and the measured data.

In figure 4.11 we present the comparison of the codes ABRABLA (dashed line) and ISABEL+ABLA (solid line) with the measured data. In this plot we have also included the projectile residues with charge  $Z=55$ , corresponding to the charge-exchange mechanism. Just mention that ABRABLA code does not take into account the charge-exchange process, this is the reason why for charge  $Z=55$  there is no calculation shown for this code in figure 4.11.

As can be seen in figure 4.11, the best agreement between the codes and the measured data correspond to the reaction at 1000 MeV/u. But this agreement deteriorates when decreasing the energy in both codes, being specially remarkable at 200 MeV/u for ABRABLA (see the isotopic chain of the xenon). We have already demonstrated that the discrepancies in ABRABLA do not come from the excitation energy introduced into the system in the first stage of the fragmentation reaction, it must then arise from another mechanism as could be the charge-exchange channels.

In the charge-exchange process, the initial projectile can increase its charge by two possible mechanisms, a quasi-elastic process or a resonance process where the  $\Delta(1232)$  particle is excited. Both mechanisms are driven by the exchange of virtual pions between projectile and target. In figure 4.12 we present the evolution of the

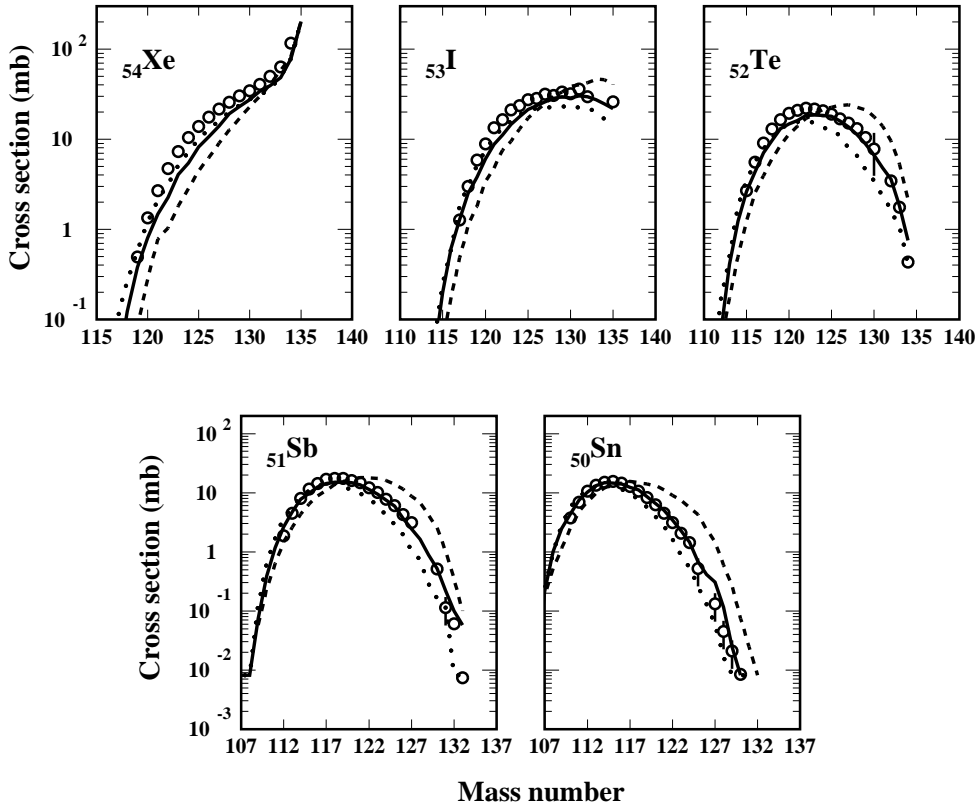


Figure 4.10: Measured isotopic cross sections in the reaction of  $^{136}\text{Xe}$  projectiles at 500 MeV/u with a  $^{48}\text{Ti}$  (open circles). The data are compared with the predictions of ABRABLA code for different values of the excitation energy per abraded nucleon, 13.5 MeV (dashed line), 27 MeV (solid line) and 40.5 MeV (dashed-dotted line).

nucleon-nucleon cross section for the total, elastic and inelastic channels. It can be seen that the probability of the elastic channel increases as decreasing the energy, following the same behavior of the charge-exchange mechanism, as already observed in many experimental works ([61], [62]) and also in this thesis (see chapter 5). This discussion, and the fact that ISABEL (where the charge-exchange is already taken into account) reproduces better the experimental data, suggests that the observed energy dependence of the measured cross sections close to the projectile and the discrepancies with ABRABLA are due to the charge-exchange process.

In order to improve the predictive power of ABRABLA, we have modified the code to incorporate the physics of the charge-exchange mechanism. In this new version the total reaction cross section is not only due to the abrasion and electro-

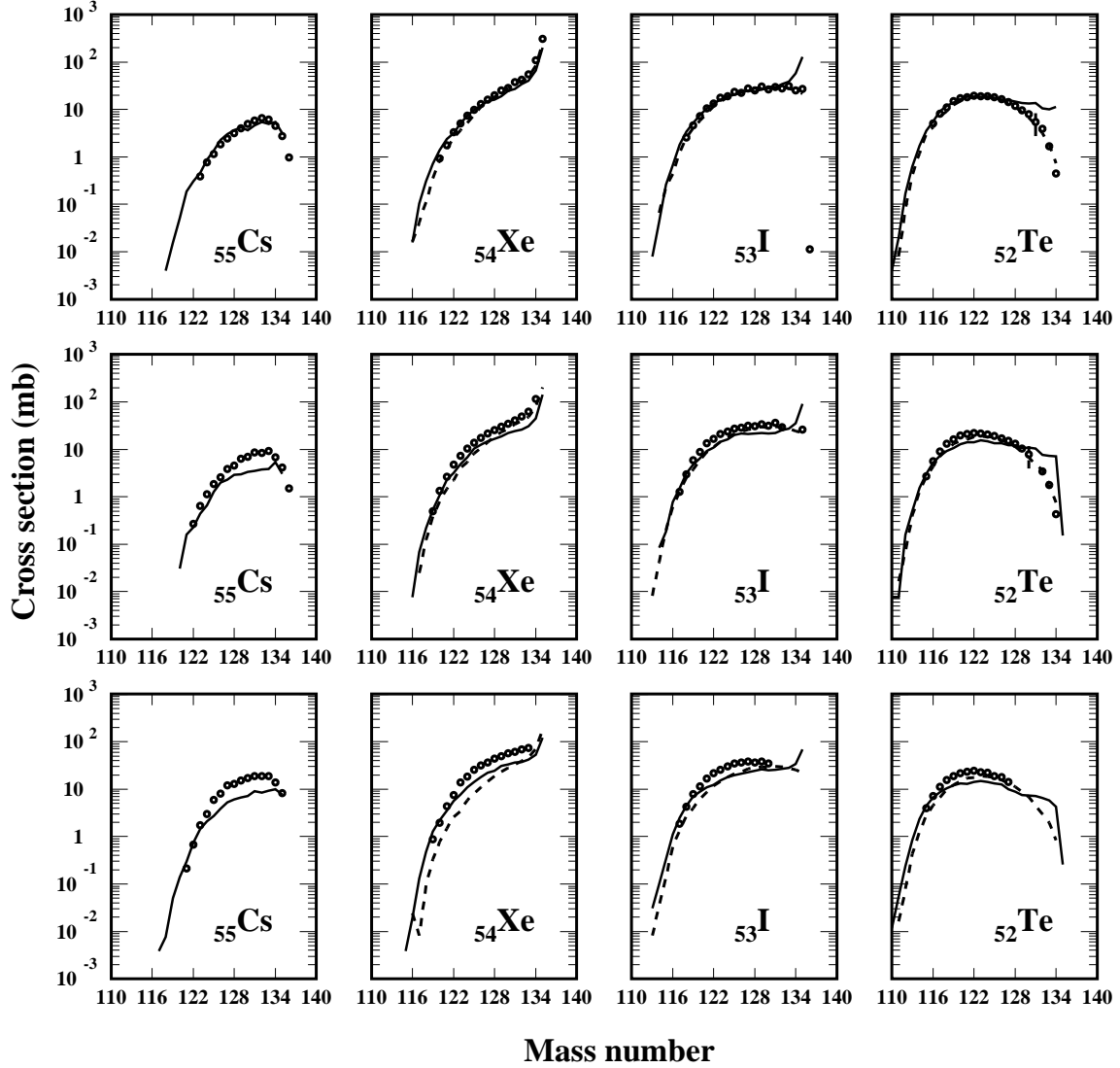


Figure 4.11: Measured isotopic distributions of projectile residue cross sections produced in the reaction  $^{136}\text{Xe} + ^{48}\text{Ti}$  at 1000 MeV/u (upper row), 500 MeV/u (middle row) and 200 MeV/u (bottom row). The data are compared with the predictions of the codes ABRABLA (dashed line) and ISABEL+ABLA (solid line).

magnetic channels, but also to the charge-pickup according to:

$$\sigma^{TOT} = \sigma^{abra} + \sigma^{EMD} + \sigma^{pickup} \quad (4.1)$$

where  $\sigma^{abra}$  is the abrasion reaction cross section,  $\sigma^{EMD}$  is the electromagnetic dissociation and  $\sigma^{pickup}$  is the charge-pickup cross section. This charge-pickup cross

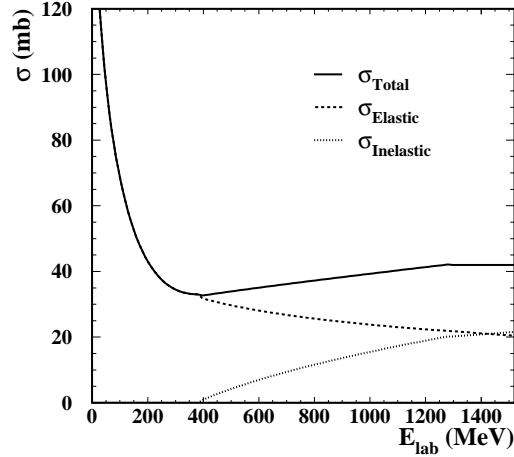


Figure 4.12: Total (solid line), elastic (dashed line) and inelastic (dotted line) nucleon-nucleon cross-sections as parametrized in reference [8].

section is calculated according to the experimental results obtained by Guoxiao et al. [63], which state that, for geometrical reasons, the probability of a charge-pickup process is proportional to the dimensions of target and projectile nuclei in the following way:

$$\sigma^{pickup} = \kappa \cdot (A_p^{1/3} + A_t^{1/3}) \cdot A_t^{2/3} \quad (4.2)$$

where  $\kappa$  is a constant which should take into account the energy dependence of the process, as we will show below.

Whenever a charge-pickup prefragment is created in the reaction, the code assigns to this nucleus an excitation energy. This energy is randomly chosen within a triangle distribution as shown in figure 4.13.

This excitation energy distribution has a zero probability at the maximum value of 290 MeV, corresponding to the mass difference between the  $\Delta$ -resonance and the *nucleon*. With this modifications, the results given by ABRABLA are compared with the previous ones in figure 4.13. We have leave the  $\kappa$  factor as a free parameter to be fit in order to get the best agreement with the experimental data. As can be observed, the improving in the predictions of the code is obvious. The isotopic chain of the charge-pickup ( $Z=55$ ) is well described for the three energies and the improving in the charge  $Z=54$  at 500 and 200 MeV/u is also patent. The energy dependence of the factor  $\kappa$  will be extensively discussed in the section 5.1 of this work and a graphical representation can be seen in figure 5.7. For clarity we reproduce here the result of the fit to the experimental data measured in this work:

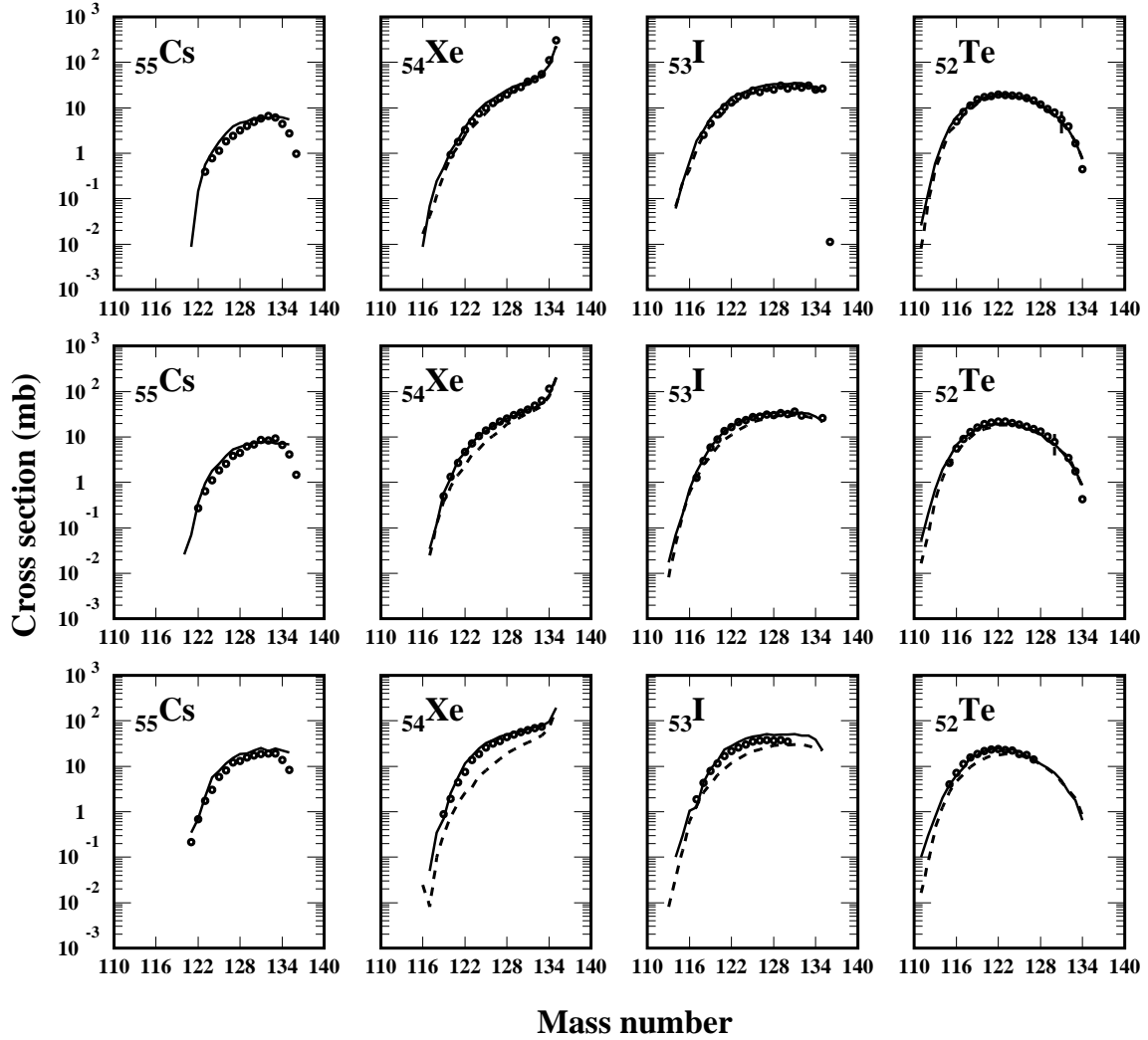


Figure 4.13: Measured isotopic cross sections in the reactions  $^{136}\text{Xe} + ^{48}\text{Ti}$  at 1000 MeV/u (upper row), 500 MeV/u (middle row) and 200 MeV/u (bottom row). The data are compared with the predictions of the ABRABLA code (dashed line) and ABRABLA modified to include the charge-pickup process (solid line), see text for details.

$$\kappa(E) = 5.05 \cdot \exp^{-6.84 \cdot 10^{-3} \cdot E} + 0.153 \quad (mb) \quad (4.3)$$

With these values of the  $\kappa$  parameter we obtain the most accurate description of the cross sections for the charge-exchange residues.

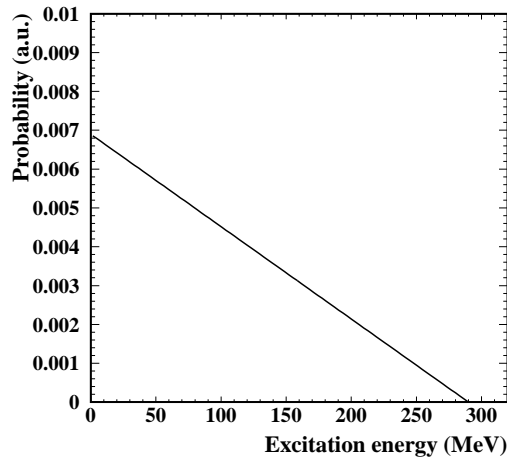


Figure 4.14: *Simulated excitation energy distribution induced by charge-exchange reactions that best describe our data.*

## 4.4 Longitudinal momentum distributions

As in the case of the residue production cross sections, the wide range of measured data allow to perform a systematical analysis on the behavior of the mean value and the width of the longitudinal momentum distributions of the fragmentation residues. We will also compare these values with the existing models to describe these physical observables.

### 4.4.1 Role of the target size

We will explore here the influence of the target size on the longitudinal velocities. In figures 4.15 and 4.16 we have plot all the measured mean longitudinal momenta for the fragments created in the reaction of  $^{136}\text{Xe}$  projectiles at 1000 and 500 MeV/u with different targets. From the model of Morrissey describing the momentum distribution of the reaction residues, we do not expect any dependence on the target mass, but only with the mass difference between projectile and residue, independently from their nature. This is what we observe in the measured data, as shown in the figures.

Another remarkable feature is the offset in the mean value of the momenta for the residues corresponding to the charge-pickup process ( $Z=55$ , Cs). This offset comes from the resonant charge-pickup channel, which implies the excitation of a  $\Delta$  resonance, where approximately 300 MeV of energy are required. For the  $^{136}\text{Xe}$  at 1000 MeV/u, a sudden loss of 300 MeV translates into a longitudinal momentum

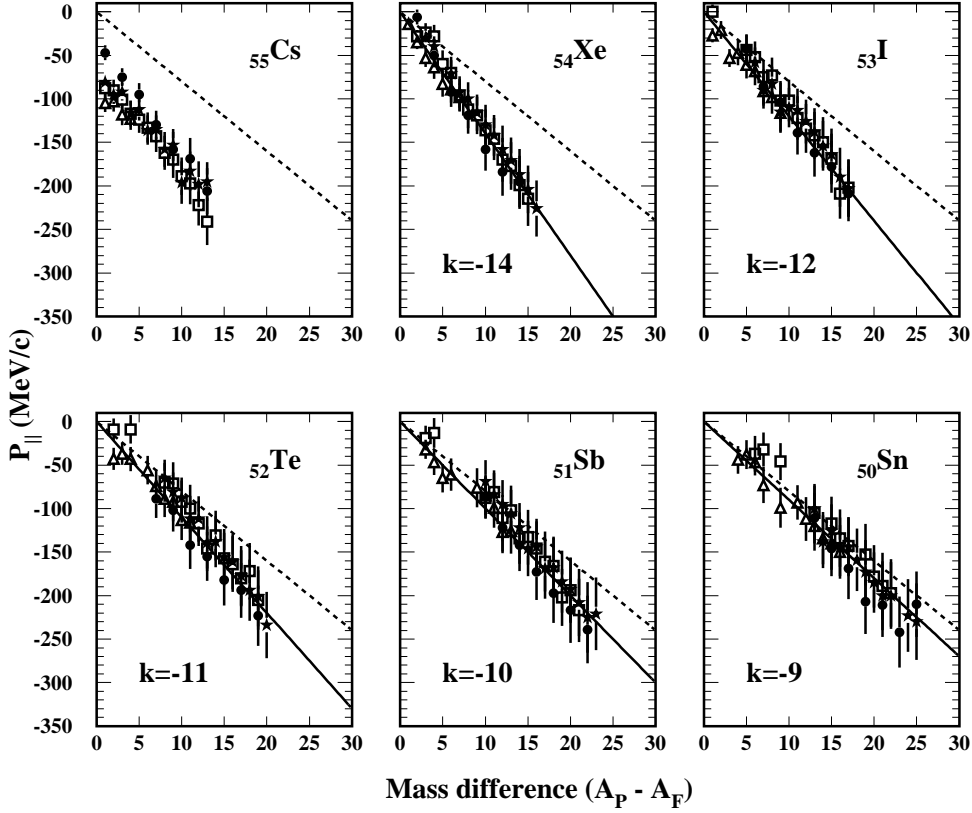


Figure 4.15: Longitudinal momentum (in the projectile frame) for some projectile fragments, as a function of their mass difference with the projectile, measured in the reactions of  $^{136}\text{Xe}$  projectiles at 1000 MeV/u with several targets, hydrogen (solid circles), beryllium (open triangles), titanium (solid stars) and lead (open squares). The data are compared with the Morrisey systematic (dashed lines) and the solid lines represent a scaling with the mass difference of the residues, the proportionality constant is given on each plot.

offset about 170 MeV/c. Since the quasi-elastic charge-pickup produces no shift shifts in momentum, the observed averaged value of the momentum distribution is around 70 MeV, as observed in figure 4.15.

The measured data in the figures 4.15 and 4.16 are also compared with the results obtained with the systematic of Morrisey (expression 1.13) (dashed lines), and also with different lines that better reproduce the experimental data (solid lines). The Morrisey formula states that the residue longitudinal momenta scales with the mass difference between the projectile and residue with a factor of -8. In our case, in

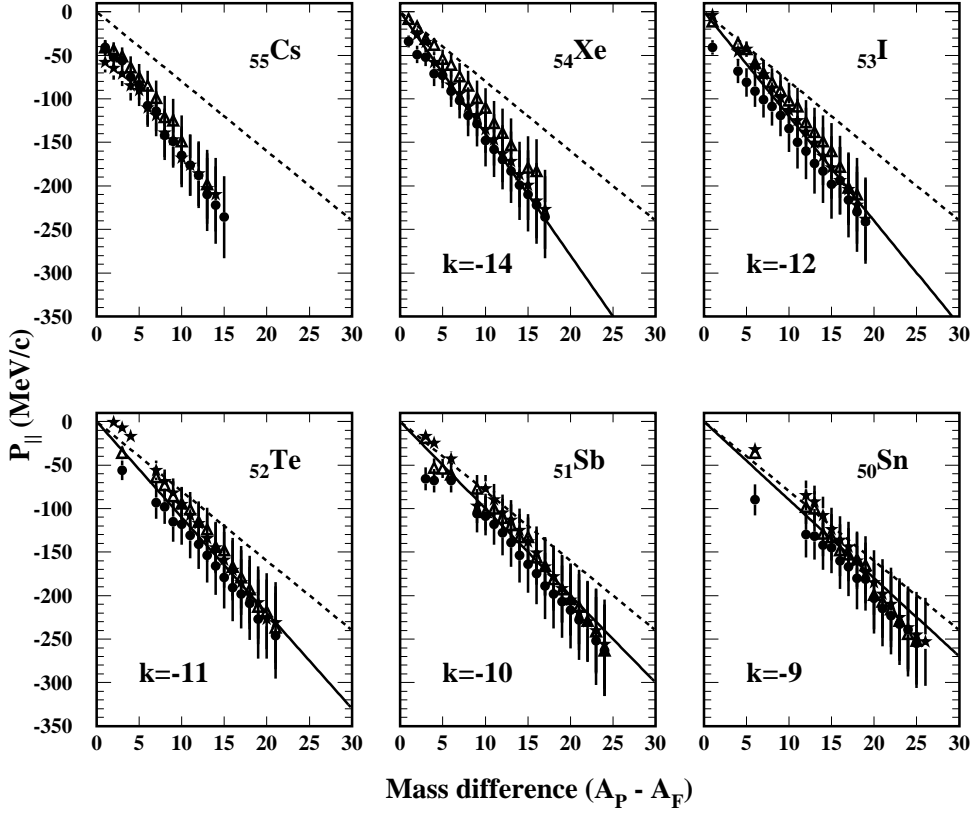


Figure 4.16: Longitudinal momentum (in the projectile frame) for some projectile fragments, as a function of the mass difference with the projectile, measured in the reactions of  $^{136}\text{Xe}$  projectiles at 500 MeV/u with several targets, hydrogen (solid circles), deuterium (open triangles) and titanium (solid stars). The data are compared with the Morrisey systematic (dashed lines) and the solid lines represent a scaling with the mass difference of the residues, the proportionality constant is given on each plot.

order to reproduce the data, we have scaled the isotopic chain corresponding to each element by the factor  $k$  shown in the figure. The slope of the distribution scales clearly with the charge of the fragments and it seems to approach the value given by Morrisey for residues close to the evaporation corridor. This effect was already observed by Weber [64] and seems to be independent of the nature of the target and also independent of the energy of the projectile, as can be seen in both figures 4.15 and 4.16.

Again, we think that this effect is related to the resonant charge-exchange reac-

tions. For the element  $Z=55$ , the effect is clear, only charge-exchange processes with a subsequent evaporation of neutrons are involved in the production of those nuclei, explaining the offset observed in the mean value of the momentum distribution of the reaction residues. However, residues with  $Z=54$  and a number of neutrons similar to the primary projectile are created by abrasion of few neutrons and cannot be created by the charge-pickup mechanism. Thus, residues very close to the projectile should not be then influenced by the charge-pickup reactions and they must follow the Morrisey systematic, as observed in figures 4.15 and 4.16. When the reaction is less peripheral, the number of nucleons involved in the reaction is larger. In this sense it is possible to obtain a residue with charge  $Z=54$  by means of a  $\Delta$ -excitation together with the abrasion of one proton and several neutrons, where the charge-exchange plays a role in the velocity distribution of residues. Then, far from the projectile, the residues should not follow the Morrisey systematics, as observed in figures 4.15 and 4.16. For lower charges, however, the process must be dominated by the abrasion reactions and hence the influence of the charge-exchange reactions should vanish as decreasing the atomic number of the projectile residues, converging to the Morrisey systematics as observed in the experimental data presented in figures 4.15 and 4.16.

In the figure 4.17 we present the same data of figure 4.15, but separated according to the target. In this case we can clearly observe the offset in the longitudinal momenta of the isotopic chain corresponding to the charge-pickup reactions. This offset is less evident in the case of the hydrogen target, but is remarkably strong in the case of the heavy targets. The data are compared with the Morrisey systematics (solid line).

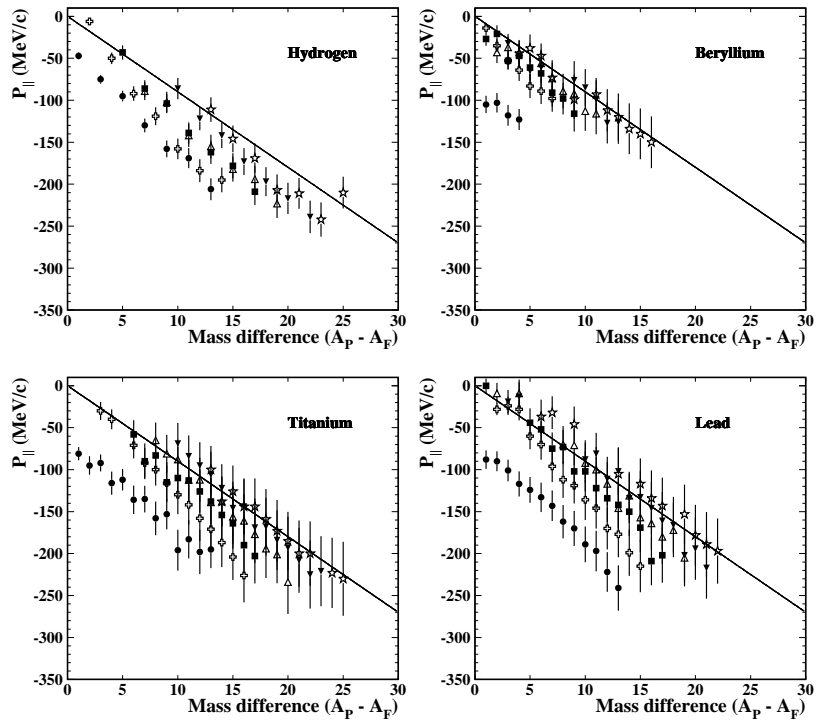


Figure 4.17: Longitudinal momentum (in the projectile frame) for some projectile fragments, as a function of the mass difference with the projectile, measured in the reactions of  $^{136}\text{Xe}$  projectiles at 1000 MeV/u with several targets, hydrogen (top left), beryllium (top right), titanium (bottom left) and lead (bottom right). The different symbols denote  $Z=55$  (solid circles),  $Z=54$  (open crosses),  $Z=53$  (solid squares),  $Z=52$  (open triangles),  $Z=51$  (solid triangles) and  $Z=50$  (open stars). The data are compared with the Morrisey systematic (solid lines).

#### 4.4.2 Neutron excess of the projectile

In this section we investigate the role of the neutron excess of the projectile in the mean value of the transferred longitudinal momentum in the collision. We can compare the mean values of the longitudinal momenta for the residues created in the reactions of the  $^{124}\text{Xe}$  and  $^{136}\text{Xe}$ , to study the possible influence of the initial isospin of the projectile. The measured data corresponding to both systems are shown in the figure 4.18

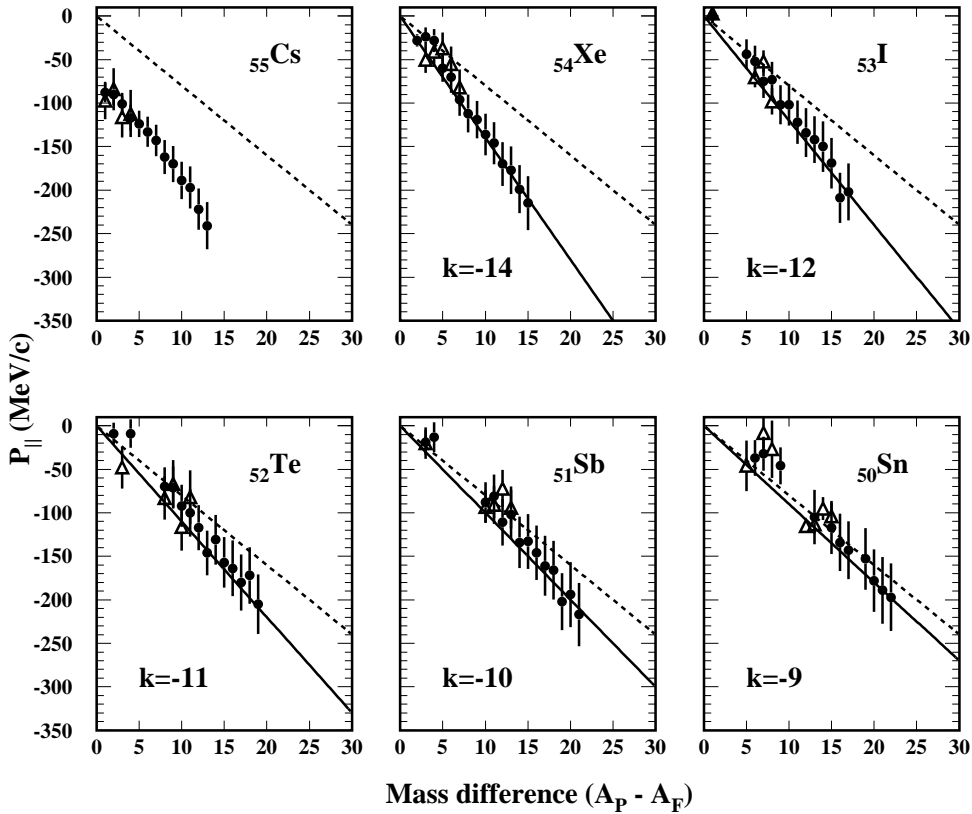


Figure 4.18: Longitudinal momentum (in the projectile frame) for all the projectile fragments, as a function of the mass difference with the projectile, measured in the reactions  $^{124}\text{Xe} + ^{208}\text{Pb}$  at 1000 MeV/u (open triangles) and  $^{136}\text{Xe} + ^{208}\text{Pb}$  at 1000 MeV/u (solid circles). The lines represent a scaling with the mass difference of the residues, the proportionality constant is given on each plot.

The general behavior of the measured data is analogous to the one discussed in the previous section. The offset in the residues corresponding to the charge-pickup is

also present in those fragments coming from the  $^{124}\text{Xe}$ . However, the mean values of the longitudinal momenta seem to be independent of the neutron-to-proton ratio of the projectile and also follow a linear dependence with the mass difference between the projectile and residue. The data also show the dependence with the charge of the residues discussed in the last section.

### 4.4.3 Role of the projectile energy

Finally we are going to discuss also the effect of the projectile energy in the longitudinal momentum distributions. Again we will perform a systematic investigation using the data obtained in the reaction  $^{136}\text{Xe} + ^{48}\text{Ti}$  at 200, 500 and 1000 MeV/u. The measured data are shown in the figure 4.19.

The results, as expected from the Morrissey systematic (dashed line), are energy independent. The measured data from the three systems follow the same behavior, they scale with the mass difference to the projectile but the slope of the distribution depends on the charge of the residues, being equivalent to other systems discussed above. This behavior is not followed by the isotopic chain of the charge-pickup residues, confirming again that the physics of this process is completely different to the physics of the fragmentation process. Moreover, in figure 4.19 we can observe how the offset has a dependence with the energy of the projectile. This effect is due to the energy dependence of the  $\Delta$  and quasi-elastic charge-exchange channels, shown in figure 4.12 as parametrized in [8]. The number of quasi-elastic reactions increases as decreasing the energy, being the opposite for the  $\Delta$  excitation, as also measured in [61] and [62].

The offset in the momentum distributions corresponds to the mean value between the elastic and resonant charge-exchange channels. As the quasi-elastic channel dominates the process when decreasing the energy, for low energies we expect a smaller momentum offset than at high energies, as observed in the measured data of figure 4.19.

### 4.4.4 Width of the longitudinal momentum distributions

The measured momentum distributions are the result of the two stages of the fragmentation reactions, the abrasion and the evaporation, as explained before. The traces of both stages are implicit in the velocity spectra measured in this work, being the momentum width mainly governed by the evaporation process and hence related to the excitation energy of the prefragment.

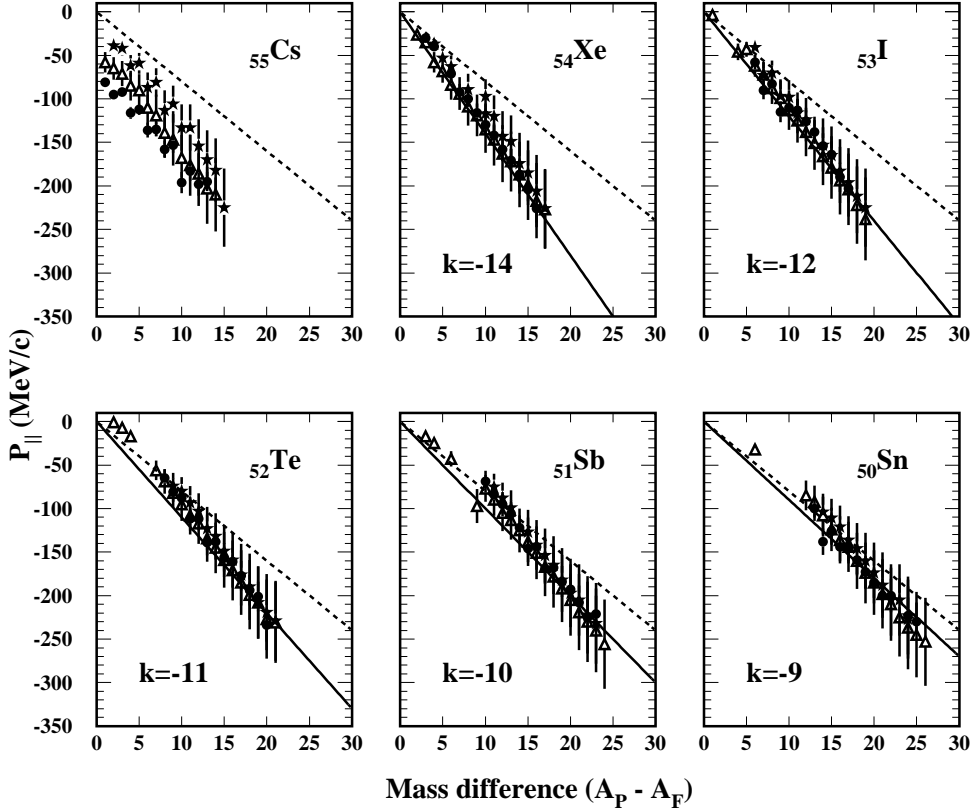


Figure 4.19: Longitudinal momentum (in the projectile frame) for all the projectile fragments, as a function of the mass difference with the projectile, measured in the reaction  $^{136}\text{Xe} + ^{48}\text{Ti}$  at 1000 MeV/u (solid circles), 500 MeV/u (open triangles) and 200 MeV/u (solid stars). The data are compared with the Morrisey systematic (dashed lines) and the solid lines represent a scaling with the mass difference of the residues, the proportionality constant is given on each plot.

In figures 4.20 to 4.23 we will show the data measured in this work. We will comment the figures in a general way because we did not find any systematic behavior of the measured data, the evolution of the momentum widths follows a general tendency, independent from the energy, the projectile or the target. The data fall below the Goldhaber predictions, as expected, due to the evaporation stage of the reaction, while the Morrisey predictions fit better the measurements. This trend has been largely observed in many works concerning relativistic heavy-ion collisions ([65] - [66] and the references cited therein).

In figure 4.20 we show the widths of the momentum distributions measured in

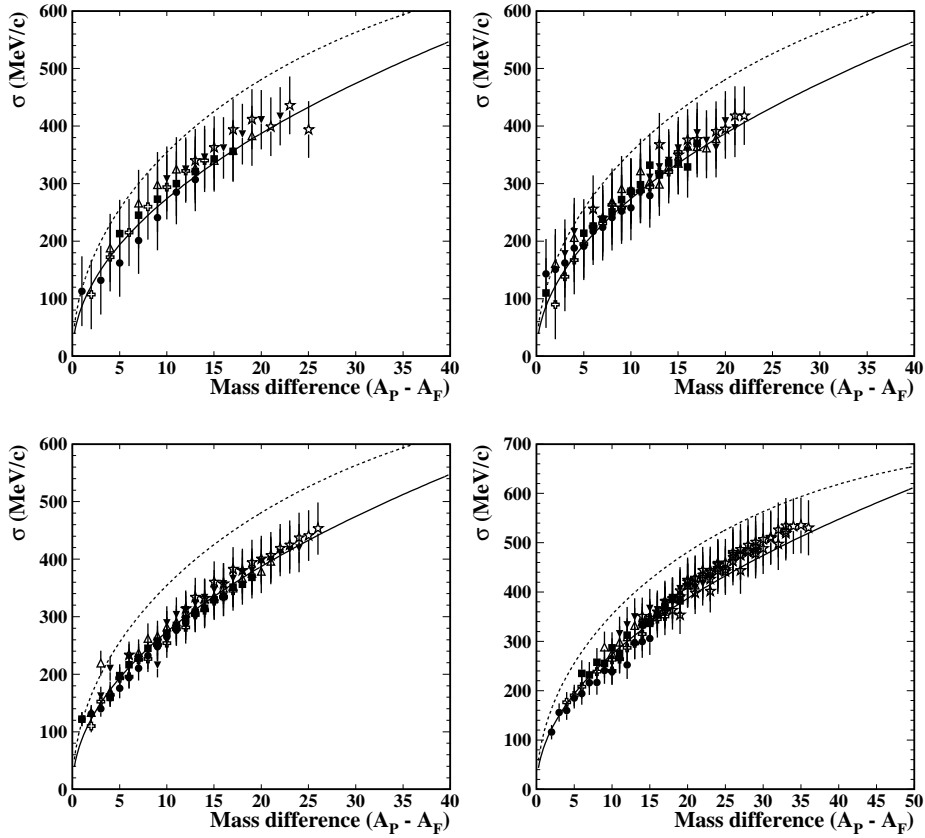


Figure 4.20: Momentum widths for all the fragments measured in the reactions of  $^{136}\text{Xe}$  projectiles with several targets, hydrogen at 1000 MeV/u (top left), lead at 1000 MeV/u (top right), titanium at 500 MeV/u (bottom left) and titanium at 200 MeV/u (bottom right). The different symbols denote  $Z=55$  (solid circles),  $Z=54$  (open crosses),  $Z=53$  (solid squares),  $Z=52$  (open triangles),  $Z=51$  (solid triangles) and  $Z=50$  (open stars). The data are compared with the Morrisey systematic (solid lines) and the Goldhaber systematics (dashed lines).

this work for all the residues from the  $^{136}\text{Xe}$  projectile fragmentation with several targets, hydrogen (upper-left panel) and lead (upper-right panel) at 1000 MeV/u, titanium at 500 MeV/u (bottom-left panel) and titanium at 200 MeV/u (bottom-right panel). The data follow closely the Morrisey systematics and there is no additional dependencies to stress. For each figure, residues corresponding to different atomic numbers are plotted with different symbols for clarity.

In the figure 4.21 we show the data measured in the reaction of  $^{136}\text{Xe}$  projectiles at 1000 MeV/u with the targets of hydrogen, beryllium, titanium and lead as a function of the atomic number of the residues. Different systems correspond to different symbols, again we can not state any significant tendency in the data.

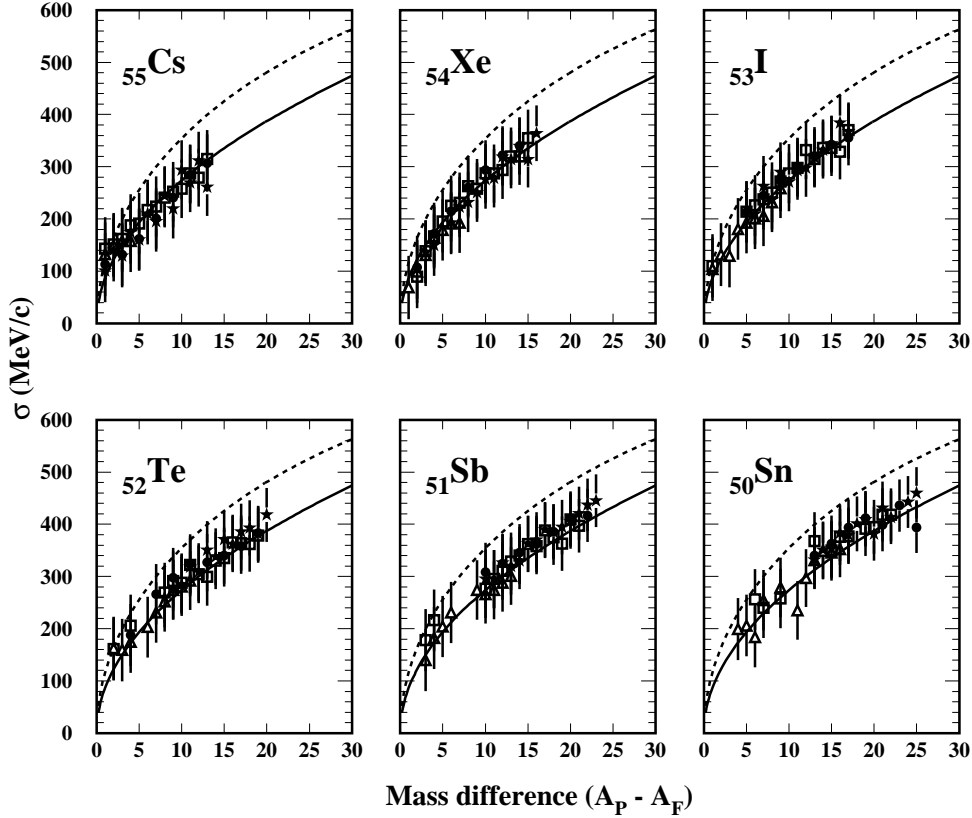


Figure 4.21: Momentum width for all the fragments measured in the reactions of  $^{136}\text{Xe}$  projectiles at 1000 MeV/u with several targets, hydrogen (solid circles), beryllium (open triangles), titanium (solid stars) and lead (open squares). The data are compared with the Morrisey systematic (solid line) and the Goldhaber systematic (dashed line).

The same discussion can be done with the measured data of residues from the reactions  $^{136}\text{Xe}$  and  $^{136}\text{Xe} + \text{Pb}$  at 1000 MeV/u. These data are shown in the figure 4.22 and, even when the data from the  $^{124}\text{Xe}$  are very few, we can say that there is no dependence on the projectile isospin (neutron excess) in the widths of the longitudinal momentum of the residues.

In the figure 4.23 we study the energy dependence of the momentum widths for the residues from the reaction  $^{136}\text{Xe} + \text{Ti}$  at 1000, 500 and 200 MeV/u. Once more we can not say that there exists any significant tendency of the measured data with the energy of the primary projectile.

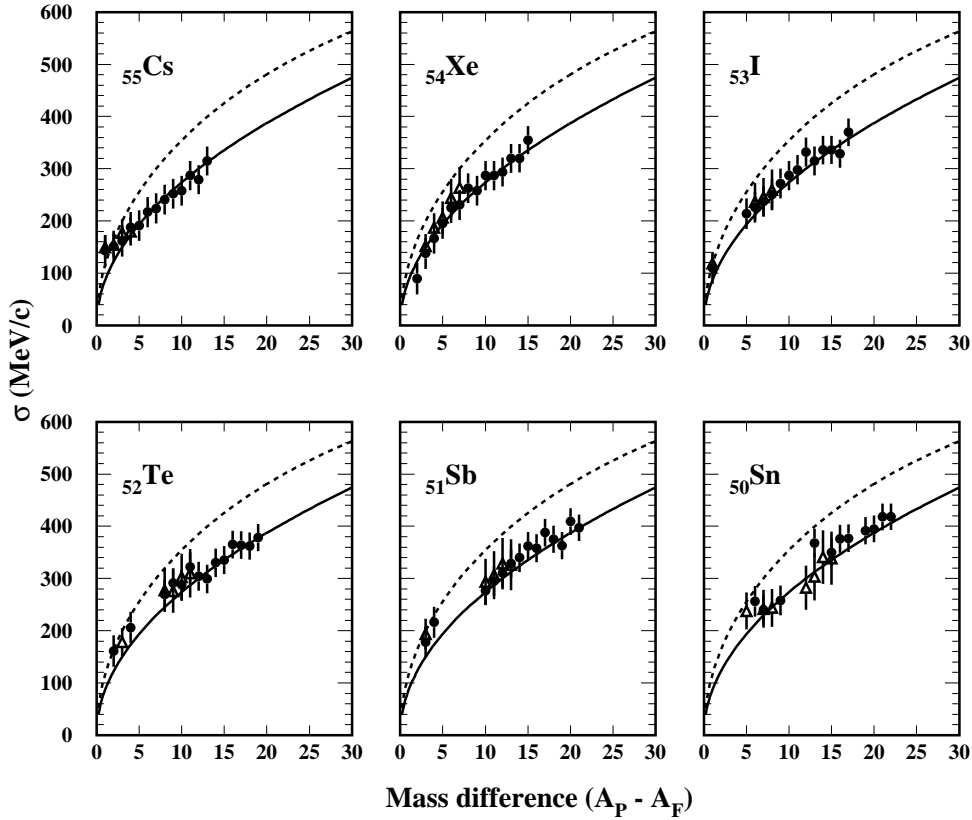


Figure 4.22: Momentum width for all the residues measured in the reactions  $^{124}\text{Xe} + ^{208}\text{Pb}$  at 1000 MeV/u (open triangles) and  $^{136}\text{Xe} + ^{208}\text{Pb}$  at 1000 MeV/u (solid circles). The data are compared with the Morrisey systematic (solid line) and the Goldhaber systematic (dashed line).

As a general conclusion we can state that the momentum widths of the fragmentation residues follow closely the Morrisey systematic, regardless the projectile energy, neutron excess and the nature of the target. This behavior of the measured data can be explained by means of the evaporation stage. This process depends mainly on the excitation energy obtained by the prefragment and this energy is almost independent from the entrance channel, being an indication of its value the number of evaporated nucleons. This is the reason for the dependence of the momentum widths on the mass difference between projectile and target.

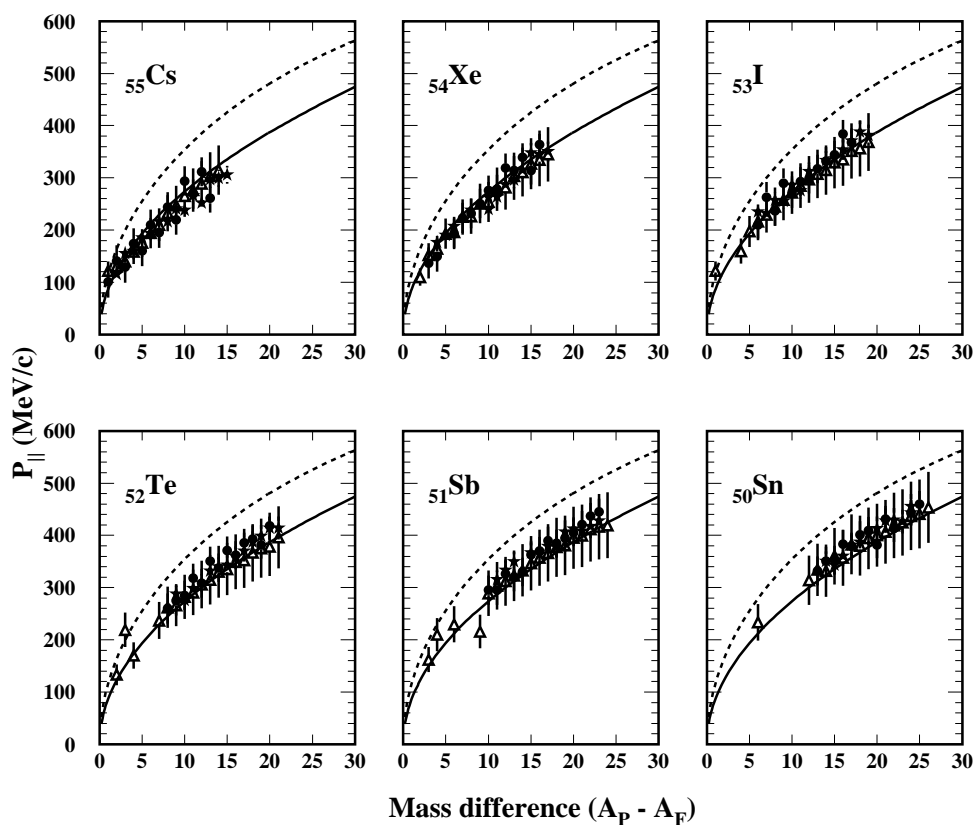


Figure 4.23: Momentum width for all the fragments measured in the reaction  $^{136}\text{Xe} + ^{48}\text{Ti}$  at 1000 MeV/u (solid circles), 500 MeV/u (open triangles) and 200 MeV/u (solid stars). The data are compared with the Morrissey (solid line) and the Goldhaber systematic (dashed line).

# Chapter 5

## Charge-exchange reactions

The experimental technique used in this work allowed not only to investigate reaction residues produced by abrasion, but also those produced in charge-exchange reactions. There are two processes responsible of the charge-exchange mechanism, as already explained by Ellegaard in 1983 [67]. First, a quasi-elastic one corresponding to nuclear particle-hole states, for example Gamow-Teller, spin-dipole and spin-quadrupole excitations. Second, the excitation of a nucleon into a  $\Delta(1232)$  resonance, that subsequently decays in the appropriate pion+nucleon channel.

The resonant channel has been used to investigate the in-medium behavior of the  $\Delta$  particles [68], and they can also provide information about the distribution of matter inside the nucleus for both, neutrons and protons [69], as will be discussed below. For these reasons, a long experimental program to measure the  $\Delta$  excitation in nucleus-nucleus collisions was carried out at the accelerator SATURNE in Saclay, after the first observation of this process in heavy-ion reactions in 1985 [70]. Despite of the experimental efforts to study these reactions, only few publications have treated the isotopic distributions of charge-exchange residues ([71] and [72]).

In this chapter we present the main results obtained on the investigations of these reaction channel with a high resolving power magnetic spectrometer. We have been able to measure, for the first time, the isotopic distributions of single and double charge-pickup processes for a variety of projectile-target-energy combinations . The chapter will open with the discussion concerning the single charge-pickup residues, where the influence of the target size, projectile isospin and energy will be explored. The predictive power of the codes used in the previous chapters will be also tested in this section. After that, we will perform a similar discussion concerning the double charge-exchange reactions.

In this work, we have also measured the isobaric proton and neutron pickup channels for the  $^{136}\text{Xe}$  projectile ( $^{136}\text{Cs}$  and  $^{136}\text{I}$  residues). Moreover, the high resolution of the FRS made it possible to disentangle the quasi-elastic and resonant processes leading to the formation of those channels. The third part of this chapter will be devoted to these topics and, finally, based on these results -and using the Glauber and Isobar models- we will propose the combined measurements of the cross-sections of the isobaric resonant proton and neutron pickup channels to get some insight into the mass and charge distributions of nuclei.

## 5.1 Single charge-pickup reactions

### 5.1.1 Measured data: isotopic distributions

In the isotopic production of projectile residues studied in this work, we have observed isotopes with atomic number beyond that of the primary projectile. These residues are produced by charge-exchange reactions, being the measurement of their isotopic cross sections already a challenge. In figure 5.1 we can see part of the isotopic chain of  $_{55}\text{Cs}$  residues produced in the reaction  $^{136}\text{Xe} + ^{48}\text{Ti}$  at 500 MeV/u. This figure was obtained overlapping several magnetic settings of the FRS.

This identification allowed us to measure, with high precision, the production cross-sections of all the single charge-pickup residues created in peripheral reactions induced by  $^{124}\text{Xe}$  and  $^{136}\text{Xe}$  with several targets. These data are shown in figure 5.31. In the top-left panel we can see the isotopic chains corresponding to residues coming from the interaction of  $^{136}\text{Xe}$  at 1000 MeV/u with different targets. The role of the target nature in the isotopic cross-sections can be explored in this figure. The general feature in the behavior of the isotopic distribution is that the measured yields scale with the mass of the target. The differences can reach a factor of 3 between the hydrogen and lead target and can not be explained only by means of the total reaction cross section, additional effects as the neutron excess of the target could play an important role in this process. Another interesting feature is the shape of the yield distribution, independent of the target nature, its maximum value is located at 3 or 4 mass units below the mass number corresponding to the projectile. This feature could be related with the excitation energy of the prefragment in the reaction. As these collisions are supposed to be very peripheral, the most probable value of the prefragment excitation energy is almost independent of the target mass, being this value around 30 MeV, corresponding to the evaporation of 3 or 4 neutrons (as will be discussed below with the help of figure 5.10). This could explain why the maximum of the mass distribution is located at the same position for all the systems. We will come back to this point while testing the predictive power of the

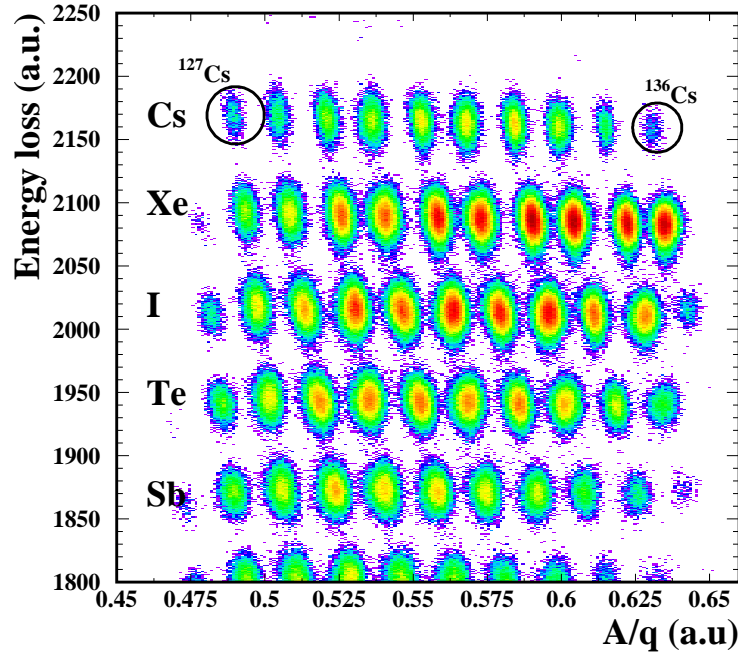


Figure 5.1:  $\Delta E-A/Q$  identification matrix of projectile residues produced in the reaction  $^{136}\text{Xe} + ^{48}\text{Ti}$  at 500 MeV/u. Part of the isotopic chain of  $^{55}\text{Cs}$  is shown in the figure. The circles identify some of the nuclei produced in charge-exchange reactions.

INCL4 code in section 5.1.3.

In the top-right panel of figure 5.31 we show the measured cross-sections for the projectiles  $^{124}\text{Xe}$  and  $^{136}\text{Xe}$  at 1000 MeV/u impinging on a lead target. These data can provide some insight into the influence of the projectile isospin in the charge-exchange reaction mechanism. The most remarkable feature of these results is the shape of the isotopic distribution, being much narrower in the case of the  $^{124}\text{Xe}$ . This effect was already discussed in section 4.2, being the difference between the projectile and the mean  $N$  value of the evaporation corridor the responsible for this behavior.

In the bottom panels of figure 5.31 we represent the measured data corresponding to  $^{136}\text{Xe}$  projectiles impinging on two targets of hydrogen (left panel) and titanium (right panel), at three different energies. These plots can be used to explore the role of the incident energy of the projectile in the production cross sections. The general trend of the measured data is that the probability of the charge-pickup process increases as decreasing the energy of the projectile from 1000 to 200 MeV/u. This behavior is more explicit in the case of the light hydrogen target, where the cross-sections at 200 MeV/u are one order of magnitude higher than the corresponding data at 1000 MeV/u. In the case of the titanium target the effect is weaker,

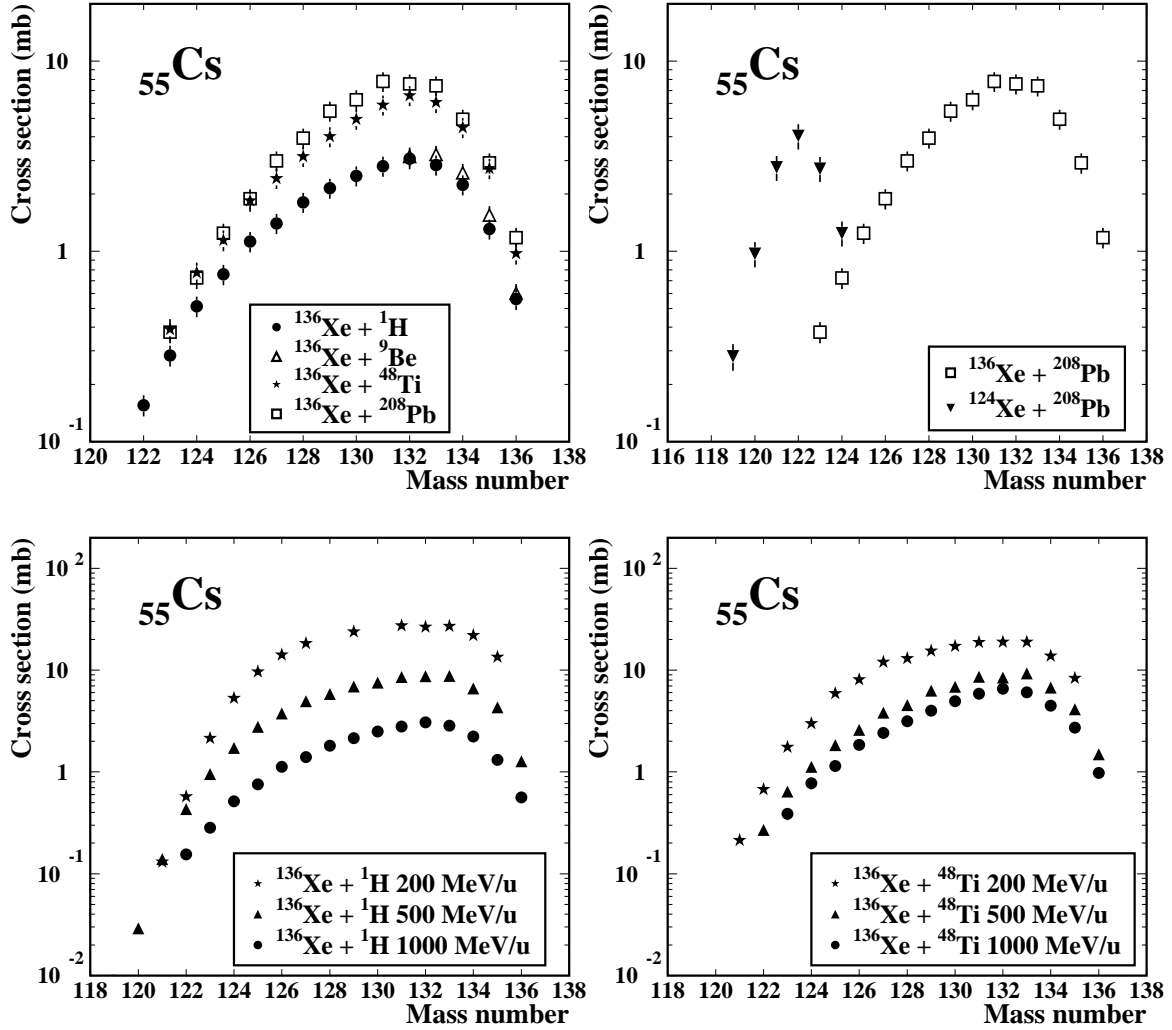


Figure 5.2: (Top left) Isotopic distributions of production cross sections of projectile residues measured in the reaction  $^{136}\text{Xe}$  projectiles at 1 GeV/u with several targets. (Top right) Isotopic distributions measured in the reaction of  $^{124}\text{Xe}$  and  $^{129}\text{Xe}$  projectiles at 1 GeV/u with a  $^{208}\text{Pb}$  target. (Bottom left) Isotopic distributions measured in the reactions of  $^{136}\text{Xe}$  projectiles at several energies with a hydrogen target. (Bottom right) Isotopic distributions measured in the reactions of  $^{136}\text{Xe}$  projectiles at several energies with a  $^{48}\text{Ti}$  target.

but it is still observed the dependence with the energy. As explained above, the charge-pickup consist on a combined effect of two processes, the quasi-elastic and the resonant. At the energies relevant in this work, the inelastic nucleon-nucleon cross section is dominated by the  $\Delta$  excitation, thus the nucleon-nucleon cross section behavior should explain the evolution of the charge-pickup process. The inelastic nucleon-nucleon cross-section decreases as decreasing the energy of the projectile.

The evolution of the charge-pickup is then dominated by the influence of the Gamow-Teller quasi-elastic mechanism, whose probability increases as decreasing the energy (see section 4.3), as observed in figure 5.3.

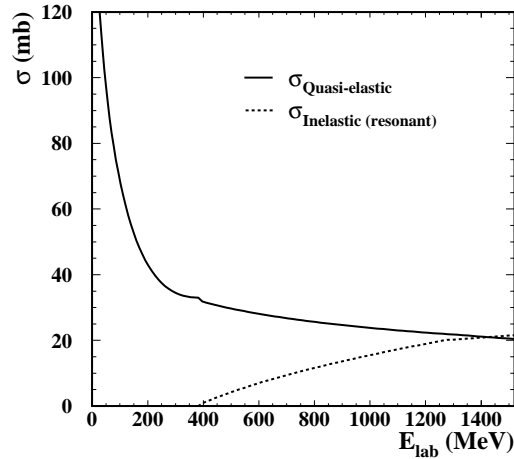


Figure 5.3: *Quasi-elastic (solid line) and resonant (dashed line) nucleon-nucleon cross-sections as parametrized in reference [8].*

### 5.1.2 Systematic comparison to other data

Most of the published data for charge-pickup reactions at relativistic energies concern total cross-sections ([61, 63, 62, 73]). Partial cross-sections for some isotopes were measured using  $\gamma$  spectroscopic techniques ([74]). As far as we know, the only experiments that made it possible measuring the isotopic cross-sections were performed at the FRS in the GSI ([71, 72, 75, 65] and the present work).

The complete isotopic distributions of single charge-pickup residues measured in this work as a function of the mass difference respect to the projectile, are compared with previous existing data in figure 5.4. In the top-left panel we compare the data from the reaction  $^{136}\text{Xe} + ^1\text{H}$  at 1000 MeV/u (measured in this work) with the data from the reactions  $^{208}\text{Pb} + ^1\text{H}$  at 1000 MeV/u [65] and  $^{197}\text{Au} + ^1\text{H}$  at 800 MeV/u [75]. Very close to the projectile, the cross-sections are independent of the projectile size for residues up to a mass difference of 4 nucleons. The width of the mass distributions is almost the same for the three systems, and this is related with the difference between the neutron number of the projectile and the neutron number corresponding to the position of the evaporation corridor, which is similar for the three projectiles. The data from  $^{197}\text{Au}$  projectiles are slightly higher than those from the  $^{208}\text{Pb}$ , due to the lower energy of the primary projectile. As discussed above, the cross-section of the charge-pickup increases as decreasing the energy of

the incident projectile, thus the observed differences are attributed to the difference in the energy, from 800 to 1000 MeV/u.

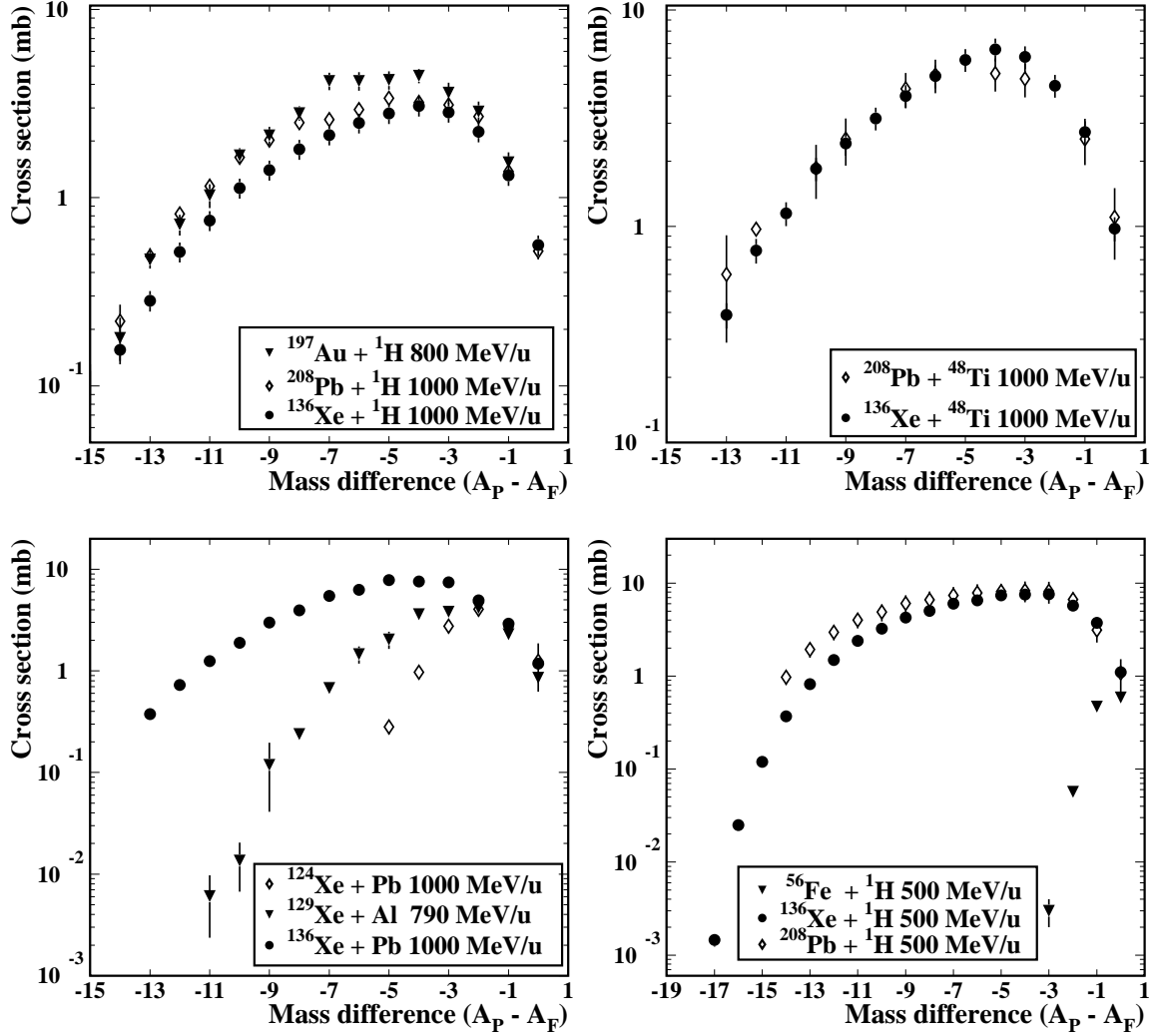


Figure 5.4: Comparison of the isotopic charge-pickup cross-sections measured in this work with available data. (Top-left) The data from the system  $^{136}\text{Xe} + ^1\text{H}$  at 1000 MeV/u are compared with the systems  $^{208}\text{Pb} + ^1\text{H}$  at 1000 MeV/u [65] and  $^{197}\text{Au} + ^1\text{H}$  at 800 MeV/u [75]. (Top-right) The data from the system  $^{136}\text{Xe} + ^{48}\text{Ti}$  at 1000 MeV/u are compared with the systems  $^{208}\text{Pb} + ^{48}\text{Ti}$  at 1000 MeV/u [72]. (Bottom-left) The data from the systems  $^{124}\text{Xe} + \text{Pb}$  and  $^{136}\text{Xe} + ^{208}\text{Pb}$  at 1000 MeV/u are compared with the system  $^{129}\text{Xe} + ^{27}\text{Al}$  at 790 MeV/u [71]. (Bottom-right) The data from the system  $^{136}\text{Xe} + ^1\text{H}$  at 500 MeV/u are compared with the systems  $^{208}\text{Pb} + ^1\text{H}$  at 500 MeV/u [53] and  $^{56}\text{Fe} + ^1\text{H}$  at 500 MeV/u.

In the top-right panel we compare the data obtained in this work for the reaction  $^{136}\text{Xe} + ^{48}\text{Ti}$  at 1000 MeV/u with previous measured data for the system  $^{208}\text{Pb} +$

$^{48}\text{Ti}$  at 1000 MeV/u [72]. These data are useful to explore the role of the size of the primary projectile. The shapes of the mass distributions are similar for both systems, being the cross sections compatible within the error bars. This indicates that the probability of a charge-exchange reaction does not depend on the size of the projectile.

In the bottom-left panel of figure 5.4 we investigate the influence of the projectile isospin. The residue isotopic cross-sections for the projectiles  $^{124}\text{Xe}$ ,  $^{129}\text{Xe}$  and  $^{136}\text{Xe}$  are shown. The data for the  $^{129}\text{Xe}$  on  $^{27}\text{Al}$  were measured at 790 MeV/u [71]. Close to the projectile, the three systems provide the same values for the cross-sections within the error bars, being independent of the projectile isospin. However, the isotopic chain from the  $^{136}\text{Xe}$  is much larger due to its neutron excess ( $N/Z$ ). This effect can also be observed in the bottom-right panel, where the data corresponding to the system  $^{136}\text{Xe} + ^1\text{H}$  at 500 MeV/u measured in this work are compared with those corresponding to the systems  $^{208}\text{Pb} + ^1\text{H}$  at 500 MeV/u [53] and  $^{56}\text{Fe} + ^1\text{H}$  at 500 MeV/u. The data from Pb and Xe are similar because their ( $N/Z$ ) ratios are also similar. However, in the Fe case, the difference between the projectile and the mean  $N$  value of the evaporation corridor is shorter and thus we observe a much narrower isotopic distribution. The differences between the Xe and Pb data very far from the projectile could be due to the Coulomb barrier. This barrier is lower in the case of the Xenon, favoring the proton emission far from the projectile, and thus decreasing the charge-pickup cross-section for these residues.

As already mentioned, most of the published data correspond to the total charge pickup cross-sections. In figure 5.5 we present systematic comparisons of these data. The total single charge-pickup cross sections have been determined by the sum of the isotopic distributions. The top-left panel shows the total cross-sections for the reaction  $^{136}\text{Xe} + ^1\text{H}$  measured in the present work, compared with the data measured in the reactions  $^{197}\text{Au} + ^1\text{H}$  [62, 75] and  $^{208}\text{Pb} + ^1\text{H}$  [65, 53]. For energies above 1000 MeV/u, the cross-section of the process seems to be independent of the projectile energy (within the error bars). This behavior is expected from the energy dependence of the nucleon-nucleon cross sections, which are flat for energies above 1500 MeV. However, below this energy, the cross-sections increases rapidly as decreasing the energy (see figure 5.3). As can be seen in the figure, the difference between 200 and 1000 MeV/u is larger than one order of magnitude. This effect is due to the quasi-elastic component of the reaction, which increases its probability at lower energies. The measured data in this work are perfectly compatible with the data measured in previous works, extending the measurements down to 200 MeV/u. The data corresponding to the  $^{136}\text{Xe}$  projectile are also compared with the predictions obtained with the INCL4+ABLA and ISABEL codes. The calculations with the first code were done using the statistical Pauli blocking (solid line) and the strict Pauli blocking (dashed line), as already explained in section 4.1. The code, with both options, reproduces the tendency of the experimental data quite

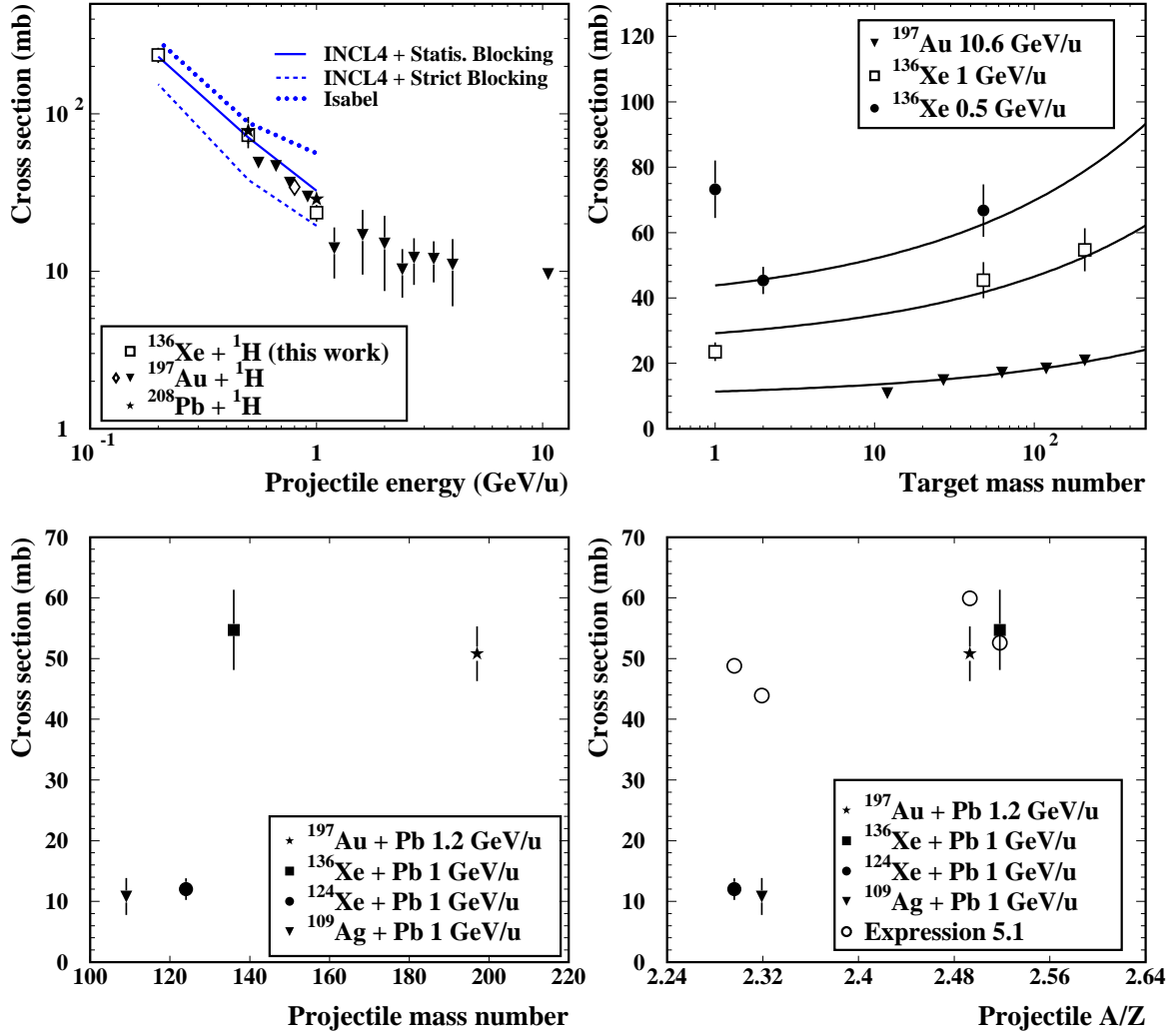


Figure 5.5: *Systematic comparison of the total charge-pickup cross-sections measured in this work with the available data as a function of the projectile energy (top left), the target mass (top right), the projectile mass (bottom left) and the projectile A/Z ratio (bottom right). The lines in the top-right panel show the trend of the total cross-sections.*

well, but the statistical blocking fits the data much better, while the strict blocking underestimates the total cross-sections. The ISABEL code (dotted line) reproduces also the tendency of the measured data, however the code clearly overestimates the results around 1000 MeV/u. At lower energy, ISABEL describes quite well the experimental data.

The role of the target nature in the total cross-section is shown in the top-right panel of figure 5.5. The data corresponding to  $^{136}\text{Xe}$  projectiles at 500 and 1000

MeV/u measured in this work are compared with those corresponding to the  $^{197}\text{Au}$  projectiles at 10.6 GeV/u [62] on several targets. Guoxiao [63] already stated in 1989 that this kind of reactions must be very peripheral, and only the nucleons at the surface of the nucleus must play a role in the reaction. Following these ideas, Kelic et al.[72] stated that the cross-section should be proportional to the nuclear radii of target and projectile ( $A_p^{1/3} + A_t^{1/3}$ ), where  $A_p$  and  $A_t$  are the mass numbers of projectile and target, respectively. In addition, scattered nucleons in the projectile must be reabsorbed by the projectile. This absorption must be, in some sense, proportional to the projectile surface ( $A_p^{2/3}$ ). Therefore, the total charge-pickup cross-section is expected to follow the expression:

$$\sigma_{TOT} = \kappa \cdot (A_p^{1/3} + A_t^{1/3}) \cdot A_p^{2/3} \quad (5.1)$$

where  $\kappa$  is a factor with the dimension of a cross-section. This factor should contain implicitly the energy dependence of the process, and can be adjusted to reproduce the experimental data. The solid lines in the top-right panel of figure 5.5 represent the best fit of the expression 5.1 to the measured data. A similar procedure can be followed in the case of the total charge-pickup cross section. In the left panel of figure 5.6 we show the values obtained for the factor  $\kappa$  in order to reproduce some of the data represented in the top-left panel of figure 5.5.

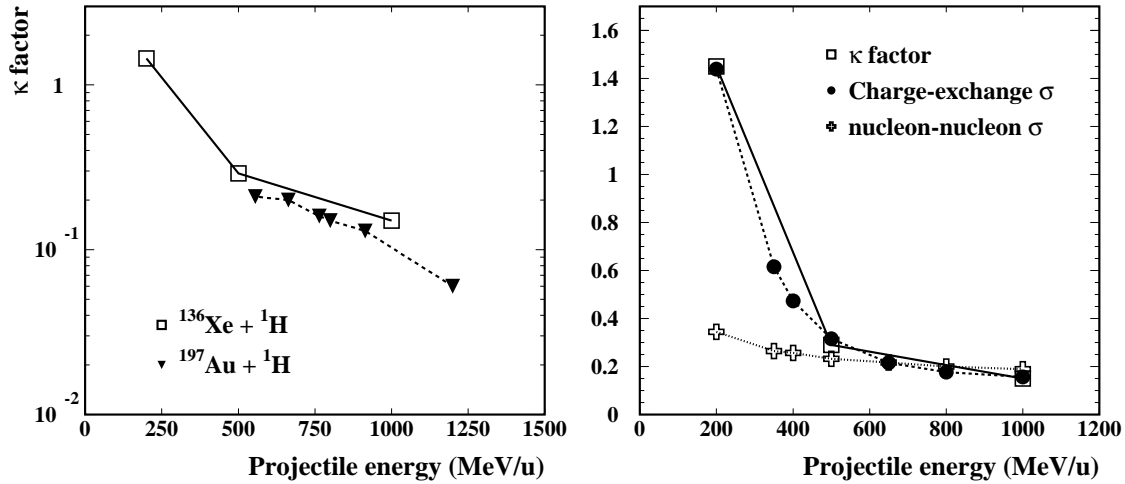


Figure 5.6: (Left)  $\kappa$  factors in expression 5.1 that reproduces some of the experimental data of the top-left panel in figure 5.5. (Right)  $\kappa$  factors (open squares) in the case of the  $^{136}\text{Xe} + \text{H}$  reactions compared with the charge-exchange cross section predicted by INCL4+ABLA with statistical Pauli blocking (solid points) and the nucleon-nucleon cross-sections (crosses) parametrized by [8]. The lines are to guide the eyes.

The factor  $\kappa$  should be expected to scale directly with the nucleon-nucleon cross

section. In order to explore this behavior we show in the right-panel of figure 5.6 the values of  $\kappa$  for the reaction  $^{136}\text{Xe} + ^1\text{H}$  at several energies measured in this work (squares and solid line). We also show the values of the nucleon-nucleon cross sections as parametrized in [8] (crosses and dotted line) and the charge-exchange cross section as calculated with INCL4+ABLA (solid circles and dashed line). The lines are to guide the eyes. It is important to keep in mind that the values of the charge-exchange and nucleon-nucleon cross sections in this plot are not absolute, but only a comparison to explore the proportionality between the different parameters. Hence, these values have been scaled for convenience by a constant value in order to compare them with the  $\kappa$  factor. As can be observed, the  $\kappa$  factor and the predictions of INCL4+ABLA present the same energy dependence. However, both quantities do not follow the same energy dependence of the nucleon-nucleon cross sections. This effect was also observed in the data of the reaction  $^{136}\text{Xe} + \text{Ti}$  measured in this work.

There exists a good agreement between the measured data, the simulated ones and the nucleon-nucleon cross sections above 500 MeV/u. However, below this energy, where the inelastic channel is not expected to play a major role (see figure 5.3), the  $\kappa$  factor and the predictions of INCL4+ABLA increase abruptly. Therefore, we conclude that the energy dependence of the quasi-elastic charge-pickup process is not simply defined by the nucleon-nucleon cross sections. In order to find out an analytical expression of the  $\kappa$  factor as a function of the energy, we have made use of the predictions of INCL4+ABLA for the system  $^{136}\text{Xe} + ^1\text{H}$ . In figure 5.6 we shown that the Monte-Carlo results agreed with the experimental data, hence we made a fit, shown in figure , providing the following expression for the energy dependence of the factor  $\kappa$ :

$$\kappa(E) = 5.05 \cdot \exp^{-6.84 \cdot 10^{-3} \cdot E} + 0.153 \quad (mb) \quad (5.2)$$

The influence of the projectile mass number is explored in the bottom-left panel of figure 5.5, where the data measured in this work for the systems  $^{124,136}\text{Xe} + ^{208}\text{Pb}$  at 1000 MeV/u are compared with the data from the reactions  $^{109}\text{Ag} + ^{208}\text{Pb}$  at 1000 MeV/u and  $^{197}\text{Au} + ^{208}\text{Pb}$  at 1200 MeV/u. On the basis of the figure, we cannot state any systematic dependence on the mass number of the projectile for the charge-pickup process. The cross-section of the system corresponding to the  $^{109}\text{Ag}$  projectile is similar to the one obtained with the  $^{124}\text{Xe}$  projectile, in addition, the cross-section obtained with the  $^{136}\text{Xe}$  is similar to the one obtained with the  $^{197}\text{Au}$  projectile, with more than 60 masses of difference. However, the cross-section for the  $^{136}\text{Xe}$  is 5 times the value corresponding to the  $^{124}\text{Xe}$ , with only a difference of 12 masses. This behavior could be related with the N/Z ratio of the projectile because  $^{109}\text{Ag}$  and  $^{124}\text{Xe}$  have similar N/Z values, as well as  $^{197}\text{Au}$  and  $^{136}\text{Xe}$  N/Z, respectively.

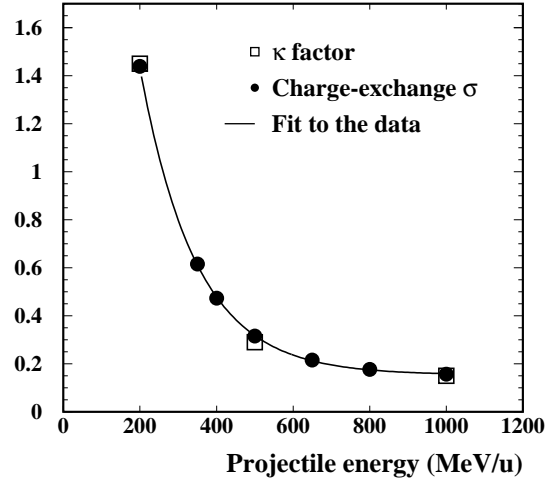


Figure 5.7: Same figure than the right-panel of 5.6 with the fit to the charge-exchange cross sections predicted by the *INCL4+ABLA* code.

This can be explored in the bottom-right panel of figure 5.5, where the same data are plot as a function of the  $A/Z$  ratio. In this figure the influence of the neutron excess of the projectile shows up in an evident way. Projectiles with similar neutron excess values have similar total charge-pickup cross-sections, as can be seen for the  $^{109}\text{Ag}$  and  $^{124}\text{Xe}$  residues (with an  $A/Z$  ratio of 2.32 and 2.30, respectively). The behavior is analogous in the case of the  $^{197}\text{Au}$  and  $^{136}\text{Xe}$  (with an  $A/Z$  ratio of 2.49 and 2.51, respectively). The large neutron excess values of these nuclei is the origin of the larger total charge-pickup cross-sections as compared to the other systems, which are closer to the evaporation corridor. In the same figure we also present the predictions of expression 5.1 (open circles). As can be observed, the value of the  $\kappa$  parameter has been fixed for the  $^{136}\text{Xe}$  projectile at 1000 MeV/u, reproducing that experimental point. The data corresponding to the  $^{197}\text{Au}$  projectile is overestimated, but this effect is explained by means of its incident energy of 1200 MeV/u which will cause a reduction in the total cross sections in comparison with the data of  $^{136}\text{Xe}$  projectile at 1000 MeV/u, as observed in the figure. However, the data from projectiles closer to the evaporation corridor ( $^{109}\text{Ag}$  and  $^{124}\text{Xe}$ ) are clearly wrong estimated.

This effect points out that the Guoxiao parametrization is incomplete and should be updated to incorporate a factor taking into account the neutron excess of the projectile. This can be introduced by means of the mass difference between the projectile and the evaporation corridor. We have rewritten the Guoxiao expression as follows:

$$\sigma_{TOT} = \kappa(N_P - N_\Gamma) \cdot (A_p^{1/3} + A_t^{1/3}) \cdot A_p^{2/3} \quad (5.3)$$

where the factor  $(N_P - N_\Gamma)$  denotes the neutron excess of the projectile. For the isotopic chain of the projectile,  $N_\Gamma$  corresponds to the isotope where the neutron and proton emission probabilities are equal<sup>1</sup>. The predictions of the expression 5.3 are shown in figure 5.8. As can be observed, with this modified Guoxiao version we can achieve a very good description of the experimental data.

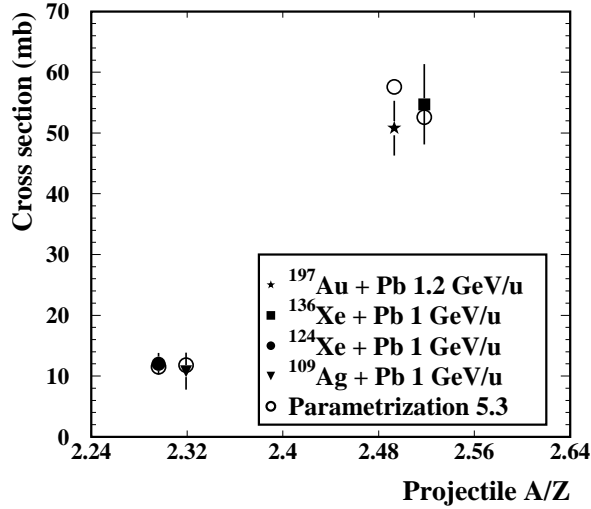


Figure 5.8: Same data as bottom-right panel of figure 5.5 compared with the predictions of the Guoxiao expression updated to take into account the neutron excess of the projectile (expression 5.3).

### 5.1.3 Benchmark of model calculations

Charge-exchange reactions are extremely useful to understand the first stage of the collision in peripheral relativistic heavy-ion reactions. In the case of microscopic models, such as the intra-nuclear cascade, this reaction channels will benchmark the proper description of N-N collisions, both elastic and inelastic channels or the  $\pi$  propagation in nuclear matter at normal density.

To compare the data from the present work with available codes we have used two different intra-nuclear cascade models: the last version of the Liege code INCL4 [8] and ISABEL [5], both coupled to the same evaporation code ABLA [12], [13]<sup>2</sup>. In figure 5.9 we compare the isotopic cross sections of the single charge-pickup measured in this work for the systems  $^{136}\text{Xe} + ^1\text{H}$  at 200, 500 and 1000 MeV/u with the predictions obtained by the two INC codes. In the left panel we show the

<sup>1</sup> $N_\Gamma$  is defined as the neutron number of the isotope whose neutron separation energy is  $S_n = S_p + B_c$ , where  $S_p$  is the proton separation energy and  $B_c$  the Coulomb barrier

<sup>2</sup>These codes were extensively discussed in the Chapter 1 and the references given therein.

cross sections calculated with INCL4+ABLA using the statistical Pauli blocking. This code reproduces quite well the energy dependence of the single charge-pickup process, increasing the cross sections as decreasing the energy of the projectile. However, there is a systematic overprediction of the cross sections close and far from the projectile, making the mass distribution wider than expected at 500 and 1000 MeV/u. This problem was already pointed out by Boudard et al.[9] for residues very close to the projectile. The explanation given is that the only quantum restriction considered in the code is the Pauli blocking, and maybe other quantum effects not considered in the model could be important in the cases where low-excited prefragments are created. For this reason we decided to investigate the strict Pauli blocking in the model, already discussed in section 4.1. The calculations performed with INCL4+ABLA using strict Pauli blocking are compared with the measured data in the central panel of figure 5.9. We can observe a clear improvement of the predictive power of the model very close to the projectile. In particular, for the nucleus  $^{136}\text{Cs}$ , the cross sections provided by INCL4+ABLA with the strict Pauli blocking decrease more than a factor of 2 at the three measured energies, describing the data quite well in this region. Unfortunately, the cross-sections corresponding to the middle-mass region of the isotopic chain are clearly underpredicted for the three energies. We conclude from this discussion that the strict Pauli blocking must be used to calculate the isobaric charge-exchange cross sections, however the statistical Pauli blocking is better suited, in general, for the isotopic distributions, as well as the total charge-exchange cross sections, as shown in the top-left panel of figure 5.5.

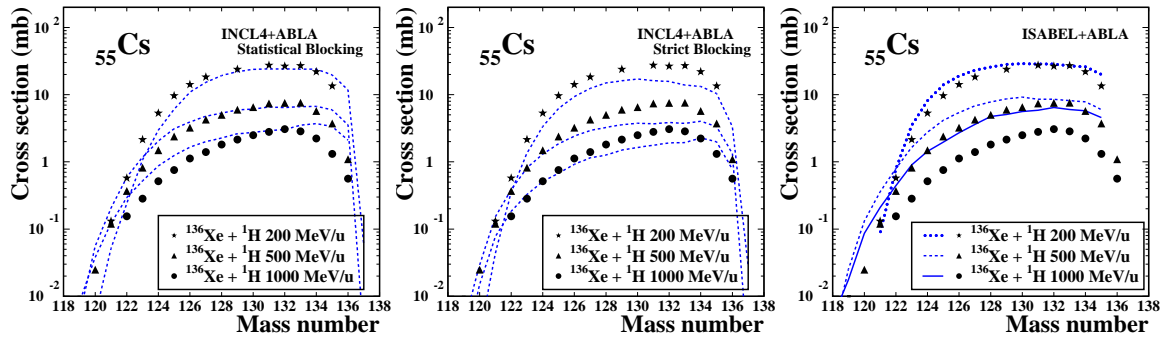


Figure 5.9: Comparison of the measured charge-pickup isotopic cross-sections in the reaction of  $^{136}\text{Xe} + \text{H}$  at several energies with the INCL4+ABLA code with statistical Pauli blocking (left panel), INCL4+ABLA with strict Pauli blocking (middle panel) and the ISABEL code (right panel).

Using the INCL4 code, we can extract also information about the excitation energy of the prefragment distribution of charge-pickup residues. This would allow us to confirm our conclusions concerning the shape of the isotopic distributions of this reaction mechanism. In the figure 5.10 we compare the excitation energy for the prefragments of  $^{136}\text{Cs}$  created in the reaction  $^{136}\text{Xe} + \text{H}$  at 1000 MeV/u, calculated with INCL4 using statistical (solid line) and strict (dashed line) Pauli blockings.

As can be seen in this figure, in both cases, the excitation energy has a maximum probability at  $\sim 25$  MeV, corresponding to the emission of 3-4 neutrons in the subsequent evaporation stage. This explains why the residues isotopic distribution has a maximum in the isotopes  $^{132-133}\text{Cs}$ , independently from the target or the energy of the reaction, because of the shape of the prefragment excitation energy.

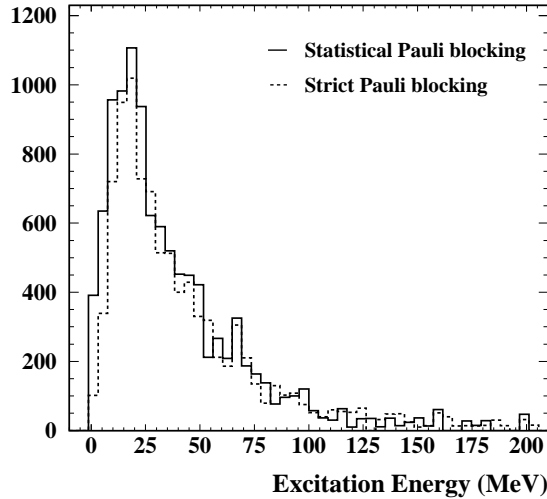


Figure 5.10: *Excitation energy of the  $^{136}\text{Cs}$  prefragments created in the reaction  $^{136}\text{Xe} + \text{H}$  at 1000 MeV/u. The effect of using statistical (solid line) and strict Pauli blocking (dashed line) are shown in the figure.*

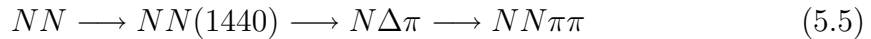
In the right panel of figure 5.9 we present the results obtained with the ISABEL code coupled to the ABLA evaporation code. As can be observed, the code clearly overpredicts cross sections at 1000 MeV/u, however it reproduces the shape of the isotopic distribution. We can conclude from here that ISABEL reproduce the charge-exchange cross sections for the titanium target (as shown in figure 4.11) but it overestimates the results for the hydrogen target at 1000 MeV/u. At 500 MeV/u and 200 MeV/u the code provides better results, being specially remarkable the accurate description of the data at 200 MeV/u. In the most neutron-deficient side of the mass distribution, at 500 MeV/u, ISABEL has the same problems than INCL4+ABLA, it overestimates the production cross sections of the projectile residues. We believe that the high excitation energy values are slightly overestimated in the prefragment distribution, resulting in a higher population of the most neutron-deficient residues.

## 5.2 Double charge-exchange reactions

In the present measurements we have also identified projectile residues with atomic number two units above the one of the projectile. These residues are created by means of double charge-exchange reactions. The origin and mechanism of this kind of reactions remains still not well understood. It is not clear whether only one nucleon from target and projectile are taking part in the reaction or, at least two nucleons of target or projectile must participate. There are theoretical models [76] that postulate this process in terms of the following reaction:



a primary collision between two nucleons excite a  $\Delta$  resonance, this particle collides with a nucleon before its decay, exciting a second  $\Delta$  resonance. Their further decays into the appropriate channel could lead to a double charge-exchange residue. Another possibility that agree with some experimental data (see [77] and references therein) is that the double charge-exchange takes place through the excitation of a  $N(1440)$  resonance as follows:



the  $N(1440)$  resonance decays into a  $\pi$  and a  $\Delta$  resonance, and the latter into a nucleon and a  $\pi$ . There exists a third possibility [78], which corresponds to two sequential  $NN$  single pion production, that is, two consecutive single charge-exchange reactions through the  $\Delta$  resonance.

In addition to these models based on the inelastic channels, the quasi-elastic channel could also play an important role in the double charge-exchange mechanism, specially at low energies. We have shown in the single charge-exchange process how the quasi-elastic channel dominates the interaction at low energies and we would expect the same behavior for the double process.

The quality of the identification procedure used in this work allows to study the isotopic distributions of the residues created by any of these processes. There is a lack of experimental data in partial cross-sections for the double charge-exchange, being the measurements on this work of great importance to obtain some insight into the physics governing this process.

### 5.2.1 Measured data: isotopic distributions

As in the case of the single charge-pickup, the measurements of the isotopic cross sections of residues created by the double charge-exchange reactions, allowed us to perform systematic studies of different factors affecting the probability of these processes, such as the target nature or the projectile energy. The measured cross-sections are shown in figure 5.11. The left panel shows the data obtained in the reaction induced by  $^{136}\text{Xe}$  projectiles at 1000 MeV/u impinging on hydrogen, titanium and lead targets. As in the case of the single charge-exchange, there is a clear dependence of the cross-sections with the target size which cannot be only explained by means of the geometrical nature of the total reaction cross section. These differences can reach a factor of 3 between the residues created in the hydrogen or in the lead targets.

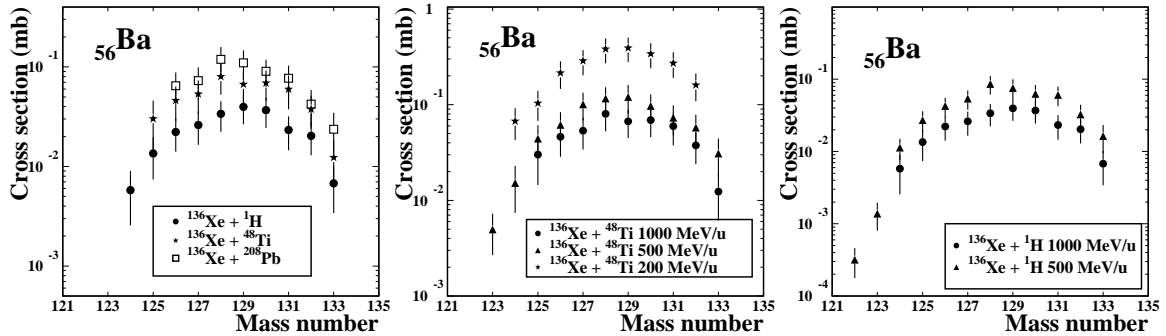


Figure 5.11: (Left) Isotopic distributions measured in the reaction of  $^{136}\text{Xe}$  projectiles at 1 GeV/u with several targets. (Middle) Isotopic distributions measured in the reactions of  $^{136}\text{Xe}$  projectiles at several energies with a  $^{48}\text{Ti}$  target. (Right) Isotopic distributions measured in the reactions of  $^{136}\text{Xe}$  projectiles at several energies with a hydrogen target.

In the central panel of figure 5.11 we present the data from the reactions  $^{136}\text{Xe} + ^{48}\text{Ti}$  at 200, 500 and 1000 MeV/u. The behavior of the experimental data is analogous to the single charge-exchange reactions, increasing as decreasing the energy. The same behavior is observed in the case of the residues created in the reactions  $^{136}\text{Xe} + ^1\text{H}$  at 500 and 1000 MeV/u (right panel of figure 5.11). The evolution of the cross-sections with the energy could be explained, as in the single charge-exchange, by an increasing in the quasi-elastic process probability. It is important to remark that the shape of the isotopic distribution, with the maximum situated around the mass number 129, seems to be independent of the system and the energy of the projectile. This could indicate that the process is very peripheral and only few nucleons of the nuclei surfaces are participating in the reaction.

There is an interesting difference in the shape of the isotopic distribution between

the single and double charge-exchange reactions, the position of the maximum of the isotopic distribution. In the single charge-exchange, the most probable process leads to the evaporation of 3 or 4 nucleons and this feature was demonstrated to be independent of the energy of the projectile, as well as its nature or the nature of the target. In the case of the double charge-exchange, however, the maximum of the isotopic distribution is located around the mass number 129. Hence, the mean excitation energy induced in the prefragment by the double charge-exchange reaction mechanism is higher than in the single case, being approximately about 50 MeV in order to evaporate 7 neutrons.

## 5.2.2 Total cross-sections: systematics

Figure 5.12 shows the total double charge-exchange cross-sections measured in this work, obtained as the sum of the isotopic cross sections. In the left panel we show the data corresponding to the reactions  $^{136}\text{Xe} + ^1\text{H}$  and  $^{48}\text{Ti}$  at 200, 500 and 1000 MeV/u as a function of the projectile energy. The behavior of the experimental data is analogous to the single charge-exchange process, the total cross-sections increase inversely with the projectile energy. We can also observe in the figure the influence of the target mass number, being evident the difference between the hydrogen and the titanium systems, as in the single charge-exchange case.

The measured data are compared in the figure with the predictions obtained with different codes. It is surprising that the INCL4 code with statistical Pauli blocking clearly overestimates the production cross-sections for the reactions induced by the hydrogen target, being the results calculated with the strict Fermi blocking in much better agreement. We should recall that, in the single charge-exchange process, the best description of the experimental data was achieved with the statistical Fermi blocking, while the strict blocking underpredicted the total cross-sections, specially at energies below 1000 MeV/u.

ISABEL code provides almost the same total cross sections at 1000 and 500 MeV/u for the reaction  $^{136}\text{Xe} + ^{48}\text{Ti}$ . It reproduces with great accuracy the data at 500 MeV/u but, unfortunately, the code does not provide results at 200 MeV/u to explore the energy dependence of the process in this code.

In the right panel of figure 5.12, we present the total cross-sections measured in this work for the reactions of  $^{136}\text{Xe}$  projectiles at 500 and 1000 MeV/u with targets of hydrogen, deuterium, titanium and lead. The behavior of the data for the double pickup channel is similar to the single one, it is remarkable the difference in the total cross-section for the proton and deuterium targets at 500 MeV/u. This effect was also present in the single pickup case (see figure 5.5) and observed by Kelic et al. [72]

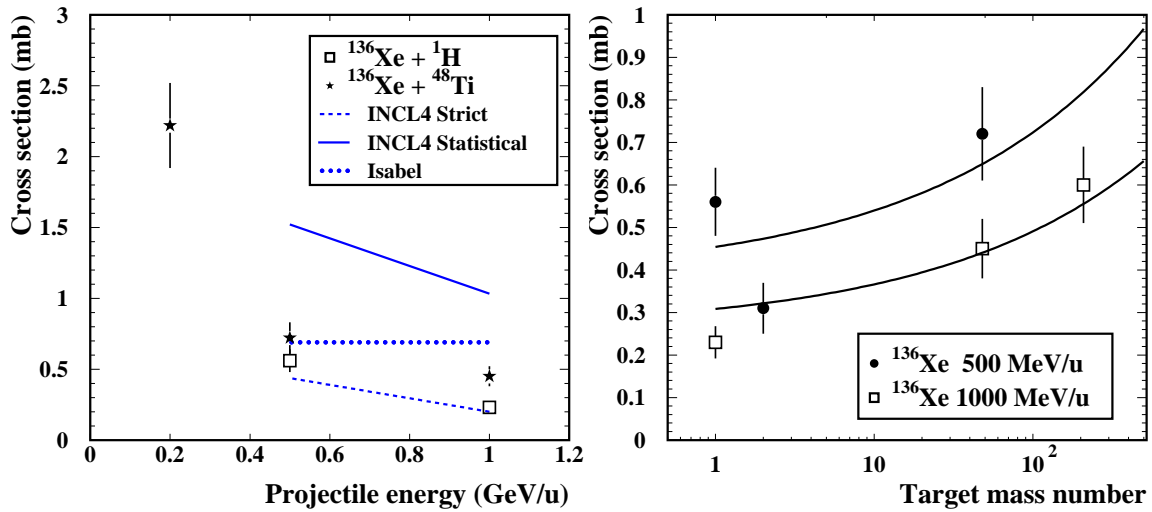


Figure 5.12: (Left) Systematic comparison of the total double charge-pickup cross-sections measured in this work as a function of the projectile energy for several targets. (Right) Measured double charge-pickup cross-sections at 500 MeV/u and 1000 MeV/u as a function of the target mass. The solid lines have been calculated with the corrected Guoxiao expression 5.3.

for the single pickup case. This is the first experimental observation of this effect in the double charge-exchange reaction channel. As in the single case, we believe that it could be related with the excitation energy gained by the prefragment in the collisions with the deuterium. This energy, higher than in the proton case, could cause a higher proton evaporation probability, resulting in a decrease of the total double charge-exchange cross-section.

In the right panel of figure 5.12 we also present, by solid lines, the predictions given by our empirical parametrization for the total charge-exchange cross section (formula 5.3). As can be observed, this expression also reproduces the experimental data in the case of the double charge-exchange, being the  $\kappa$  parameter approximately a factor of 100 lower than the single charge-exchange case.

### 5.2.3 Benchmark of model calculations

Figure 5.13 shows the data measured in the reactions  $^{136}\text{Xe} + \text{H}$  at 1000 and 500 MeV/u compared with several simulation codes. In the left panel of the figure we can see the comparison with INCL4+ABLA with statistical Pauli blocking. From figure 5.12 we already knew that the total double charge-pickup cross-sections were clearly overpredicted by this code at 1000 and 500 MeV/u, being exactly what we observe in the figure 5.13. In both cases the shape of the isotopic distribution is

broader than expected. We believe that this effect is related with the shape of the excitation energy distribution, however the code estimates roughly the position of the maximum of the yield distribution. The comparison of the measured data with the predictions given by INCL4+ABLA with the strict Pauli blocking are shown in the middle panel of figure 5.13. In this case, the code describes with more accuracy the measured data, they reproduce nicely the data at 1000 MeV/u and 500 MeV/u, they reproduce the position of the maximum of the mass distribution, but the isotopic distribution is wider than the measured one.

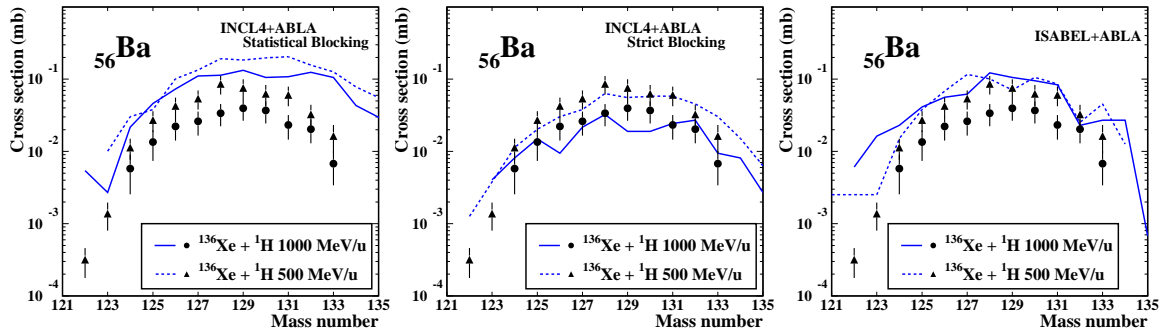


Figure 5.13: Comparison of the measured double charge-pickup isotopic cross-sections in the reaction of  $^{136}\text{Xe} + \text{H}$  at 1000 and 500 MeV/u energies with the INCL4+ABLA code with statistical (left panel) and strict (middle panel) Pauli blockings. The results of the ISABEL+ABLA code are also shown (right panel).

In the right panel of figure 5.13 we also show the comparison with the ISABEL+ABLA code, it clearly overpredicts the cross-sections at 1000 MeV/u and also the shape of the distribution is broader than expected. At 500 MeV/u the results improve as expected from figure 5.12, where we already show that the total cross-section was correctly reproduced. The shape of the cross sections distribution is also reproduced, as well as the position of its maximum. Unfortunately, ISABEL does not provide results at 200 MeV/u to see whether the predictive power of the code could be extended down in energy.

### 5.3 Isobaric charge-exchange reactions.

The mass resolution achieved with the FRS allowed the unambiguous identification of both isobaric charge-exchange channels, the (p,n)-like and (n,p)-like reactions. In figure 5.14 we show an identification matrix for the reaction  $^{136}\text{Xe} + \text{H}$  at 500 MeV/u, obtained combining several magnetic tunings of the FRS. We can see in the figure the primary  $^{136}\text{Xe}$  beam and its first charge state. We can also observe the isobaric proton-pickup ( $^{136}\text{Cs}$ ) and neutron-pickup ( $^{136}\text{I}$ ) channels, as well as other charge-exchange residues as  $^{135}\text{Cs}$  or  $^{135}\text{Te}$ .

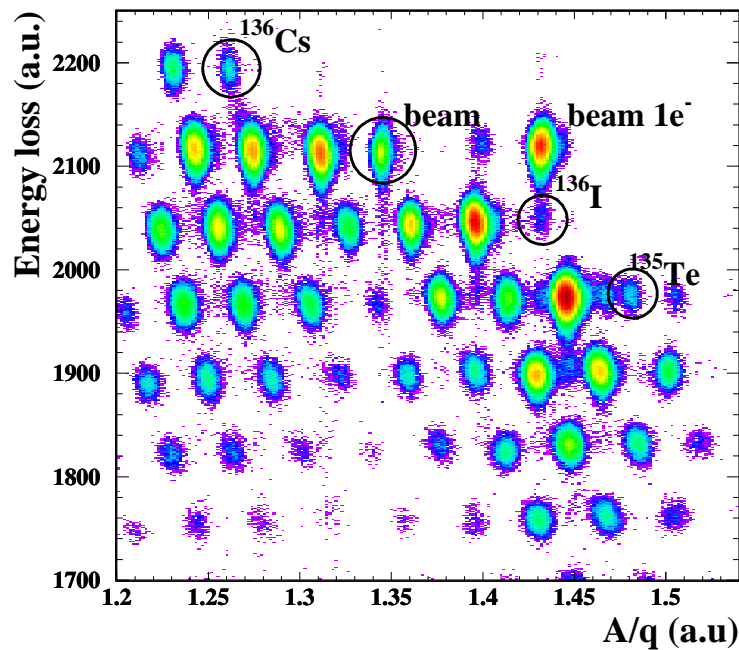


Figure 5.14:  $\Delta E$ - $A/Q$  identification matrix of projectile residues produced in the reaction  $^{136}\text{Xe} + \text{H}$  at 500 MeV/u. The circles identify some of the nuclei produced in charge-exchange reactions. The spots corresponding to the primary beam and its 1-1 charge-state are also shown.

The charge-exchange reactions can take place by two processes, the quasi-elastic mechanism or the resonant excitation of the  $\Delta$ -1232, being both reactions mediated mainly by virtual pions at the energies studied in this work. The former mechanism does not change the longitudinal momentum of the projectile residue, while in the resonant one, the additional energy needed for the creation of the  $\Delta$ -resonance results in a velocity loss of the projectile residue. Hence, the study of the velocity distributions of the residues should display these two regions of nuclear excitation [79]. However, as will be discussed later, the resonant and quasi-elastic processes can be separated in the velocity spectrum only for residues very close to the projectile because of the evaporation of neutrons.

We will then concentrate our study in a very specific case, the isobar charge-exchange reactions, characterized by the conservation of the mass number in the final residue. These processes are expected to be very peripheral [80] and we can restrict the discussion to those reactions where a single nucleon-nucleon collision is assumed to take place, escaping the pion from the nucleus in the resonant case, remaining the rest of nucleons in the projectile undisturbed as spectators and the resulting prefragment with an excitation energy below the evaporation threshold.

Based on this restrictive mechanism we will propose a method to study the distribution of matter (neutrons and protons) in the periphery of the nucleus. The method is based on the resonant charge-exchange reactions and relies on the ratio  $(n,p)/(p,n)$  reactions. Measuring the yield of the resonant channel, we can determine the number of collisions with the proton and neutron shells in the periphery of the nucleus, being possible to explore the proton and neutron distribution radii and, hence, the neutron skin.

The neutron skins are a general feature of nuclei, and may provide fundamental information on the properties of neutron-rich matter and the nuclear force [81]. Neutron skins are already a kind of neutron-rich matter, which could be studied in stable or unstable nuclei to give some insight about some questions as determining the neutron drip line more precisely, extract some information about the Equation of State of nuclear matter (EOS) or study the dependence of the nuclear force on the isospin. In his recent work [82], Furnstahl stated that we can learn something about the EOS by measuring the thicknesses of the neutron-skins. He calculated these values in various models with different parametrization and investigated their sensitivity. He found that there exist a well-defined correlation between the symmetry-energy term of the nucleus-energy function and the neutron-skin thickness. According to this, it is possible to constraint the symmetry-energy term of EOS by measuring the thickness of the neutron-skin.

### 5.3.1 Mechanism of the resonant charge-exchange: isobar model

Not all the combinations of possible nucleon-nucleon collisions in the periphery of the nucleus can produce an isobar charge-exchange reaction. By means of the isobar model [83], and using the Feynman graphical representation, we can calculate the relative probability of each kind of nucleon-nucleon collision to produce an isobar charge-exchange reaction. These calculations are carefully discussed in Appendix C, we will reproduce here the expression of those probabilities. For an isobar proton-pickup, a nucleon (either proton or neutron) of the target must collide with a neutron of the projectile surface, exciting a  $\Delta$ -resonance which will subsequently decay into

the appropriate channel. This probability is given by:

$$P_{AA}^{Z+1} \propto \left(\frac{N}{A}\right)_P \cdot \left[ \left(\frac{Z}{A}\right)_T \sigma_{np}^{ine}(E) \cdot \left(\frac{1}{2}\right)_{n-p} + \left(\frac{N}{A}\right)_T \sigma_{nn}^{ine}(E) \cdot \left(\frac{5}{12}\right)_{n-n} \right] \quad (5.6)$$

In the case of a neutron-pickup, however, a nucleon of the target must collide with a proton of the projectile surface, being this probability:

$$P_{AA}^{N+1} \propto \left(\frac{Z}{A}\right)_P \cdot \left[ \left(\frac{N}{A}\right)_T \sigma_{pn}^{ine}(E) \cdot \left(\frac{1}{2}\right)_{p-n} + \left(\frac{Z}{A}\right)_T \sigma_{pp}^{ine}(E) \cdot \left(\frac{5}{12}\right)_{p-p} \right] \quad (5.7)$$

where the subindex  $T$  and  $P$  denotes target and projectile, respectively and  $\sigma^{ine}(E)$  denotes the inelastic nucleon-nucleon cross-sections as parametrized in reference [8]. The index  $(Z + 1)$  and  $(N + 1)$  denote the (n,p) and (p,n) channels, respectively. The resonant isobar charge-exchange probabilities in the case of collisions within a hydrogen target are simplified versions of expressions 5.6 and 5.7, where  $(N/A)_T = 0$ . As we will discuss in detail this case further in this chapter, we will reproduce here these expressions:

$$P_{pA}^{Z+1} \propto \left(\frac{N}{A}\right)_P \cdot \sigma_{np}^{ine}(E) \cdot \left(\frac{1}{2}\right)_{n-p} \quad (5.8)$$

$$P_{pA}^{N+1} \propto \left(\frac{Z}{A}\right)_P \cdot \sigma_{pp}^{ine}(E) \cdot \left(\frac{5}{12}\right)_{p-p} \quad (5.9)$$

### 5.3.2 Mechanism for quasielastic charge-exchanges: Gamow-Teller strengths

The second mechanism leading to the charge-exchange process is the quasielastic one, producing a residue with a kinetic energy close to the one the primary projectile, contrary to the resonant channel, where  $\sim 300$  MeV are used in creating the  $\Delta$ -resonance. As explained by Bertulani [84], the quasi-elastic mechanism can be reliably calculated within the eikonal approximation for the reaction part. These kind of reactions, in both modes (n,p) or (p,n), can help to access useful information

on  $\beta$ -decay transition strengths, providing a measure of the Gamow-Teller functions in the nuclear excitation spectrum [85], [86]. The main contribution to this reaction channel is given by the exchange of  $\pi$  mesons (the exchange of  $\rho$  mesons is also possible but with very low probability at the relevant energies studied in this work [85]).

For the purposes of this work, we are not interested in this mechanism of the charge-exchange reactions. We mention them here for clarity and to stress their importance in the study of the nuclear structure.

## 5.4 Determination of matter and charge radii using $\Delta$ -resonance excitation in isobaric charge-exchange reactions

### 5.4.1 Existing methods for matter and charge radii determination

We would start this section with a short review of the methods applied for measuring the matter distributions inside the nuclei. The charge distribution can be measured very precisely by using electromagnetic probes like elastic electron scattering [87]. Since the electromagnetic interaction is precisely known and the wave length of high energy electrons can be much shorter than the size of the nucleus, it is possible to study the charge distribution accurately. However, the situation in determining the neutron or matter r.m.s. radius is much worse. It is necessary to use probes whose interaction is mediated by the strong force, which is not known precisely and, in addition, different nuclear models have to be employed, which makes the results less precise than in the case of the charge radius. In spite of these difficulties, there are different methods for determining the mass radius of the nuclei. In what follows we will briefly resume each of them.

1. **Hadron scattering:** This technique has been used for studying the mass distributions of nuclei for over three decades. It is based in the Relativistic Impulse Approximation (RIA) with free nucleon-nucleon interactions. Ray et al. ([88],[89]) could determine the neutron rms radii of a few stable spherical nuclei with better than 1% error. Other authors also measured neutron densities with this technique, but it is difficult to judge about the model dependence of these values.

2.  **$\pi^-$  elastic scattering:** The cross-sections of this process is relatively large in the  $\Delta(1232)$  resonance region and is about three times larger for neutrons than for protons. This makes  $\pi^-$  elastic scattering a promising tool for studying the neutron distribution of nuclei. This method was used by Takahashi [90] to determine the neutron distribution of the  $^{208}\text{Pb}$  and his results agreed with those obtained by other probes.
3. **Antiprotonic atoms:** A slow antiproton can be captured into an atom like an electron. Since its mass is about 1800 times larger than that of the electron, the radius of atomic orbits becomes extremely small, reaching the surface of the nucleus already at  $n=9,10$ . Lubinski et al. ([91], [92]) and Trzcinska et al. ([93]) proposed a simple radiochemical method, and in-beam antiprotonic X-ray measurements for studying the nuclear stratosphere. The former method consist on the study of the annihilation residues with a mass number one unit smaller than the target mass. The relative yields of the  $N-1$  and  $Z-1$  isotopes are related to the proton and neutron densities at the annihilation site. The position of the annihilation is calculated to be at about 2.5 fm larger than the half-density charge-radius. Assuming the validity of a two-parameter Fermi neutron and proton distributions they could determine the neutron-skin thickness.
4. **Parity-violating electron scattering:** This method is based on the idea that the  $Z$ -boson couples primarily to the neutron at the nuclear surface. By measuring the parity violation in electron scattering, the weak-charge density can be mapped out and the neutron density can be determined. This is described in a proposal accepted recently at Jefferson Laboratory, and it aims to measure the mass radius of  $^{208}\text{Pb}$  within a 1% in a model-independent way [94] and [95].
5. **The GDR method:** This method is based on the excitation of the Giant Dipole Resonance. With this method the neutron density distribution is difficult to obtain, but the difference in radii of the neutron and proton density distributions is more accessible. There are works on inelastic  $\alpha$ -scattering where the excitation of the giant dipole resonance (GDR) was used to extract the neutron-skin thickness of nuclei [96], [97]. The cross-section of this process depends strongly on  $\Delta R_{PN}/R_0$ , the relative neutron-skin thickness [98].
6. **The SDR method:** This method is based in the excitation of the Spin-Dipole Resonance [99]. The  $L=1$  strength of the SDR is sensitive to the neutron-skin thickness [100], [101]. Krazsnaorkay et al [97] demonstrated that the correlation between the SDR cross-section and the neutron-skin of nuclei thickness is predictable by means of the difference between the  $\beta^-$  and  $\beta^+$  strengths:

$$S_{SDR}^- - S_{SDR}^+ = \frac{9}{2\pi}(N\langle r^2 \rangle_n - Z\langle r^2 \rangle_p) \quad (5.10)$$

where  $\langle r^2 \rangle_n$  and  $\langle r^2 \rangle_p$  represent the r.m.s. radii of the neutron and proton distributions, respectively. The measurements obtained from the  $\text{Sn}(^3\text{He}, t)$  reactions are in good agreement with theoretical predictions [102], [103] and previous measurements [104] along the stable Sn isotopes. These investigations can be extended to unstable nuclei using (p,n) reactions with radioactive nuclear beams in inverse kinematics.

7. **Inclusive  $\pi^+$  and  $\pi^-$  production:** This method relies in the fact that, if proton and neutron distributions are symmetric, the number of  $\pi^+$  and  $\pi^-$  emitted in light nuclei collisions must be similar, being the parameter

$$E = \frac{\sigma(\pi^-) - \sigma(\pi^+)}{\sigma(\pi^-) + \sigma(\pi^+)} \quad (5.11)$$

a measure of the symmetry of the reaction. The cross sections  $\sigma(\pi^+, \pi^-)$  denotes the inclusive pion production, which have implicit the distributions of matter in the nucleus. Determining the parameter  $E$ , we can extract some valuable information concerning the matter distributions. This method has been successfully used in collisions of light ions as He or Li [105] and [106].

8. **Antiproton annihilation:** This novel method proposes to measure neutron and proton distributions of stable and unstable nuclei, the latter produced by projectile fragmentation or fission, by studying medium energy antiproton absorption in a collider mode. This new approach allows an independent measurement of proton and neutron radii within the same experiment. This is of utmost importance since most nuclear matter radii are deduced with different techniques than the charge radii of the same nucleus, making a direct comparison often difficult. This method can be applied to nuclei with production rates of about  $10^5 \text{ s}^{-1}$  and half-lives of about 1 sec. It proposes to measure the exclusive absorption cross-sections on the neutrons and the protons, and from these measurements, derive rms radii with reliable reaction models for the neutron and proton distributions. Microscopic calculations by Lenske et al. [107] show that the absorption cross-sections are almost directly proportional to the rms radii.

### 5.4.2 $\Delta$ -resonance excitation in isobar charge-exchange reactions

In this work we propose a new method to determine the neutron and proton root-mean-squared radii of nuclei based on the excitation of  $\Delta$ -resonance in isobaric charge-exchange reactions. The relative cross sections for the proton (n,p) and neutron (p,n) pickup channels are sensitive to the neutron and proton radial distributions in nuclei. The power of this new method relies on two basic features: first, it is possible to determine the relative neutron and proton distributions radii simultaneously in the same experiment, avoiding subsequent problems in the normalizations and being able to compare the data directly. Second, with the FRS it is possible to determine the matter distributions of exotic nucleus because the complete identification is achieved within a time shorter than 300 ns. This last feature is of great importance because this technique represents an alternative to other methods, as the one based on the anti-proton annihilation previously discussed, which needs a storage-ring and the isotope under study has to live few seconds for its measuring. The SDR method mentioned above is the complementary one to our method. We make it use of the resonant channel in the charge-exchange reactions, while the SDR method make it use of the quasi-elastic part of those reactions. The experimental setup would be analogous and could be also performed with our data.

#### 5.4.2.1 Determination of the experimental resonant cross section in isobar charge-exchange reactions

As proposed above, measuring the ration of resonant (n,p) and (p,n) reactions, we can determine the number of collisions with the proton or neutron shells. Hence, a method to extract the resonant part from the velocity distribution of the residues will be discussed in what follows. Due to the accuracy in the velocity measurements of the projectile residues achieved with the FRS ( $\frac{\Delta\beta\gamma}{\beta\gamma} \sim 5 \times 10^{-4}$ ), we can disentangle both, the resonant and quasielastic channels of the reaction. These two contributions are not directly evident from the measured spectra because several factors are contributing to spoil the velocity resolution. We will call  $M(x)$  the measured velocity spectrum, while the spectrum due to the reaction mechanism that remains hidden in there will be denoted by  $P(x)$ . We can then state that:

$$M(x) = P(x) * R(x) \quad (5.12)$$

where the symbol  $*$  denotes a convolution and  $R(x)$  is a response function depending on the measurement method. Extracting the velocity spectrum due to the

reaction mechanism is the key point of our analysis. Thus, the parameters affecting the response function  $R(x)$  will be carefully described in what follows:

- **Target thickness and energy-loss straggling in the target:** The target thickness affects the mean value and width of the longitudinal velocity distributions. The contribution of these effects can be represented as a convolution of a Gaussian function given by the energy-straggling and a square function given by the location straggling [108]. For each fragment, the parameters of these two contributions were calculated with the code AMADEUS [52]
- **Momentum spread of the beam and position resolution of the scintillator:** The first effect results in an enhancement in the width of the momentum distribution of the residues that must be corrected. The second effect also contributes, additionally, to an enhancement in the width of the distribution. The magnitude of these parameters can be determined from the calibration measurements performed with the primary projectile along the beam line, resulting in a gaussian function.

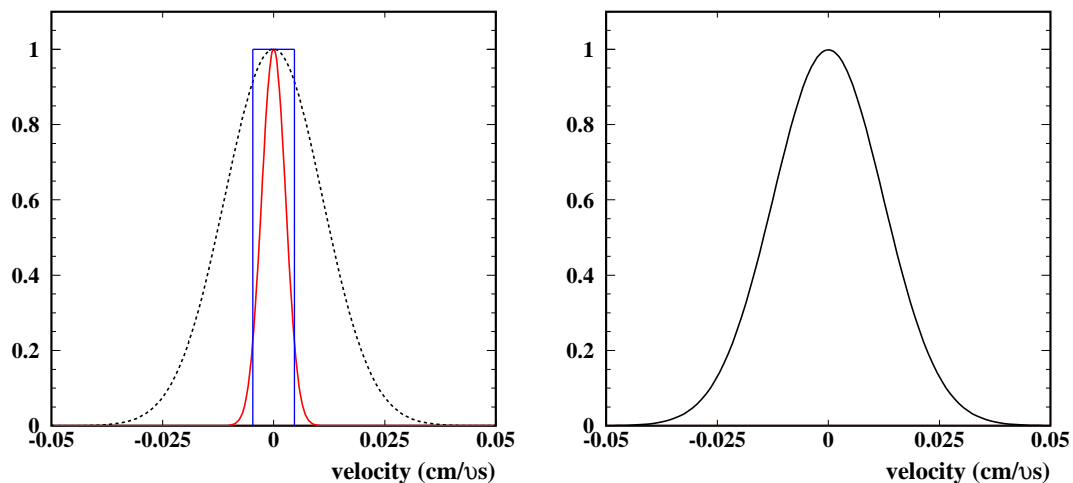


Figure 5.15: (Left) Contributions of the target thickness (square distribution), energy-loss straggling (thin gaussian distribution) and the beam emittance and position resolution of the FRS (dashed gaussian) to the response function. (Right) Convolution of the three distributions to construct the response function  $R(x)$  in expression 5.12.

The response function  $R(x)$  is then constructed as the convolution of all the contributions described above. In figure 5.15 we show a typical response function constructed with this procedure. At this point, the method can follow two alternative ways:

1. Build the response function  $R(x)$  and perform a discrete deconvolution of expression 5.12 to extract the spectrum  $M(x)$ , and a subsequent fit of the deconvoluted spectrum to two gaussian distributions, as doing by Kelic et al. [72]. The results of this method, as a discrete deconvolution, depend on the selected binning of the spectrum.
2. Postulate that the  $P(x)$  consist on two gaussians (quasi-elastic and resonant), build the convolution  $M'(x) = P(x) * R(x)$  analytically, leaving all the parameters corresponding to  $P(x)$  free. The best fit of  $M'(x)$  to the measured distribution  $M(x)$  will give us the parameters of the two gaussians and, hence, the information of the reaction hidden in the velocity spectrum. This method relies on an analytic expression and can be performed in a discrete procedure (being bin dependent) or with a maximum likelihood approach, thus being bin independent. The hypothesis that  $P(x)$  consists on two gaussians is empirically supported by several experimental results [70] and [109].

We have performed the analysis of the velocity distributions measured in this work with both methods described above. In figure 5.33 we show the comparison of two methods. Both provide compatible results, in the case of the resonant channel the Kelic method provides a mean value of the distribution given by  $p_1 = -46.5 \pm 3.6$  cm/ms, while our fit method provides  $p_1 = -42.4 \pm 3.2$  cm/ms. In the case of the width of the distribution the Kelic method provides a value of  $\sigma_1 = 25.4 \pm 3.1$  cm/ms while our method provides  $\sigma_1 = 29.1 \pm 1.5$  cm/ms. As can be observed, the values provided from both methods are perfectly compatible within uncertainties. Similar agreements are obtained for the width of the quasielastic channel.

We have decided to use the second method for two main reasons: first, a maximum likelyhood procedure is performed for each individual measured data and no binning has to be selected a priory for the velocity distribution. Consequently, the results do not depend on the selected bin of the velocity distribution. Second, an accurate estimation of the uncertainties associated to the fit to the  $M(x)$  distribution can be calculated using Minuit [110]. As explained above, the  $M'(x)$  analytic function is calculated by the convolution of two gaussian distributions (corresponding to the quasielastic and resonant channels) with a response function corresponding to the experimental setup.  $M'(x)$  can be given by the following expression:

$$M'(x) = \frac{A \left( \frac{1}{2} \operatorname{erf} \left( \frac{(x+t-p_1)}{\sqrt{2} \cdot \sqrt{\sigma_1^2 + \sigma_R^2}} \right) - \frac{1}{2} \operatorname{erf} \left( \frac{(x-t-p_1)}{\sqrt{2} \cdot \sqrt{\sigma_1^2 + \sigma_R^2}} \right) \right)}{2 \cdot t} + \frac{(1-A) \left( \frac{1}{2} \operatorname{erf} \left( \frac{(x+t-p_2)}{\sqrt{2} \cdot \sqrt{\sigma_2^2 + \sigma_R^2}} \right) - \frac{1}{2} \operatorname{erf} \left( \frac{(x-t-p_2)}{\sqrt{2} \cdot \sqrt{\sigma_2^2 + \sigma_R^2}} \right) \right)}{2 \cdot t} \quad (5.13)$$

where  $p_1$ ,  $p_2$ ,  $\sigma_1$  and  $\sigma_2$  are the mean values and widths of the resonant and quasielastic channels, respectively.  $\sigma_R$  is the width of the gaussian corresponding to the convolution of the beam emittance, the resolution of the position detectors and the energy-loss straggling within the target.  $t$  is the thickness of the square distribution due to the location straggling within the target and  $A$  is a normalization constant that takes into account the relative weight of both channels, quasielastic and resonant. The parameters  $\sigma_R$  and  $t$  are calculated with the AMADEUS code and fixed in the fit. The rest of the parameters are obtained from the best fit of the  $M'(x)$  function to the measured data.

In the right panel of figure 5.33 we show the results of this method. The histogram shown in this figure corresponds to the velocity spectra for the  $^{136}\text{Cs}$  projectile residues created in the reaction  $^{136}\text{Xe} + ^1\text{H}$  at 1000 MeV/u. The function  $M'(x)$  (black line) is the result of the expression 5.13 for the best fit to the measured velocity distribution. The two gaussians correspond to the underlying structure of the reaction mechanism, a peak at the beam velocity corresponding to the quasielastic channel and an additional peak compatible with an energy transfer of  $\sim 300$  MeV corresponding to the  $\Delta(1232)$  resonance excitation. This latter structure is broader than the quasi-elastic channel, as expected from the previous work of [109].

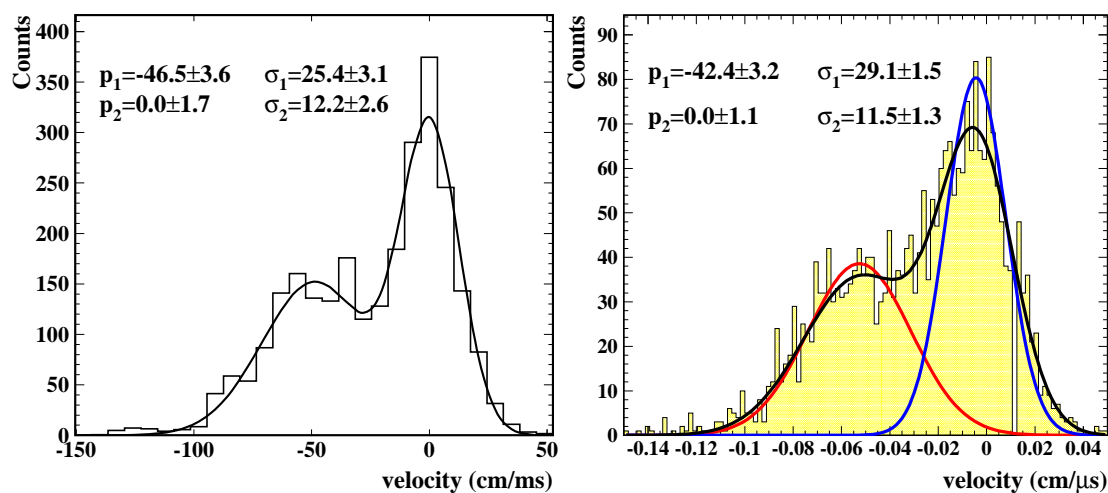


Figure 5.16: (Left) Deconvoluted velocity spectrum of the isotope  $^{136}\text{Cs}$  produced in the reaction  $^{136}\text{Xe} + ^1\text{H}$  at 1000 MeV/u performed with the method used by Kelic et al. [72]. The black line corresponds to the fit of the spectra to two gaussians, whose parameters are shown in the plot. (Right) The same experimental data deconvoluted with the fit method. The histogram corresponds to the measured spectra. The black line is the  $M'(x)$  function of expression 5.13 which best fit the measured spectrum. The blue and red lines are the quasi-elastic and resonant channels, respectively, that leads to the best fit.

For lighter projectile residues, the neutron evaporation causes a broader distribu-

tion for the quasielastic reaction channel which spoils out the separation procedure, that has only sense for isotopes very close to the projectile. In the figure 5.17 we show the deconvoluted spectra for several Cesium isotopes created in the reaction  $^{136}\text{Xe} + ^1\text{H}$  at 1000 MeV/u. The deconvolution of these spectra have been performed using the method of Kelic described above. As can be observed in the figure, as decreasing the mass of the residue, the resolution in the separation of both reaction mechanisms deteriorates gradually. This behavior is so strong that for masses below 133 the deconvolution process cannot disentangle both reaction channels.

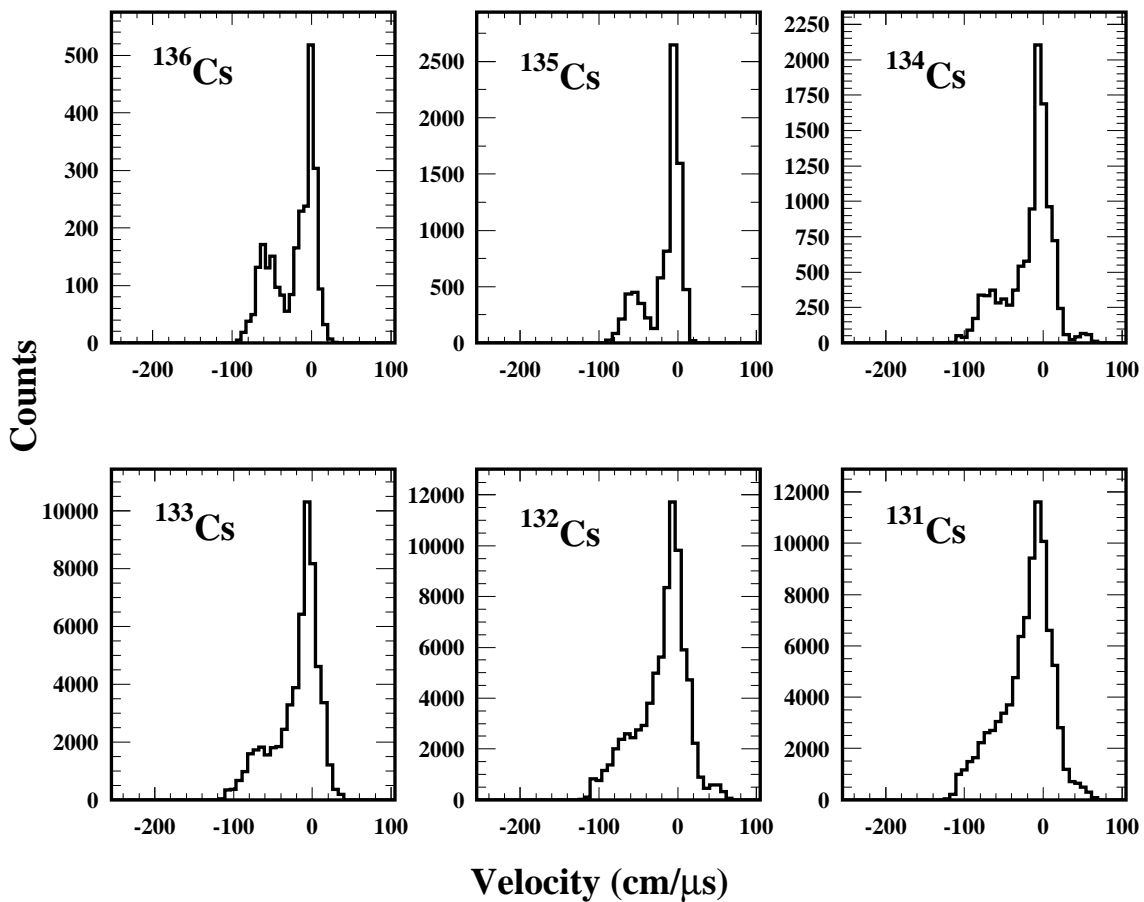


Figure 5.17: *Velocity spectra of some isotopes of charge  $Z=55$  produced in the reaction  $^{136}\text{Xe} + ^1\text{H}$  at 1000 MeV/u. The deconvolutions have been performed with an unrealistically thick response function, in order to make the effect appreciable.*

The method to separate the quasielastic and resonant channels relies in the accurate velocity measurements and the precise identification of the measured residues, avoiding any source of contamination. It is then very important to determine the

Contaminant	$P_{tar}$	$P_{s2}$	$P_{s4}$	$P_{music1}$	$P_{music2}$	$P_{total}$	Contamination
$^{136}\text{Xe} + ^1\text{H}$ at 1000 MeV/u							
$^{133}\text{Cs}$	0.0302	0.0164	0.985	0.986	0.986	4.7E-4	1.36E-3 ( <b>0.24%</b> )
$^{136}\text{Xe} + ^9\text{Be}$ at 1000 MeV/u							
$^{133}\text{Cs}$	0.0080	0.0167	0.984	0.986	0.986	1.3E-4	4.19E-4 ( <b>0.07%</b> )
$^{136}\text{Xe} + ^{48}\text{Ti}$ at 1000 MeV/u							
$^{133}\text{Cs}$	0.0065	0.0161	0.985	0.987	0.987	1.01E-4	6.18E-4 ( <b>0.04%</b> )
$^{136}\text{Xe} + ^{208}\text{Pb}$ at 1000 MeV/u							
$^{133}\text{Cs}$	0.0122	0.0158	0.985	0.986	0.986	1.85E-4	1.39E-3 ( <b>0.14%</b> )
$^{136}\text{Xe} + ^1\text{H}$ at 500 MeV/u							
$^{133}\text{Cs}$	0.0833	0.0559	0.947	0.945	0.945	3.94E-3	3.65E-2 ( <b>2.9%</b> )
$^{136}\text{Xe} + ^2\text{H}$ at 500 MeV/u							
$^{133}\text{Cs}$	0.0892	0.0562	0.946	0.945	0.945	4.23E-3	2.61E-2 ( <b>2.6%</b> )
$^{136}\text{Xe} + ^{48}\text{Ti}$ at 500 MeV/u							
$^{133}\text{Cs}$	0.0245	0.0536	0.949	0.948	0.948	1.14E-3	1.11E-2 ( <b>1.5%</b> )

Table 5.1: Contamination of the  $Z + 1$  charge-pickup isotopes due to charge states. The factors  $P_{tar}$ ,  $P_{s2}$ ,  $P_{s4}$ ,  $P_{music1}$ ,  $P_{music2}$  are the probabilities of the required charge-states after the target area, after  $S_2$ , at  $S_4$  and after the first music and after the second music, respectively.

possible contamination due to the charge-states that could affect the identification. In order to do that, precise simulations taking into account all the layers of matter that the residues traverse in their path through the FRS experimental setup were performed using a Monte-Carlo method based in the code AMADEUS [52]. For a given nucleus ( $Z, A$ ), there are two possible sources of contamination: the isotope ( $Z, A-3$ ) that traverses both stages of the FRS with a hydrogen-like charge state, and in the ionization chambers changes its charge-state being detected with the correct atomic number  $Z$ . The other possible contamination source is the isotope ( $Z+1, A$ ) that traverses both stages of the FRS as a hydrogen-like charge state and in the musics conserves this electron.

In the tables 5.1 and 5.2 we have shown the results of the contamination estimations of the  $^{136}\text{Cs}$  and  $^{136}\text{I}$  residues, respectively. In the case of the  $^{136}\text{Cs}$ , this isotope can be only contaminated by the  $^{133}\text{Cs}$  and the column  $P_{tot}$  denotes the probability for this isotope to traverse the FRS with one electron and to lose it in the MUSIC chambers. The last column (*Contamination*) has been calculated by multiplying the production yield of the isotope  $^{133}\text{Cs}$  by the  $P_{tot}$  column, denoting the contamination yield affecting the  $^{136}\text{Cs}$  residue. Concerning the  $^{136}\text{I}$  residue (table 5.2), this can be contaminated by the  $^{133}\text{I}$  and by the  $^{136}\text{Xe}$ , that is the primary projectile. As

Contaminant	$P_{tar}$	$P_{s2}$	$P_{s4}$	$P_{music1}$	$P_{music2}$	$P_{total}$	Contamination
$^{136}\text{Xe} + ^1\text{H}$ at 1000 MeV/u							
$^{136}\text{Xe}$	0.0271	0.0143	0.0131	0.0117	0.0098	5.86E-10	(<1.0%)
$^{133}\text{I}$	0.0241	0.0125	0.988	0.989	0.989	2.92E-4	1.47E-4 (40.6%)
$^{136}\text{Xe} + ^9\text{Be}$ at 1000 MeV/u							
$^{136}\text{Xe}$	0.0072	0.0148	0.0136	0.0124	0.0105	1.86E-10	(<1.0%)
$^{133}\text{I}$	0.0061	0.0134	0.988	0.989	0.989	8.08E-5	6.46E-5 (4.25%)
$^{136}\text{Xe} + ^1\text{H}$ at 500 MeV/u							
$^{136}\text{Xe}$	0.0743	0.0489	0.0455	0.0465	0.0411	3.17E-7	(<1.0%)
$^{136}\text{Xe} + ^2\text{H}$ at 500 MeV/u							
$^{136}\text{Xe}$	0.0795	0.0493	0.0460	0.0470	0.0414	3.50E-07	(<1.0%)

Table 5.2: Contamination of the  $N + 1$  charge-pickup isotopes due to charge states. The factors  $P_{tar}$ ,  $P_{s2}$ ,  $P_{s4}$ ,  $P_{music1}$ ,  $P_{music2}$  are the probabilities of the required charge-states after the target area, after  $S2$ , at  $S4$  and after the first music and after the second music, respectively.

can be extracted from the tables, the contamination due to the charge-states is very low for the isotopes with charge  $Z=55$ . For the neutron-pickup, the most critical case is the residue  $^{136}\text{I}$  created in the reaction  $^{136}\text{Xe} + ^1\text{H}$  at 1000 MeV/u. In this case the residue is contaminated with the primary beam, reaching a contamination of 40%. At lower energies, due to the optical properties of the FRS, the charge-states of the hydrogen-like residues does not contaminate any isotope, as already explained in the section 3.3.2.5 of this work.

In the tables 5.1 and 5.2 we have shown the results of the contamination estimations of the  $^{136}\text{Cs}$  and  $^{136}\text{I}$  residues. As can be extracted from the tables, the contamination due to the charge-states is very low for the isotopes with charge  $Z=55$ . For the neutron-pickup, the most critical case is the residue  $^{136}\text{I}$  created in the reaction  $^{136}\text{Xe} + ^1\text{H}$  at 1000 MeV/u. In this case the residue is contaminated with the primary beam, reaching a contamination of 40%. At lower energies, due to the optical properties of the FRS, the charge-states of the hydrogen-like residues does not contaminate any isotope, as already explained in the section 3.3.2.5 of this work.

### 5.4.3 Experimental Results.

We have applied the procedure described above to analyze the velocity distributions of several isobar charge-exchange residues produced in this work. In the

figure 5.18 we show the resonant channel extracted from the deconvolution process, as well as the  $M'(x)$  function of expression 5.13. The results of the fit parameters are shown in the table 5.3, where the mean value and width of the resonant ( $p1, \sigma_1$ ) and quasielastic ( $p2, \sigma_2$ ) distributions are shown.

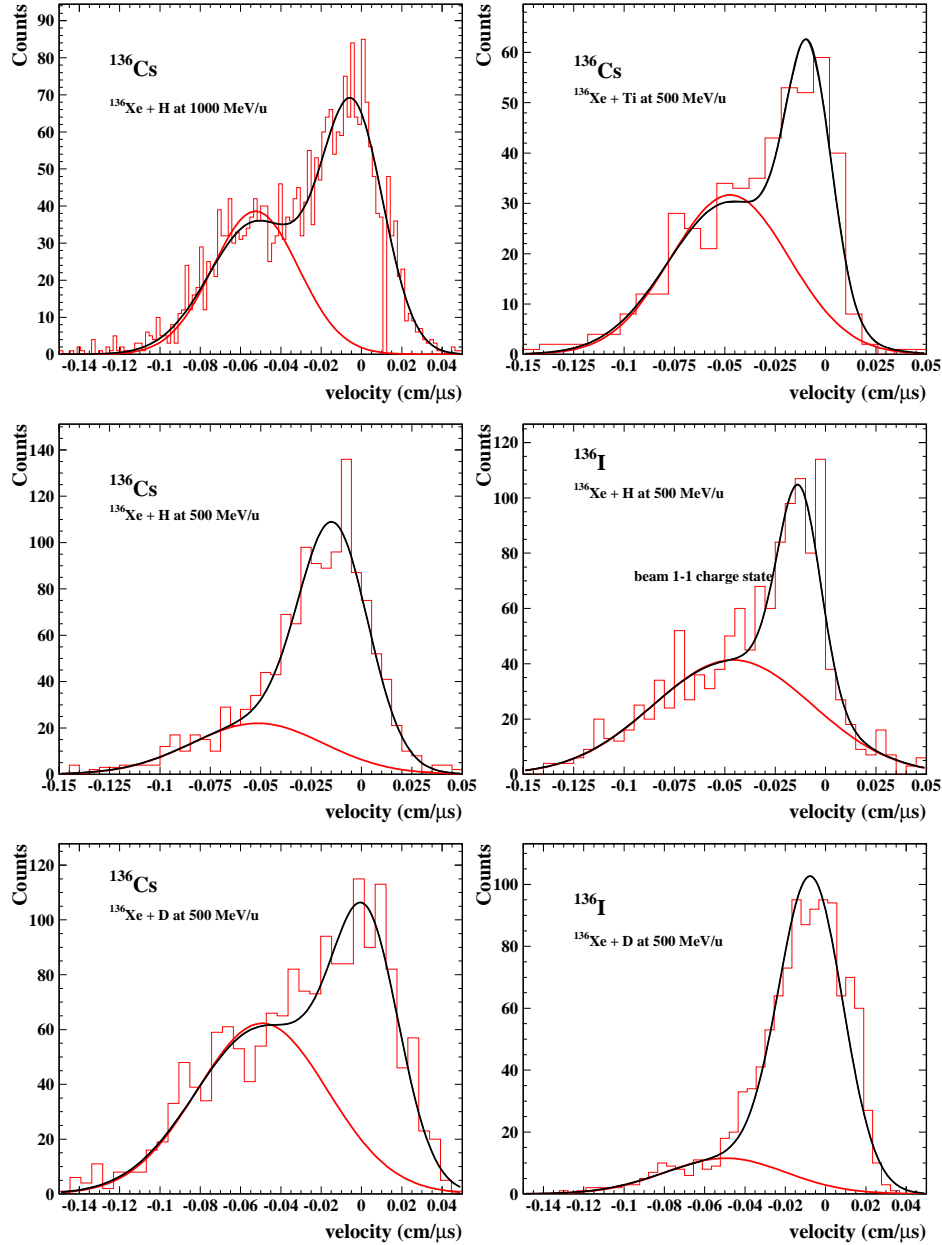


Figure 5.18: Deconvoluted velocity spectrum of several charge-exchange residues measured in this work (see table 5.3). The red line corresponds to the obtained resonant channel. The black line is the  $M'(x)$  function of expression 5.13.

The mean values were corrected by a small offset, where necessary, to fix the

$^{136}\text{Cs}$	$A$	$p_1$ (cm/ $\mu\text{s}$ )	$\sigma_1$ (cm/ $\mu\text{s}$ )	$p_2$ (cm/ $\mu\text{s}$ )	$\sigma_2$ (cm/ $\mu\text{s}$ )
H 1000 MeV/u	0.59 $\pm$ 0.05	-42.4 $\pm$ 3.2	29.1 $\pm$ 1.5	0.0 $\pm$ 1.1	11.5 $\pm$ 1.3
H 500 MeV/u	0.37 $\pm$ 0.07	-34.4 $\pm$ 5.7	35.4 $\pm$ 2.2	0.0 $\pm$ 1.4	15.2 $\pm$ 1.6
D 500 MeV/u	0.54 $\pm$ 0.06	-53.0 $\pm$ 4.9	33.1 $\pm$ 2.21	0.0 $\pm$ 2.2	16.5 $\pm$ 1.6
Ti 500 MeV/u	0.64 $\pm$ 0.07	-41.6 $\pm$ 4.4	30.7 $\pm$ 2.1	0.0 $\pm$ 2.4	8.5 $\pm$ 2.3
$^{136}\text{I}$	$A$	$p_1$ (cm/ $\mu\text{s}$ )	$\sigma_1$ (cm/ $\mu\text{s}$ )	$p_2$ (cm/ $\mu\text{s}$ )	$\sigma_2$ (cm/ $\mu\text{s}$ )
H 500 MeV/u	——	-33.4 $\pm$ 2.5	37.0 $\pm$ 1.4	——	——
D 500 MeV/u	0.20 $\pm$ 0.05	-43.2 $\pm$ 8.0	28.9 $\pm$ 3.1	0.0 $\pm$ 1.3	14.1 $\pm$ 1.0

Table 5.3: Mean values and widths of the resonant ( $p_1$ ,  $\sigma_1$ ) and quasielastic ( $p_2$ ,  $\sigma_2$ ) velocity distributions of the proton-pickup ( $^{136}\text{Cs}$ ) and neutron-pickup ( $^{136}\text{I}$ ) channels measured in this work. The relative area of the resonant channel  $A$  is also shown. The parameters have been determined by a maximum likelihood method (see text for details).

quasielastic channel at zero velocity. In most of the cases, the error in the fit parameters is below the velocity resolution of the FRS, 2.6 cm/ms (with a position resolution of 4 mm in the scintillator detector at the intermediate focal plane, F2). There is an important feature remarkable in these data, the width of the velocity distribution corresponding to the resonant channel is broader than the quasi-elastic one, more than a factor of two. This feature was expected as measured by Roy-Stephan in the reactions for projectiles of  $^{12}\text{C}$ ,  $^{16}\text{O}$  and  $^{20}\text{Ne}$  at 900 and 1100 MeV/u (see [70] and [109]) and is related to the energy width of the  $\Delta$ -resonance.

From the fit we have also obtained the relative contribution of both channels (parameter  $A$  in expression 5.13). We can compare the ratio of the resonant channel for the  $^{136}\text{Cs}$  created in the Hydrogen target at 1000 and 500 MeV/u, being  $\Delta_{1000}/\Delta_{500}=1.6 \pm 0.3$ . This result agrees, within the experimental error, with the predictions obtained with the INCL4 code, being 1.4. We can also compare the ratio of the resonant channel for hydrogen and deuterium at 500 MeV/u, being  $\Delta_D/\Delta_H=1.5 \pm 0.3$ . This was also calculated by Kelic [72] at 1000 MeV/u for  $^{208}\text{Pb}$  projectiles on hydrogen and deuterium targets, being the obtained value 1.7.

As can be seen in the table 5.3, in certain cases we were able to measure both reaction residues, the (n,p) and (p,n) channels. As already indicated, we will use these data to get some insight into the proton and neutron matter distributions inside the  $^{136}\text{Xe}$  projectile. By comparing the relative weight of each channel we can estimate whether the collision took place with a neutron or a proton in the  $^{136}\text{Xe}$  surface.

In the table 5.4 we show the measured cross sections for the isobar charge-

exchange channels and the predictions obtained with the Isobar Model and the INCL4 code, calculated as follows:

- Isobar model** We will consider for simplicity the reaction  $^{136}\text{Xe} + \text{Hydrogen}$ . To undergo a charge-pickup reaction the target proton can only collide with a neutron of the Xenon surface, and with a proton to undergo a neutron-pickup. With the help of the isobar model (equations 5.8 and 5.9) we can determine the relative weight of the charge-pickup (expression 5.14) neutron-pickup (expression 5.15) probabilities.

$$\frac{P_{pA}^{Z+1}}{P_{pA}^{Z+1} + P_{pA}^{N+1}} = \frac{\left(\frac{N}{A}\right)_P \cdot \sigma_{np}^{ine}(E) \cdot \left(\frac{1}{2}\right)_{n-p}}{\left(\frac{N}{A}\right)_P \cdot \sigma_{np}^{ine}(E) \cdot \left(\frac{1}{2}\right)_{n-p} + \left(\frac{Z}{A}\right)_P \cdot \sigma_{pp}^{ine}(E) \cdot \left(\frac{5}{12}\right)_{p-p}} \quad (5.14)$$

$$\frac{P_{pA}^{N+1}}{P_{pA}^{Z+1} + P_{pA}^{N+1}} = \frac{\left(\frac{Z}{A}\right)_P \cdot \sigma_{pp}^{ine}(E) \cdot \left(\frac{5}{12}\right)_{p-p}}{\left(\frac{N}{A}\right)_P \cdot \sigma_{np}^{ine}(E) \cdot \left(\frac{1}{2}\right)_{n-p} + \left(\frac{Z}{A}\right)_P \cdot \sigma_{pp}^{ine}(E) \cdot \left(\frac{5}{12}\right)_{p-p}} \quad (5.15)$$

These ratios can be easily calculated if the inelastic  $\sigma_{pp}^{ine}(E)$  and  $\sigma_{np}^{ine}(E)$  are known. As mentioned above these have been parametrized by Cugnon et al. [8] and can be seen in the figure 5.19. It should be considered that, due to isospin reasons,  $\sigma_{pp}^{ine}(E) = \sigma_{nn}^{ine}(E)$  and  $\sigma_{np}^{ine}(E) = \sigma_{pn}^{ine}(E)$ .

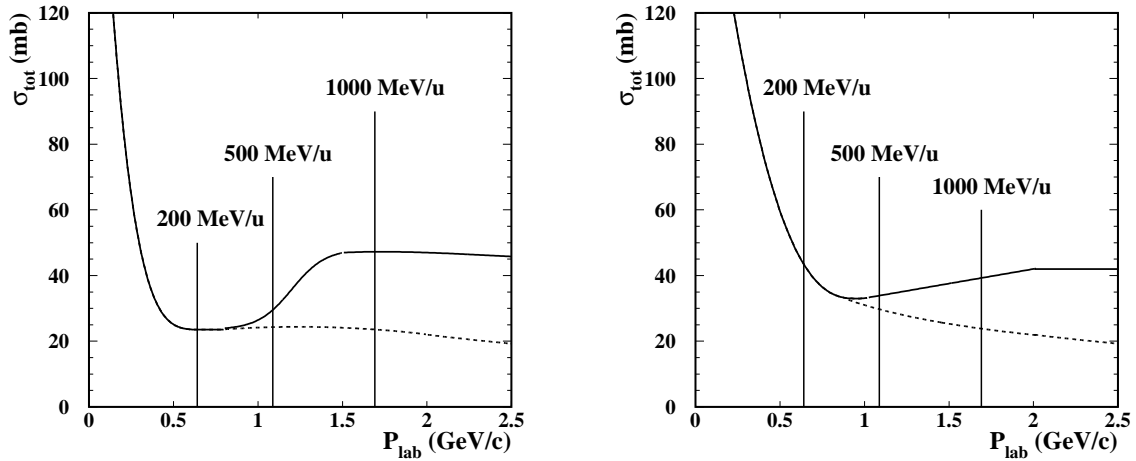


Figure 5.19: Total (solid line) and elastic (dashed line) nucleon-nucleon cross-sections as parametrized in reference [8] for neutron-neutron or proton-proton reactions (left panel) and neutron-proton or proton-neutron reactions (right panel). The vertical lines denotes the three energies investigated in this work.

- **INCL4** In the intra-nuclear cascade code INCL4 we can extract also information about how the  $\Delta$ -resonance was created in the abrasion stage of the reaction, this information is obtained indirectly from the number of pions after the  $\Delta$  decay. Thus, we can determine from the code the number of  $^{136}\text{Cs}$  and  $^{136}\text{I}$  created through a resonant reaction.

As can be observed in the table 5.4, there exists a clear discrepancy between the models (Isobar and INCL4) and the measured data. The probability of collision within the neutron shell of the projectile is extremely enhanced as compared with the models. This relevant result clearly denotes that the resonant channel of the isobar charge-exchange reactions is sensitive to the neutron distribution of the projectile. We see experimentally that, in very peripheral reactions, 96% of the collisions take place with a neutron and only a 4% of the times with a proton. These results cannot be explained by the difference between neutrons and protons in the projectile (N/Z ratio) and must arise from other reason. We believe that the  $^{136}\text{Xe}$  nucleus has a neutron skin, that is, the r.m.s. of the neutron distribution is larger than the r.m.s. of the proton distribution and the surface of the nucleus is covered by neutrons.

Reaction	Isotope	cross-section (mb)	Percentage	Isobar model	INCL4
H 500 MeV/u	$^{136}\text{Cs}$	$0.469\pm 0.05$	95.1 %	54.6 %	51.0 %
H 500 MeV/u	$^{136}\text{I}$	$0.024\pm 0.003$	4.9 %	45.4 %	49.0 %
D 500 MeV/u	$^{136}\text{Cs}$	$0.54\pm 0.07$	97.8 %	59.9 %	59.4 %
D 500 MeV/u	$^{136}\text{I}$	$0.012\pm 0.003$	2.2 %	40.1 %	40.5 %

Table 5.4: *Resonant cross-sections for the production of  $^{136}\text{Cs}$  and  $^{136}\text{I}$  residues in isobar charge-exchange reactions induced by  $^{136}\text{Xe}$  projectiles with the targets shown in the table. The relative weight of both isobar charge-exchange channels are given for the measured data as well as for the predictions obtained with the isobar model and the INCL4 code.*

From our results we can conclude that:

- Isobar charge-exchange reactions are very peripheral processes, and can be then used to estimate the ratio of collisions with the protons and neutrons at the projectile surface.
- This ratio of collision is directly related to the asymmetry in the neutron and proton distributions at the nucleus surface.
- Due to our experimental results we strongly believe that the  $^{136}\text{Xe}$  projectile has a neutron skin.

#### 5.4.4 Neutron and proton r.m.s. radii determination using Glauber model calculations

In this section we would go a step ahead and will try to estimate the r.m.s. radii of the proton and neutron distributions for  $^{136}\text{Xe}$  from the measured probabilities for the inelastic proton and neutron isobar pickup channels. For this goal we have developed a model based on the Glauber theory to calculate the probabilities for the isobar charge-exchange reactions through the  $\Delta$ -resonance excitation as a function of the proton and neutron distributions of the colliding nuclei. The idea is to perform a systematic analysis of the parameters of the neutron and proton distributions and estimate the values which better describe the experimental data.

We will make here a brief description of the theory underlying the model, for a deeper discussion on the Glauber theory applied to the heavy-ion collisions the reader can look at the appendix D and references cited therein. We describe the  $^{136}\text{Xe}$  nucleus by a matter density given by a 3-parameters Fermi distribution:

$$\rho(\mathbf{r}) = \rho(\mathbf{b}, z) = \rho_0 \frac{1 + \frac{z^2 + b^2}{c^2}}{1 + e^{\frac{\sqrt{z^2 + b^2} - c}{h}}} \quad (5.16)$$

where  $\rho_0$  is a normalization constant,  $z$  is the direction of the incoming particle,  $\mathbf{b}$  is the bi-dimensional impact parameter,  $h$  is the smoothness of the distribution and  $c$  is the nuclear radius at the half-density. Sometimes it is confuse in the literature the difference between the half-density radius and the root-mean-square (r.m.s.) radius. The half-density radius appears directly in the expression 5.16, while the r.m.s. radius must be obtained from that expression as follows:

$$R_{rms} \equiv \sqrt{\langle r^2 \rangle} = \sqrt{\frac{\int \rho(\mathbf{r}) r^2 d^3\mathbf{r}}{\int \rho(\mathbf{r}) d^3\mathbf{r}}} \quad (5.17)$$

Since the experimental method we propose here is only sensitive to one of the parameters of the matter distribution, the half-density radius, we have performed Hartree-Fock-Bogoliubov calculations using the code HFBRAD [111] developed by Dobaczewski, to obtain realistic values of the smoothness parameter being the optimal value  $h=0.54$  for both, the neutron and proton radial distribution of  $^{136}\text{Xe}$ . In these calculations we have closely followed the methodology described in [112] and we have compared two different Skyrme parametrizations, SkP [113] and SLy4 [114] as shown in Fig. 5.20 where we represent the calculated proton and neutron density distributions for  $^{136}\text{Xe}$ .

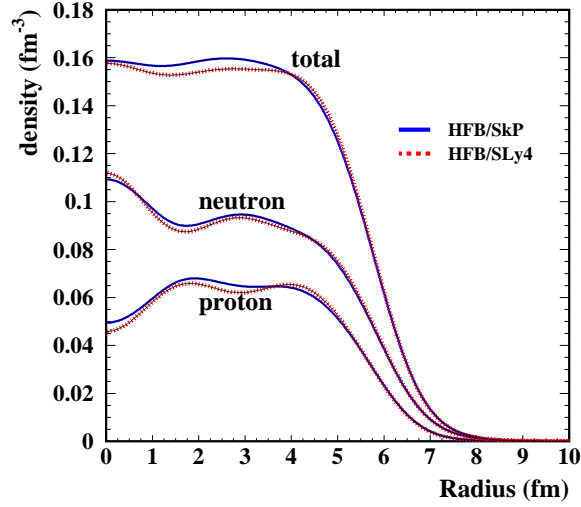


Figure 5.20: Total, neutron and proton density distributions of the  $^{136}\text{Xe}$  nucleus calculated with a Hartree-Fock-Bogoliubov model with a Skyrme interaction. Two different parametrization of this interaction *SkP* and *SLy4* are shown in the figure.

In order to determine the role of the proton and neutron radial distributions, expression 5.16 can be expressed as the sum of these two contributions according to the following equation:

$$\rho_A(\mathbf{r}) = \rho_P(\mathbf{r}) + \rho_N(\mathbf{r}) \quad (5.18)$$

This will allow us to perform systematic calculations to test the influence of the radius on each distribution, protons and neutrons. Both distributions are normalized to their number of nucleons as follows:

$$4\pi \int r^2 \rho_P(\mathbf{r}) dr = Z \quad \text{and} \quad 4\pi \int r^2 \rho_N(\mathbf{r}) dr = N \quad (5.19)$$

Consequently, the total matter density from expression 5.18 is normalized to the total number of nucleons,  $A$ . From this expression, and following the Glauber discussion, we can calculate the profile or thickness function corresponding to this matter density:

$$T_A(\mathbf{b}) = \int \rho_A(\mathbf{b}, z) dz = \int [\rho_N(\mathbf{b}, z) + \rho_P(\mathbf{b}, z)] dz = T_N(\mathbf{b}) + T_P(\mathbf{b}) \quad (5.20)$$

In the figure 5.21 we can see a plot of the thickness functions of the  $^{136}\text{Xe}$  nucleus, the total  $T_A(b)$ , the proton  $T_p(b)$  and the neutron  $T_n(b)$  as a function of the impact parameter  $b$ .

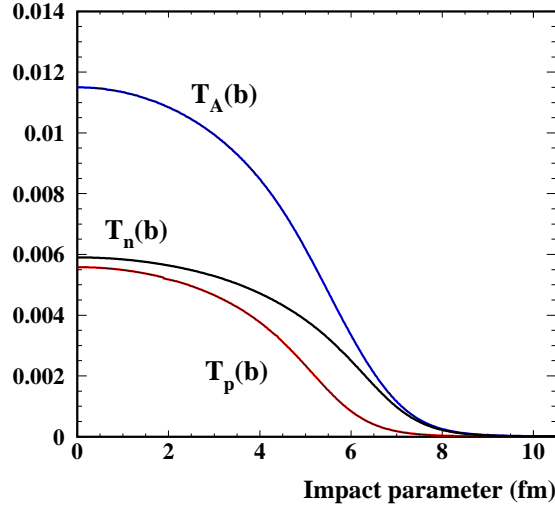


Figure 5.21: Thickness functions of the  $^{136}\text{Xe}$  nucleus calculated according the expression 5.20. The neutron  $T_n(b)$ , proton  $T_p(b)$  and total  $T_A(b)$  are shown in the figure.

According to the Glauber model, and following the procedure described in the appendix D, we can determine for a proton-nucleus reaction, the probability of having one, and only one collision between the proton and one nucleon in the projectile surface. This probability is given by:

$$P(1, \mathbf{b}) = A \cdot \sigma_{NN}(E) \cdot T_A(\mathbf{b}) \cdot [1 - T_A(\mathbf{b}) \cdot \sigma_{NN}(E)]^{A-1} \quad (5.21)$$

Where  $\sigma_{NN}$  is the total interaction nucleon-nucleon cross-section. Since we are interested in the  $\Delta$ -resonance excitation we will consider the inelastic nucleon-nucleon cross section  $\sigma_{NN}^{ine}$ . At the energies relevant for this work, the main part of the inelastic cross-section in nucleon-nucleon collisions leads to pion production through  $\Delta$  formation and its further decay (being the rest of the inelastic contribution, mediated by higher-mass mesons as  $\rho$  or  $\omega$ , negligible at these energies [85]). We can then calculate the probability of a  $\Delta$  excitation in a collision with a proton (expression 5.22) or a neutron (expression 5.23) in the surface of the projectile according to the following equations:

$$P_p(1, \mathbf{b}) = A \cdot \sigma_{pp}^{ine}(E) \cdot T_p(\mathbf{b}) \cdot [1 - (T_n(\mathbf{b}) \cdot \sigma_{pn}^{ine}(E) + T_p(\mathbf{b}) \cdot \sigma_{pp}^{ine}(E))]^{A-1} \quad (5.22)$$

$$P_n(1, \mathbf{b}) = A \cdot \sigma_{pn}^{ine}(E) \cdot T_n(\mathbf{b}) \cdot [1 - (T_n(\mathbf{b}) \cdot \sigma_{pn}^{ine}(E) + T_p(\mathbf{b}) \cdot \sigma_{pp}^{ine}(E))]^{A-1} \quad (5.23)$$

A graphical representation of these probabilities is shown in the left-panel of figure 5.23. However, it is still remaining one ingredient in the model, the pion absorption. After an inelastic collision, where a  $\Delta$ -resonance was excited, its further decay into the  $\Delta \rightarrow N + \pi$  channel must fulfill one requirement, the pion must escape from the nucleus for a double reason: first, if it remains within the nucleus its net charge does not change and we cannot speak about a charge-exchange and, second, for the  $\pi^0$  remaining within the nucleus the excitation energy induced in the system would lead to neutron evaporation, which do not corresponds to the isobar charge-exchange. Following the arguments given by Braun [115] we can calculate the probability of missing the pion as:

$$P_{miss} = e^{-\sigma_{n\pi} \cdot A \int_z^\infty \rho(\mathbf{b}, z') dz'} \quad (5.24)$$

where  $\sigma_{n\pi}$  is the absorption nucleon-pion cross-sections as parametrized in the work of Cugnon [8]. This probability will be higher as more peripheral is the collision. Actually, the strong absorption of the pions by the nucleus is the main reason to state that the charge-exchange reactions must be very peripheral [80].

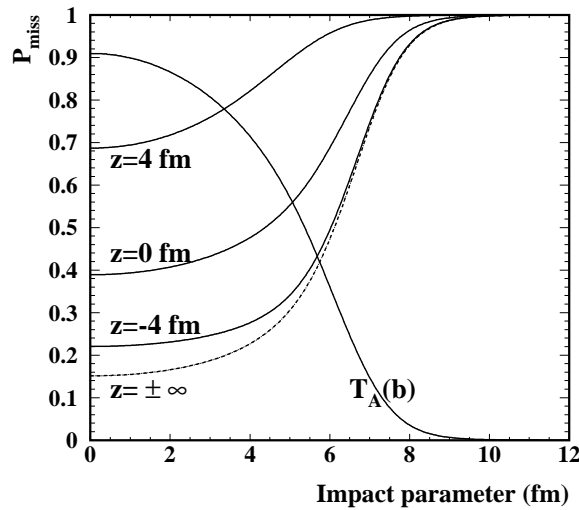


Figure 5.22: Probability of pion miss from the nucleus calculated with the expression 5.24 for several values of the integration limit  $z$ . This value is identified with the depth inside the nucleus where the  $\Delta$ -resonance is created. The thickness function of the  $^{136}\text{Xe}$  nucleus calculated according the expression 5.18 is also plot on the figure.

The  $P_{miss}$  function is plot in the figure 5.22 for several integration paths, depending on the position ( $z$ ) of the  $\Delta$ -decay inside the nucleus. The thickness function

of expression 5.20 is also shown in the figure. In our model, the lifetime of the  $\Delta$  is considered negligible, the decay follows immediately the formation. The effect of this approximation can be studied by solving the integral 5.24 with the lower limit  $z + \delta$ , where  $\delta$  would take into account a delay in the decaying of the  $\Delta$ -resonance. This effect was observed to be no relevant for realistic values of the  $\Delta$  lifetime, hence the resonance is considered to decay instantaneously.

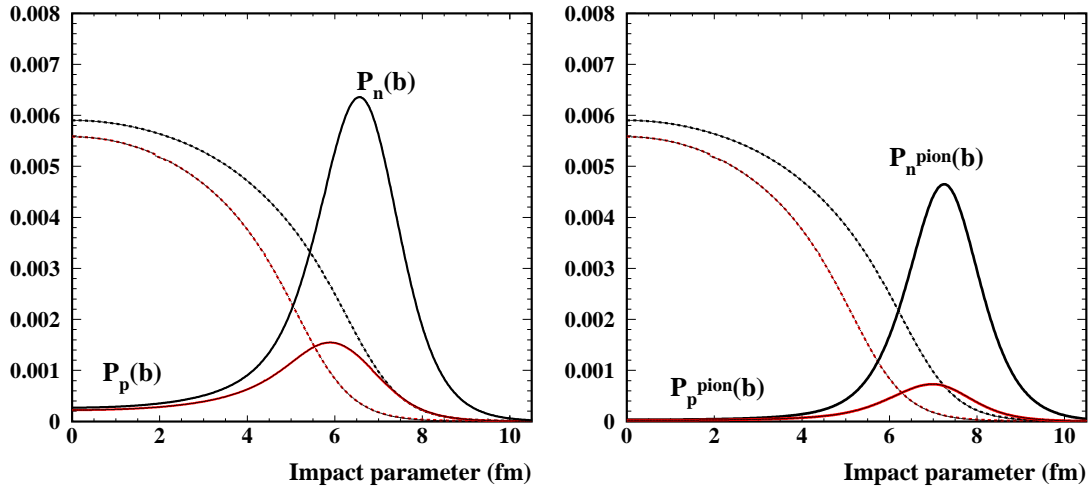


Figure 5.23: (Left Panel) Probability of single inelastic collision within the neutron and proton matter distributions. (Right Panel) Probability of single inelastic collision within the neutron and proton matter distributions corrected by the probability of missing the pion after the  $\Delta$  decay, as calculated with the expression 5.24.

As can be observed in the figure, the probability of missing the pion depends strongly on the depth where the resonance is excited inside the nucleus. In the right-panel of figure 5.23 we have represented how the escape probability of the pion affects the probabilities of colliding with the neutron and proton shell. This effect is an additional contribution to the different probabilities for the proton and neutron pickup channels. The proton pickup is more probable to occur due to three main reasons:

1. There are more neutrons (82) than protons (54) in the  $^{136}\text{Xe}$  nucleus. Hence it is more probable to collide within a neutron in the xenon surface.
2. The profile function of the neutron distribution reach regions with larger impact parameters than the proton one. Thus, it is more probable to suffer a peripheral collision with a neutron than with a proton.
3. The scape probability of the pion is higher for very peripheral collisions, which take place mainly within the neutron distribution as shown in figure 5.23.

Even when the charge-exchange reactions are very peripheral, the collision can take place with a deeply bound nucleon, leading to an excited prefragment and, consequently, to a not isobaric charge-exchange. This effect is not taken into account in our model. This could affect the absolute probabilities for the isobar proton and neutron pickup, but in principle, the relative values should not be modified.

Isotope	Probability	Proton Radius	Neutron Radius	Total Radius
$^{136}\text{Cs}$	95.1 %	4.80 fm (fixed)	$5.7 \pm 0.07 \pm 0.22$ fm	$5.3 \pm 0.07 \pm 0.22$ fm
$^{136}\text{I}$	4.9 %			

Table 5.5: *Experimental probabilities of the (n,p) and (p,n) channels for the reaction  $^{136}\text{Xe} + H$  at 500 MeV/u. The proton, neutron and total r.m.s. radii of the  $^{136}\text{Xe}$  obtained in order to reproduce the experimental results are also shown in the table. The first uncertainty value refers to the experimental procedure and the second one to the model calculations.*

In the table 5.5 we show the proton, neutron and total r.m.s. radii of  $^{136}\text{Xe}$  obtained in order to reproduce the resonant (p,n) and (n,p) probabilities. The proton r.m.s. radius has been fixed to 4.80 fm according to measurements performed using electromagnetic probes [116]. The value of the density smoothness was fixed to 0.54, for both the neutron and proton radial distributions according to the results of the HFBRAD code. There are two main sources of uncertainty, those associated to the experimental determination of the isobar charge-exchange cross section through the  $\Delta$ -resonance excitation and then those associated to the model calculation we use to determine the proton and neutron r.m.s radii.

Concerning the experimental procedure, most of the systematic uncertainties discussed in chapter 2 (target thickness, projectile flux, ...) do not affect our method since we are only interested in the relative values of the (p,n) and (n,p) channels. Therefore the only remaining uncertainty sources are the statistical uncertainty and the systematic uncertainty introduced by the method we use to separate the elastic and inelastic charge-exchange channels. We estimate that these two uncertainties amount to 7 %, translating into a r.m.s. radius uncertainty of  $\sim 0.07$  fm.

In the model calculations we have three possible contributions to our uncertainty. The first one is that we are not considering the possible excitation of the residual nuclei by removal of deeply bound nuclei in the inter-nuclear nucleon-nucleon collisions. As already mention, at the present stage we consider that this effect should not affect the relative cross sections for the (p,n) and (n,p) processes. The second parameter is the pion escaping probability. Since our Glauber model is not a Monte-Carlo code, the pion kinetic energy after the  $\Delta$ -decay is fixed. The value of the kinetic energy of the emitted pion will affect its escaping probability calculated in expression 5.24. Exploring (by means of the INCL4 code) the energy spectrum

of the pions emitted after the  $\Delta$ -resonance excitation, we have determined the most probable value for the pion kinetic energy and its dispersion, being  $117 \pm 46$  MeV. This energy dispersion leads to a r.m.s. radius uncertainty  $\sim 0.22$  fm. Finally the value of the smoothness parameter ( $h$  in equation 5.16) describing the neutron and proton radial distributions will also affect our calculated probabilities. The role of this parameter will be discussed in the next section.

### 5.4.5 Discussion of the results

In table 5.6 we present the neutron r.m.s radii of  $^{136}\text{Xe}$  that we obtain from our measurements and Glauber calculations compared with other calculation models. With our Glauber code, we have determined the neutron r.m.s. radius required in order to reproduce the value of the total cross section given by the Karol code (1263 mb), this is shown in the first column of table 5.6. The value obtained for the neutron distribution was  $5.1 \pm 0.25$  fm, a 6% higher than the proton r.m.s. radius (fixed to 4.80 fm according to [116]). The total r.m.s. radius of the  $^{136}\text{Xe}$  corresponds to  $5.0 \pm 0.25$  fm, and it has been calculated as  $R_{Total}^2 = 1/2 * (R_{Proton}^2 + R_{Neutron}^2)$ .

	Karol	Charge-Exchange	INCL4	HFBRAD
$R_{Proton}$	4.80 fm (fixed)	4.8 fm (fixed)	—	4.75 fm
$R_{Neutron}$	$5.1 \pm 0.25$ fm	$5.7 \pm 0.25$ fm	—	4.91 fm
$R_{Total}$	$5.0 \pm 0.25$ fm	$5.3 \pm 0.25$ fm	4.85 fm	4.85 fm

Table 5.6: *r.m.s. radii results obtained with our code based on the Glauber model. The results obtained with other models are also shown in the table (see text for details).*

In the second column we present the value for the r.m.s. radii obtained with our Glauber code in order to reproduce the experimental (n,p) and (p,n) probabilities presented in the table 5.5. The r.m.s. neutron radius was found to be  $5.7 \pm 0.25$  fm, a 16% higher than the proton r.m.s. radius. The total r.m.s. radius obtained in this case was  $5.3 \pm 0.25$  fm, 8.5 % larger than the r.m.s. radius of the Wood-Saxon distribution used by the INCL4 code (4.85 fm). INCL4, for the moment, can not treat the proton and neutron distributions separately, thus no information is available concerning the neutron or proton radii separately. In the fourth column of table 5.6 we consider the predictions of the Hartree-Fock-Bogoliubov method as calculated with the HFBRAD code [111].

The value of the neutron r.m.s. radius obtained with our model seems to be slightly larger than expected from previous experiments with other stable isotopes ([97] and [99]) which obtained a difference between the proton and neutron radii

of heavy stable nucleus of the order of a few percent. The reason for this apparent discrepancy could be in one of the parameters we use in our calculations, the smoothness parameter of the Fermi distribution describing the radial density distributions.

As the charge-exchange reactions are very peripheral processes, the smoothness of the density distribution (factor  $h$  in expression 5.16) should play an important role in the probability of collision within the proton and the neutron shells. We have explored the influence of the smoothness parameter (also called nuclear diffuseness or surface thickness parameter) in our Glauber code by fixing the smoothness of the proton distribution to  $h_p=0.54$  fm and changing systematically the smoothness of the neutron density. In the left panel of figure 5.24 we can explore the influence of the smoothness in the neutron density distribution of  $^{136}\text{Xe}$ . In the right panel of figure 5.24 we represent the evolution of the neutron radius required to reproduce our experimental ratio of isobar (n,p) and (p,n) resonant reactions as a function of the value of the neutron smoothness parameter. As can be observed, the radius necessary to reproduce our results depends strongly on the smoothness of the neutron distribution. Actually, increasing the smoothness by a 10 % ( $h_n=0.60$  fm) we reproduce our experimental (n,p) and (p,n) ratios with a r.m.s. neutron radius of  $5.1 \pm 0.25$  fm, which is compatible with the value given by the HFBRAD code (see table 5.6). We also obtain a total reaction cross sections of  $1343 \pm 110$  mb, which perfectly agrees with the  $1263 \pm 120$  mb given by the Karol code.

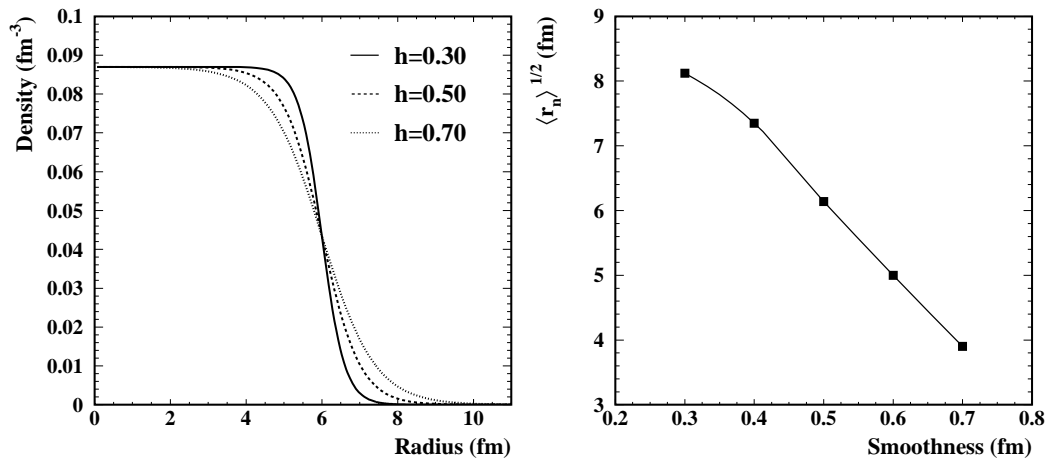


Figure 5.24: **(Left)** Influence of the smoothness parameter in the neutron density distributions. **(Right)** Evolution of the neutron r.m.s. radius required to reproduce the experimental resonant charge-exchange reactions as a function of the smoothness of the density distribution.

Based on this analysis we can conclude that the  $\Delta$ -resonance excitation in isobar charge-exchange reactions provide a useful tool to determine the r.m.s proton and neutron radii of nuclei. In contrast to other methods, this technique proves the

neutron and proton distributions very close to the half-density radius, as observed in Fig. 5.23. In this figure, the mean value of the probability for a  $\Delta$ -resonance excitation in isobar charge-exchange reaction within the neutron shell takes place at 6.7 fm. This value is located very close to the half-density neutron radius of 6.9 fm (equivalent to 5.7 fm of r.m.s. radius) obtained with our Glauber code.

Finally, Applying this method we obtain a neutron r.m.s. radius for  $^{136}\text{Xe}$  compatible with the results given by other models and previous experimental results concerning neutron skin measurements in other stable nuclei. This is an innovative method that can be applied to isotopes with extremely low half-lives impossible to study with other available methods. We claim for new dedicated measurements on the charge-exchange reactions at several energies and with heavier projectiles to compare with previous existing data and model calculations.

#### 5.4.6 Comparison with the antiproton annihilation method

In section 5.4.1 we made a brief description of several experimental methods used to characterize the radial distribution of nuclei. One of those methods, the one based in the antiproton annihilation [107], has a particular interest for us since it has some similarities with the method we propose in this work. Both methods are based on different physical mechanisms, but on the same phenomenological principle: it is possible to isolate the collisions within the neutron or the proton shells. However, we think that the charge-exchange method can be applied to a wide range of half lives and with a well known and widely used experimental procedure. The validity of the antiproton annihilation method relies on the hypothesis that the total absorption cross-section of the antiproton can be separated in two contributions, one given by the neutrons ( $\sigma_{abs}^{(n)}$ ) and other one given by the protons ( $\sigma_{abs}^{(p)}$ ):

$$\sigma_{abs} = \sigma_{abs}^{(p)} + \sigma_{abs}^{(n)} \quad (5.25)$$

This is demonstrated by Lenske [107], and it is related with the fact that  $\sigma_{abs}^{(p)}$  is proportional to the proton shell radius, while  $\sigma_{abs}^{(n)}$  is proportional to the neutron shell radius, as will be discussed below. In the left panel of figure 5.25 we show the total annihilation cross section of antiprotons with different Ni isotopes at 400 MeV, as well as the partial annihilation cross sections with protons and neutrons. In this panel we also show the r.m.s. matter radii of the Ni isotopes normalized to the total annihilation cross section. As can be observed, both quantities follow the same isotopic dependence, and hence, Lenske et al. conclude that the antiproton annihilation at intermediate energies is an appropriate probe for nuclear size and

shapes. Moreover, the r.m.s. matter radii are directly proportional to the total annihilation cross section.

In the case of the charge-exchange reactions, we have performed simulations with our Glauber code to test whether the cross section of the resonant process is also proportional to the r.m.s. matter radii. We have used the HFBRAD code to calculate the proton and neutron radii. The results are shown in the right panel of figure 5.25. As can be observed, the probability of an isobar charge-exchange process, within the neutron or the proton shells, follow a similar isotopic behavior than the antiproton annihilation with protons and neutrons. As increasing the neutron number of the nucleus, the probability of an isobar exchange within the proton shell decreases, being the opposite in the case of the neutron shell. The total isobar charge-exchange cross section (black squares) is proportional to the total matter radius, similar to the antiproton annihilation technique.

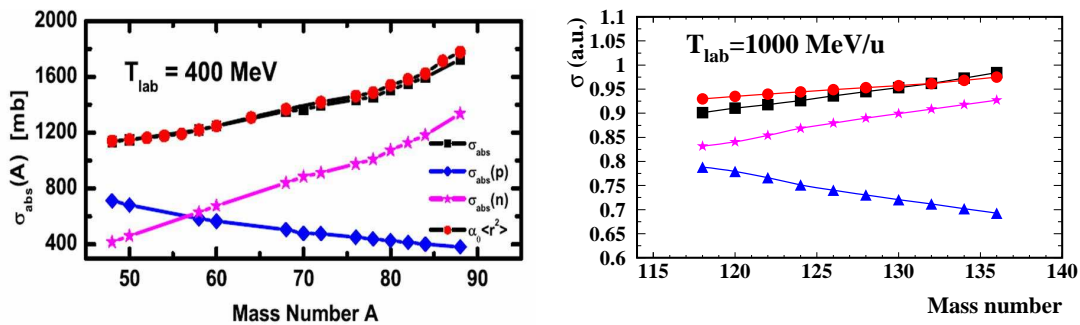


Figure 5.25: *(Left Panel, from [107])* Absorption cross-sections (squares) for antiproton annihilation on Ni isotopes at a kinetic energy of 400 MeV/u. (Circles) The rms-radii of the nuclear matter densities. (Diamonds) Partial cross-sections for absorption on the target protons and neutrons (stars). *(Right Panel)* Charge-exchange cross sections for Sn isotopes calculated with our Glauber code. The total (neutron + proton) radii have been arbitrarily scaled for clarity in the figure.

However, our method presents some advantages compared to the antiproton annihilation. The method based on the antiproton annihilation can only be applied to nuclei with production rates of about  $10^5 \text{ s}^{-1}$  and half lives of about 1 s or longer. By contrast, our method can be used with nuclei with a production rate as low as  $5 \times 10^3 \text{ s}^{-1}$  provided we accumulate statistics in one day with a  $1 \text{ g/cm}^2$  target. An additional advantage of the charge-exchange method is that it allows to measure, with a magnetic spectrometer, the matter distributions of nuclei with half-lives as short as 300 ns. With the future fragment separator (SuperFRS) at the FAIR facility, the measurement time can be reduced by one order of magnitude.

*Determination of matter and charge radii using  $\Delta$ -resonance excitation in isobaric charge-exchange react*

Moreover, the experimental procedure we propose is simpler since we do not need to produce a second exotic beam of antiprotons and use two colliding rings.



# Conclusions

In this manuscript we have presented the results of an experimental program aiming at characterizing the intra-nuclear cascade produced during collisions of relativistic heavy nuclei. The elastic or inelastic character of the nucleon-nucleon collisions, the excitation energy generated in this process or the radial distribution of protons and neutrons were some of the subjects addressed in this investigation.

The experiments were performed at the GSI facilities in Darmstadt (Germany). In these experiments, reactions induced by  $^{136}\text{Xe}$  and  $^{124}\text{Xe}$  projectiles at 200, 500 and 1000 MeV/u impinging targets made of hydrogen, beryllium, titanium and lead, were investigated. Projectile residues were analyzed in momentum by using the zero degree magnetic separator FRS. This separator together with its detection setup allowed us to isotopically identify the projectile residues and determine its production cross sections and longitudinal momentum. Peripheral reactions were selected by considering only those residual fragments with a mass number difference with respect to the projectile below 30 units.

The large variety of measured data allowed us to perform systematic investigations of the influence of the nature of the target, the projectile energy or the projectile neutron excess in peripheral relativistic collisions between heavy ions. The most salient results are the following:

- Isotopic cross sections measured with different targets (Be, Ti and Pb) just scale according to the respective total interaction cross sections. However, the cross sections obtained with the hydrogen target show a different behavior. Comparisons to different model calculations allow us to conclude that the number of abraded nucleons is smaller in the case of the hydrogen target while the excitation energy induced per abraded nucleon is similar. Consequently, collisions induced by the hydrogen target lead to a larger production of residual nuclei with a mass number close to the one of the projectile.
- The role of the neutron excess of the projectile was also investigated by comparing the measured cross sections of residual nuclei produced in collisions

induced by  $^{124}\text{Xe}$  and  $^{136}\text{Xe}$  projectiles. The larger neutron excess of  $^{136}\text{Xe}$  leads to wider isotopic distributions of residual nuclei. This observation was explained in terms of the *evaporation corridor* defined by the equilibrium between neutron and proton evaporation at the end of the evaporation chain. This universal region in the chart of the nuclei is valid for any reaction provided the initial excitation energy of the prefragment is sufficient to reach this equilibrium between proton and neutron evaporation. Projectiles with a larger neutron excess need to evaporate a larger amount of neutrons before they reach this equilibrium. This larger evaporation chain until the evaporation corridor leads to a wider isotopic distribution of residual nuclei with an atomic number close to the one of the projectile.

Concerning the predictive power of the codes, ABRABLA provided a better global description of the experimental data as compared to EPAX, specially in the neutron-rich region. In general, EPAX has problems to describe the shape of the yield distributions, it provided too broad isotopic distributions in the case of the  $^{124}\text{Xe}$  projectiles and too narrow in the case of the  $^{136}\text{Xe}$ . This effect translated into an overestimation of the cross sections of the most neutron-rich residues and an underestimation of the neutron-deficient ones, in particular for the projectiles with a large neutron excess as  $^{136}\text{Xe}$ .

- The role of the projectile energy was investigated by using the reactions  $^{136}\text{Xe} + \text{Ti}$  at 200, 500 and 1000 MeV/u. From the Glauber model we did not expect any dependence of the production cross sections of residual nuclei with the energy of the projectile. Our data have confirmed this energy independent mechanism down to 200 MeV/u for residual nuclei with atomic numbers below  $Z=53$ . However, the isotopic chains of xenon and iodine residues presented cross sections that clearly depended on the energy of the projectile. Using the ISABEL code we concluded that the discrepancy between the data and the models was larger at lower projectile energies being caused by charge-exchange reactions. The energy dependence of our data follows that of the quasi-elastic charge-exchange process, being larger at lower energies. We modified the ABRABLA code in order to incorporate the charge-exchange mechanism using a parametrization deduced from the data obtained in this work.

We have also investigated the longitudinal momentum distributions of the projectile residues measured in this work. We have found two interesting effects: first, the mean value of the momentum distributions for projectile residues created in peripheral reactions do not follow the expected values according to the Morrissey's systematic. Second, we observed an offset in the mean value of the momentum for charge-pickup residues. Indeed both effects were explained as due to the resonant charge exchange channels. The excitation of the  $\Delta(1232)$  resonance requires around 300 MeV affecting the longitudinal momentum of the projectile.

The last chapter of this work was devoted, specifically, to the charge-exchange mechanism. We have measured, with high accuracy, the production cross-sections of approximately 150 charge-exchange residues created by single and double charge pickup in the reactions induced by  $^{136}\text{Xe}$  projectiles with several targets. Only few previous experimental works were able to provide isotopic cross sections for this process, consequently our data provided valuable information concerning this reaction mechanism.

The cross sections of charge-exchange residues scale opposite to the energy of the primary projectile. We demonstrated that this energy dependence was due to the quasi-elastic charge-exchange channel. The shape of the isotopic distributions, either for single and double processes, seem to be independent of the target nature or the projectile energy, being these results compatible with those measured in previous experiments. However, the shape of the isotopic distributions strongly depend on the projectile neutron excess. We have demonstrated that this behavior was also related with the *memory effect*, concluding that the residues keep information of the N/Z ratio of the primary projectile.

The large variety of data measured in this work also allowed to improved existing parametrizations for the production cross sections of residual nuclei produced in charge-pickup reactions, as the one proposed by Guoxiao. The new parametrization we propose takes into account dependencies on the energy and the neutron excess of the projectile, describing accurately those cases where the Guoxiao expression failed. This parametrization also describes the total cross section in the case of the double charge-exchange.

Concerning the double charge-exchange reactions, systematic investigations were also performed according to the target size and projectile energy and neutron excess. The most salient observation is that when compared to the single charge exchange process, the isotopic distribution was centered on more neutron-deficient nuclei independently on the target and the projectile energy. This observation would indicate a larger excitation energy induced in this reaction channel.

In the last part of this work we have investigated the sensitivity of the charge-exchange reactions to the radial distributions of protons and neutrons inside the nucleus. In particular, we have proposed to use the  $\Delta$ -resonance excitation in isobaric charge-exchange reactions leading to neutron (p,n) and proton (n,p) pickup processes, to determine the root mean square radius for neutrons and protons, respectively. This particular reaction channel selects reactions where a single nucleon-nucleon collision at the nuclear surface leads to a charge-exchange process through a  $\Delta$ -resonance excitation. Since the inelastic nucleon-nucleon cross sections is well established, the probability for the (n,p) and (p,n) channels is expected to be directly related to the radial distribution of neutrons and protons, respectively. Experiments

tally, the high resolving power of the FRS allowed us not only to unambiguously identify the isobar charge changing residues of  $^{136}\text{Xe}$ , ( $^{136}\text{Cs}$  and  $^{136}\text{I}$ ), but also separate the  $\Delta$ -resonance from the quasi-elastic contributions from the analysis of the longitudinal momentum distributions of those particular residual nuclei.

This method has been applied to the reaction  $^{136}\text{Xe} + \text{H}$  at 500 MeV/u. In this case we found a probability for the (n,p) isobar channel of 95.1 % while for the (p,n) channel the probability was 4.9 %. In order to interpret these results we have developed a code based on the Glauber model to describe the above reaction channels. In these model calculations we use measured inelastic nucleon-nucleon cross sections and realistic descriptions of the radial distributions of neutrons and protons based on Hartree-Fock-Bogoliubov calculations.

The neutron r.m.s. radius obtained with our method for  $^{136}\text{Xe}$  ( $5.5 \pm 0.07 \pm 0.15$  fm) is slightly larger than the one predicted by HFB calculations (4.91 fm). However, a 10 % increase in the smoothness parameter used in the Fermi distribution describing the radial distribution of neutrons allows to reproduce the calculated radius. We concluded from our analysis that the isobar charge-exchange reactions could provide a useful tool to study the matter distribution at the periphery of the nucleus. This kind of reactions are sensitive to the neutron and proton distributions at regions very close to the half-density radius. This is an innovative method that can be applied to nuclei with a production rate as low as  $5 \times 10^3 \text{ s}^{-1}$  and half-lives as short as ( $\sim 300$  ns) impossible to study with other available methods. We claim for new dedicated measurements on the charge-exchange reactions at several energies and with heavier projectiles to compare with previous existing data and model calculations.

# Bibliography

- [1] R. Serber. *Phys. Rev.*, 72:1114, 1947.
- [2] M.L. Goldberger. *Phys. Rev.*, 74:1269, 1948.
- [3] N. Metropolis. *Phys. Rev.*, 110:185, 1958.
- [4] H. Bertini. *Phys. Rev.*, 131:1801, 1963.
- [5] Y. Yariv and Z. Fraenkel. *Phys. Rev. C*, 20:2227, 1979.
- [6] Y. Yariv and Z. Fraenkel. *Phys. Rev.*, C24:488–494, 1981.
- [7] J. Cugnon, C. Volant, and S. Vuillier. *Nucl. Phys.*, A620:475–509, 1997.
- [8] J. Cugnon, J. Vandermeulen, and D. L'Hote. *Nucl. Instr. Meth. B*, 111:215–220, 1996.
- [9] A. Boudard, J. Cugnon, S. Leray, and C. Volant. *Phys. Rev. C*, 66:044615, 2002.
- [10] J.D. Bowman, W.J. Swiatecki, and C.E. Tsang. *Lawrence Berkeley Laboratory Report LBL-2908*. 1973.
- [11] R. J. Glauber. In New York 1970, Proceedings, High-Energy Physics And Nuclear Structure\*, New York 1970, 207-264.
- [12] J. J. Gaimard and K. H. Schmidt. *Nucl. Phys.*, A531:709–746, 1991.
- [13] A.R. Junghans, M. de Jong, H.-G. Clerc, A.V. Ignatyuk, G.A. Kudyaev, and K.-H. Schmidt. *Nucl. Phys. A*, 629:635, 1998.
- [14] V. Weisskopf. *Phys. Rev.*, 52:295–303, 1937.
- [15] J. Hufner. *Phys. Rep.*, 125:129, 1985.
- [16] J. Benecke, T. T. Chou, Chen-Ning Yang, and E. Yen. *Phys. Rev.*, 188:2159–2169, 1969.

- [17] H. H. Heckman, D. E. Greiner, P. J. Lindstrom, and F. S. Bieser. *Phys. Rev. C*, 28:926–929, 1972.
- [18] J. B. Cumming, P. E. Haustein, R. W. Stoenner, L. Mausner, and R. A. Naumann. *Phys. Rev.*, C10:739–755, 1974.
- [19] K. et al. Summerer. *Phys. Rev.*, C42:2546, 1990.
- [20] H.W.Barz et al. *Nucl. Phys. A*, 448:753, 1986.
- [21] M. Blann, M. G. Mustafa, G. Peilert, Horst Stoecker, and W. Greiner. *Phys. Rev.*, C44:431, 1991.
- [22] J.P. Dufour, H. Delagrange, R. del Moral, A. Fleury, F. Hubert, Y. Llabador, M.B. Mauhurat, and K.-H. Schmidt. *Nucl. Phys. A*, 387:157c, 1982.
- [23] C. H. Tsao, R. Silberberg, A. F. Barghouty, L. Sihver, and T. Kanai. *Phys. Rev.*, C47, 1993.
- [24] D. I. Olson et al. *Phys. Rev.*, C28, 1983.
- [25] K. Summerer and B. Blank. *Phys. Rev.*, C61:034607, 2000.
- [26] K. H. Schmidt et al. *Phys. Lett.*, B300:313–316, 1993.
- [27] M. de Jong et al. *Nucl. Phys.*, A613:435, 1997.
- [28] K. H. Schmidt, M. V. Ricciardi, A. S. Botvina, and T. Enqvist. *Nucl. Phys.*, A710:157–179, 2002.
- [29] I. Weisskopf. *Phys. Rev.*, 82:690, 1951.
- [30] W. Hausser and H. Feshbach. *Phys. Rev.*, 87:336, 1952.
- [31] T. Erics. *Adv. Phys.*, 9:425, 1960.
- [32] T. Darrah-Thomas. *Nucl. Phys.*, 53:558, 1964.
- [33] N. Bohr and J.A Wheeler. *Phys. Rev.*, 56:426–450, 1939.
- [34] L.G. Moretto. *Nucl. Phys. A*, 247:211, 1975.
- [35] A.J. Sierk. *Phys. Rev. C*, 33:2039, 1986.
- [36] K.-H. Schmidt and W. Morawek. *Rep. Prog. Phys.*, 55:949, 1991.
- [37] B.L.Cohen. *Concepts of Nuclear Physics*. 1975.
- [38] D.J.Morrisey. *Phys. Rev. C*, 39:460, 1989.

- [39] A.S.Goldhaber. *Phys. Lett. B*, 53:306, 1974.
- [40] E.J.Monitz, I.Sick, R.R.Whitney, J.R.Ficenec, R.D.Kephart, and W.P.Trower. *Phys. Rev. Lett.*, 26:445, 1971.
- [41] M.Steiner, M.Blasche, H.G.Clerc, H.Eickhoff, B.Franczack, H.Geissel, G.Muenzenberg, K.H.Schmidt, H.Stelzer, and K.Suemmerer. *Nucl. Instr. Meth. A*, 312:420, 1992.
- [42] R.Anne, A.Lefol, G.Milleret, and R.Perret. *Nucl. Instr. Meth.*, 152:395, 1985.
- [43] B.Jurado, K.H.Schmidt, and K.H.Behr. *Nucl. Instr. Meth. A*, 483:603, 2002.
- [44] Ph.Chesny, A.Forgeas, J.M.Gheller, G.Guiller, P.Pariset, L.Tassan-Got, P.Armsbruster, K.H.Behr, J.Benlliure, K.Burkard, A.Brunle, T.Enqvist, F.Farget, and K.H.Schmidt. *GSI Internal Reports*, page 73, 1993.
- [45] K.-H. Schmidt, E. Hanelt, H. Geissel, G. Muenzenberg, and J.-P. Dufour. *Nucl. Instr. Meth. A*, 260:287–303, 1987.
- [46] B.Mustapha. 1999.
- [47] H. Geissel, P. Armbruster, K.H. Behr, A. Brünle, K. Burkard, M. Chen, H. Folger, B. Franczak, H. Keller, O. Klepper, B. Langenbeck, F. Nickel, E. Pfeng, M. Pfützner, E. Roeckl, K. Rykaczewski, I. Schall, D. Schardt, C. Scheidenberger, K.H. Schmidt, A. Schröter, T. Schwab, K. Sümmerer, M. Weber, G. Muenzenberg, T. Brohm, H.-G. Clerc, M. Fauerbach, J.-J. Gaimard, A. Grewe, E. Hanelt, B. Knödler, M. Steiner, B. Voss, J. Weckenmann, C. Ziegler, A. Magel, H. Wollnik, J.P. Dufour, Y. Fujita, D.J. Vieira, and B. Sherrill. *Nucl. Instr. Meth. B*, 70:286, 1992.
- [48] David C.Carey. *The Optics of the Charged Particle Beams*. 1987.
- [49] H.Stelzer. *Nucl. Instr. Meth. A*, 310:103, 1991.
- [50] M.Steiner and et al. *Nucl. Instr. Meth. A*, 312:420, 1992.
- [51] B.Voss, T.Brohm, H.-G.Clerc, A.Grewe, E.Hanelt, A.Heinz, M.de Jong, A.Junhans, W.Morawek, C.Röhl, S.Steinhäuser, C.Ziegler, K.-H.Schmidt, K.H.Behr, H.Geissel, G.Muenzenberg, F.Nickel, C.Schedenberger, K.Sümmerer, A.Magel, and M.Pfützner. *Nucl. Instr. Meth. A*, 364:150, 1995.
- [52] K.-H. Schmidt, E. Hanelt, H. Geissel, G. Munzenberg, and J.P. Dufour. *Nucl. Instr. Meth. A*, 260:150, 1987.
- [53] L. Audouin et al. *Nucl. Instrum. Meth.*, A548:517–539, 2005.

- [54] M.Pfützner, H.Geissel, G.Münzenberg, F.Nickel, C.Scheidenberger, K.-H.Schmidt, K.Sümmerer, T.Brohm, B.Voss, and H.Bischel. *Nucl. Instr. Meth. B*, 86:213, 1994.
- [55] J. Benlliure, J. Pereira-Conca, and K. H. Schmidt. *Nucl. Instrum. Meth.*, A478:493–505, 2002.
- [56] P. Napolitani, L. Tassan-Got, P. Armbruster, and M. Bernas. *Nucl. Phys. A*, 727:120–138, 2003.
- [57] P.J.Karol. *Phys. Rev. C*, 11:1203, 1975.
- [58] <http://www.ganil.fr/eurisol/FinalReport>.
- [59] K. Helariutta, J. Benlliure, M. V. Ricciardi, and K. H. Schmidt. Model calculations of a two-step reaction scheme for the production of neutron-rich secondary beams. *Eur. Phys. J.*, A17:181–193, 2003.
- [60] J. Reinhold et al. *Phys. Rev.*, C58:247–255, 1998.
- [61] C. J. Waddington, J. R. Cummings, and B. S. Nilsen. *Phys. Rev.*, C61:024910, 2000.
- [62] W. R. Binns et al. *Phys. Rev.*, C39:1785–1798, 1989.
- [63] Guo-Xiao Ren, P. B. Price, and W. T. Williams. *Phys. Rev.*, C39:1351–1358, 1989.
- [64] M. Weber, Donzau.C, J.P Dufour, H. Geissel, A. Grewe, D. Guillemaud-Mueller, H. Kellera, M. Lewitowicze, A. Magelf, A.C. Mueller, G. Münzenberg, F. Nickel, M. Pfützner, A. Piechaczeka, C. Pravikoff, E. Roeckl, K. Rykaczewska, M.G. Saint-Laurent, I. Schalla, C. Stéphan, K. Sümmerer, L. Tassan-Got, D.J. Vieira, and B. Voss. *Nucl. Phys.*, A578:659–672, 1994.
- [65] T. Enqvist et al. *Nucl. Phys.*, A686:481–524, 2001.
- [66] P. Armbruster et al. *Phys. Rev. Lett.*, 93:212701, 2004.
- [67] C. Ellegaard et al. *Phys. Rev. Lett.*, 50:1745–1748, 1983.
- [68] T. Udagawa, P. Oltmanns, F. Osterfeld, and S. W. Hong. *Phys. Rev.*, C49:3162–3181, 1994.
- [69] V. P. Koptev, E. M. Maev, M. M. Makarov, and A. V. Khanzadeev. *Yad. Fiz.*, 31:1501–1509, 1980.
- [70] M. Roy-Stephan et al. *Nucl. Phys.*, A447:635c–641c, 1986.
- [71] K. Summerer et al. *Phys. Rev.*, C52:1106–1109, 1995.

- [72] A. Kelic et al. *Phys. Rev. C*, 70:064608, 2004.
- [73] B. S. Nilsen et al. *Phys. Rev.*, C50:1065–1076, 1994.
- [74] S. B. Kaufmann and E.P. Steinberg. *Phys. Rev.*, C22:167, 1980.
- [75] F. Rejmund et al. *Nucl. Phys.*, A683:540–565, 2001.
- [76] C. A. Mosbacher and F. Osterfeld. *Phys. Rev.*, C56:2014–2028, 1997.
- [77] Toru Tsuboyama, Fuminori Sai, Nobu Katayama, Takashi Kishida, and Sukeyasu Steven Yamamoto. *Phys. Rev.*, C62:034001, 2000.
- [78] D.C Brunt, M.J. Clayton, and B.A. Westwood. *Phys. Rev.*, 187:1856, 1969.
- [79] C. Gaarde. *Annu.Rev.Nucl.Part.Sci*, 41:187, 1991.
- [80] D. Bachelier et al. *Phys. Lett.*, B172:23–26, 1986.
- [81] A. Krasznahorkay. *Nucl. Phys. A*, 731:224–234, 2004.
- [82] R.J. Furnstahl. *Nucl. Phys. A*, 706:85, 2002.
- [83] B.J VerWest and R.A Arndt. *Phys. Rev. C*, 25:1979–1985, 1982.
- [84] C.A. Bertulani and D.S. Dolci. *Nucl. Phys. A*, 674:527–538, 2000.
- [85] C.A. Bertulani. *Nucl. Phys. A*, 554:493–508, 1993.
- [86] G.F. Bertsch and H. Esbensen. *Rep. Prog. Phys*, 50:607, 1987.
- [87] R.C. Barret and D.F. Jackson. *Nuclear Sizes and Structure*. 1977.
- [88] L. Ray et al. *Phys. Rev. C*, 19:1855, 1979.
- [89] G.W Hoffmann et al. *Phys. Rev. Lett.*, 47:1436, 1981.
- [90] T. Takahashi. *PhD, University of Tokyo*, 1995.
- [91] P. Lubinski et al. *Phys. Rev. Lett.*, 73:3199, 1994.
- [92] P. Lubinski et al. *Phys. Rev. C*, 57:2962, 1998.
- [93] A. Trzcinska et al. *Phys. Rev. Lett.*, 87:82501, 2001.
- [94] C.J. Horowitz and J. Piekarewicz. *Phys. Rev. Lett.*, 86:5647, 2001.
- [95] C.J. Horowitz et al. *Phys. Rev. C*, 63:5501, 2001.
- [96] A. Krasznahorkay et al. *Phys. Rev. Lett.*, 66:1297, 1991.

- [97] A. Krasznahorkay et al. *Nucl. Phys. A*, 567:521, 1994.
- [98] G.R. Satchler. *Nucl. Phys. A*, 472:215, 1987.
- [99] A. Krasznahorkay et al. *Phys. Rev. Lett.*, 82:3216, 1999.
- [100] C. Gaarde et al. *Nucl. Phys. A*, 369:258, 1981.
- [101] W.P. Alford and B.M. Spicer. *Adv. Nucl. Phys.*, 24:1, 1998.
- [102] I. Angeli et al. *J. Phys. G*, 6:303, 1980.
- [103] J. Decharge and D. Gogny. *Phys. Rev. C*, 21:1568, 1980.
- [104] C. Batty et al. *Adv. Nucl. Phys.*, 19:1, 1989.
- [105] A. Tellez-Arenas, R.J. Lombard, and J.P Maillet. *J. Phys. G*, 13:311–319, 1987.
- [106] R.J. Lombard and J.P Maillet. *Europhys. Lett.*, 6 (4):323–327, 1988.
- [107] H. Lenske and P. Kienle. 2005.
- [108] J.P. Dufour, R. del Moral, H. Emmermann, F. Hubert, D. Jean, C Poinot, A. Pravikoff, A. Fleury, H. Delagrange, and K.-H. Schmidt. *Nucl. Instr. Meth. A*, 248:267, 1986.
- [109] M. Roy-Stephan et al. *Nucl. Phys.*, A482:373c–382c, 1988.
- [110] <http://cmd.inp.nsk.su/old/cmd2/manuals/cernlib/minuit/minmain.html>.
- [111] J. Dobaczewski. *Computer Physic Communications*, 168:96–122, 2005.
- [112] S. Mizutori, J. Dobaczewski, G. A. Lalazissis, W. Nazarewicz, and P.-G. Reinhard. *Phys. Rev. C*, 61(4):044326, 2000.
- [113] J. Dobaczewski, H. Flocard, and J. Treiner. *Nucl. Phys. A*, 422:103, 1984.
- [114] E. Chabanat, P. Bonche, P. Haensel, J. Meyer, and F. Schaeffer. *Nucl. Phys. A*, 627:710, 1997.
- [115] M.A. Braun, C. Pajares, C.A. Salgado, N. Armesto, and A. Capella. *Nucl. Phys. B*, 509:357–377, 1998.
- [116] E. Wesolowski. *J. Phys. G*, 10:321–330, 1984.

# Resumen en Castellano

## Introducción

La Física Nuclear, como cualquier otra disciplina científica, es un área en permanente evolución en la que se abren nuevas fronteras de manera continua. La comunidad científica ha focalizado sus esfuerzos en este ámbito de la física durante el último siglo, pero sin embargo, aún hoy, no somos capaces de llevar a cabo una descripción global de los procesos nucleares a partir de interacciones fundamentales. Los núcleos atómicos poseen un interés especial, ya que constituyen unos mini-laboratorios privilegiados en los que tres de las cuatro interacciones presentes en el Universo juegan un papel primordial. Sabemos muchas cosas de la materia nuclear, sin embargo muchas otras permanecen aún sin revelar.

Con el propósito de profundizar en el conocimiento de las reacciones nucleares a energías relativistas, en el laboratorio europeo GSI-Darmstadt (Alemania) se ha llevado a cabo durante los últimos años una extensiva campaña de medidas, estando esta tesis doctoral enmarcada dentro de ese ámbito de colaboración. El propósito de ese proyecto era el estudio de un amplio grupo de reacciones nucleares para obtener una visión sistemática de los procesos de fisión y fragmentación, así como establecer un conjunto de datos para validar y mejorar los códigos y modelos que describen este tipo de reacciones. Todo ese trabajo se desarrolló en el seno de una colaboración europea con la implicación de varias instituciones como el *Gesellschaft für Schwerionenforschung* (GSI, Alemania), el *Institute de Physique Nucleaire IPN* (Orsay, Francia), el *Commissariat a l'Energie Atomique DAPNIA/SPhN* (Saclay, Francia) o la propia *Universidad de Santiago de Compostela*.

El objeto de esta tesis doctoral es el estudio de los fenómenos nucleares que aparecen en las reacciones de fragmentación más periféricas, cuando colisionan dos iones pesados a energías relativistas. En particular, nuestra región de interés se centra en la zona de masas intermedias de la carta de núcleos. Nuestros estudios pretenden arrojar algo de luz sobre algunos de los mecanismos de reacción que tienen

lugar en este tipo de colisiones cuando las energías de excitación de los prefragmentos son bajas, cosa que sucede cuando los parámetros de impacto de la colisión son grandes. Hemos estudiado varias reacciones:  $^{136}\text{Xe} + \text{H}$ ,  $\text{Be}$ ,  $\text{Ti}$ ,  $\text{Pb}$  a 1000 MeV/u,  $^{136}\text{Xe} + \text{H}$ ,  $\text{D}$ ,  $\text{Ti}$  a 500 MeV/u,  $^{136}\text{Xe} + \text{H}$ ,  $\text{Ti}$  a 200 MeV/u todas ellas medidas a finales de 2002 y  $^{124}\text{Xe} + \text{Be}$ ,  $\text{Pb}$  a 1000 MeV/u medidas en 2003. Esta variedad de blancos, proyectiles y energías nos van a permitir desarrollar estudios sistemáticos sobre la influencia de esos factores en las secciones eficaces de producción.

## Física con iones pesados: reacciones periféricas

Las interacciones de los constituyentes del núcleo atómico son bien conocidas cuando éstos están libres en la naturaleza. Sin embargo, cuando se encuentran en el seno de un núcleo, sus interacciones se modifican debido a las propiedades del medio nuclear, cuya naturaleza permanece aún sin revelar. El principal objetivo de este trabajo consiste en el estudio de los procesos microscópicos que tienen lugar en las reacciones entre iones pesados a energías relativistas y, en particular, la influencia de las propiedades del medio en las interacciones nucleón-nucleón y la distribución de materia (protones y neutrones) dentro del núcleo.

Las reacciones entre iones pesados a energías relativistas se pueden describir mediante la imagen de participante-espectador. En realidad, esto no es más que una división geométrica basada en la siguiente observación: los residuos con grandes momentos longitudinales vienen de reacciones con ángulos de dispersión muy pequeños, lo que significa que durante la colisión los nucleones se mueven casi en línea recta. Esta observación nos lleva directamente a la siguiente conclusión: para un parámetro de impacto dado, los nucleones que se encuentren en la región de solapamiento entre el proyectil y el blanco son los que interactúan (*participantes*), mientras que los que estén fuera de esa zona serán los *espectadores*. En la zona de interacción, una parte considerable de la energía del proyectil se transforma en calor, mientras que los espectadores permanecen relativamente fríos. Esta primera fase de la reacción se denomina *abrasión*. El conjunto de espectadores (prefragmento) se encuentra excitado debido a varias causas, como el exceso de energía de superficie, difusión de energía desde la zona de interacción o la creación de huecos en el esquema de niveles del núcleo al arrancar (abradir) varios nucleones. Esta energía de excitación puede romper el prefragmento en uno o varios fragmentos pesados más un número de nucleones por varios mecanismos como la fisión, la evaporación o la multifragmentación. Esta segunda fase de la reacción, mucho más lenta que la primera, se denomina *desexcitación*.

Existen varios modelos y códigos para describir las reacciones entre iones pe-

sados a energías relativistas. Con una visión general del problema tenemos los modelos semiempíricos, como el de Silberberg-Tsao. Este modelo describe las secciones eficaces de las reacciones núcleo-núcleo aplicando un factor de escala a la correspondiente reacción protón-núcleo. Por otro lado tenemos el código EPAX, una parametrización empírica que predice las secciones eficaces de reacción entre iones pesados para núcleos comprendidos entre el argón y el plomo.

Una descripción más detallada corresponde a los códigos que calculan, de modo independiente, las dos etapas de la reacción: abrasión y desexcitación. En cuanto a los que calculan la primera etapa de la reacción tenemos los llamados códigos de cascada intranuclear, cuyos más famosos exponentes son INCL4 e ISABEL. Ambos códigos describen la abrasión como un conjunto sucesivo de colisiones entre nucleones, de tal modo que pueden ser considerados códigos de transporte entre hadrones en el interior del núcleo. Hay muchas diferencias entre ambos códigos, especialmente en lo concerniente al tratamiento de las densidades nucleares, del tiempo entre colisiones, la distancia entre colisiones o las restricciones a la hora de hacer el seguimiento de las partículas en el medio. Por otro lado tenemos también el código ABRA, que se basa únicamente en consideraciones geométricas para determinar el volumen de la zona de solapamiento entre proyectil y blanco. A partir del número de nucleones abradidos y de su naturaleza, el código determina las características del prefragmento.

Estos tres códigos tienen algo en común, el resultado final es un prefragmento con unas características definidas: número atómico, número másico, energía de excitación y momento angular. Estos parámetros son los puntos de partida de los códigos que describen la segunda fase de la reacción: la desexcitación. Tal vez uno de los más utilizados sea el código ABLA, que se basa en el modelo estadístico propuesto por Weisskopf y que calcula la probabilidad de cada canal de desexcitación.

Uno de los objetivos de este trabajo consistirá en comparar las predicciones de estos códigos con los datos medidos experimentalmente, con el fin de mejorar el poder predictivo de los mismos.

## Método experimental

Los experimentos descritos en este trabajo fueron realizados acelerando proyectiles de  $^{124}\text{Xe}$  y  $^{136}\text{Xe}$  a diferentes energías y haciéndolos incidir sobre varios blancos diferentes. Los núcleos residuales salen del blanco a energías similares a las del proyectil incidentes, debido a la cinemática de la reacción. De este modo pueden ser analizados con la ayuda de un espectrómetro magnético, el cual nos permitirá

identificar de forma inequívoca sus números másico y atómico. Esta técnica, denominada *cinemática inversa*, constituye un gran avance respecto a otras técnicas más convencionales empleadas en el estudio de las colisiones de iones pesados. En la actualidad, este tipo de estudios únicamente pueden realizarse en el GSI, donde es posible acelerar núcleos de  $^{238}\text{U}$  hasta energías de 1 GeV/u gracias al sincrotrón SIS y analizar sus residuos con el separador de masas FRS. Este aparato es un espectrómetro magnético de 70 m de longitud (ver la figura 5.26) que permite obtener unas resoluciones en masa del orden de  $\Delta A/A \sim 10^{-3}$ .

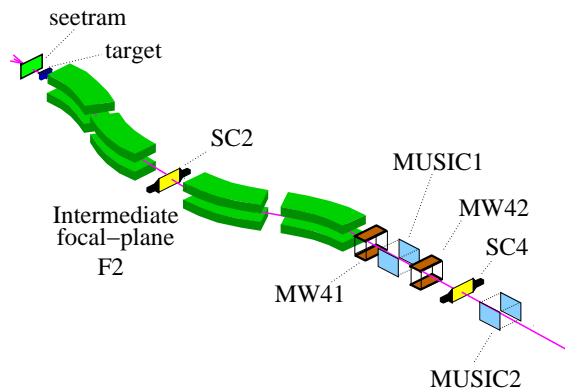


Figure 5.26: *Vista esquemática del separador de fragmentos FRS y el dispositivo experimental utilizado en este trabajo.*

El objetivo primordial de este trabajo es determinar las secciones eficaces de producción de los residuos del proyectil provenientes de la reacción con el blanco y, para ello, son tres las medidas independientes que hay que llevar a cabo: la tasa de producción de cada núcleo, la intensidad del haz incidente y el espesor del blanco de producción, siendo estos dos últimos necesarios para normalizar la primera de las cantidades. Para la monitorización del haz incidente se utilizó un detector que utiliza la emisión de partículas inducida por el flujo de partículas. Para la calibración del espesor de los blancos se utiliza la pérdida de energía del haz primario al atravesar los mismos, siendo la tarea más compleja de las tres la determinación de la tasa de producción de cada una de las especies isotópicas, que describiremos a continuación.

Cuando una partícula cargada atraviesa un campo magnético su trayectoria se curva, siendo esa curvatura descrita por la expresión:

$$B\rho = \frac{p}{Q} = \beta\gamma\frac{u}{c}\frac{A}{Q} \quad (5.26)$$

donde la cantidad  $B\rho$  se conoce como rigidez magnética,  $p$  es el momento de la partícula,  $Q$  su carga,  $\beta$  y  $\gamma$  son los factores relativistas,  $u$  la unidad de masa,  $c$  la velocidad de la luz y  $A$  la masa de la partícula. En nuestro dispositivo experimental

(ver figura 5.26) hacemos uso de varios detectores de posición para determinar la rigidez magnética de los residuos y su tiempo de vuelo, que nos da el factor  $\beta\gamma$ . De este modo podemos conocer el cociente  $A/Q$  de la partícula y, mediante cámaras de ionización, podemos determinar su carga  $Q$ , ya que ésta está relacionada con su pérdida de energía en un medio material. Con este dispositivo experimental podemos identificar en masa y carga, de forma unívoca, cualquier residuo que haya sido creado en la reacción con el blanco de producción.

El propósito inicial de este tipo de experimentos es determinar las secciones eficaces de producción con una gran precisión, siendo necesario para ello hacer un estudio detallado de todos los efectos que contribuyen a la contaminación de las tasas de producción. Estas correcciones afectan a los estados de carga iónicos de los residuos, que son seleccionados durante la identificación; las pérdidas por reacciones secundarias tanto en el propio blanco como en los materiales de todo el dispositivo experimental; las pérdidas debido a la transmisión del FRS y las pérdidas debido al tiempo muerto de los detectores. En este trabajo hemos determinado, con gran precisión, las secciones eficaces y momentos longitudinales de más de 1000 isótopos medidos en varias combinaciones proyectil-blanco-energía, constituyendo en sí mismos una colección importante de datos para el estudio de las reacciones de fragmentación a energías relativistas en la zona de masas intermedias de la carta de núcleos.

## Resultados y discusión

Debido a la cantidad de datos medidos y la diversidad de su procedencia, hemos sido capaces de efectuar análisis sistemáticos en los que se han puesto de manifiesto la influencia de varios factores como las naturalezas del blanco y proyectil o la propia energía de este último en las secciones eficaces de producción y las distribuciones de momento longitudinal. La figura 5.27 es un buen ejemplo de estos estudios sistemáticos, en ella podemos ver las secciones eficaces isotópicas de los residuos creados en la reacción de proyectiles de  $^{136}\text{Xe}$  a 1000 MeV/u con varios blancos.

Tal y como se observa en la figura, las secciones eficaces dependen claramente del tamaño del blanco. Este comportamiento es el esperado y debería ser explicado por la sección eficaz total de reacción, siendo así en el caso de los tres blancos pesados, pero no en el caso del hidrógeno. Este hecho pone de manifiesto que la física con el blanco de hidrógeno tiene un origen que no viene dado exclusivamente por la geometría. Las diferencias entre estos sistemas provienen de la fase de abrasión, en la cual las reacciones con el blanco de hidrógeno arrancan menos nucleones que con los blancos más pesados, concentrándose toda la producción en regiones más

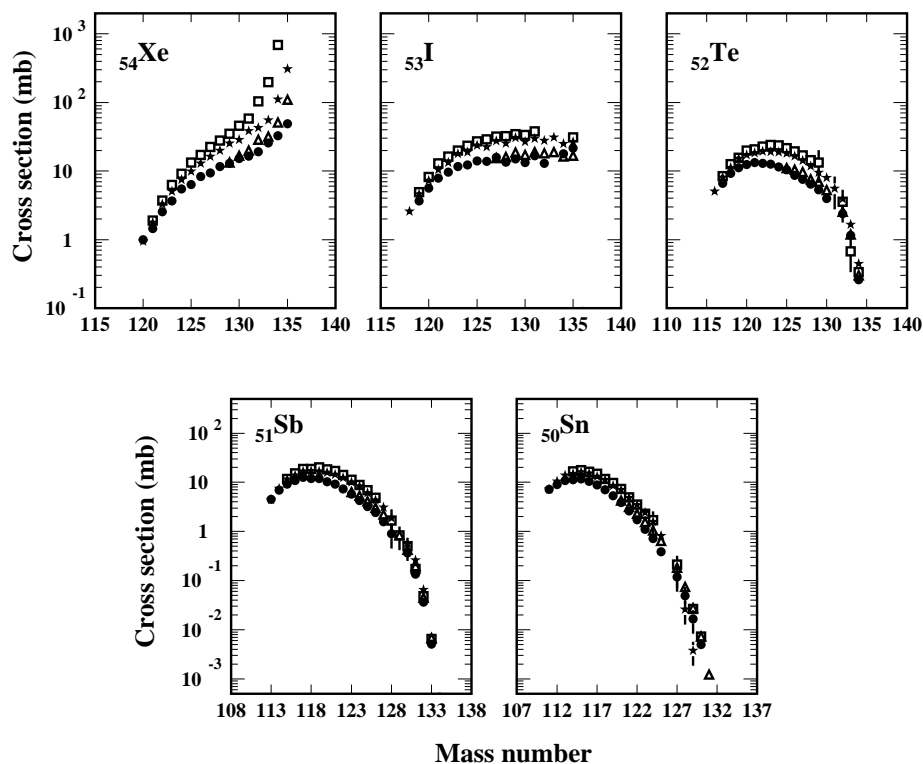


Figure 5.27: *Secciones eficaces isotópicas de los residuos producidos en las reacciones inducidas por proyectiles de  $^{136}\text{Xe}$  a 1000 MeV/u con varios blancos,  $^{208}\text{Pb}$  (cuadrados),  $^{48}\text{Ti}$  (estrellas),  $^9\text{Be}$  (triángulos) y  $^1\text{H}$  (círculos).*

cercanas al proyectil.

Hemos efectuado medidas con proyectiles de  $^{124}\text{Xe}$  y  $^{136}\text{Xe}$ , encontrando que la anchura de las distribuciones isotópicas depende de forma muy evidente del exceso de neutrones del proyectil, siendo más ancha cuanto mayor es ese exceso. Este hecho está relacionado con el concepto de *corredor de evaporación*, que establece que para colisiones muy energéticas de iones pesados, los prefragmentos siguen una cadena de evaporación hasta que las probabilidades de emisión de protones y neutrones son similares. La longitud de la cadena de evaporación depende de la distancia en masa del proyectil al corredor de evaporación, tal y como podemos ver en la figura 5.28 para proyectiles de  $^{124}\text{Xe}$ ,  $^{129}\text{Xe}$  y  $^{136}\text{Xe}$ .

En lo que concierne al papel de la energía del proyectil incidente, tenemos que comentar que esperamos que las secciones eficaces no presenten dependencia alguna

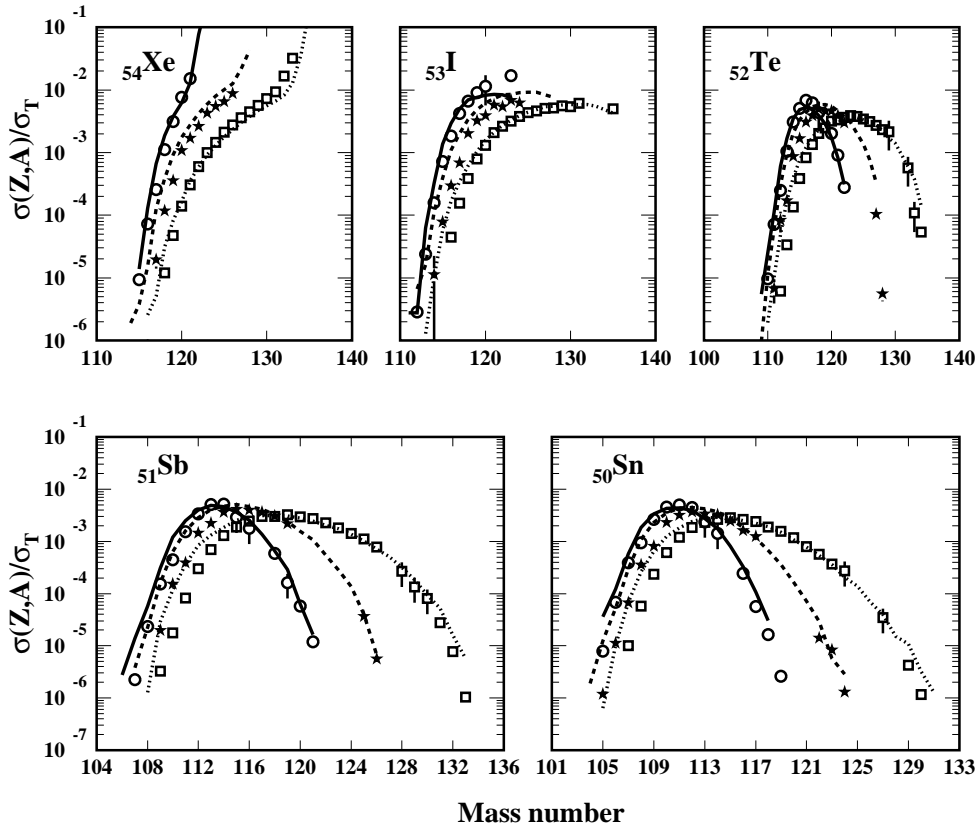


Figure 5.28: *Secciones eficaces isotópicas medidas en las reacciones de proyectiles de  $^{124}\text{Xe}$  a 1000 MeV/u con  $^{208}\text{Pb}$  (círculos), de  $^{129}\text{Xe}$  a 790 MeV/u con  $^{27}\text{Al}$  (estrellas) y de  $^{136}\text{Xe}$  a 1000 MeV/u con  $^{208}\text{Pb}$  (cuadrados). Los datos están normalizados a la sección eficaz total calculada con el código Karol. Las líneas que aparecen en la figura son las predicciones del código ABRABLA para cada uno de los sistemas.*

con la misma, tal y como establece el concepto de *limiting fragmentation*. Según este principio, la sección eficaz de producción de un fragmento determinado se aproximaría a un límite en el cual no dependiera de la energía del proyectil incidente, a partir de una energía lo suficientemente alta. En nuestro trabajo hemos analizado colisiones relativistas a energías de 200, 500 y 1000 MeV/u, constatando la validez de esta hipótesis hasta 200 MeV/u.

Únicamente para residuos próximos al proyectil no se cumple la hipótesis de *limiting fragmentation*, pero este hecho proviene de una física completamente diferente al proceso de fragmentación. Hemos entendido y aislado el origen de la discrepancia de los datos con respecto a la hipótesis de limiting fragmentation, y la causa recae en

las reacciones de intercambio de carga, que serán tratadas en detalle más adelante. El código ABRABLA, que no reproducía las secciones eficaces de los residuos con carga  $Z=54$  (especialmente a bajas energías), fue modificado y se le incorporó la física de las reacciones de intercambio de carga. De este modo sus poder predictivo mejoró de forma notable, tal y como puede apreciarse en la figura 5.29.

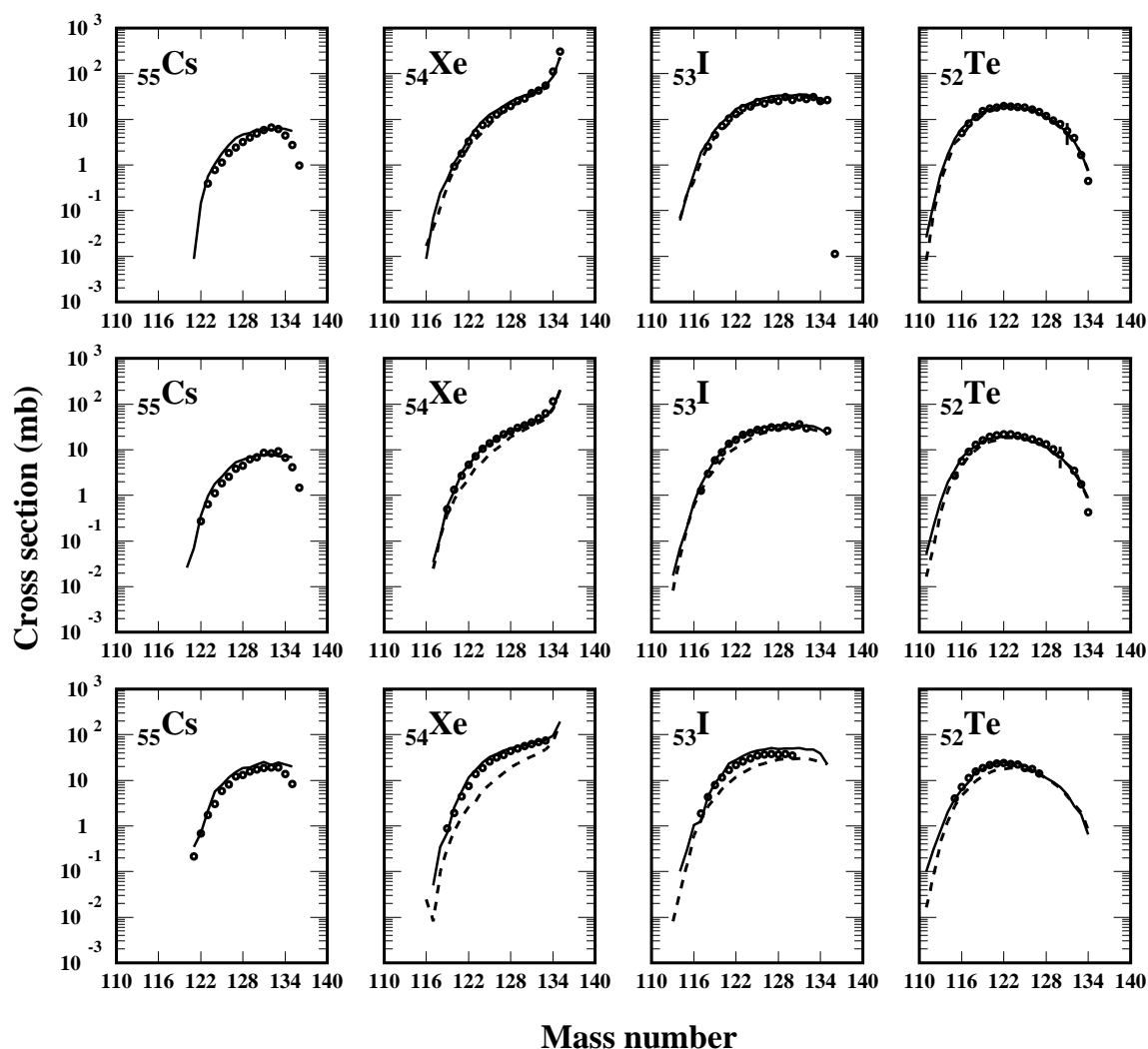


Figure 5.29: Secciones eficaces isotópicas medidas en las reacciones  $^{136}\text{Xe} + ^{48}\text{Ti}$  a  $1000\text{ MeV/u}$  (fila superior),  $500\text{ MeV/u}$  (fila intermedia) y  $200\text{ MeV/u}$  (fila inferior). Los datos están comparados con las predicciones del código ABRABLA original (líneas discontinuas) y después de incorporarle las reacciones de intercambio de carga (línea continua).

En este trabajo hemos desarrollado también estudios sistemáticos acerca de las

distribuciones de momento longitudinal de los residuos originados en las distintas reacciones. Dos son los observables a tener en cuenta en este tipo de estudios, el valor medio y la anchura de dichas distribuciones. En cuanto al primero, cabe mencionar que existe una recopilación de datos empíricos realizada por Morrisey en la que se observa un comportamiento sistemático para estos valores medios. Éstos siguen una dependencia lineal con la diferencia de masas entre proyectil y fragmento, cuya constante de proporcionalidad fue establecida en 8 unidades. Nosotros hemos demostrado que esa proporcionalidad constituye en realidad un límite asintótico para cargas lejos del proyectil y que, además, la constante de proporcionalidad depende de la carga de los residuos, tal y como podemos observar en la figura 5.30. Este comportamiento de los datos experimentales ya había sido observado con anterioridad, pero no pudo ser explicado, sin embargo creemos que es también debido a la influencia de las reacciones de intercambio de carga.

No hemos encontrado en nuestros datos ningún tipo de dependencia de los momentos longitudinales con la naturaleza del blanco, el exceso de neutrones del proyectil o su energía incidente. Sin embargo, hemos observado un efecto interesante en los residuos correspondientes a la carga  $Z=55$ , es decir, los núcleos que provienen de las reacciones de intercambio de carga. Existe un offset en el valor medio de las distribuciones de momento, teniendo unos valores más negativos de los que deberían (ver figura 5.30), debido a la excitación de la resonancia  $\Delta(1232)$ . Se necesita una energía de aproximadamente unos 300 MeV para crear dicha resonancia, y esa pérdida de energía debería observarse en la velocidad del residuo final. La probabilidad de excitación de la resonancia  $\Delta$  disminuye con la energía, por tanto a 200 MeV/u el offset debería ser menor que a 1000 MeV/u, tal y como observamos en nuestros datos.

El otro de los observables que hemos mencionado lo constituyen las anchuras de las distribuciones de momento. En este caso, existen dos modelos que describen el comportamiento de estos valores, uno desarrollado por Morrisey y otro por Goldhaber. El primero responde a una sistemática empírica observada en muchos datos experimentales, mientras que el segundo procede de consideraciones teóricas. Ambos modelos predicen un comportamiento parabólico con la diferencia de masas entre proyectil y fragmento, y la diferencia entre ellos recae en que Goldhaber no considera el proceso de evaporación en sus desarrollos. Nuestros datos experimentales se ajustan perfectamente al modelo de Morrisey, siendo nuestras medidas consistentes con experimentos previos. No hemos encontrado ninguna dependencia en nuestros datos con la naturaleza del blanco, del proyectil o la energía de este último. Este efecto era esperable ya que la anchura de las distribuciones de momento viene determinada por el número de nucleones evaporados, siendo éste independiente del canal de entrada.

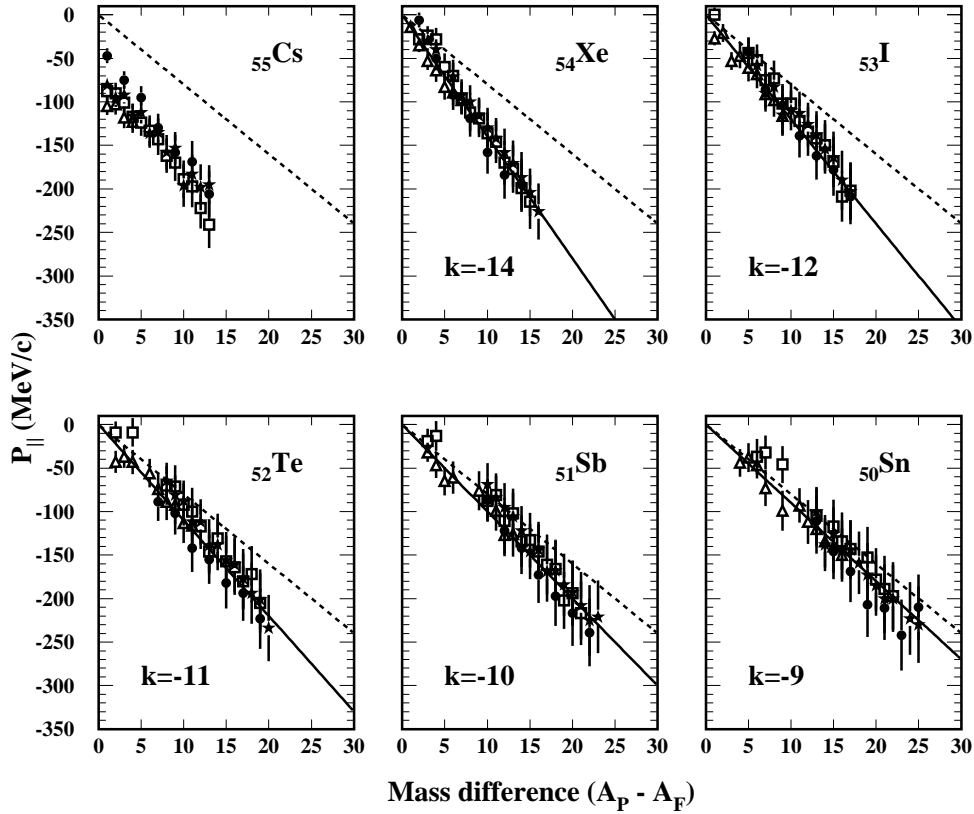


Figure 5.30: Valores medios de las distribuciones de momento longitudinal para los residuos creados en las reacciones de proyectiles de  $^{136}\text{Xe}$  a 1000 MeV/u con varios blancos; hidrógeno (cálculos), berilio (triángulos), titanio (estrellas) y plomo (cuadrados). Los datos están comparados con la sistemática postulada por Morrisey (líneas de trazos) y con distintas constantes de proporcionalidad dependiendo de la carga de los residuos  $p = k \cdot \Delta A$  (líneas continuas).

## Reacciones de intercambio de carga

La técnica experimental descrita en este trabajo ha permitido no sólo investigar las reacciones de fragmentación, sino también aquellas reacciones conocidas como de *intercambio de carga*. Existen dos mecanismos responsables de este tipo de reacciones, uno cuasielástico (excitaciones Gamow-Teller) y uno resonante a través de la excitación de la resonancia  $\Delta$ -1232. Ambos procesos están mediados por el intercambio de piones virtuales entre el proyectil y el blanco. Este tipo de reacciones son muy periféricas y pueden, por tanto, proporcionarnos algún tipo de información

sobre la distribución de protones y neutrones en la periferia del núcleo.

A pesar del interés de este tipo de reacciones, casi todos los esfuerzos dedicados a su estudio han dado lugar a datos sobre la sección eficaz total. La medida de secciones eficaces isotópicas es un éxito en sí mismo, y en este trabajo hemos determinado las cadenas isotópicas completas no sólo del intercambio de carga simple, sino también del doble para varias combinaciones tanto del blanco como de la energía. Estas medidas nos van a permitir estudiar sistemáticamente los parámetros más relevantes que influyen en este tipo de reacciones, así como explorar la precisión de los códigos en la descripción de estos procesos.

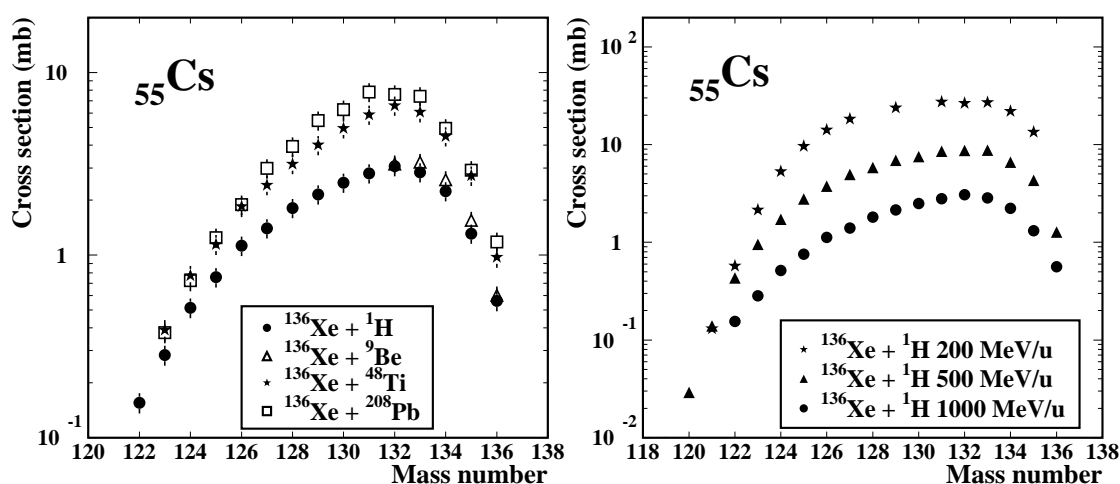


Figure 5.31: (Izquierda) Distribución isotópica de las secciones eficaces de producción de los residuos medidos en la reacción de proyectiles de  $^{136}\text{Xe}$  a 1000 MeV/u con diferentes blancos. (Derecha) Distribuciones isotópicas medidas en la reacción  $^{136}\text{Xe} + \text{H}$  a 200, 500 y 1000 MeV/u.

Algunos ejemplos de la influencia de la naturaleza del blanco, así como de la energía del proyectil en las secciones eficaces de producción se muestran en la figura 5.31. Podemos ver en el panel de la izquierda cómo las secciones eficaces isotópicas dependen del tamaño del blanco. En el panel de la derecha de la figura 5.31 vemos cómo la probabilidad de un intercambio de carga crece al disminuir la energía del proyectil. Este efecto se debe a la dependencia de la sección eficaz del proceso cuasielástico con la energía. Su probabilidad crece al disminuir la energía de forma que domina la producción de residuos de intercambio de carga del modo observado en la figura. Estos resultados han sido comparados con varios datos medidos en experimentos previos, siendo los resultados compatibles.

Hemos mencionado anteriormente que la mayoría de los estudios sobre reacciones de intercambio de carga arrojaron resultados que proporcionaban información únicamente sobre la sección eficaz total del proceso. Uno de los trabajos más rele-

vantes en este campo fue el de Guoxiao, que postuló una expresión empírica para la sección eficaz total del proceso de intercambio de carga dada por:

$$\sigma_{TOT} = 1.7 \times 10^{-4} \cdot (A_p^{1/3} + A_t^{1/3}) \cdot A_p^2 \quad (5.27)$$

Como vemos, esta expresión es totalmente independiente de la energía y, por tanto, incompleta. Además, la expresión de Guoxiao no tiene en cuenta el exceso de neutrones del proyectil, factor de vital importancia, como veremos a continuación. En el panel izquierdo de la figura 5.32 podemos ver las secciones eficaces totales en función del cociente N/Z del proyectil para cuatro combinaciones diferentes proyectil-blanco (dos de ellas medidas en este trabajo) y las predicciones de la expresión de Guoxiao para cada sistema.

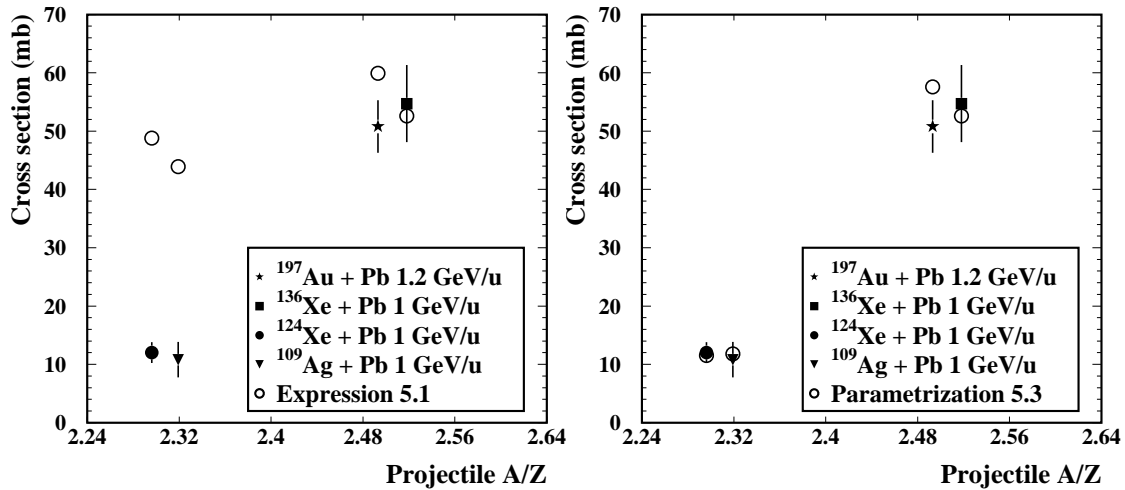


Figure 5.32: (Izquierda) Sección eficaz total de intercambio de carga en función del cociente N/Z del proyectil. Los datos experimentales están comparados con la fórmula empírica de Guoxiao (círculos abiertos). (Derecha) Mismos datos comparados con la expresión de Guoxiao corregida para tener en cuenta la distancia (en número de neutrones) del proyectil al corredor de evaporación (ver texto para los detalles)

La primera conclusión extraíble de la gráfica 5.32 es que la sección eficaz total es sensible al N/Z del proyectil, y no únicamente a su masa tal y como predice la sistemática de Guoxiao. Proyectiles como el  $^{136}\text{Xe}$  y el  $^{197}\text{Au}$ , que distan más de 60 masas poseen secciones eficaces similares, mientras que el  $^{124}\text{Xe}$  que dista apenas 12 masas del  $^{136}\text{Xe}$  posee una sección eficaz un factor 4 por debajo de aquél. En este trabajo hemos demostrado que, en realidad, la sección eficaz total está dominada por la distancia (en número de neutrones) del proyectil al corredor de evaporación. Modificando la parametrización de Guoxiao para que tenga en cuenta este factor, además de la energía del proyectil, obtuvimos esta expresión:

$$\sigma_{TOT} = \kappa(E) \cdot (N_P - N_\Gamma) \cdot (A_p^{1/3} + A_t^{1/3}) \cdot A_p^{2/3} \quad (5.28)$$

donde  $(N_P - N_\Gamma)$  es la distancia en número de neutrones del proyectil al corredor de evaporación y  $\kappa(E)$  es un factor que tiene en cuenta la energía del proyectil. Las predicciones de esta expresión reproducen los datos experimentales con gran precisión, como podemos ver en el panel derecho de la figura 5.32. También hemos conseguido parametrizar la dependencia del factor  $\kappa(E)$  con la energía, siendo:

$$\kappa(E) = 5.05 \cdot \exp^{-6.84 \cdot 10^{-3} \cdot E} + 0.153 \quad (mb) \quad (5.29)$$

Nuestra nueva expresión para la sección eficaz total de intercambio de carga describe también los datos para el intercambio de carga doble, simplemente escalando el factor  $\kappa(E)$ , que en este caso es un factor 100 más pequeño que en el caso del intercambio de carga simple.

## Reacciones de intercambio de carga isóbaras: radios r.m.s.

Los dos procesos que pueden conducir a una reacción de intercambio de carga (cuasielástico y resonante) tienen una dinámica completamente diferente. En un caso, el residuo apenas pierde velocidad, mientras que en el caso resonante los aproximadamente 300 MeV necesarios para excitar la resonancia  $\Delta$  se traducen en una pérdida de velocidad del residuo. Desafortunadamente, la evaporación de neutrones ensancha la distribución de velocidad, estropeando la resolución de nuestras medidas. De este modo, únicamente somos capaces de separar el proceso cuasielástico del resonante para aquellos residuos en los que no se produzca pérdida alguna de masa. Hemos denominado a este canal de reacción tan restrictivo **intercambio de carga isóbaro**.

Basándonos en estas reacciones tan específicas, hemos propuesto un nuevo método para determinar el radio de la distribución de neutrones en la periferia del núcleo. El método se basa en determinar el cociente de las reacciones (n,p)/(p,n) resonantes y de este modo estimar cuál es la probabilidad de colisionar con un neutrón o un protón de la periferia nuclear. Posteriormente, estas tasas de reacción deben ser reproducidas por un código basado en el modelo de Glauber, en el cual el radio de neutrones es el parámetro a determinar.

Por tanto es de vital importancia poder aislar el canal resonante en el espectro de velocidades de los residuos. Estas distribuciones de velocidad están afectadas por varios aspectos, como son la emitancia del haz, la resolución en posición de los detectores, la dispersión en energía en el blanco y lo que se conoce como *location straggling*, que viene determinado por espesor del blanco. Los tres primeros efectos siguen una distribución gaussiana, mientras que el último sigue una distribución cuadrada. Podemos, por tanto, construir una función respuesta que será la convolución de todos estos factores y posteriormente desconvolucionarla con el espectro medido de las velocidades. El resultado debe ser la distribución de velocidad debida únicamente a la física de la reacción, no contaminada por ningún efecto espurio. Un ejemplo del proceso de desconvolución puede verse en la figura, donde se muestran las dos distribuciones gaussianas (correspondientes al canal cuasielástico y al resonante) que subyacen bajo el espectro medido de velocidades (representado por el histograma en la figura).

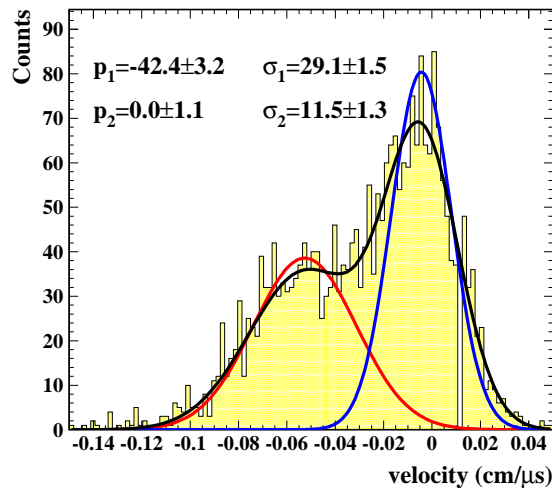


Figure 5.33: *Espectro de velocidad longitudinal para el residuo  $^{136}\text{Cs}$  creado en la reacción  $^{136}\text{Xe} + \text{H}$  at 500 MeV/u. Las dos gaussianas representadas en la figura corresponden a las distribuciones de velocidad de los canales cuasielástico y resonante.*

De este modo podemos determinar la sección eficaz del canal resonante, tanto en las reacciones (n,p) como en las (p,n), y por tanto la probabilidad de colisión con los neutrones o los protones en la periferia del núcleo. A modo de ejemplo, en el caso de la reacción  $^{136}\text{Xe} + \text{H}$  at 500 MeV/u, hemos determinado experimentalmente que estas probabilidades son 95.1 % en el caso de colisión con un neutrón y 4.9 % en el caso de colisión con un protón. Estos resultados dejan entrever, de forma muy clara, que el núcleo de  $^{136}\text{Xe}$  está poblado en su periferia mayormente por neutrones, es decir, posee lo que conocemos como **piel de neutrones**.

Con el propósito de cuantificar este efecto, nos hemos propuesto determinar cuál

es el radio de neutrones que, en el marco del modelo de Glauber, reproduce nuestros resultados experimentales. Para ello hemos parametrizado el núcleo de  $^{136}\text{Xe}$  mediante dos distribuciones de materia independientes para protones y neutrones, calculadas con un potencial tipo Skyrme y de acuerdo al método de Hartree-Fock-Bogoliubov (HFB). El modelo de Glauber establece cuáles son las probabilidades de excitar la resonancia  $\Delta$ , dependiendo de si la colisión tuvo lugar con un protón o un neutrón. Estas probabilidades dependen de las secciones eficaces nucleón-nucleón inelásticas, así como de integrales de las distribuciones de materia (funciones espesor). Además de esto, en el decaimiento posterior de la resonancia  $\Delta$  se emite un pión, que debe necesariamente abandonar el núcleo. Si esto no sucediera, la energía cinética del pión excitaría el residuo de tal modo que evaporaría alguna partícula en su desexcitación. En este caso no estaríamos ante una reacción de intercambio de carga fría e isóbara, quedando el residuo fuera de nuestro rango de estudio, al no poder separar el canal resonante del cuasielástico.

En el panel izquierdo de la figura 5.34 vemos representadas las integrales de la densidad de materia para protones y neutrones, así como la probabilidad de sufrir una única colisión inelástica con un neutrón ( $P_n(b)$ ) o un protón ( $P_p(b)$ ). En el panel derecho mostramos las mismas probabilidades, pero introduciendo en nuestro código basado en el modelo de Glauber la condición de que el pión debe escapar después del decaimiento de la resonancia  $\Delta$ . Como podemos observar, esta última condición disminuye considerablemente la probabilidad de efectuar una reacción de intercambio de carga con un protón del  $^{136}\text{Xe}$ .

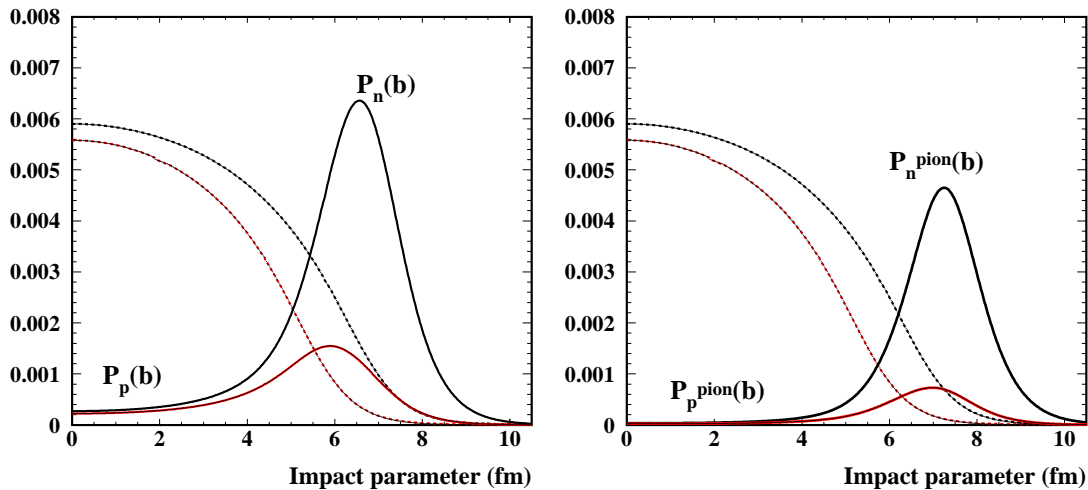


Figure 5.34: (Izquierda) Funciones espesor para la distribución de protones y neutrones (líneas discontinuas). La probabilidad de una colisión única con un neutrón ( $P_n(b)$ ) o un protón ( $P_p(b)$ ) se muestra también en la figura. (Derecha) Mismas funciones que la gráfica de la izquierda, pero teniendo en cuenta que el pión debe escapar del núcleo.

Con todos los factores descritos incluidos en nuestro código, obtenemos un valor para el radio de neutrones de  $5.5 \pm 0.2$  fm, un 14 % superior al radio de protones, que ha sido fijado a 4.80 fm mediante experimentos de dispersión Coulombiana. El radio de neutrones obtenido mediante nuestros cálculos es ligeramente superior al que predicen otros métodos como el HFB. Sin embargo, al ser las reacciones de intercambio de carga procesos muy periféricos, el *smoothness* de la densidad nuclear tiene que jugar un papel muy importante en la descripción de nuestros resultados. Hemos encontrado que, incrementando el valor del *smoothness* en un 10 % (de 0.54 a 0.59 fm), el valor del radio r.m.s. de neutrones obtenido es perfectamente compatible con el predicho por los métodos HFB. Además el espesor de la piel de neutrones estimada a partir de nuestros datos se corresponde con la estudiada en otros trabajos experimentales dedicados a otros isótopos estables de la carta de núcleos. Otro de los resultados relevantes de nuestro trabajo es que hemos establecido que las reacciones de intercambio de carga son sensibles a una región de la densidad nuclear muy cercana al radio nuclear a la mitad de la densidad, y no a la estratosfera nuclear como sucede con otros métodos.

Concluimos, por tanto, que mediante las reacciones de intercambio de carga somos sensibles a la distribución de nucleones en la periferia del núcleo, y que ésta está poblada en gran medida por neutrones. Consideramos de gran importancia dedicar nuevos experimentos a determinar el porcentaje relativo de los canales resonantes (n,p)/(p,n), ya que este método permitiría estudiar los radios de neutrones y de materia para núcleos con vidas medias del orden de 300 ns y con un dispositivo experimental en funcionamiento. Es, por tanto, un método novedoso que puede ser aplicado a núcleos exóticos muy ricos en neutrones que no podrían ser medidos por otros métodos convencionales.

# Appendix A

## Layers of matter in the beam line

List of the layers of matter used in the experiments described in this work. These layers are placed in the beam line of the particles analyzed in this work, from the exit of the SIS synchrotron to the final focal area (S4).

The layers of matter are clasified depending on the projectile-target combination:

- (1)  $^{136}\text{Xe} + ^1\text{H}$  at 1000 MeV/u
- (2)  $^{136}\text{Xe} + ^9\text{Be}$  at 1000 MeV/u
- (3)  $^{136}\text{Xe} + ^{48}\text{Ti}$  at 1000 MeV/u
- (4)  $^{136}\text{Xe} + ^{208}\text{Pb}$  at 1000 MeV/u
- (5)  $^{136}\text{Xe} + ^1\text{H}$  at 500 MeV/u
- (6)  $^{136}\text{Xe} + ^2\text{H}$  at 500 MeV/u
- (7)  $^{136}\text{Xe} + ^{48}\text{Ti}$  at 500 MeV/u
- (8)  $^{136}\text{Xe} + ^1\text{H}$  at 200 MeV/u
- (9)  $^{136}\text{Xe} + ^{48}\text{Ti}$  at 200 MeV/u
- (10)  $^{124}\text{Xe} + ^9\text{Be}$  at 1000 MeV/u
- (11)  $^{124}\text{Xe} + ^{208}\text{Pb}$  at 1000 MeV/u

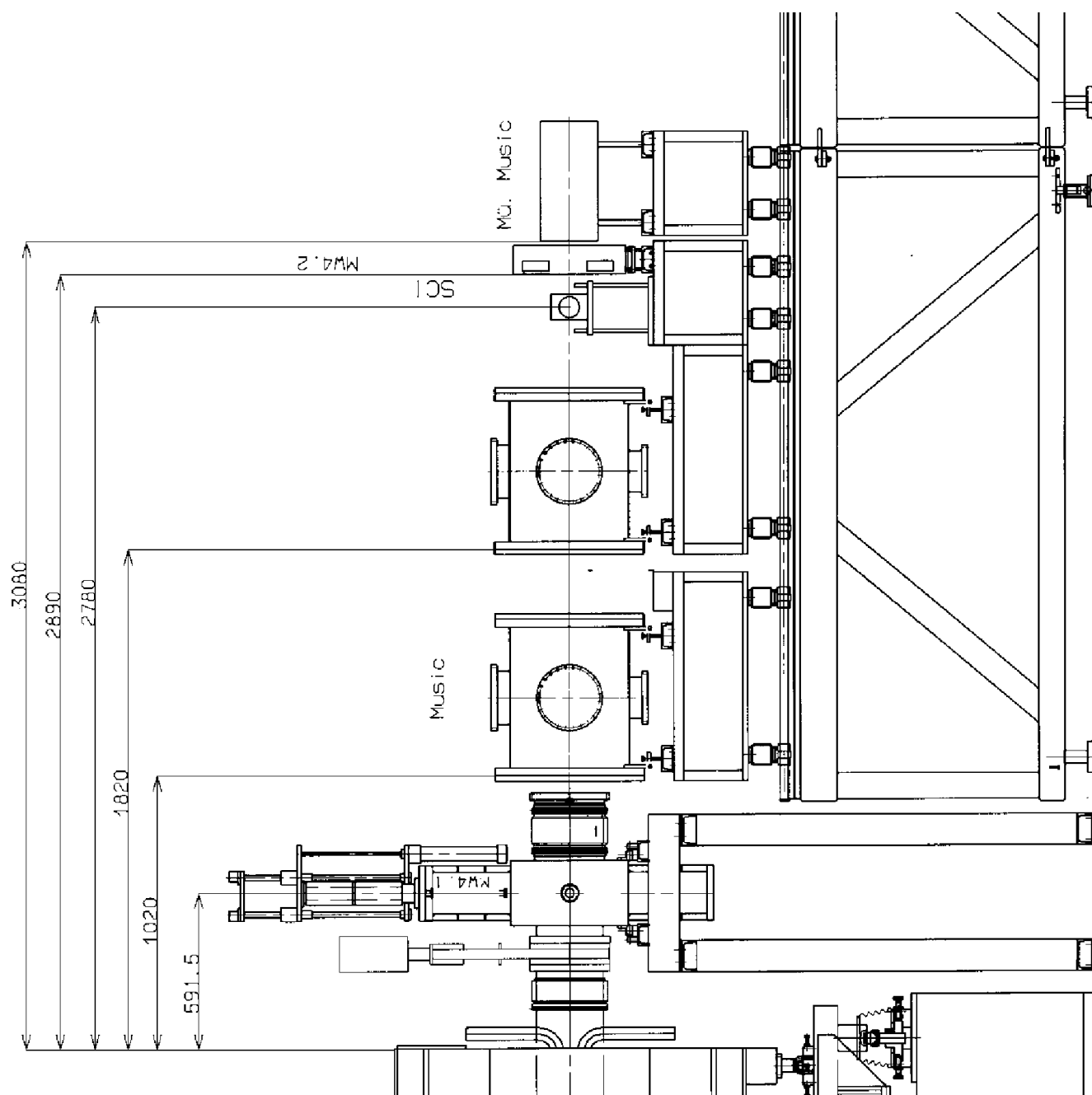


Figure A.1: Schematic view of the experimental setup placed at  $S_4$  for the measurements developed in this work at 200 MeV/u. The experimental setup at 1000 and 500 MeV/u is analogous, but removing the TU-Music.

Place	Material	Thickness ( $mg/cm^2$ )	Layer	System
S0	Ti	4.5	SIS window	All systems
	Ti	13.5	SEETRAM	All systems
Target	Ti	16.2	Dummy	(1),(3),(5),(6),(7),(8)
	H	87.3	Hydrogen	(1),(5),(8)
	D	201.0	Deuterium	(6)
	Ti	16.2	Dummy	(1),(3),(5),(6),(7),(8)
	Be	1023.0	Berillium (thin)	(2),(10)
	Be	2523.76	Berillium (thick)	(2)
	Pb	635.0	Lead	(1),(5),(8)
	Nb	221.0	Niobium (stripper)	(2),(10)
S2	H	44.02	Scintillator	(1)-(7),(10),(11)
	C	475.45	Scintillator	(1)-(7),(10),(11)
	H	4.40	Scintillator	(8),(9)
	C	47.55	Scintillator	(8),(9)
	Al	54.0	Stripper	(8),(9)
S4	Ti	5.0	Vacuum window	All Systems
	Ar	107.0	Music 1	All Systems
	O	4.25	Air gap	All Systems
	N	13.83	Air gap	All Systems
	Ar	107.0	Music 2	All Systems
	H	26.4	Scintillator	All systems
	C	285.3	Scintillator	All systems
	O	4.25	Air gap	(8),(9)
	N	13.83	Air gap	(8),(9)
	Ar	107.0	Music 3	(8),(9)

Table A.1: *List of layers of matter used in the experiments described in this work. See the text for details.*



# Appendix B

## Measured cross-sections

In this appendix we present the isotopic cross sections measured in this work:

- Table B.1: Reaction  $^{136}\text{Xe} + \text{H}$  at 1000 MeV/u.
- Table B.2: Reaction  $^{136}\text{Xe} + ^9\text{Be}$  at 1000 MeV/u.
- Table B.3: Reaction  $^{136}\text{Xe} + ^{48}\text{Ti}$  at 1000 MeV/u.
- Table B.4: Reaction  $^{136}\text{Xe} + ^{208}\text{Pb}$  at 1000 MeV/u.
- Table B.5: Reaction  $^{136}\text{Xe} + \text{H}$  at 500 MeV/u.
- Table B.6: Reaction  $^{136}\text{Xe} + \text{D}$  at 500 MeV/u.
- Table B.7: Reaction  $^{136}\text{Xe} + ^{48}\text{Ti}$  at 500 MeV/u.
- Tables B.8 and B.9: Reaction  $^{136}\text{Xe} + ^{48}\text{Ti}$  at 200 MeV/u.
- Table B.10: Reaction  $^{124}\text{Xe} + ^9\text{Be}$  at 1000 MeV/u.
- Table B.11: Reaction  $^{124}\text{Xe} + ^{208}\text{Be}$  at 1000 MeV/u.

nucleus	$\sigma$ (mb)	$\epsilon_\sigma$ (mb)	nucleus	$\sigma$ (mb)	$\epsilon_\sigma$ (mb)	nucleus	$\sigma$ (mb)	$\epsilon_\sigma$ (mb)
$^{124}_{56}\text{Ba}$	0.579E-02	0.147E-02	$^{134}_{54}\text{Xe}$	0.325E+02	0.390E+01	$^{115}_{51}\text{Sb}$	0.912E+01	0.110E+01
$^{125}_{56}\text{Ba}$	0.135E-01	0.278E-02	$^{135}_{54}\text{Xe}$	0.487E+02	0.584E+01	$^{116}_{51}\text{Sb}$	0.110E+02	0.132E+01
$^{126}_{56}\text{Ba}$	0.222E-01	0.369E-02	$^{119}_{53}\text{I}$	0.366E+01	0.441E+00	$^{117}_{51}\text{Sb}$	0.127E+02	0.152E+01
$^{127}_{56}\text{Ba}$	0.261E-01	0.434E-02	$^{120}_{53}\text{I}$	0.563E+01	0.677E+00	$^{118}_{51}\text{Sb}$	0.119E+02	0.143E+01
$^{128}_{56}\text{Ba}$	0.338E-01	0.524E-02	$^{121}_{53}\text{I}$	0.782E+01	0.940E+00	$^{119}_{51}\text{Sb}$	0.119E+02	0.143E+01
$^{129}_{56}\text{Ba}$	0.397E-01	0.594E-02	$^{122}_{53}\text{I}$	0.967E+01	0.116E+01	$^{120}_{51}\text{Sb}$	0.102E+02	0.123E+01
$^{130}_{56}\text{Ba}$	0.368E-01	0.563E-02	$^{123}_{53}\text{I}$	0.117E+02	0.140E+01	$^{121}_{51}\text{Sb}$	0.914E+01	0.110E+01
$^{131}_{56}\text{Ba}$	0.232E-01	0.392E-02	$^{124}_{53}\text{I}$	0.122E+02	0.147E+01	$^{122}_{51}\text{Sb}$	0.728E+01	0.874E+00
$^{132}_{56}\text{Ba}$	0.203E-01	0.334E-02	$^{125}_{53}\text{I}$	0.140E+02	0.169E+01	$^{123}_{51}\text{Sb}$	0.578E+01	0.695E+00
$^{133}_{56}\text{Ba}$	0.678E-02	0.154E-02	$^{126}_{53}\text{I}$	0.138E+02	0.165E+01	$^{124}_{51}\text{Sb}$	0.425E+01	0.511E+00
$^{122}_{55}\text{Cs}$	0.155E+00	0.198E-01	$^{127}_{53}\text{I}$	0.158E+02	0.189E+01	$^{125}_{51}\text{Sb}$	0.322E+01	0.387E+00
$^{123}_{55}\text{Cs}$	0.283E+00	0.355E-01	$^{128}_{53}\text{I}$	0.134E+02	0.161E+01	$^{126}_{51}\text{Sb}$	0.243E+01	0.292E+00
$^{124}_{55}\text{Cs}$	0.515E+00	0.634E-01	$^{129}_{53}\text{I}$	0.150E+02	0.180E+01	$^{127}_{51}\text{Sb}$	0.156E+01	0.188E+00
$^{125}_{55}\text{Cs}$	0.756E+00	0.922E-01	$^{130}_{53}\text{I}$	0.132E+02	0.159E+01	$^{128}_{51}\text{Sb}$	0.900E+00	0.450E+00
$^{126}_{55}\text{Cs}$	0.112E+01	0.137E+00	$^{131}_{53}\text{I}$	0.168E+02	0.201E+01	$^{130}_{51}\text{Sb}$	0.364E+00	0.438E-01
$^{127}_{55}\text{Cs}$	0.140E+01	0.170E+00	$^{132}_{53}\text{I}$	0.130E+02	0.156E+01	$^{131}_{51}\text{Sb}$	0.136E+00	0.165E-01
$^{128}_{55}\text{Cs}$	0.181E+01	0.219E+00	$^{134}_{53}\text{I}$	0.179E+02	0.215E+01	$^{132}_{51}\text{Sb}$	0.362E-01	0.435E-02
$^{129}_{55}\text{Cs}$	0.215E+01	0.259E+00	$^{135}_{53}\text{I}$	0.215E+02	0.259E+01	$^{133}_{51}\text{Sb}$	0.513E-02	0.618E-03
$^{130}_{55}\text{Cs}$	0.249E+01	0.300E+00	$^{136}_{53}\text{I}$	0.103E-01	0.129E-02	$^{111}_{50}\text{Sn}$	0.718E+01	0.863E+00
$^{131}_{55}\text{Cs}$	0.280E+01	0.337E+00	$^{117}_{52}\text{Te}$	0.659E+01	0.792E+00	$^{112}_{50}\text{Sn}$	0.899E+01	0.108E+01
$^{132}_{55}\text{Cs}$	0.307E+01	0.369E+00	$^{118}_{52}\text{Te}$	0.919E+01	0.110E+01	$^{113}_{50}\text{Sn}$	0.109E+02	0.131E+01
$^{133}_{55}\text{Cs}$	0.284E+01	0.342E+00	$^{119}_{52}\text{Te}$	0.111E+02	0.134E+01	$^{114}_{50}\text{Sn}$	0.114E+02	0.137E+01
$^{134}_{55}\text{Cs}$	0.223E+01	0.269E+00	$^{120}_{52}\text{Te}$	0.124E+02	0.148E+01	$^{115}_{50}\text{Sn}$	0.117E+02	0.141E+01
$^{135}_{55}\text{Cs}$	0.131E+01	0.158E+00	$^{121}_{52}\text{Te}$	0.133E+02	0.160E+01	$^{116}_{50}\text{Sn}$	0.104E+02	0.125E+01
$^{136}_{55}\text{Cs}$	0.561E+00	0.682E-01	$^{122}_{52}\text{Te}$	0.129E+02	0.155E+01	$^{117}_{50}\text{Sn}$	0.886E+01	0.107E+01
$^{120}_{54}\text{Xe}$	0.988E+00	0.120E+00	$^{123}_{52}\text{Te}$	0.126E+02	0.151E+01	$^{118}_{50}\text{Sn}$	0.711E+01	0.855E+00
$^{121}_{54}\text{Xe}$	0.144E+01	0.174E+00	$^{124}_{52}\text{Te}$	0.114E+02	0.137E+01	$^{119}_{50}\text{Sn}$	0.537E+01	0.645E+00
$^{122}_{54}\text{Xe}$	0.255E+01	0.308E+00	$^{125}_{52}\text{Te}$	0.105E+02	0.126E+01	$^{120}_{50}\text{Sn}$	0.391E+01	0.470E+00
$^{123}_{54}\text{Xe}$	0.366E+01	0.440E+00	$^{126}_{52}\text{Te}$	0.869E+01	0.104E+01	$^{121}_{50}\text{Sn}$	0.261E+01	0.313E+00
$^{124}_{54}\text{Xe}$	0.544E+01	0.654E+00	$^{127}_{52}\text{Te}$	0.756E+01	0.908E+00	$^{122}_{50}\text{Sn}$	0.174E+01	0.210E+00
$^{125}_{54}\text{Xe}$	0.631E+01	0.759E+00	$^{128}_{52}\text{Te}$	0.641E+01	0.770E+00	$^{123}_{50}\text{Sn}$	0.111E+01	0.134E+00
$^{126}_{54}\text{Xe}$	0.833E+01	0.100E+01	$^{129}_{52}\text{Te}$	0.531E+01	0.638E+00	$^{124}_{50}\text{Sn}$	0.720E+00	0.873E-01
$^{127}_{54}\text{Xe}$	0.940E+01	0.113E+01	$^{130}_{52}\text{Te}$	0.394E+01	0.474E+00	$^{125}_{50}\text{Sn}$	0.388E+00	0.473E-01
$^{128}_{54}\text{Xe}$	0.117E+02	0.140E+01	$^{132}_{52}\text{Te}$	0.239E+01	0.287E+00	$^{127}_{50}\text{Sn}$	0.119E+00	0.595E-01
$^{129}_{54}\text{Xe}$	0.130E+02	0.156E+01	$^{133}_{52}\text{Te}$	0.115E+01	0.139E+00	$^{128}_{50}\text{Sn}$	0.490E-01	0.246E-01
$^{130}_{54}\text{Xe}$	0.151E+02	0.182E+01	$^{134}_{52}\text{Te}$	0.261E+00	0.313E-01	$^{129}_{50}\text{Sn}$	0.167E-01	0.836E-02
$^{131}_{54}\text{Xe}$	0.164E+02	0.197E+01	$^{135}_{52}\text{Te}$	0.346E-03	0.423E-04	$^{130}_{50}\text{Sn}$	0.499E-02	0.610E-03
$^{132}_{54}\text{Xe}$	0.192E+02	0.230E+01	$^{113}_{51}\text{Sb}$	0.452E+01	0.543E+00	$^0_{51}\text{Sb}$	0.000E+00	0.000E+00
$^{133}_{54}\text{Xe}$	0.258E+02	0.310E+01	$^{114}_{51}\text{Sb}$	0.694E+01	0.834E+00	$^0_{51}\text{Sb}$	0.000E+00	0.000E+00

Table B.1: Isotopic cross sections measured in the reaction  $^{136}\text{Xe} + ^1\text{H}$  at 1000 MeV/u.

nucleus	$\sigma$ (mb)	$\epsilon_\sigma$ (mb)	nucleus	$\sigma$ (mb)	$\epsilon_\sigma$ (mb)	nucleus	$\sigma$ (mb)	$\epsilon_\sigma$ (mb)
<sup>132</sup> <sub>55</sub> Cs	0.316E+01	0.352E+00	<sup>125</sup> <sub>51</sub> Sb	0.410E+01	0.456E+00	<sup>115</sup> <sub>48</sub> Cd	0.178E+01	0.201E+00
<sup>133</sup> <sub>55</sub> Cs	0.322E+01	0.360E+00	<sup>126</sup> <sub>51</sub> Sb	0.302E+01	0.337E+00	<sup>116</sup> <sub>48</sub> Cd	0.118E+01	0.135E+00
<sup>134</sup> <sub>55</sub> Cs	0.259E+01	0.289E+00	<sup>127</sup> <sub>51</sub> Sb	0.222E+01	0.252E+00	<sup>117</sup> <sub>48</sub> Cd	0.835E+00	0.974E-01
<sup>135</sup> <sub>55</sub> Cs	0.155E+01	0.175E+00	<sup>129</sup> <sub>51</sub> Sb	0.840E+00	0.937E-01	<sup>118</sup> <sub>48</sub> Cd	0.440E+00	0.535E-01
<sup>136</sup> <sub>55</sub> Cs	0.603E+00	0.703E-01	<sup>130</sup> <sub>51</sub> Sb	0.422E+00	0.476E-01	<sup>119</sup> <sub>48</sub> Cd	0.291E+00	0.361E-01
<sup>129</sup> <sub>54</sub> Xe	0.133E+02	0.147E+01	<sup>131</sup> <sub>51</sub> Sb	0.195E+00	0.215E-01	<sup>121</sup> <sub>48</sub> Cd	0.803E-01	0.404E-01
<sup>130</sup> <sub>54</sub> Xe	0.167E+02	0.184E+01	<sup>132</sup> <sub>51</sub> Sb	0.449E-01	0.495E-02	<sup>123</sup> <sub>48</sub> Cd	0.129E-01	0.388E-02
<sup>131</sup> <sub>54</sub> Xe	0.199E+02	0.219E+01	<sup>133</sup> <sub>51</sub> Sb	0.669E-02	0.737E-03	<sup>124</sup> <sub>48</sub> Cd	0.488E-02	0.551E-03
<sup>132</sup> <sub>54</sub> Xe	0.288E+02	0.317E+01	<sup>134</sup> <sub>51</sub> Sb	0.309E-04	0.370E-05	<sup>125</sup> <sub>48</sub> Cd	0.136E-02	0.164E-03
<sup>133</sup> <sub>54</sub> Xe	0.317E+02	0.349E+01	<sup>120</sup> <sub>50</sub> Sn	0.423E+01	0.470E+00	<sup>126</sup> <sub>48</sub> Cd	0.378E-03	0.422E-04
<sup>134</sup> <sub>54</sub> Xe	0.510E+02	0.562E+01	<sup>121</sup> <sub>50</sub> Sn	0.317E+01	0.354E+00	<sup>127</sup> <sub>48</sub> Cd	0.830E-04	0.975E-05
<sup>135</sup> <sub>54</sub> Xe	0.110E+03	0.121E+02	<sup>122</sup> <sub>50</sub> Sn	0.228E+01	0.256E+00	<sup>128</sup> <sub>48</sub> Cd	0.206E-04	0.230E-05
<sup>127</sup> <sub>53</sub> I	0.155E+02	0.171E+01	<sup>123</sup> <sub>50</sub> Sn	0.156E+01	0.176E+00	<sup>129</sup> <sub>48</sub> Cd	0.257E-05	0.311E-06
<sup>128</sup> <sub>53</sub> I	0.159E+02	0.176E+01	<sup>124</sup> <sub>50</sub> Sn	0.104E+01	0.126E+00	<sup>130</sup> <sub>48</sub> Cd	0.139E-06	0.303E-07
<sup>129</sup> <sub>53</sub> I	0.186E+02	0.205E+01	<sup>125</sup> <sub>50</sub> Sn	0.638E+00	0.780E-01	<sup>126</sup> <sub>47</sub> Ag	0.547E-05	0.632E-06
<sup>130</sup> <sub>53</sub> I	0.171E+02	0.189E+01	<sup>127</sup> <sub>50</sub> Sn	0.183E+00	0.213E-01	<sup>127</sup> <sub>47</sub> Ag	0.819E-06	0.116E-06
<sup>131</sup> <sub>53</sub> I	0.189E+02	0.209E+01	<sup>128</sup> <sub>50</sub> Sn	0.745E-01	0.916E-02	<sup>128</sup> <sub>47</sub> Ag	0.677E-07	0.217E-07
<sup>132</sup> <sub>53</sub> I	0.181E+02	0.201E+01	<sup>129</sup> <sub>50</sub> Sn	0.276E-01	0.304E-02	<sup>123</sup> <sub>46</sub> Pd	0.624E-05	0.717E-06
<sup>133</sup> <sub>53</sub> I	0.188E+02	0.208E+01	<sup>130</sup> <sub>50</sub> Sn	0.729E-02	0.816E-03	<sup>124</sup> <sub>46</sub> Pd	0.134E-05	0.177E-06
<sup>134</sup> <sub>53</sub> I	0.163E+02	0.180E+01	<sup>131</sup> <sub>50</sub> Sn	0.122E-02	0.135E-03	<sup>125</sup> <sub>46</sub> Pd	0.938E-07	0.271E-07
<sup>135</sup> <sub>53</sub> I	0.168E+02	0.184E+01	<sup>132</sup> <sub>50</sub> Sn	0.119E-03	0.132E-04	<sup>120</sup> <sub>45</sub> Rh	0.536E-05	0.619E-06
<sup>136</sup> <sub>53</sub> I	0.362E-01	0.399E-02	<sup>119</sup> <sub>49</sub> In	0.224E+01	0.251E+00	<sup>121</sup> <sub>45</sub> Rh	0.149E-05	0.191E-06
<sup>125</sup> <sub>52</sub> Te	0.109E+02	0.121E+01	<sup>120</sup> <sub>49</sub> In	0.158E+01	0.179E+00	<sup>122</sup> <sub>45</sub> Rh	0.205E-06	0.469E-07
<sup>126</sup> <sub>52</sub> Te	0.105E+02	0.116E+01	<sup>121</sup> <sub>49</sub> In	0.103E+01	0.119E+00	<sup>118</sup> <sub>44</sub> Ru	0.142E-05	0.185E-06
<sup>127</sup> <sub>52</sub> Te	0.960E+01	0.106E+01	<sup>122</sup> <sub>49</sub> In	0.627E+00	0.737E-01	<sup>119</sup> <sub>44</sub> Ru	0.272E-06	0.524E-07
<sup>128</sup> <sub>52</sub> Te	0.754E+01	0.834E+00	<sup>124</sup> <sub>49</sub> In	0.378E+00	0.499E-01	<sup>115</sup> <sub>43</sub> Tc	0.343E-05	0.445E-06
<sup>129</sup> <sub>52</sub> Te	0.697E+01	0.779E+00	<sup>125</sup> <sub>49</sub> In	0.135E+00	0.678E-01	<sup>116</sup> <sub>43</sub> Tc	0.223E-06	0.460E-07
<sup>130</sup> <sub>52</sub> Te	0.524E+01	0.585E+00	<sup>126</sup> <sub>49</sub> In	0.580E-01	0.746E-02	<sup>117</sup> <sub>43</sub> Tc	0.528E-07	0.208E-07
<sup>132</sup> <sub>52</sub> Te	0.255E+01	0.282E+00	<sup>127</sup> <sub>49</sub> In	0.189E-01	0.568E-02	<sup>113</sup> <sub>42</sub> Mo	0.259E-06	0.513E-07
<sup>133</sup> <sub>52</sub> Te	0.118E+01	0.131E+00	<sup>128</sup> <sub>49</sub> In	0.649E-02	0.720E-03	<sup>110</sup> <sub>41</sub> Nb	0.251E-06	0.512E-07
<sup>134</sup> <sub>52</sub> Te	0.302E+00	0.332E-01	<sup>129</sup> <sub>49</sub> In	0.178E-02	0.197E-03	<sup>111</sup> <sub>41</sub> Nb	0.408E-07	0.173E-07
<sup>135</sup> <sub>52</sub> Te	0.271E-02	0.309E-03	<sup>130</sup> <sub>49</sub> In	0.365E-03	0.408E-04	<sup>108</sup> <sub>40</sub> Zr	0.605E-07	0.224E-07
<sup>123</sup> <sub>51</sub> Sb	0.625E+01	0.693E+00	<sup>131</sup> <sub>49</sub> In	0.535E-04	0.629E-05	<sup>0</sup> <sub>0</sub> In	0.000E+00	0.000E+00
<sup>124</sup> <sub>51</sub> Sb	0.531E+01	0.590E+00	<sup>131</sup> <sub>49</sub> In	0.675E-05	0.773E-06	<sup>0</sup> <sub>0</sub> In	0.000E+00	0.000E+00

Table B.2: Isotopic cross sections measured in the reaction <sup>136</sup>Xe + <sup>9</sup>Be at 1000 MeV/u.

nucleus	$\sigma$ (mb)	$\epsilon_\sigma$ (mb)	nucleus	$\sigma$ (mb)	$\epsilonpsilon_\sigma$ (mb)	nucleus	$\sigma$ (mb)	$\epsilon_\sigma$ (mb)
$^{125}_{56}Ba$	0.301E-01	0.714E-02	$^{135}_{54}Xe$	0.309E+03	0.371E+02	$^{134}_{52}Te$	0.444E+00	0.540E-01
$^{126}_{56}Ba$	0.461E-01	0.799E-02	$^{118}_{53}I$	0.256E+01	0.313E+00	$^{113}_{51}Sb$	0.441E+01	0.536E+00
$^{127}_{56}Ba$	0.535E-01	0.891E-02	$^{119}_{53}I$	0.457E+01	0.554E+00	$^{114}_{51}Sb$	0.750E+01	0.905E+00
$^{128}_{56}Ba$	0.801E-01	0.124E-01	$^{120}_{53}I$	0.723E+01	0.874E+00	$^{115}_{51}Sb$	0.114E+02	0.138E+01
$^{129}_{56}Ba$	0.669E-01	0.100E-01	$^{121}_{53}I$	0.104E+02	0.126E+01	$^{116}_{51}Sb$	0.138E+02	0.166E+01
$^{130}_{56}Ba$	0.690E-01	0.106E-01	$^{122}_{53}I$	0.132E+02	0.159E+01	$^{117}_{51}Sb$	0.166E+02	0.200E+01
$^{131}_{56}Ba$	0.598E-01	0.101E-01	$^{123}_{53}I$	0.178E+02	0.214E+01	$^{118}_{51}Sb$	0.171E+02	0.206E+01
$^{132}_{56}Ba$	0.376E-01	0.618E-02	$^{124}_{53}I$	0.189E+02	0.227E+01	$^{119}_{51}Sb$	0.168E+02	0.201E+01
$^{133}_{56}Ba$	0.123E-01	0.280E-02	$^{125}_{53}I$	0.237E+02	0.285E+01	$^{120}_{51}Sb$	0.159E+02	0.191E+01
$^{123}_{55}Cs$	0.389E+00	0.519E-01	$^{126}_{53}I$	0.224E+02	0.269E+01	$^{121}_{51}Sb$	0.143E+02	0.173E+01
$^{124}_{55}Cs$	0.773E+00	0.101E+00	$^{127}_{53}I$	0.275E+02	0.331E+01	$^{122}_{51}Sb$	0.124E+02	0.149E+01
$^{125}_{55}Cs$	0.115E+01	0.145E+00	$^{128}_{53}I$	0.253E+02	0.304E+01	$^{123}_{51}Sb$	0.100E+02	0.121E+01
$^{126}_{55}Cs$	0.184E+01	0.229E+00	$^{129}_{53}I$	0.307E+02	0.369E+01	$^{124}_{51}Sb$	0.830E+01	0.100E+01
$^{127}_{55}Cs$	0.242E+01	0.294E+00	$^{130}_{53}I$	0.267E+02	0.321E+01	$^{125}_{51}Sb$	0.613E+01	0.740E+00
$^{128}_{55}Cs$	0.315E+01	0.382E+00	$^{131}_{53}I$	0.299E+02	0.360E+01	$^{126}_{51}Sb$	0.433E+01	0.527E+00
$^{129}_{55}Cs$	0.401E+01	0.485E+00	$^{132}_{53}I$	0.279E+02	0.336E+01	$^{127}_{51}Sb$	0.311E+01	0.381E+00
$^{130}_{55}Cs$	0.495E+01	0.598E+00	$^{133}_{53}I$	0.311E+02	0.374E+01	$^{128}_{51}Sb$	0.188E+01	0.939E+00
$^{131}_{55}Cs$	0.588E+01	0.709E+00	$^{134}_{53}I$	0.250E+02	0.300E+01	$^{130}_{51}Sb$	0.577E+00	0.705E-01
$^{132}_{55}Cs$	0.659E+01	0.795E+00	$^{135}_{53}I$	0.268E+02	0.322E+01	$^{131}_{51}Sb$	0.260E+00	0.325E-01
$^{133}_{55}Cs$	0.606E+01	0.732E+00	$^{136}_{53}I$	0.111E-01	0.165E-02	$^{132}_{51}Sb$	0.650E-01	0.857E-02
$^{134}_{55}Cs$	0.447E+01	0.541E+00	$^{116}_{52}Te$	0.507E+01	0.614E+00	$^{111}_{51}Sn$	0.715E+01	0.865E+00
$^{135}_{55}Cs$	0.273E+01	0.332E+00	$^{117}_{52}Te$	0.811E+01	0.979E+00	$^{112}_{50}Sn$	0.105E+02	0.127E+01
$^{136}_{55}Cs$	0.976E+00	0.124E+00	$^{118}_{52}Te$	0.112E+02	0.134E+01	$^{113}_{50}Sn$	0.139E+02	0.167E+01
$^{120}_{54}Xe$	0.937E+00	0.118E+00	$^{119}_{52}Te$	0.152E+02	0.183E+01	$^{114}_{50}Sn$	0.150E+02	0.181E+01
$^{121}_{54}Xe$	0.178E+01	0.218E+00	$^{120}_{52}Te$	0.172E+02	0.207E+01	$^{115}_{50}Sn$	0.162E+02	0.194E+01
$^{122}_{54}Xe$	0.331E+01	0.404E+00	$^{121}_{52}Te$	0.183E+02	0.220E+01	$^{116}_{50}Sn$	0.153E+02	0.184E+01
$^{123}_{54}Xe$	0.505E+01	0.613E+00	$^{122}_{52}Te$	0.194E+02	0.234E+01	$^{117}_{50}Sn$	0.131E+02	0.157E+01
$^{124}_{54}Xe$	0.744E+01	0.897E+00	$^{123}_{52}Te$	0.191E+02	0.229E+01	$^{118}_{50}Sn$	0.113E+02	0.136E+01
$^{125}_{54}Xe$	0.989E+01	0.119E+01	$^{124}_{52}Te$	0.188E+02	0.226E+01	$^{119}_{50}Sn$	0.858E+01	0.103E+01
$^{126}_{54}Xe$	0.129E+02	0.155E+01	$^{125}_{52}Te$	0.180E+02	0.216E+01	$^{120}_{50}Sn$	0.707E+01	0.854E+00
$^{127}_{54}Xe$	0.163E+02	0.196E+01	$^{126}_{52}Te$	0.165E+02	0.199E+01	$^{121}_{50}Sn$	0.485E+01	0.587E+00
$^{128}_{54}Xe$	0.198E+02	0.237E+01	$^{127}_{52}Te$	0.143E+02	0.172E+01	$^{122}_{50}Sn$	0.345E+01	0.419E+00
$^{129}_{54}Xe$	0.254E+02	0.305E+01	$^{128}_{52}Te$	0.118E+02	0.141E+01	$^{123}_{50}Sn$	0.241E+01	0.300E+00
$^{130}_{54}Xe$	0.287E+02	0.345E+01	$^{129}_{52}Te$	0.954E+01	0.115E+01	$^{124}_{50}Sn$	0.157E+01	0.196E+00
$^{131}_{54}Xe$	0.382E+02	0.458E+01	$^{130}_{52}Te$	0.797E+01	0.965E+00	$^{125}_{50}Sn$	0.817E+00	0.105E+00
$^{132}_{54}Xe$	0.429E+02	0.515E+01	$^{131}_{52}Te$	0.551E+01	0.276E+01	$^{127}_{50}Sn$	0.141E+00	0.707E-01
$^{133}_{54}Xe$	0.552E+02	0.663E+01	$^{132}_{52}Te$	0.389E+01	0.468E+00	$^{128}_{50}Sn$	0.258E-01	0.129E-01
$^{134}_{54}Xe$	0.110E+03	0.133E+02	$^{133}_{52}Te$	0.166E+01	0.200E+00	$^{129}_{50}Sn$	0.376E-02	0.190E-02

Table B.3: Isotopic cross sections measured in the reaction  $^{136}Xe + ^{48}Ti$  at 1000 MeV/u.

nucleus	$\sigma(\text{mb})$	$\epsilon_\sigma$ (mb)	nucleus	$\sigma(\text{mb})$	$\epsilon_\sigma$ (mb)	nucleus	$\sigma(\text{mb})$	$\epsilon_\sigma$ (mb)
$^{126}_{56}\text{Ba}$	0.647E-01	0.105E-01	$^{132}_{54}\text{Xe}$	0.104E+03	0.125E+02	$^{115}_{51}\text{Sb}$	0.118E+02	0.142E+01
$^{127}_{56}\text{Ba}$	0.728E-01	0.119E-01	$^{133}_{54}\text{Xe}$	0.199E+03	0.239E+02	$^{116}_{51}\text{Sb}$	0.152E+02	0.183E+01
$^{128}_{56}\text{Ba}$	0.119E+00	0.177E-01	$^{134}_{54}\text{Xe}$	0.692E+03	0.831E+02	$^{117}_{51}\text{Sb}$	0.187E+02	0.224E+01
$^{129}_{56}\text{Ba}$	0.110E+00	0.166E-01	$^{119}_{53}\text{I}$	0.492E+01	0.593E+00	$^{118}_{51}\text{Sb}$	0.189E+02	0.227E+01
$^{130}_{56}\text{Ba}$	0.905E-01	0.125E-01	$^{120}_{53}\text{I}$	0.816E+01	0.983E+00	$^{119}_{51}\text{Sb}$	0.202E+02	0.242E+01
$^{131}_{56}\text{Ba}$	0.772E-01	0.119E-01	$^{121}_{53}\text{I}$	0.129E+02	0.156E+01	$^{120}_{51}\text{Sb}$	0.183E+02	0.220E+01
$^{132}_{56}\text{Ba}$	0.422E-01	0.748E-02	$^{122}_{53}\text{I}$	0.163E+02	0.196E+01	$^{121}_{51}\text{Sb}$	0.171E+02	0.206E+01
$^{133}_{56}\text{Ba}$	0.237E-01	0.501E-02	$^{123}_{53}\text{I}$	0.199E+02	0.238E+01	$^{122}_{51}\text{Sb}$	0.141E+02	0.170E+01
$^{123}_{55}\text{Cs}$	0.376E+00	0.479E-01	$^{124}_{53}\text{I}$	0.235E+02	0.282E+01	$^{123}_{51}\text{Sb}$	0.112E+02	0.135E+01
$^{124}_{55}\text{Cs}$	0.725E+00	0.897E-01	$^{125}_{53}\text{I}$	0.270E+02	0.324E+01	$^{124}_{51}\text{Sb}$	0.881E+01	0.106E+01
$^{125}_{55}\text{Cs}$	0.124E+01	0.152E+00	$^{126}_{53}\text{I}$	0.290E+02	0.348E+01	$^{125}_{51}\text{Sb}$	0.688E+01	0.830E+00
$^{126}_{55}\text{Cs}$	0.189E+01	0.230E+00	$^{127}_{53}\text{I}$	0.318E+02	0.382E+01	$^{126}_{51}\text{Sb}$	0.484E+01	0.586E+00
$^{127}_{55}\text{Cs}$	0.299E+01	0.360E+00	$^{128}_{53}\text{I}$	0.321E+02	0.386E+01	$^{128}_{51}\text{Sb}$	0.166E+01	0.828E+00
$^{128}_{55}\text{Cs}$	0.393E+01	0.474E+00	$^{129}_{53}\text{I}$	0.347E+02	0.416E+01	$^{129}_{51}\text{Sb}$	0.836E+00	0.418E+00
$^{129}_{55}\text{Cs}$	0.546E+01	0.658E+00	$^{130}_{53}\text{I}$	0.336E+02	0.404E+01	$^{130}_{51}\text{Sb}$	0.498E+00	0.249E+00
$^{130}_{55}\text{Cs}$	0.626E+01	0.754E+00	$^{131}_{53}\text{I}$	0.379E+02	0.455E+01	$^{131}_{51}\text{Sb}$	0.174E+00	0.209E-01
$^{131}_{55}\text{Cs}$	0.781E+01	0.939E+00	$^{135}_{53}\text{I}$	0.311E+02	0.373E+01	$^{132}_{51}\text{Sb}$	0.485E-01	0.589E-02
$^{132}_{55}\text{Cs}$	0.758E+01	0.912E+00	$^{117}_{52}\text{Te}$	0.843E+01	0.101E+01	$^{133}_{51}\text{Sb}$	0.645E-02	0.845E-03
$^{133}_{55}\text{Cs}$	0.742E+01	0.894E+00	$^{118}_{52}\text{Te}$	0.126E+02	0.152E+01	$^{114}_{50}\text{Sn}$	0.166E+02	0.199E+01
$^{134}_{55}\text{Cs}$	0.495E+01	0.597E+00	$^{119}_{52}\text{Te}$	0.155E+02	0.187E+01	$^{115}_{50}\text{Sn}$	0.178E+02	0.214E+01
$^{135}_{55}\text{Cs}$	0.292E+01	0.354E+00	$^{120}_{52}\text{Te}$	0.198E+02	0.238E+01	$^{116}_{50}\text{Sn}$	0.163E+02	0.196E+01
$^{136}_{55}\text{Cs}$	0.118E+01	0.146E+00	$^{121}_{52}\text{Te}$	0.207E+02	0.249E+01	$^{117}_{50}\text{Sn}$	0.149E+02	0.178E+01
$^{121}_{54}\text{Xe}$	0.190E+01	0.231E+00	$^{122}_{52}\text{Te}$	0.229E+02	0.274E+01	$^{118}_{50}\text{Sn}$	0.118E+02	0.142E+01
$^{122}_{54}\text{Xe}$	0.372E+01	0.449E+00	$^{123}_{52}\text{Te}$	0.241E+02	0.290E+01	$^{119}_{50}\text{Sn}$	0.971E+01	0.117E+01
$^{123}_{54}\text{Xe}$	0.625E+01	0.753E+00	$^{124}_{52}\text{Te}$	0.235E+02	0.283E+01	$^{120}_{50}\text{Sn}$	0.732E+01	0.882E+00
$^{124}_{54}\text{Xe}$	0.909E+01	0.109E+01	$^{125}_{52}\text{Te}$	0.215E+02	0.259E+01	$^{121}_{50}\text{Sn}$	0.498E+01	0.602E+00
$^{125}_{54}\text{Xe}$	0.132E+02	0.159E+01	$^{126}_{52}\text{Te}$	0.194E+02	0.233E+01	$^{122}_{50}\text{Sn}$	0.351E+01	0.423E+00
$^{126}_{54}\text{Xe}$	0.171E+02	0.205E+01	$^{127}_{52}\text{Te}$	0.168E+02	0.202E+01	$^{123}_{50}\text{Sn}$	0.228E+01	0.278E+00
$^{127}_{54}\text{Xe}$	0.223E+02	0.268E+01	$^{128}_{52}\text{Te}$	0.144E+02	0.173E+01	$^{124}_{50}\text{Sn}$	0.171E+01	0.853E+00
$^{128}_{54}\text{Xe}$	0.279E+02	0.335E+01	$^{129}_{52}\text{Te}$	0.134E+02	0.668E+01	$^{127}_{50}\text{Sn}$	0.214E+00	0.107E+00
$^{129}_{54}\text{Xe}$	0.351E+02	0.422E+01	$^{132}_{52}\text{Te}$	0.355E+01	0.177E+01	$^{129}_{50}\text{Sn}$	0.264E-01	0.324E-02
$^{130}_{54}\text{Xe}$	0.455E+02	0.547E+01	$^{133}_{52}\text{Te}$	0.672E+00	0.336E+00	$^{130}_{50}\text{Sn}$	0.725E-02	0.930E-03
$^{131}_{54}\text{Xe}$	0.586E+02	0.704E+01	$^{134}_{52}\text{Te}$	0.336E+00	0.403E-01	$^{0}_{0}\text{Te}$	0.000E+00	0.000E+00

Table B.4: Isotopic cross sections measured in the reaction  $^{136}\text{Xe} + ^{208}\text{Pb}$  at 1000 MeV/u.

nucleus	$\sigma$ (mb)	$\epsilon_\sigma$ (mb)	nucleus	$\sigma$ (mb)	$\epsilon_\sigma$ (mb)	nucleus	$\sigma$ (mb)	$\epsilon_\sigma$ (mb)
<sup>122</sup> <sub>56</sub> Ba	0.319E-03	0.643E-04	<sup>131</sup> <sub>54</sub> Xe	0.343E+02	0.412E+01	<sup>135</sup> <sub>52</sub> Te	0.452E-03	0.551E-04
<sup>123</sup> <sub>56</sub> Ba	0.138E-02	0.265E-03	<sup>132</sup> <sub>54</sub> Xe	0.354E+02	0.425E+01	<sup>112</sup> <sub>51</sub> Sb	0.117E+01	0.140E+00
<sup>124</sup> <sub>56</sub> Ba	0.113E-01	0.166E-02	<sup>133</sup> <sub>54</sub> Xe	0.390E+02	0.469E+01	<sup>113</sup> <sub>51</sub> Sb	0.324E+01	0.389E+00
<sup>125</sup> <sub>56</sub> Ba	0.272E-01	0.398E-02	<sup>134</sup> <sub>54</sub> Xe	0.480E+02	0.576E+01	<sup>114</sup> <sub>51</sub> Sb	0.637E+01	0.765E+00
<sup>126</sup> <sub>56</sub> Ba	0.426E-01	0.588E-02	<sup>135</sup> <sub>54</sub> Xe	0.669E+02	0.803E+01	<sup>115</sup> <sub>51</sub> Sb	0.100E+02	0.120E+01
<sup>127</sup> <sub>56</sub> Ba	0.539E-01	0.729E-02	<sup>117</sup> <sub>53</sub> I	0.150E+01	0.180E+00	<sup>116</sup> <sub>51</sub> Sb	0.129E+02	0.155E+01
<sup>128</sup> <sub>56</sub> Ba	0.861E-01	0.113E-01	<sup>118</sup> <sub>53</sub> I	0.373E+01	0.448E+00	<sup>117</sup> <sub>51</sub> Sb	0.156E+02	0.187E+01
<sup>129</sup> <sub>56</sub> Ba	0.759E-01	0.108E-01	<sup>119</sup> <sub>53</sub> I	0.745E+01	0.895E+00	<sup>118</sup> <sub>51</sub> Sb	0.158E+02	0.189E+01
<sup>130</sup> <sub>56</sub> Ba	0.628E-01	0.918E-02	<sup>120</sup> <sub>53</sub> I	0.115E+02	0.139E+01	<sup>119</sup> <sub>51</sub> Sb	0.161E+02	0.193E+01
<sup>131</sup> <sub>56</sub> Ba	0.607E-01	0.837E-02	<sup>121</sup> <sub>53</sub> I	0.166E+02	0.199E+01	<sup>120</sup> <sub>51</sub> Sb	0.139E+02	0.167E+01
<sup>132</sup> <sub>56</sub> Ba	0.327E-01	0.528E-02	<sup>122</sup> <sub>53</sub> I	0.200E+02	0.240E+01	<sup>121</sup> <sub>51</sub> Sb	0.123E+02	0.148E+01
<sup>133</sup> <sub>56</sub> Ba	0.163E-01	0.313E-02	<sup>123</sup> <sub>53</sub> I	0.249E+02	0.299E+01	<sup>122</sup> <sub>51</sub> Sb	0.952E+01	0.114E+01
<sup>119</sup> <sub>55</sub> Cs	0.146E-02	0.224E-03	<sup>124</sup> <sub>53</sub> I	0.267E+02	0.320E+01	<sup>123</sup> <sub>51</sub> Sb	0.774E+01	0.930E+00
<sup>120</sup> <sub>55</sub> Cs	0.250E-01	0.313E-02	<sup>125</sup> <sub>53</sub> I	0.292E+02	0.351E+01	<sup>124</sup> <sub>51</sub> Sb	0.551E+01	0.664E+00
<sup>121</sup> <sub>55</sub> Cs	0.120E+00	0.148E-01	<sup>126</sup> <sub>53</sub> I	0.281E+02	0.337E+01	<sup>125</sup> <sub>51</sub> Sb	0.421E+01	0.509E+00
<sup>122</sup> <sub>55</sub> Cs	0.370E+00	0.448E-01	<sup>127</sup> <sub>53</sub> I	0.296E+02	0.355E+01	<sup>126</sup> <sub>51</sub> Sb	0.278E+01	0.337E+00
<sup>123</sup> <sub>55</sub> Cs	0.818E+00	0.990E-01	<sup>128</sup> <sub>53</sub> I	0.269E+02	0.323E+01	<sup>127</sup> <sub>51</sub> Sb	0.188E+01	0.228E+00
<sup>124</sup> <sub>55</sub> Cs	0.149E+01	0.179E+00	<sup>129</sup> <sub>53</sub> I	0.275E+02	0.330E+01	<sup>130</sup> <sub>51</sub> Sb	0.319E+00	0.384E-01
<sup>125</sup> <sub>55</sub> Cs	0.239E+01	0.287E+00	<sup>130</sup> <sub>53</sub> I	0.232E+02	0.279E+01	<sup>131</sup> <sub>51</sub> Sb	0.130E+00	0.158E-01
<sup>126</sup> <sub>55</sub> Cs	0.323E+01	0.390E+00	<sup>131</sup> <sub>53</sub> I	0.242E+02	0.291E+01	<sup>132</sup> <sub>51</sub> Sb	0.224E-01	0.270E-02
<sup>127</sup> <sub>55</sub> Cs	0.427E+01	0.514E+00	<sup>132</sup> <sub>53</sub> I	0.195E+02	0.234E+01	<sup>133</sup> <sub>51</sub> Sb	0.239E-02	0.288E-03
<sup>128</sup> <sub>55</sub> Cs	0.501E+01	0.603E+00	<sup>135</sup> <sub>53</sub> I	0.165E+02	0.198E+01	<sup>110</sup> <sub>51</sub> Sn	0.176E+01	0.211E+00
<sup>129</sup> <sub>55</sub> Cs	0.599E+01	0.720E+00	<sup>136</sup> <sub>53</sub> I	0.215E-01	0.268E-02	<sup>111</sup> <sub>51</sub> Sn	0.384E+01	0.461E+00
<sup>130</sup> <sub>55</sub> Cs	0.651E+01	0.784E+00	<sup>115</sup> <sub>52</sub> Te	0.258E+01	0.310E+00	<sup>112</sup> <sub>50</sub> Sn	0.647E+01	0.778E+00
<sup>131</sup> <sub>55</sub> Cs	0.738E+01	0.888E+00	<sup>116</sup> <sub>52</sub> Te	0.586E+01	0.704E+00	<sup>113</sup> <sub>50</sub> Sn	0.885E+01	0.106E+01
<sup>132</sup> <sub>55</sub> Cs	0.754E+01	0.907E+00	<sup>117</sup> <sub>52</sub> Te	0.978E+01	0.117E+01	<sup>114</sup> <sub>50</sub> Sn	0.103E+02	0.124E+01
<sup>133</sup> <sub>55</sub> Cs	0.760E+01	0.914E+00	<sup>118</sup> <sub>52</sub> Te	0.143E+02	0.172E+01	<sup>115</sup> <sub>50</sub> Sn	0.112E+02	0.135E+01
<sup>134</sup> <sub>55</sub> Cs	0.573E+01	0.689E+00	<sup>119</sup> <sub>52</sub> Te	0.179E+02	0.215E+01	<sup>116</sup> <sub>50</sub> Sn	0.106E+02	0.127E+01
<sup>135</sup> <sub>55</sub> Cs	0.373E+01	0.452E+00	<sup>120</sup> <sub>52</sub> Te	0.210E+02	0.252E+01	<sup>117</sup> <sub>50</sub> Sn	0.947E+01	0.114E+01
<sup>136</sup> <sub>55</sub> Cs	0.110E+01	0.135E+00	<sup>121</sup> <sub>52</sub> Te	0.225E+02	0.270E+01	<sup>118</sup> <sub>50</sub> Sn	0.756E+01	0.909E+00
<sup>119</sup> <sub>54</sub> Xe	0.626E+00	0.756E-01	<sup>122</sup> <sub>52</sub> Te	0.224E+02	0.269E+01	<sup>119</sup> <sub>50</sub> Sn	0.587E+01	0.706E+00
<sup>120</sup> <sub>54</sub> Xe	0.187E+01	0.225E+00	<sup>123</sup> <sub>52</sub> Te	0.212E+02	0.255E+01	<sup>120</sup> <sub>50</sub> Sn	0.404E+01	0.487E+00
<sup>121</sup> <sub>54</sub> Xe	0.377E+01	0.454E+00	<sup>124</sup> <sub>52</sub> Te	0.191E+02	0.230E+01	<sup>121</sup> <sub>50</sub> Sn	0.276E+01	0.333E+00
<sup>122</sup> <sub>54</sub> Xe	0.670E+01	0.804E+00	<sup>125</sup> <sub>52</sub> Te	0.169E+02	0.202E+01	<sup>122</sup> <sub>50</sub> Sn	0.191E+01	0.233E+00
<sup>123</sup> <sub>54</sub> Xe	0.969E+01	0.116E+01	<sup>126</sup> <sub>52</sub> Te	0.140E+02	0.168E+01	<sup>123</sup> <sub>50</sub> Sn	0.110E+01	0.135E+00
<sup>124</sup> <sub>54</sub> Xe	0.136E+02	0.164E+01	<sup>127</sup> <sub>52</sub> Te	0.119E+02	0.143E+01	<sup>124</sup> <sub>50</sub> Sn	0.770E+00	0.941E-01
<sup>125</sup> <sub>54</sub> Xe	0.171E+02	0.205E+01	<sup>128</sup> <sub>52</sub> Te	0.938E+01	0.113E+01	<sup>125</sup> <sub>50</sub> Sn	0.369E+00	0.185E+00
<sup>126</sup> <sub>54</sub> Xe	0.209E+02	0.250E+01	<sup>129</sup> <sub>52</sub> Te	0.745E+01	0.896E+00	<sup>127</sup> <sub>50</sub> Sn	0.693E-01	0.347E-01
<sup>127</sup> <sub>54</sub> Xe	0.231E+02	0.278E+01	<sup>130</sup> <sub>52</sub> Te	0.564E+01	0.282E+01	<sup>128</sup> <sub>50</sub> Sn	0.229E-01	0.282E-02
<sup>128</sup> <sub>54</sub> Xe	0.265E+02	0.318E+01	<sup>132</sup> <sub>52</sub> Te	0.248E+01	0.124E+01	<sup>129</sup> <sub>50</sub> Sn	0.102E-01	0.510E-02
<sup>129</sup> <sub>54</sub> Xe	0.286E+02	0.344E+01	<sup>133</sup> <sub>52</sub> Te	0.995E+00	0.120E+00	<sup>130</sup> <sub>50</sub> Sn	0.214E-02	0.258E-03
<sup>130</sup> <sub>54</sub> Xe	0.309E+02	0.371E+01	<sup>134</sup> <sub>52</sub> Te	0.222E+00	0.266E-01	<sup>0</sup> <sub>0</sub> Te	0.000E+00	0.000E+00

Table B.5: Isotopic cross sections measured in the reaction  $^{136}\text{Xe} + ^1\text{H}$  at 500 MeV/u.

nucleus	$\sigma(\text{mb})$	$\epsilon_\sigma$ (mb)	nucleus	$\sigma(\text{mb})$	$\epsilon_\sigma$ (mb)	nucleus	$\sigma(\text{mb})$	$\epsilon_\sigma$ (mb)
<sup>123</sup> <sub>56</sub> Ba	0.758E-03	0.249E-03	<sup>133</sup> <sub>54</sub> Xe	0.427E+02	0.384E+01	<sup>112</sup> <sub>51</sub> Sb	0.242E+01	0.222E+00
<sup>124</sup> <sub>56</sub> Ba	0.839E-02	0.229E-02	<sup>134</sup> <sub>54</sub> Xe	0.588E+02	0.530E+01	<sup>113</sup> <sub>51</sub> Sb	0.575E+01	0.521E+00
<sup>125</sup> <sub>56</sub> Ba	0.184E-01	0.352E-02	<sup>135</sup> <sub>54</sub> Xe	0.950E+02	0.855E+01	<sup>114</sup> <sub>51</sub> Sb	0.100E+02	0.904E+00
<sup>126</sup> <sub>56</sub> Ba	0.337E-01	0.601E-02	<sup>117</sup> <sub>53</sub> I	0.145E+01	0.134E+00	<sup>115</sup> <sub>51</sub> Sb	0.146E+02	0.132E+01
<sup>127</sup> <sub>56</sub> Ba	0.458E-01	0.773E-02	<sup>118</sup> <sub>53</sub> I	0.355E+01	0.323E+00	<sup>116</sup> <sub>51</sub> Sb	0.179E+02	0.161E+01
<sup>128</sup> <sub>56</sub> Ba	0.468E-01	0.784E-02	<sup>119</sup> <sub>53</sub> I	0.684E+01	0.620E+00	<sup>117</sup> <sub>51</sub> Sb	0.204E+02	0.184E+01
<sup>129</sup> <sub>56</sub> Ba	0.447E-01	0.761E-02	<sup>120</sup> <sub>53</sub> I	0.104E+02	0.938E+00	<sup>118</sup> <sub>51</sub> Sb	0.209E+02	0.189E+01
<sup>130</sup> <sub>56</sub> Ba	0.417E-01	0.725E-02	<sup>121</sup> <sub>53</sub> I	0.148E+02	0.134E+01	<sup>119</sup> <sub>51</sub> Sb	0.205E+02	0.185E+01
<sup>131</sup> <sub>56</sub> Ba	0.288E-01	0.571E-02	<sup>122</sup> <sub>53</sub> I	0.183E+02	0.166E+01	<sup>120</sup> <sub>51</sub> Sb	0.180E+02	0.162E+01
<sup>132</sup> <sub>56</sub> Ba	0.224E-01	0.463E-02	<sup>123</sup> <sub>53</sub> I	0.230E+02	0.207E+01	<sup>121</sup> <sub>51</sub> Sb	0.164E+02	0.148E+01
<sup>133</sup> <sub>56</sub> Ba	0.184E-01	0.369E-02	<sup>124</sup> <sub>53</sub> I	0.248E+02	0.224E+01	<sup>122</sup> <sub>51</sub> Sb	0.128E+02	0.116E+01
<sup>121</sup> <sub>55</sub> Cs	0.666E-01	0.744E-02	<sup>125</sup> <sub>53</sub> I	0.282E+02	0.255E+01	<sup>123</sup> <sub>51</sub> Sb	0.104E+02	0.942E+00
<sup>122</sup> <sub>55</sub> Cs	0.176E+00	0.192E-01	<sup>126</sup> <sub>53</sub> I	0.290E+02	0.262E+01	<sup>124</sup> <sub>51</sub> Sb	0.766E+01	0.692E+00
<sup>123</sup> <sub>55</sub> Cs	0.468E+00	0.466E-01	<sup>127</sup> <sub>53</sub> I	0.317E+02	0.285E+01	<sup>125</sup> <sub>51</sub> Sb	0.581E+01	0.525E+00
<sup>124</sup> <sub>55</sub> Cs	0.892E+00	0.852E-01	<sup>128</sup> <sub>53</sub> I	0.296E+02	0.267E+01	<sup>126</sup> <sub>51</sub> Sb	0.419E+01	0.380E+00
<sup>125</sup> <sub>55</sub> Cs	0.135E+01	0.127E+00	<sup>129</sup> <sub>53</sub> I	0.309E+02	0.278E+01	<sup>127</sup> <sub>51</sub> Sb	0.296E+01	0.269E+00
<sup>126</sup> <sub>55</sub> Cs	0.205E+01	0.190E+00	<sup>130</sup> <sub>53</sub> I	0.283E+02	0.255E+01	<sup>130</sup> <sub>51</sub> Sb	0.568E+00	0.518E-01
<sup>127</sup> <sub>55</sub> Cs	0.279E+01	0.257E+00	<sup>131</sup> <sub>53</sub> I	0.328E+02	0.295E+01	<sup>131</sup> <sub>51</sub> Sb	0.205E+00	0.185E-01
<sup>128</sup> <sub>55</sub> Cs	0.337E+01	0.309E+00	<sup>132</sup> <sub>53</sub> I	0.278E+02	0.251E+01	<sup>132</sup> <sub>51</sub> Sb	0.476E-01	0.431E-02
<sup>129</sup> <sub>55</sub> Cs	0.431E+01	0.394E+00	<sup>135</sup> <sub>53</sub> I	0.232E+02	0.209E+01	<sup>133</sup> <sub>51</sub> Sb	0.571E-02	0.517E-03
<sup>130</sup> <sub>55</sub> Cs	0.471E+01	0.429E+00	<sup>136</sup> <sub>53</sub> I	0.645E-01	0.612E-02	<sup>110</sup> <sub>51</sub> Sn	0.455E+01	0.413E+00
<sup>131</sup> <sub>55</sub> Cs	0.558E+01	0.507E+00	<sup>115</sup> <sub>52</sub> Te	0.338E+01	0.307E+00	<sup>111</sup> <sub>50</sub> Sn	0.874E+01	0.790E+00
<sup>132</sup> <sub>55</sub> Cs	0.565E+01	0.513E+00	<sup>116</sup> <sub>52</sub> Te	0.711E+01	0.645E+00	<sup>112</sup> <sub>50</sub> Sn	0.133E+02	0.120E+01
<sup>133</sup> <sub>55</sub> Cs	0.582E+01	0.529E+00	<sup>117</sup> <sub>52</sub> Te	0.109E+02	0.984E+00	<sup>113</sup> <sub>50</sub> Sn	0.165E+02	0.149E+01
<sup>134</sup> <sub>55</sub> Cs	0.434E+01	0.393E+00	<sup>118</sup> <sub>52</sub> Te	0.157E+02	0.142E+01	<sup>114</sup> <sub>50</sub> Sn	0.181E+02	0.163E+01
<sup>135</sup> <sub>55</sub> Cs	0.276E+01	0.251E+00	<sup>119</sup> <sub>52</sub> Te	0.194E+02	0.175E+01	<sup>115</sup> <sub>50</sub> Sn	0.183E+02	0.165E+01
<sup>136</sup> <sub>55</sub> Cs	0.102E+01	0.949E-01	<sup>120</sup> <sub>52</sub> Te	0.224E+02	0.202E+01	<sup>116</sup> <sub>50</sub> Sn	0.168E+02	0.152E+01
<sup>119</sup> <sub>54</sub> Xe	0.516E+00	0.500E-01	<sup>121</sup> <sub>52</sub> Te	0.239E+02	0.215E+01	<sup>117</sup> <sub>50</sub> Sn	0.146E+02	0.132E+01
<sup>120</sup> <sub>54</sub> Xe	0.139E+01	0.129E+00	<sup>122</sup> <sub>52</sub> Te	0.249E+02	0.225E+01	<sup>118</sup> <sub>50</sub> Sn	0.118E+02	0.107E+01
<sup>121</sup> <sub>54</sub> Xe	0.252E+01	0.231E+00	<sup>123</sup> <sub>52</sub> Te	0.238E+02	0.215E+01	<sup>119</sup> <sub>50</sub> Sn	0.914E+01	0.827E+00
<sup>122</sup> <sub>54</sub> Xe	0.486E+01	0.442E+00	<sup>124</sup> <sub>52</sub> Te	0.221E+02	0.200E+01	<sup>120</sup> <sub>50</sub> Sn	0.642E+01	0.582E+00
<sup>123</sup> <sub>54</sub> Xe	0.730E+01	0.662E+00	<sup>125</sup> <sub>52</sub> Te	0.201E+02	0.181E+01	<sup>121</sup> <sub>50</sub> Sn	0.445E+01	0.404E+00
<sup>124</sup> <sub>54</sub> Xe	0.104E+02	0.939E+00	<sup>126</sup> <sub>52</sub> Te	0.169E+02	0.153E+01	<sup>122</sup> <sub>50</sub> Sn	0.296E+01	0.269E+00
<sup>125</sup> <sub>54</sub> Xe	0.134E+02	0.121E+01	<sup>127</sup> <sub>52</sub> Te	0.147E+02	0.132E+01	<sup>123</sup> <sub>50</sub> Sn	0.191E+01	0.175E+00
<sup>126</sup> <sub>54</sub> Xe	0.167E+02	0.150E+01	<sup>128</sup> <sub>52</sub> Te	0.123E+02	0.111E+01	<sup>124</sup> <sub>50</sub> Sn	0.127E+01	0.117E+00
<sup>127</sup> <sub>54</sub> Xe	0.200E+02	0.180E+01	<sup>129</sup> <sub>52</sub> Te	0.105E+02	0.951E+00	<sup>125</sup> <sub>50</sub> Sn	0.609E+00	0.305E+00
<sup>128</sup> <sub>54</sub> Xe	0.241E+02	0.217E+01	<sup>130</sup> <sub>52</sub> Te	0.739E+01	0.668E+00	<sup>127</sup> <sub>50</sub> Sn	0.113E+00	0.567E-01
<sup>129</sup> <sub>54</sub> Xe	0.269E+02	0.243E+01	<sup>132</sup> <sub>52</sub> Te	0.416E+01	0.208E+01	<sup>128</sup> <sub>50</sub> Sn	0.377E-01	0.353E-02
<sup>130</sup> <sub>54</sub> Xe	0.307E+02	0.277E+01	<sup>133</sup> <sub>52</sub> Te	0.167E+01	0.151E+00	<sup>129</sup> <sub>50</sub> Sn	0.185E-01	0.925E-02
<sup>131</sup> <sub>54</sub> Xe	0.328E+02	0.296E+01	<sup>134</sup> <sub>52</sub> Te	0.322E+00	0.291E-01	<sup>130</sup> <sub>50</sub> Sn	0.574E-02	0.539E-03
<sup>132</sup> <sub>54</sub> Xe	0.378E+02	0.341E+01	<sup>135</sup> <sub>52</sub> Te	0.358E-02	0.343E-03	<sup>132</sup> <sub>50</sub> Sn	0.567E-04	0.919E-05

Table B.6: Isotopic cross sections measured in the reaction <sup>136</sup>Xe + Deuterium at 500 MeV/u.

nucleus	$\sigma$ (mb)	$\epsilon_\sigma$ (mb)	nucleus	$\sigma$ (mb)	$\epsilonpsilon_\sigma$ (mb)	nucleus	$\sigma$ (mb)	$\epsilon_\sigma$ (mb)
<sup>123</sup> <sub>56</sub> Ba	0.497E-02	0.104E-02	<sup>133</sup> <sub>54</sub> Xe	0.631E+02	0.757E+01	<sup>114</sup> <sub>51</sub> Sb	0.800E+01	0.963E+00
<sup>124</sup> <sub>56</sub> Ba	0.152E-01	0.354E-02	<sup>134</sup> <sub>54</sub> Xe	0.116E+03	0.139E+02	<sup>115</sup> <sub>51</sub> Sb	0.115E+02	0.139E+01
<sup>125</sup> <sub>56</sub> Ba	0.441E-01	0.771E-02	<sup>117</sup> <sub>53</sub> I	0.127E+01	0.155E+00	<sup>116</sup> <sub>51</sub> Sb	0.144E+02	0.173E+01
<sup>126</sup> <sub>56</sub> Ba	0.616E-01	0.994E-02	<sup>118</sup> <sub>53</sub> I	0.300E+01	0.363E+00	<sup>117</sup> <sub>51</sub> Sb	0.169E+02	0.203E+01
<sup>127</sup> <sub>56</sub> Ba	0.101E+00	0.147E-01	<sup>119</sup> <sub>53</sub> I	0.588E+01	0.708E+00	<sup>118</sup> <sub>51</sub> Sb	0.175E+02	0.211E+01
<sup>128</sup> <sub>56</sub> Ba	0.116E+00	0.165E-01	<sup>120</sup> <sub>53</sub> I	0.890E+01	0.107E+01	<sup>119</sup> <sub>51</sub> Sb	0.175E+02	0.211E+01
<sup>129</sup> <sub>56</sub> Ba	0.120E+00	0.183E-01	<sup>121</sup> <sub>53</sub> I	0.134E+02	0.161E+01	<sup>120</sup> <sub>51</sub> Sb	0.161E+02	0.193E+01
<sup>130</sup> <sub>56</sub> Ba	0.968E-01	0.143E-01	<sup>122</sup> <sub>53</sub> I	0.165E+02	0.198E+01	<sup>121</sup> <sub>51</sub> Sb	0.147E+02	0.177E+01
<sup>131</sup> <sub>56</sub> Ba	0.731E-01	0.114E-01	<sup>123</sup> <sub>53</sub> I	0.211E+02	0.254E+01	<sup>122</sup> <sub>51</sub> Sb	0.121E+02	0.146E+01
<sup>132</sup> <sub>56</sub> Ba	0.575E-01	0.949E-02	<sup>124</sup> <sub>53</sub> I	0.236E+02	0.284E+01	<sup>123</sup> <sub>51</sub> Sb	0.102E+02	0.122E+01
<sup>133</sup> <sub>56</sub> Ba	0.309E-01	0.604E-02	<sup>125</sup> <sub>53</sub> I	0.273E+02	0.328E+01	<sup>124</sup> <sub>51</sub> Sb	0.780E+01	0.941E+00
<sup>122</sup> <sub>55</sub> Cs	0.270E+00	0.351E-01	<sup>126</sup> <sub>53</sub> I	0.284E+02	0.341E+01	<sup>125</sup> <sub>51</sub> Sb	0.600E+01	0.724E+00
<sup>123</sup> <sub>55</sub> Cs	0.641E+00	0.798E-01	<sup>127</sup> <sub>53</sub> I	0.315E+02	0.378E+01	<sup>126</sup> <sub>51</sub> Sb	0.429E+01	0.519E+00
<sup>124</sup> <sub>55</sub> Cs	0.112E+01	0.138E+00	<sup>128</sup> <sub>53</sub> I	0.305E+02	0.366E+01	<sup>127</sup> <sub>51</sub> Sb	0.311E+01	0.383E+00
<sup>125</sup> <sub>55</sub> Cs	0.184E+01	0.223E+00	<sup>129</sup> <sub>53</sub> I	0.335E+02	0.402E+01	<sup>130</sup> <sub>51</sub> Sb	0.512E+00	0.694E-01
<sup>126</sup> <sub>55</sub> Cs	0.260E+01	0.314E+00	<sup>130</sup> <sub>53</sub> I	0.318E+02	0.383E+01	<sup>131</sup> <sub>51</sub> Sb	0.114E+00	0.573E-01
<sup>127</sup> <sub>55</sub> Cs	0.382E+01	0.462E+00	<sup>131</sup> <sub>53</sub> I	0.359E+02	0.432E+01	<sup>132</sup> <sub>51</sub> Sb	0.601E-01	0.730E-02
<sup>128</sup> <sub>55</sub> Cs	0.453E+01	0.546E+00	<sup>132</sup> <sub>53</sub> I	0.296E+02	0.356E+01	<sup>133</sup> <sub>51</sub> Sb	0.735E-02	0.963E-03
<sup>129</sup> <sub>55</sub> Cs	0.627E+01	0.755E+00	<sup>135</sup> <sub>53</sub> I	0.259E+02	0.312E+01	<sup>110</sup> <sub>50</sub> Sn	0.372E+01	0.449E+00
<sup>130</sup> <sub>55</sub> Cs	0.688E+01	0.829E+00	<sup>115</sup> <sub>52</sub> Te	0.268E+01	0.324E+00	<sup>111</sup> <sub>50</sub> Sn	0.694E+01	0.836E+00
<sup>131</sup> <sub>55</sub> Cs	0.862E+01	0.104E+01	<sup>116</sup> <sub>52</sub> Te	0.558E+01	0.673E+00	<sup>112</sup> <sub>50</sub> Sn	0.106E+02	0.127E+01
<sup>132</sup> <sub>55</sub> Cs	0.847E+01	0.102E+01	<sup>117</sup> <sub>52</sub> Te	0.910E+01	0.110E+01	<sup>113</sup> <sub>50</sub> Sn	0.133E+02	0.160E+01
<sup>133</sup> <sub>55</sub> Cs	0.930E+01	0.112E+01	<sup>118</sup> <sub>52</sub> Te	0.130E+02	0.157E+01	<sup>114</sup> <sub>50</sub> Sn	0.151E+02	0.181E+01
<sup>134</sup> <sub>55</sub> Cs	0.673E+01	0.812E+00	<sup>119</sup> <sub>52</sub> Te	0.164E+02	0.197E+01	<sup>115</sup> <sub>50</sub> Sn	0.154E+02	0.185E+01
<sup>135</sup> <sub>55</sub> Cs	0.413E+01	0.499E+00	<sup>120</sup> <sub>52</sub> Te	0.194E+02	0.233E+01	<sup>116</sup> <sub>50</sub> Sn	0.146E+02	0.175E+01
<sup>136</sup> <sub>55</sub> Cs	0.149E+01	0.191E+00	<sup>121</sup> <sub>52</sub> Te	0.208E+02	0.250E+01	<sup>117</sup> <sub>50</sub> Sn	0.128E+02	0.154E+01
<sup>119</sup> <sub>54</sub> Xe	0.495E+00	0.620E-01	<sup>122</sup> <sub>52</sub> Te	0.222E+02	0.266E+01	<sup>118</sup> <sub>50</sub> Sn	0.106E+02	0.128E+01
<sup>120</sup> <sub>54</sub> Xe	0.134E+01	0.163E+00	<sup>123</sup> <sub>52</sub> Te	0.217E+02	0.261E+01	<sup>119</sup> <sub>50</sub> Sn	0.831E+01	0.100E+01
<sup>121</sup> <sub>54</sub> Xe	0.267E+01	0.324E+00	<sup>124</sup> <sub>52</sub> Te	0.206E+02	0.247E+01	<sup>120</sup> <sub>50</sub> Sn	0.622E+01	0.751E+00
<sup>122</sup> <sub>54</sub> Xe	0.475E+01	0.572E+00	<sup>125</sup> <sub>52</sub> Te	0.190E+02	0.229E+01	<sup>121</sup> <sub>50</sub> Sn	0.446E+01	0.539E+00
<sup>123</sup> <sub>54</sub> Xe	0.726E+01	0.874E+00	<sup>126</sup> <sub>52</sub> Te	0.169E+02	0.203E+01	<sup>122</sup> <sub>50</sub> Sn	0.311E+01	0.377E+00
<sup>124</sup> <sub>54</sub> Xe	0.104E+02	0.126E+01	<sup>127</sup> <sub>52</sub> Te	0.150E+02	0.181E+01	<sup>123</sup> <sub>50</sub> Sn	0.207E+01	0.252E+00
<sup>125</sup> <sub>54</sub> Xe	0.139E+02	0.167E+01	<sup>128</sup> <sub>52</sub> Te	0.131E+02	0.158E+01	<sup>124</sup> <sub>50</sub> Sn	0.142E+01	0.182E+00
<sup>126</sup> <sub>54</sub> Xe	0.176E+02	0.212E+01	<sup>129</sup> <sub>52</sub> Te	0.104E+02	0.126E+01	<sup>125</sup> <sub>50</sub> Sn	0.521E+00	0.261E+00
<sup>127</sup> <sub>54</sub> Xe	0.217E+02	0.260E+01	<sup>130</sup> <sub>52</sub> Te	0.782E+01	0.392E+01	<sup>116</sup> <sub>50</sub> Sn	0.132E+00	0.661E-01
<sup>128</sup> <sub>54</sub> Xe	0.257E+02	0.309E+01	<sup>132</sup> <sub>52</sub> Te	0.345E+01	0.423E+00	<sup>128</sup> <sub>50</sub> Sn	0.449E-01	0.225E-01
<sup>129</sup> <sub>54</sub> Xe	0.302E+02	0.363E+01	<sup>133</sup> <sub>52</sub> Te	0.175E+01	0.219E+00	<sup>129</sup> <sub>50</sub> Sn	0.211E-01	0.106E-01
<sup>130</sup> <sub>54</sub> Xe	0.343E+02	0.412E+01	<sup>134</sup> <sub>52</sub> Te	0.433E+00	0.521E-01	<sup>130</sup> <sub>50</sub> Sn	0.850E-02	0.110E-02
<sup>131</sup> <sub>54</sub> Xe	0.407E+02	0.489E+01	<sup>112</sup> <sub>51</sub> Sb	0.187E+01	0.226E+00	<sup>0</sup> <sub>50</sub> Sb	0.000E+00	0.000E+00
<sup>132</sup> <sub>54</sub> Xe	0.498E+02	0.598E+01	<sup>113</sup> <sub>51</sub> Sb	0.449E+01	0.541E+00	<sup>0</sup> <sub>50</sub> Sb	0.000E+00	0.000E+00

Table B.7: Isotopic cross sections measured in the reaction  $^{136}\text{Xe} + ^{48}\text{Ti}$  at 500 MeV/u.

nucleus	$\sigma$ (mb)	$\epsilon_\sigma$ (mb)	nucleus	$\sigma$ (mb)	$\epsilon_{\sigma}$ (mb)	nucleus	$\sigma$ (mb)	$\epsilon_\sigma$ (mb)
$^{132}_{56}\text{Ba}$	0.160E+00	0.235E-01	$^{121}_{52}\text{Te}$	0.233E+02	0.280E+01	$^{112}_{47}\text{Ag}$	0.219E+01	0.270E+00
$^{131}_{56}\text{Ba}$	0.272E+00	0.371E-01	$^{120}_{52}\text{Te}$	0.219E+02	0.264E+01	$^{111}_{47}\text{Ag}$	0.366E+01	0.446E+00
$^{130}_{56}\text{Ba}$	0.339E+00	0.450E-01	$^{119}_{52}\text{Te}$	0.188E+02	0.227E+01	$^{110}_{47}\text{Ag}$	0.565E+01	0.685E+00
$^{129}_{56}\text{Ba}$	0.392E+00	0.511E-01	$^{118}_{52}\text{Te}$	0.155E+02	0.187E+01	$^{109}_{47}\text{Ag}$	0.805E+01	0.972E+00
$^{128}_{56}\text{Ba}$	0.382E+00	0.506E-01	$^{117}_{52}\text{Te}$	0.112E+02	0.135E+01	$^{108}_{47}\text{Ag}$	0.105E+02	0.126E+01
$^{127}_{56}\text{Ba}$	0.287E+00	0.382E-01	$^{116}_{52}\text{Te}$	0.720E+01	0.870E+00	$^{107}_{47}\text{Ag}$	0.129E+02	0.155E+01
$^{126}_{56}\text{Ba}$	0.215E+00	0.313E-01	$^{115}_{52}\text{Te}$	0.395E+01	0.478E+00	$^{106}_{47}\text{Ag}$	0.122E+02	0.148E+01
$^{125}_{56}\text{Ba}$	0.104E+00	0.162E-01	$^{125}_{51}\text{Sb}$	0.510E+01	0.620E+00	$^{105}_{47}\text{Ag}$	0.115E+02	0.138E+01
$^{124}_{56}\text{Ba}$	0.674E-01	0.111E-01	$^{124}_{51}\text{Sb}$	0.690E+01	0.832E+00	$^{111}_{46}\text{Pd}$	0.570E+00	0.791E-01
$^{135}_{55}\text{Cs}$	0.832E+01	0.101E+01	$^{123}_{51}\text{Sb}$	0.893E+01	0.108E+01	$^{110}_{46}\text{Pd}$	0.117E+01	0.148E+00
$^{134}_{55}\text{Cs}$	0.138E+02	0.166E+01	$^{122}_{51}\text{Sb}$	0.112E+02	0.135E+01	$^{109}_{46}\text{Pd}$	0.204E+01	0.253E+00
$^{133}_{55}\text{Cs}$	0.189E+02	0.228E+01	$^{121}_{51}\text{Sb}$	0.138E+02	0.166E+01	$^{108}_{46}\text{Pd}$	0.358E+01	0.437E+00
$^{132}_{55}\text{Cs}$	0.189E+02	0.228E+01	$^{120}_{51}\text{Sb}$	0.157E+02	0.189E+01	$^{107}_{46}\text{Pd}$	0.559E+01	0.678E+00
$^{131}_{55}\text{Cs}$	0.188E+02	0.226E+01	$^{119}_{51}\text{Sb}$	0.179E+02	0.215E+01	$^{106}_{46}\text{Pd}$	0.703E+01	0.863E+00
$^{130}_{55}\text{Cs}$	0.172E+02	0.206E+01	$^{118}_{51}\text{Sb}$	0.186E+02	0.224E+01	$^{105}_{46}\text{Pd}$	0.916E+01	0.112E+01
$^{129}_{55}\text{Cs}$	0.154E+02	0.185E+01	$^{117}_{51}\text{Sb}$	0.183E+02	0.220E+01	$^{104}_{46}\text{Pd}$	0.107E+02	0.130E+01
$^{128}_{55}\text{Cs}$	0.130E+02	0.157E+01	$^{116}_{51}\text{Sb}$	0.168E+02	0.202E+01	$^{103}_{46}\text{Pd}$	0.112E+02	0.136E+01
$^{127}_{55}\text{Cs}$	0.120E+02	0.144E+01	$^{115}_{51}\text{Sb}$	0.135E+02	0.163E+01	$^{108}_{45}\text{Rh}$	0.574E+00	0.759E-01
$^{126}_{55}\text{Cs}$	0.809E+01	0.976E+00	$^{114}_{51}\text{Sb}$	0.875E+01	0.106E+01	$^{107}_{45}\text{Rh}$	0.125E+01	0.159E+00
$^{125}_{55}\text{Cs}$	0.589E+01	0.712E+00	$^{113}_{51}\text{Sb}$	0.517E+01	0.625E+00	$^{106}_{45}\text{Rh}$	0.229E+01	0.282E+00
$^{124}_{55}\text{Cs}$	0.300E+01	0.364E+00	$^{122}_{50}\text{Sn}$	0.270E+01	0.332E+00	$^{105}_{45}\text{Rh}$	0.398E+01	0.485E+00
$^{123}_{55}\text{Cs}$	0.176E+01	0.217E+00	$^{121}_{50}\text{Sn}$	0.401E+01	0.491E+00	$^{104}_{45}\text{Rh}$	0.594E+01	0.721E+00
$^{122}_{55}\text{Cs}$	0.676E+00	0.846E-01	$^{120}_{50}\text{Sn}$	0.534E+01	0.650E+00	$^{103}_{45}\text{Rh}$	0.883E+01	0.107E+01
$^{121}_{55}\text{Cs}$	0.213E+00	0.288E-01	$^{119}_{50}\text{Sn}$	0.784E+01	0.948E+00	$^{102}_{45}\text{Rh}$	0.922E+01	0.111E+01
$^{133}_{54}\text{Xe}$	0.743E+02	0.893E+01	$^{118}_{50}\text{Sn}$	0.102E+02	0.123E+01	$^{101}_{45}\text{Rh}$	0.101E+02	0.122E+01
$^{132}_{54}\text{Xe}$	0.688E+02	0.826E+01	$^{117}_{50}\text{Sn}$	0.123E+02	0.148E+01	$^{100}_{45}\text{Rh}$	0.989E+01	0.120E+01
$^{131}_{54}\text{Xe}$	0.618E+02	0.742E+01	$^{116}_{50}\text{Sn}$	0.147E+02	0.177E+01	$^{105}_{44}\text{Ru}$	0.651E+00	0.858E-01
$^{130}_{54}\text{Xe}$	0.565E+02	0.679E+01	$^{115}_{50}\text{Sn}$	0.168E+02	0.202E+01	$^{104}_{44}\text{Ru}$	0.143E+01	0.180E+00
$^{129}_{54}\text{Xe}$	0.496E+02	0.597E+01	$^{114}_{50}\text{Sn}$	0.172E+02	0.207E+01	$^{103}_{44}\text{Ru}$	0.255E+01	0.315E+00
$^{128}_{54}\text{Xe}$	0.443E+02	0.533E+01	$^{113}_{50}\text{Sn}$	0.151E+02	0.182E+01	$^{102}_{44}\text{Ru}$	0.447E+01	0.545E+00
$^{127}_{54}\text{Xe}$	0.362E+02	0.435E+01	$^{112}_{50}\text{Sn}$	0.120E+02	0.145E+01	$^{101}_{44}\text{Ru}$	0.673E+01	0.817E+00
$^{126}_{54}\text{Xe}$	0.315E+02	0.379E+01	$^{111}_{50}\text{Sn}$	0.744E+01	0.898E+00	$^{100}_{44}\text{Ru}$	0.906E+01	0.110E+01
$^{125}_{54}\text{Xe}$	0.256E+02	0.308E+01	$^{120}_{49}\text{In}$	0.104E+01	0.133E+00	$^{99}_{44}\text{Ru}$	0.810E+01	0.983E+00
$^{124}_{54}\text{Xe}$	0.186E+02	0.224E+01	$^{119}_{49}\text{In}$	0.184E+01	0.231E+00	$^{102}_{43}\text{Tc}$	0.841E+00	0.111E+00
$^{123}_{54}\text{Xe}$	0.138E+02	0.166E+01	$^{118}_{49}\text{In}$	0.273E+01	0.337E+00	$^{101}_{43}\text{Tc}$	0.176E+01	0.221E+00
$^{122}_{54}\text{Xe}$	0.758E+01	0.915E+00	$^{117}_{49}\text{In}$	0.433E+01	0.526E+00	$^{100}_{43}\text{Tc}$	0.294E+01	0.361E+00
$^{121}_{54}\text{Xe}$	0.437E+01	0.531E+00	$^{116}_{49}\text{In}$	0.633E+01	0.766E+00	$^{99}_{43}\text{Tc}$	0.490E+01	0.598E+00
$^{120}_{54}\text{Xe}$	0.195E+01	0.236E+00	$^{115}_{49}\text{In}$	0.882E+01	0.106E+01	$^{98}_{43}\text{Tc}$	0.707E+01	0.857E+00
$^{119}_{54}\text{Xe}$	0.874E+00	0.108E+00	$^{114}_{49}\text{In}$	0.111E+02	0.134E+01	$^{97}_{43}\text{Tc}$	0.784E+01	0.952E+00

Table B.8: Isotopic cross sections measured in the reaction  $^{136}\text{Xe} + ^{48}\text{Ti}$  at 200 MeV/u. Continue in the next page.

nucleus	$\sigma$ (mb)	$\epsilon_\sigma$ (mb)	nucleus	$\sigma$ (mb)	$\epsilonpsilon_{\sigma}$ (mb)	nucleus	$\sigma$ (mb)	$\epsilon_\sigma$ (mb)
$^{130}_{53}I$	0.352E+02	0.423E+01	$^{113}_{49}In$	0.136E+02	0.164E+01	$^{99}_{42}Mo$	0.104E+01	0.135E+00
$^{129}_{53}I$	0.380E+02	0.456E+01	$^{112}_{49}In$	0.151E+02	0.182E+01	$^{98}_{42}Mo$	0.186E+01	0.234E+00
$^{128}_{53}I$	0.369E+02	0.444E+01	$^{111}_{49}In$	0.145E+02	0.175E+01	$^{97}_{42}Mo$	0.337E+01	0.414E+00
$^{127}_{53}I$	0.382E+02	0.459E+01	$^{110}_{49}In$	0.127E+02	0.154E+01	$^{96}_{42}Mo$	0.514E+01	0.627E+00
$^{126}_{53}I$	0.364E+02	0.438E+01	$^{109}_{49}In$	0.952E+01	0.115E+01	$^{95}_{42}Mo$	0.577E+01	0.709E+00
$^{125}_{53}I$	0.346E+02	0.416E+01	$^{118}_{48}Cd$	0.476E+00	0.652E-01	$^{94}_{42}Mo$	0.738E+01	0.896E+00
$^{124}_{53}I$	0.304E+02	0.366E+01	$^{117}_{48}Cd$	0.890E+00	0.117E+00	$^{97}_{41}Nb$	0.588E+00	0.850E-01
$^{123}_{53}I$	0.258E+02	0.310E+01	$^{116}_{48}Cd$	0.145E+01	0.184E+00	$^{96}_{41}Nb$	0.132E+01	0.171E+00
$^{122}_{53}I$	0.216E+02	0.260E+01	$^{115}_{48}Cd$	0.221E+01	0.273E+00	$^{95}_{41}Nb$	0.218E+01	0.271E+00
$^{121}_{53}I$	0.168E+02	0.202E+01	$^{114}_{48}Cd$	0.364E+01	0.444E+00	$^{94}_{41}Nb$	0.400E+01	0.491E+00
$^{120}_{53}I$	0.116E+02	0.140E+01	$^{113}_{48}Cd$	0.548E+01	0.665E+00	$^{94}_{40}Zr$	0.627E+00	0.851E-01
$^{119}_{53}I$	0.782E+01	0.944E+00	$^{112}_{48}Cd$	0.780E+01	0.943E+00	$^{93}_{40}Zr$	0.142E+01	0.180E+00
$^{118}_{53}I$	0.431E+01	0.522E+00	$^{111}_{48}Cd$	0.112E+02	0.135E+01	$^{92}_{40}Zr$	0.240E+01	0.301E+00
$^{117}_{53}I$	0.187E+01	0.227E+00	$^{110}_{48}Cd$	0.127E+02	0.154E+01	$^{91}_{40}Zr$	0.375E+01	0.464E+00
$^{127}_{52}Te$	0.141E+02	0.170E+01	$^{109}_{48}Cd$	0.144E+02	0.173E+01	$^{90}_{40}Zr$	0.600E+01	0.735E+00
$^{126}_{52}Te$	0.178E+02	0.215E+01	$^{108}_{48}Cd$	0.143E+02	0.173E+01	$^{89}_{39}Y$	0.181E+01	0.228E+00
$^{125}_{52}Te$	0.186E+02	0.225E+01	$^{107}_{48}Cd$	0.132E+02	0.160E+01	$^{86}_{38}Sr$	0.495E+01	0.612E+00
$^{124}_{52}Te$	0.221E+02	0.266E+01	$^{106}_{48}Cd$	0.927E+01	0.112E+01	$^{85}_{38}Sr$	0.609E+01	0.741E+00
$^{123}_{52}Te$	0.225E+02	0.271E+01	$^{114}_{47}Ag$	0.667E+00	0.901E-01	$^0_0Ag$	0.000E+00	0.000E+00
$^{122}_{52}Te$	0.242E+02	0.290E+01	$^{113}_{47}Ag$	0.125E+01	0.160E+00	$^0_0Ag$	0.000E+00	0.000E+00

Table B.9: Continuation of the isotopic cross sections measured in the reaction  $^{136}Xe + ^{48}Ti$  at 200 MeV/u.

nucleus	$\sigma$ (mb)	$\epsilon_\sigma$ (mb)	nucleus	$\sigma$ (mb)	$\epsilon_\sigma$ (mb)	nucleus	$\sigma$ (mb)	$\epsilon_\sigma$ (mb)
$^{123}_{53}I$	0.341E+02	0.410E+01	$^{119}_{51}Sb$	0.811E+00	0.244E+00	$^{117}_{50}Sn$	0.316E+00	0.950E-01
$^{120}_{52}Te$	0.881E+01	0.106E+01	$^{120}_{51}Sb$	0.391E+00	0.472E-01	$^{118}_{50}Sn$	0.986E-01	0.297E-01
$^{121}_{52}Te$	0.345E+01	0.104E+01	$^{121}_{51}Sb$	0.874E-01	0.264E-01	$^{119}_{50}Sn$	0.124E-01	0.374E-02
$^{122}_{52}Te$	0.177E+01	0.533E+00	$^{115}_{50}Sn$	0.208E+01	0.625E+00	$^{120}_{50}Sn$	0.184E-02	0.555E-03
$^{118}_{51}Sb$	0.283E+01	0.344E+00	$^{116}_{50}Sn$	0.105E+01	0.319E+00	$^0_0Sn$	0.000E+00	0.000E+00

Table B.10: Isotopic cross sections measured in the reaction  $^{124}Xe + ^9Be$  at 1000 MeV/u.

nucleus	$\sigma$ (mb)	$\epsilon_\sigma$ (mb)	nucleus	$\sigma$ (mb)	$\epsilon_\sigma$ (mb)	nucleus	$\sigma$ (mb)	$\epsilon_\sigma$ (mb)
$^{119}_{55}Cs$	0.281E+00	0.449E-01	$^{112}_{52}Te$	0.153E+01	0.232E+00	$^{118}_{51}Sb$	0.363E+01	0.545E+00
$^{120}_{55}Cs$	0.971E+00	0.149E+00	$^{113}_{52}Te$	0.638E+01	0.959E+00	$^{119}_{51}Sb$	0.981E+00	0.491E+00
$^{121}_{55}Cs$	0.276E+01	0.417E+00	$^{114}_{52}Te$	0.189E+02	0.283E+01	$^{120}_{51}Sb$	0.352E+00	0.530E-01
$^{122}_{55}Cs$	0.404E+01	0.609E+00	$^{115}_{52}Te$	0.309E+02	0.464E+01	$^{121}_{51}Sb$	0.730E-01	0.111E-01
$^{123}_{55}Cs$	0.272E+01	0.410E+00	$^{116}_{52}Te$	0.417E+02	0.626E+01	$^{108}_{50}Sn$	0.581E+01	0.874E+00
$^{124}_{55}Cs$	0.125E+01	0.624E+00	$^{117}_{52}Te$	0.378E+02	0.568E+01	$^{109}_{50}Sn$	0.160E+02	0.241E+01
$^{117}_{54}Xe$	0.156E+01	0.237E+00	$^{118}_{52}Te$	0.266E+02	0.133E+02	$^{110}_{50}Sn$	0.280E+02	0.421E+01
$^{118}_{54}Xe$	0.684E+01	0.103E+01	$^{120}_{52}Te$	0.123E+02	0.185E+01	$^{111}_{50}Sn$	0.306E+02	0.460E+01
$^{119}_{54}Xe$	0.192E+02	0.288E+01	$^{121}_{52}Te$	0.559E+01	0.838E+00	$^{112}_{50}Sn$	0.271E+02	0.407E+01
$^{120}_{54}Xe$	0.467E+02	0.701E+01	$^{122}_{52}Te$	0.171E+01	0.256E+00	$^{113}_{50}Sn$	0.144E+02	0.720E+01
$^{121}_{54}Xe$	0.926E+02	0.139E+02	$^{110}_{51}Sb$	0.271E+01	0.410E+00	$^{114}_{50}Sn$	0.865E+01	0.433E+01
$^{116}_{53}I$	0.113E+02	0.170E+01	$^{111}_{51}Sb$	0.939E+01	0.141E+01	$^{116}_{50}Sn$	0.149E+01	0.224E+00
$^{117}_{53}I$	0.257E+02	0.386E+01	$^{112}_{51}Sb$	0.206E+02	0.309E+01	$^{117}_{50}Sn$	0.346E+00	0.522E-01
$^{118}_{53}I$	0.406E+02	0.609E+01	$^{113}_{51}Sb$	0.311E+02	0.468E+01	$^{118}_{50}Sn$	0.101E+00	0.152E-01
$^{119}_{53}I$	0.557E+02	0.835E+01	$^{114}_{51}Sb$	0.315E+02	0.473E+01	$^{119}_{50}Sn$	0.160E-01	0.254E-02
$^{120}_{53}I$	0.698E+02	0.349E+02	$^{115}_{51}Sb$	0.178E+02	0.890E+01	$^0_0Sb$	0.000E+00	0.000E+00
$^{123}_{53}I$	0.104E+03	0.156E+02	$^{116}_{51}Sb$	0.108E+02	0.540E+01	$^0_0Sb$	0.000E+00	0.000E+00

Table B.11: Isotopic cross sections measured in the reaction  $^{124}Xe + ^{208}Pb$  at 1000 MeV/u.



# Appendix C

## Isobar Model description

In the chapter 5 of this work we have studied the charge-exchange mechanism. We postulated there the relative probabilities of undergoing a proton or neutron-pickup reaction based on the Feynman diagrams responsible for that processes. In this appendix we will develop the necessary tools for that discussion within the frame of the isospin model. As discussed by VerWest [83], this model is based in the isospin conservation on the transition from an initial state of isospin  $I$  of the two nucleons to a final state of isospin  $J$  of two nucleons coupled to isospin 1 for the pion to give a total final isospin  $I$ .

In many works has been stated that the the main mechanism for pion production at the relevant energies treated on this work, is through a  $\Delta$ -resonance excitation. The isospin components of the particles involved in the charge-pickup process (nucleons, pions and  $\Delta$ ) are shown in the figure C.1 in a  $|T T_z\rangle$  formalism, where  $T$  is the isospin number and  $T_z$  its projection on the  $z$ -axis.

$$\begin{aligned} p &\equiv \left| \frac{1}{2} \quad +\frac{1}{2} \right\rangle & n &\equiv \left| \frac{1}{2} \quad -\frac{1}{2} \right\rangle \\ \pi^+ &\equiv |1 \quad +1\rangle & \pi^0 &\equiv |1 \quad 0\rangle & \pi^- &\equiv |1 \quad -1\rangle \\ \Delta^{++} &\equiv \left| \frac{3}{2} \quad +\frac{3}{2} \right\rangle & \Delta^+ &\equiv \left| \frac{3}{2} \quad +\frac{1}{2} \right\rangle & \Delta^0 &\equiv \left| \frac{3}{2} \quad -\frac{1}{2} \right\rangle & \Delta^- &\equiv \left| \frac{3}{2} \quad -\frac{3}{2} \right\rangle \end{aligned}$$

Figure C.1: Isospin quantum number and its projection  $|T T_z\rangle$  for the different particles involved in the proton and neutron pickup-reactions.

As can be seen in the figure, the nucleons, pions and  $\Delta$ -resonances are isospin doublets, triplets and quadruplets, respectively. From this starting point and using the Clebsch-Gordan coefficients, we can calculate the isospin couplings of the different possible reaction

channels in a nucleon-nucleon collision. We will calculate here the amplitude of the process  $pp \rightarrow n\Delta^{++}$ , this process is mediated by a  $\pi^+$ , as shown in Diagram 3 of figure C.4. We have then two vertex on that diagram:

$$\langle n \pi^+ | p \rangle \otimes \langle p \pi^+ | \Delta^{++} \rangle \implies \langle \frac{1}{2} \quad -\frac{1}{2}; 1 \quad +1 | \frac{1}{2} \quad +\frac{1}{2} \rangle \otimes \langle \frac{3}{2} \quad +\frac{3}{2} | \frac{1}{2} \quad +\frac{1}{2}; 1 \quad +1 \rangle$$

We will calculate the amplitude of each vertex separately:

$$\text{Vertex1} \implies \langle \frac{1}{2} \quad -\frac{1}{2} | \otimes \langle 1 \quad +1 | = \frac{1}{3} \cdot \langle \frac{3}{2} \quad +\frac{1}{2} | + \frac{2}{3} \cdot \langle \frac{1}{2} \quad +\frac{1}{2} |$$

Thus, coupling with the initial proton state we obtain an amplitude for the first vertex of  $A_{V1} = 2/3$ . The second vertex is given by:

$$\text{Vertex2} \implies | \frac{1}{2} \quad +\frac{1}{2} \rangle \otimes | 1 \quad +1 \rangle = | \frac{3}{2} \quad +\frac{3}{2} \rangle$$

Which coupled with the final  $\Delta^{++}$  state leads to an amplitude for the second vertex of  $A_{V2} = 1$ . The total amplitude of the process is then given by the product of both vertex, that is  $A = A_{V1} \cdot A_{V2} = 2/3$ . We can perform the same analysis for all the possible nucleon-nucleon combinations, this is schematically shown in the figure C.2.

$$\begin{aligned} pp \longrightarrow n\Delta^{++} &\implies \langle \frac{1}{2} \quad -\frac{1}{2}; 1 \quad +1 | \frac{1}{2} \quad +\frac{1}{2} \rangle \otimes \langle \frac{3}{2} \quad +\frac{3}{2} | \frac{1}{2} \quad +\frac{1}{2}; 1 \quad +1 \rangle \implies A = \frac{2}{3} \\ pp \longrightarrow p\Delta^+ &\implies \langle \frac{1}{2} \quad +\frac{1}{2}; 1 \quad 0 | \frac{1}{2} \quad +\frac{1}{2} \rangle \otimes \langle \frac{3}{2} \quad +\frac{1}{2} | \frac{1}{2} \quad +\frac{1}{2}; 1 \quad 0 \rangle \implies A = \frac{2}{9} \\ nn \longrightarrow n\Delta^0 &\implies \langle \frac{1}{2} \quad -\frac{1}{2}; 1 \quad 0 | \frac{1}{2} \quad -\frac{1}{2} \rangle \otimes \langle \frac{3}{2} \quad -\frac{1}{2} | \frac{1}{2} \quad -\frac{1}{2}; 1 \quad 0 \rangle \implies A = \frac{2}{9} \\ nn \longrightarrow p\Delta^- &\implies \langle \frac{1}{2} \quad +\frac{1}{2}; 1 \quad -1 | \frac{1}{2} \quad -\frac{1}{2} \rangle \otimes \langle \frac{3}{2} \quad -\frac{3}{2} | \frac{1}{2} \quad -\frac{1}{2}; 1 \quad -1 \rangle \implies A = \frac{2}{3} \\ np \longrightarrow n\Delta^+ &\implies \langle \frac{1}{2} \quad -\frac{1}{2}; 1 \quad +1 | \frac{1}{2} \quad +\frac{1}{2} \rangle \otimes \langle \frac{3}{2} \quad +\frac{1}{2} | \frac{1}{2} \quad -\frac{1}{2}; 1 \quad +1 \rangle \implies A = \frac{2}{9} \\ np \longrightarrow p\Delta^0 &\implies \langle \frac{1}{2} \quad +\frac{1}{2}; 1 \quad 0 | \frac{1}{2} \quad +\frac{1}{2} \rangle \otimes \langle \frac{3}{2} \quad -\frac{1}{2} | \frac{1}{2} \quad -\frac{1}{2}; 1 \quad 0 \rangle \implies A = \frac{2}{9} \end{aligned}$$

Figure C.2: Probability amplitudes corresponding to the different reaction channels according to the isospin conservation given by the Clebsch-Gordan coefficients.

From these amplitudes, given by isospin conservation, we can derive the following reaction probability ratios:

$$\frac{P(pp \longrightarrow n\Delta^{++})}{P(pp \longrightarrow p\Delta^+)} = 3 \quad \frac{P(nn \longrightarrow p\Delta^-)}{P(nn \longrightarrow n\Delta^0)} = 3 \quad \frac{P(np \longrightarrow p\Delta^0)}{P(np \longrightarrow n\Delta^+)} = 1 \quad (\text{C.1})$$

This has to be understood as, for example, whenever a proton-proton collision occurs, it is three times more possible for the reaction to excite a  $\Delta^{++}$  resonance than a  $\Delta^+$ . The reader must regard that the origin of this ratios relies on the isospin conservation. We can follow the same argument and study the further decay of the resonance after its formation in a nucleon-nucleon collision. We can perform the same analysis based on the Clebsch-Gordan coefficients, being the isospin couplings for all the possible decay channels those shown in the figure C.3.

$$\begin{aligned} \Delta^{++} \longrightarrow p\pi^+ &\implies \left|\frac{1}{2} \ + \frac{1}{2}\right\rangle \otimes |1 \ + 1\rangle = \left|\frac{3}{2} \ + \frac{3}{2}\right\rangle \implies A = 1 \\ \Delta^+ \longrightarrow p\pi^0 &\implies \left|\frac{1}{2} \ + \frac{1}{2}\right\rangle \otimes |1 \ 0\rangle = \frac{2}{3}\left|\frac{3}{2} \ + \frac{1}{2}\right\rangle - \frac{1}{3}\left|\frac{1}{2} \ + \frac{1}{2}\right\rangle \implies A = \frac{2}{3} \\ \Delta^+ \longrightarrow n\pi^+ &\implies \left|\frac{1}{2} \ - \frac{1}{2}\right\rangle \otimes |1 \ 1\rangle = \frac{1}{3}\left|\frac{3}{2} \ + \frac{1}{2}\right\rangle - \frac{2}{3}\left|\frac{1}{2} \ + \frac{1}{2}\right\rangle \implies A = \frac{1}{3} \\ \Delta^0 \longrightarrow p\pi^- &\implies \left|\frac{1}{2} \ + \frac{1}{2}\right\rangle \otimes |1 \ - 1\rangle = \frac{1}{3}\left|\frac{3}{2} \ - \frac{1}{2}\right\rangle - \frac{2}{3}\left|\frac{1}{2} \ - \frac{1}{2}\right\rangle \implies A = \frac{1}{3} \\ \Delta^0 \longrightarrow n\pi^0 &\implies \left|\frac{1}{2} \ - \frac{1}{2}\right\rangle \otimes |1 \ 0\rangle = \frac{2}{3}\left|\frac{3}{2} \ - \frac{1}{2}\right\rangle - \frac{1}{3}\left|\frac{1}{2} \ - \frac{1}{2}\right\rangle \implies A = \frac{2}{3} \\ \Delta^- \longrightarrow n\pi^- &\implies \left|\frac{1}{2} \ - \frac{1}{2}\right\rangle \otimes |1 \ - 1\rangle = \left|\frac{3}{2} \ - \frac{3}{2}\right\rangle \implies A = 1 \end{aligned}$$

Figure C.3: Probability amplitudes corresponding to the decay of the different  $\Delta$  resonances given by the Clebsch-Gordan coefficients.

This Clebsch-Gordan coefficients lead directly to a probability ratio for the different channels in the  $\Delta$ -resonance decay, this is shown in the expression C.2.

$$\frac{P(\Delta^+ \longrightarrow p\pi^0)}{P(\Delta^+ \longrightarrow n\pi^+)} = 2 \quad \frac{P(\Delta^0 \longrightarrow n\pi^0)}{P(\Delta^0 \longrightarrow p\pi^-)} = 2 \quad (\text{C.2})$$

Both expressions, C.1 and C.2 are the basis of our discussion based on the isobar model. In the following sections we will apply these results to the specific reaction channels leading to a proton or neutron-pickup processes.

## C.1 Proton-pickup reactions

We will study here the reactions where the charge of the projectile is increased in one unit. Several are the open channels resulting on this process, we will start with the

simplest case, where the target is hydrogen. This single target proton can collide with a projectile neutron or proton, both cases will be discussed in the following. Finally we will perform the general extension to a heavy target.

### C.1.1 In proton-Nucleus reactions

We will study here the simplest case, a proton-Nucleus (p-N) inelastic collision, regarding that inelastic means through a  $\Delta$ -resonance excitation. All the possible reactions which can take place in such a scenario are represented by the Feynman diagrams shown in the figure C.4. In these diagram as, the top channel represents the projectile, while the bottom one is the target, in this case a single proton. Every diagram on this figure has a certain probability of take place in a proton-Nucleus collision, but not all of them will lead to a proton-pickup reaction. Actually, only 4 of them contribute to increase the Nucleus charge. These are the diagrams 5 and 7 exciting the  $\Delta^0$  and  $\Delta^+$  in the projectile, respectively, and diagrams 13 and 14 exciting the  $\Delta^0$  resonance in the proton target itself. We must stress that exciting the resonance within the target or projectile nucleons is indistinguishable in our measurements, in both cases the observable is a velocity loss in the primary residue.

Based on the theoretical isospin arguments given above, the relative probability of each diagram can be determined. We will discuss carefully one of them as an example, the rest are analog processes to this one. Diagram 5 in figure C.4 states that:



That is, the proton target and a neutron of the projectile exchange a  $\pi^0$  boson, exciting a  $\Delta^0$  resonance in the target, it further decays into a proton and a  $\pi^-$ . As derived in expression C.1, whenever an inelastic proton-neutron collision occurs, the probability of exciting a  $\Delta^0$  resonance is equal than exciting a  $\Delta^+$ , this means that half of the inelastic collisions will excite the  $\Delta^0$ , we get a factor 1/2 from here. In the resonance decay, the  $n + \pi^0$  channel has double probability than the  $p + \pi^-$  channel, and from here we get a 1/3 factor.

In addition, we have to take into account that we can excite, with equal probability, the resonance  $\Delta^0$  either in the target or the projectile, but diagram 5 accounts only for the excitation in the projectile (the excitation in the target is taken into account in the diagram 13). From here we have to introduce another 1/2 factor. Taking into account all these factors, the diagram 5 contributes with 1/12 of the number of proton-neutron inelastic collisions.

An analogous discussion can be derived for diagrams 7,13 and 14. The relative probability of each diagram are given in table C.1, where also the nature of the pion emitted

in the  $\Delta$  decay are shown.

Diagram	Probability	Pion nature
diagram 5	1/12	$\pi^-$
diagram 7	1/6	$\pi^0$
diagram 13	1/6	$\pi^0$
diagram 14	1/12	$\pi^-$
TOTAL	1/2	$\pi^0, \pi^-$

Table C.1: *Relative probability of the diagrams from figure C.4 with respect to the number of proton-neutron inelastic collisions. The nature of the emitted  $\pi$  in each case is also shown.*

As summary, a proton-pickup reaction in a proton-Nucleus collision can take place only when the proton collides with a neutron of the projectile, taking into account the contributions of all the diagrams involved in this process we get that a proton-pickup would take place in the half of the total proton-neutron number of inelastic collisions. In this process only  $\pi^-$  and  $\pi^0$  are emitted.

### C.1.2 In neutron-Nucleus reactions

Imagine that we have a target of neutrons instead of hydrogen. This is not realistic but it will be helpful to generalize the discussion to the Nucleus-Nucleus collision that will be done in the next section. We can derive a similar discussion to the previous case of proton-Nucleus. All the Feynman diagrams contributing in this case to the proton-pickup are shown in the figure C.5. Of course, not all of these diagrams contribute to the proton-pickup process, actually only diagrams 16 and 28 does. In table C.2

Diagram	Probability	Pion nature
diagram 16	1/24	$\pi^-$
diagram 28	3/8	$\pi^-$
TOTAL	5/12	$\pi^-$

Table C.2: *Relative probability of the diagrams from figure C.5 with respect to the number of neutron-neutron inelastic collisions. The nature of the emitted  $\pi$  in each case is also shown.*

### C.1.3 Extension to the Nucleus-Nucleus reactions

We can develop here the generalization to the Nucleus-Nucleus collisions, that will be a combination of both cases discussed previously. That is:

$$P_{N-N}^{Z+1} = \binom{1}{2}_{n-p} + \binom{5}{12}_{n-n} \quad (\text{C.4})$$

The reader must regard that, in order to have a proton-pickup reaction, the nucleon (either neutron or proton) of the target must collide only with a proton of the projectile. This selective process could be used to extract some information about the proton distribution matter in the projectile nucleus. It is also important to stress that in this proton-pickup reactions only  $\pi^0$  and  $\pi^-$  are emitted.

## C.2 Neutron-pickup reactions

Analogous to the preceding case, we can calculate the probability of each channel resulting on a neutron-pickup process. We Will start with the simplest case, the basis for the Nucleus-Nucleus collision generalization.

### C.2.1 In proton-Nucleus reactions

Only two diagrams of the figure C.4 are contributing to this process. Their relative probabilities are shown in the table C.3

Diagram	Probability	Pion nature
diagram 2	1/24	$\pi^+$
diagram 10	3/8	$\pi^+$
TOTAL	5/12	$\pi^+$

Table C.3: *Relative probability of the diagrams from figure C.4 with respect to the number of proton-proton inelastic collisions. The nature of the emitted  $\pi$  in each case is also shown.*

### C.2.2 In neutron-Nucleus reactions

Only two diagrams of the figure C.5 are contributing to this process. Their relative probabilities are shown in the table C.4

Diagram	Probability	Pion nature
diagram 18	1/12	$\pi^+$
diagram 20	1/6	$\pi^0$
diagram 24	1/12	$\pi^+$
diagram 25	1/6	$\pi^0$
TOTAL	1/2	$\pi^+, \pi^0$

Table C.4: *Relative probability of the diagrams from figure C.5 with respect to the number of proton-proton inelastic collisions. The nature of the emitted  $\pi$  in each case is also shown.*

### C.2.3 Extension to the Nucleus-Nucleus reactions

The extension to the general case of a Nucleus-Nucleus collision is easily done at this point:

$$P_{N-N}^{Z+1} = \binom{1}{2}_{n-p} + \binom{5}{12}_{n-n} \quad (\text{C.5})$$

It is important to note that, in this case, the only possibility to achieve such a reaction is colliding with a neutron in the projectile surface. In this sense, this mechanism should be sensitive somehow to the neutron distribution inside the projectile nucleus. Another key point is that only  $\pi^0$  and  $\pi^+$  are emitted in these reactions.

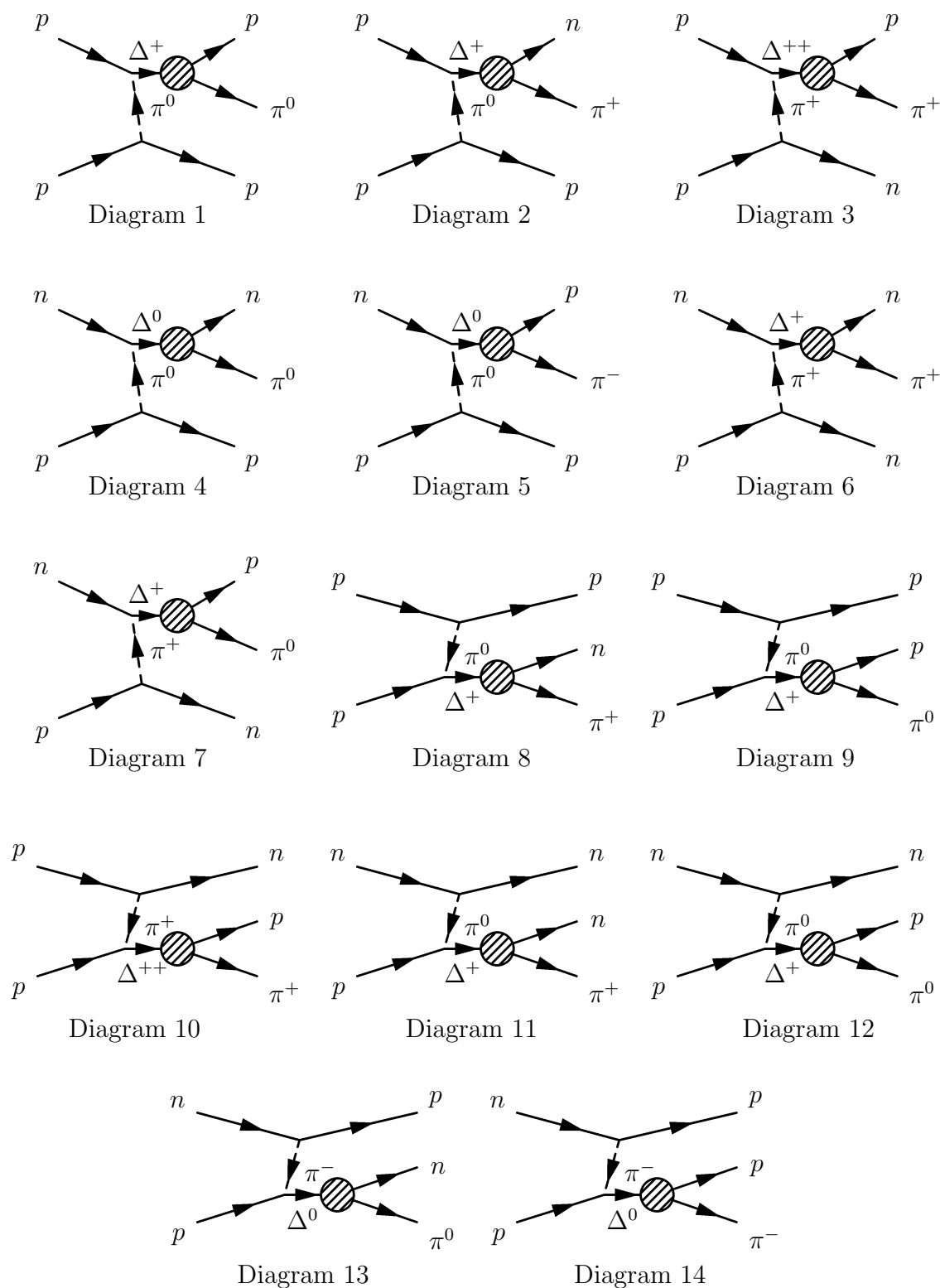


Figure C.4: All the possible Feynman diagrams corresponding to the proton-Nucleus inelastic reactions with a  $\Delta$  excitation, either in the projectile or the target.

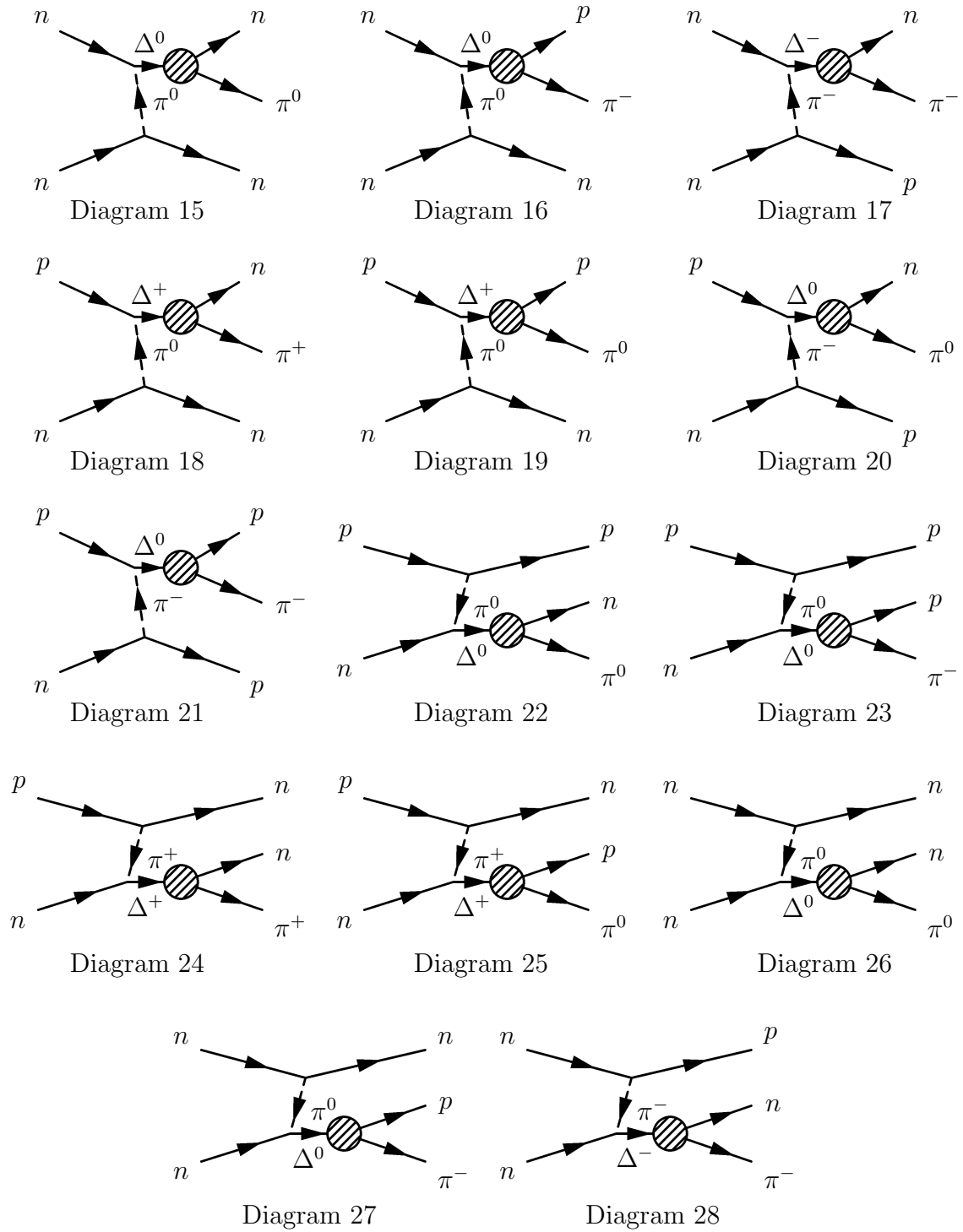


Figure C.5: All the possible Feynman diagrams corresponding to the neutron-Nucleus inelastic reactions with a  $\Delta$  excitation, either in the projectile or the target.



# Appendix D

## Glauber model notes

We will consider here the collision of two nuclei A and B. The normalized probability of finding a nucleon in the volume element  $d\mathbf{b}_A dz_A$  of the nucleus A is given by:

$$\int \rho_A(\mathbf{b}_A, z_A) d\mathbf{b}_A dz_A = 1 \quad (\text{D.1})$$

where  $\rho$  is the nuclear density,  $\mathbf{b}$  is the impact parameter (2-dimensional) and  $z$  is the "thickness" of the nucleus A at an impact parameter  $\mathbf{b}$ . In an analog way, the probability for the nucleus B would be:

$$\int \rho_B(\mathbf{b}_B, z_B) d\mathbf{b}_B dz_B = 1 \quad (\text{D.2})$$

The probability element  $dP$  of a nucleon-nucleon inelastic collision in a nucleus-nucleus collision is given by the products of three contributions, the probability of finding a nucleon of A inside the volume of B, the probability of finding a nucleon of B inside the volume of A and the probability of a nucleon-nucleon inelastic collision:

$$dP = \rho_A(\mathbf{b}_A, z_A) d\mathbf{b}_A dz_A \rho_B(\mathbf{b}_B, z_B) d\mathbf{b}_B dz_B t(\mathbf{b} - \mathbf{b}_A - \mathbf{b}_B) \sigma_{inel} \quad (\text{D.3})$$

We can define from here the "Thickness function" for the collision of nuclei A and B at an impact parameter  $\mathbf{b}$  relative to each other:

$$T(\mathbf{b}) = \int \rho_A(\mathbf{b}_A, z_A) d\mathbf{b}_A dz_A \rho_B(\mathbf{b}_B, z_B) d\mathbf{b}_B dz_B t(\mathbf{b} - \mathbf{b}_A - \mathbf{b}_B) \quad (\text{D.4})$$

This thickness function is automatically normalized according to expression D.1 and D.2:

$$\int T(\mathbf{b})d\mathbf{b} = 1 \quad (\text{D.5})$$

It is interesting now to introduce the normalized thickness function for each of the nucleus:

$$T_A(\mathbf{b}_A) = \int \rho_A(\mathbf{b}_A, z_A)dz_A \quad (\text{D.6})$$

$$\int T_A(\mathbf{b}_A)d\mathbf{b}_A = 1 \quad (\text{D.7})$$

Expression D.4 can then be written according to the previous equation as:

$$T(\mathbf{b}) = \int d\mathbf{b}_Ad\mathbf{b}_BT_A(\mathbf{b}_A)T_B(\mathbf{b}_B)(\mathbf{b} - \mathbf{b}_A - \mathbf{b}_B) \quad (\text{D.8})$$

The basis of the Glauber model have been presented easily, now we are able to extract from the expressions described above some specific features of nucleus-nucleus collisions. We will start with the probability of  $n$  nucleon-nucleon collisions in a nucleus-nucleus collision at impact parameter  $\mathbf{b}$ . We will consider  $A$  and  $B$  the mass numbers of both nuclei, respectively:

$$P(n, \mathbf{b}) = \binom{AB}{n} [T(\mathbf{b})\sigma_{NN}^{inel}]^n [1 - T(\mathbf{b})\sigma_{NN}^{inel}]^{AB-n} \quad (\text{D.9})$$

From here, we can extract the total probability for an inelastic event in the collision of  $A$  and  $B$  at an impact parameter  $\mathbf{b}$ . This is just the sum of D.9 from  $n = 1$  to  $n = AB$ :

$$\frac{d\sigma_{inel}^{AB}}{d\mathbf{b}} = \sum_{n=1}^{AB} P(n, \mathbf{b}) = 1 - [1 - T(\mathbf{b})\sigma_{NN}^{inel}]^{AB} \quad (\text{D.10})$$

Therefore, integrating we can extract the total inelastic cross-section for the collision between  $A$  and  $B$ :

$$\sigma_{inel}^{AB} = \int d\mathbf{b} \left\{ 1 - [1 - T(\mathbf{b})\sigma_{NN}^{inel}]^{AB} \right\} \quad (\text{D.11})$$

In order to clarify, we have to mention that the impact parameter is a 2-dimensional vector. The total inelastic cross-section is then given by:

$$\sigma_{inel}^{AB} = 2\pi \int b db \left\{ 1 - [1 - T(b)\sigma_{NN}^{inel}]^{AB} \right\} \quad (\text{D.12})$$

## D.1 Special simplifications for the charge-pickup reactions

The expressions derived above from the Glauber model, will be rather simples in the case of a cold charge-pickup reaction. These processes are very peripheral and take place in a single collision. In the case of the proton, its thickness function is given by a  $\delta$  function, the expression D.8 will translate as:

$$T_{pN}(\mathbf{b}) = \int d\mathbf{b}_A d\mathbf{b}_B T_A(\mathbf{b}_A) \delta(\mathbf{b}_B) \delta(\mathbf{b} - \mathbf{b}_A - \mathbf{b}_B) \quad (\text{D.13})$$

and then, integrating we obtain:

$$\boxed{T_{pN}(\mathbf{b}) = T_A(\mathbf{b})} \quad (\text{D.14})$$

We can calculate now the probability of a single nucleon-nucleon collision in a proton-Nucleus reaction. The expression D.9 will be rewritten as:

$$P(1, \mathbf{b}) = A [T_A(\mathbf{b})\sigma_{NN}^{inel}] [1 - T_A(\mathbf{b})\sigma_{NN}^{inel}]^{A-1} \quad (\text{D.15})$$

And, finally, the total inelastic cross-section in a proton-Nucleus reaction will be expressed in this special case as:

$$\sigma_{inel}^{pA} = 2\pi \int b db \left\{ 1 - [1 - T_A(b)\sigma_{NN}^{inel}]^A \right\} \quad (\text{D.16})$$